Vertical integration of an electro-absorption modulator onto a VCSEL for high-speed communications

Ludovic Marigo-Lombart

▶ **To cite this version:**

Ludovic Marigo-Lombart. Vertical integration of an electro-absorption modulator onto a VCSEL for high-speed communications. Micro and nanotechnologies/Microelectronics. Université Toulouse 3 Paul Sabatier (UT3 Paul Sabatier), 2018. English. NNT : . tel-01975484v1

HAL Id: tel-01975484

https://laas.hal.science/tel-01975484v1

Submitted on 9 Jan 2019 (v1), last revised 18 Nov 2019 (v2)

HAL is a multi-disciplinary open access archive for the deposit and dissemination of scientific research documents, whether they are published or not. The documents may come from teaching and research institutions in France or abroad, or from public or private research centers.

L'archive ouverte pluridisciplinaire **HAL**, est destinée au dépôt et à la diffusion de documents scientifiques de niveau recherche, publiés ou non, émanant des établissements d'enseignement et de recherche français ou étrangers, des laboratoires publics ou privés.

Université Fédérale
Toulouse Midi-Pyrénées

THÈSE

En vue de l'obtention du

DOCTORAT DE L'UNIVERSITÉ DE TOULOUSE

Délivré par :

Université Toulouse 3 Paul Sabatier (UT3 Paul Sabatier)

Cotutelle internationale avec "VRIJE UNIVERSITEIT BRUSSEL (VUB)"

Présentée et soutenue par :
Ludovic Marigo-Lombart
le 05 Novembre 2018

Titre :

Vertical integration of an electro-absorption modulator onto a VCSEL for high-speed communications

---

École doctorale et discipline ou spécialité :
ED GEET : Photonique et Systèmes Optoélectroniques

Unité de recherche :
Laboratoire d'Analyse et d'Architecture des Systèmes (LAAS-CNRS)

Directeur/trice(s) de Thèse :

Guilhem ALMUNEAU, Chargé de Recherche CNRS, LAAS-CNRS
Krassimir PANAJOTOV, Professeur, TONA-VUB

Jury :

Isabelle SAGNES, Directrice de Recherche, C2N-CNRS (Rapporteur)
Laurent CERUTTI, Maître de Conférence, IES-Université de Montpellier (Rapporteur)
Heidi OTTEVAERE, Professeur, TONA-VUB (Examinateur)
Olivier LLOPIS, Directeur de Recherche, LAAS-CNRS (Examinateur)
Elyahou KAPON, Professeur, EPFL (Invité)

ABSTRACT

In this PhD thesis, we describe experimental and theoretical studies on Electro-Absorption Modulator (EAM) for its vertical integration onto a Vertical-Cavity Surface-Emitting Laser (VCSEL) to reach high-speed modulation for optical communications. The external modulation of the emitted light by the VCSEL, biased in continuous-wave, avoids the physical limitation due to the carrier dynamics encountered in directly-modulated lasers and thus enables very high frequency bandwidth. Furthermore, this fully monolithic integrated approach decreases the footprint and thus the energy consumption.

In the first part of the manuscript, we describe the design of the EAM-VCSEL device. First, we explain the electro-absorption effect and its modelling; its combination with the transfer matrix method, and the implementation of the combined model for optimization of the quantum well parameters: thickness, barrier Al-content and applied electric field. Then, based on the state-of-the-art of the vertical modulators, we design an Asymmetric Fabry-Perot modulator structure to improve the electro-absorption in the top cavity. This EAM structure is integrated onto a standard VCSEL device while considering the decoupling between the two cavities.

I present afterwards the fabrication of these complex devices. The epitaxial growth of EAM and EAM-VCSEL structures is presented as an implementation of pre-growth calibration routine to achieve the expected characteristics and the post-growth characterization of the wafers. Then, we present an innovative technological solution used to facilitate the global process. We used a double resist stack for a self-aligned process for the modulator, useful for the mesa etch, the sidewalls passivation and the metallization, all realized with only one single photolithography step. This process is used for the static characterization of the EAM. We demonstrate the feasibility of these devices by carrying out static reflectivity measurements as a function of the temperature and the applied EAM voltage. This allows to validate the previous absorption model. We also present the static characterization of the EAM-VCSEL with LIV curves and spectrum measurements.

Finally, the last two chapters present the high-frequency aspect of the project. Based on BCB on an innovative planarization process about the use of a nano-imprint tool to ensure a perfect flat BCB layer surface, we present the global process flow step by step. Then, thanks to our BCB electrical characterization we compared two access line designs to decrease as much as possible the parasitic capacitance. Finally, we characterize the modulator cut-off frequency as a proof of concept and demonstrate a modulation of 29 GHz after its integration onto the VCSEL, comparable to the best results in the VCSEL litterature.

RÉSUMÉ

Dans cette thèse nous décrivons l'étude expérimentale et théorique d'un modulateur à électro-absorption (EAM) en vue de son intégration verticale sur un VCSEL (Laser à Cavité Verticale Emettant par la Surface) pour des communications optiques à très hautes fréquences. La modulation externe de la lumière émise par le VCSEL, alimenté en continu, permet de s'affranchir de la limite physique due à la dynamique des porteurs et devrait donc permettre d'augmenter la bande passante comparé à un VCSEL à modulation directe. Notre approche permet de considérablement diminuer la surface utile de par son intégration monolithique verticale et ainsi la consommation électrique.

La première partie est consacrée au design du composant EAM-VCSEL. Tout d'abord nous expliquerons l'effet d'électro-absorption et comment le modéliser, sa combinaison avec la méthode de transfert matricielle, et son implémentation pour optimiser les paramètres physiques des puits quantiques tels que : l'épaisseur, la concentration d'aluminium dans les barrières et le champ électrique à appliquer. Ensuite, basé sur l'état de l'art des modulateurs verticaux, nous présenterons la conception d'une structure Fabry-Pérot asymétrique pour augmenter l'effet d'absorption dans la cavité. Cette structure optimisée du modulateur sera ensuite intégrée sur une structure standard de VCSEL tout en considérant le découplage optique entre ces cavités.

Je présenterai ensuite la fabrication de ces composants complexes. Nous aborderons la croissance des structures EAM et EAM-VCSEL avec notamment l'optimisation de la calibration des cellules et les caractérisations après croissance. Ensuite nous présentons un procédé lift-off innovant visant à faciliter le procédé complet. Ce procédé sera utilisé pour fabriquer le modulateur afin de le caractériser en régime statique. Nous démontrons ainsi son fonctionnement en mesurant la réflectivité en fonction de la température et de la tension appliquée ce qui nous permet d'avoir une validation du modèle précédent. Nous présentons enfin la caractéristique LIV du modulateur-VCSEL ainsi que son spectre en longueur d'onde.

Les deux derniers chapitres seront consacrés à la partie fabrication et caractérisation hyper-fréquence du composant. Nous avons conçu, à partir de nos caractérisations du BCB, des accès optimums pour diminuer les pertes électriques lors de l'injection. Nous présenterons ensuite un procédé innovant pour la planarisation du BCB en vue de l'injection électrique hyper-fréquence. Nous décrirons le procédé de fabrication complet du modulateur-VCSEL étape par étape. Enfin, nous montrerons les résultats hyper-fréquence du modulateur seul et intégré sur le VCSEL. Nous avons ainsi atteint une modulation de 29 GHz, comparable a l'état de l'art actuel des VCSELs.

PUBLICATIONS

- **International peer reviewed journal**
  - **paper A: L. Marigo-Lombart**, A. Arnoult, L. Mazenq, P. Dubreuil, B. Reig, N. Mauran, H. Thienpont, K. Panajotov, G. Almuneau, "Single lithography-step self-aligned fabrication process for Vertical-Cavity Surface-Emitting Lasers", Materials Science in Semiconductor Processing, vol. 61, April 2017, pp 35-38, http://dx.doi.org/10.1016/j.mssp.2016.12.026
  - **paper B: L. Marigo-Lombart**, S.Calvez, A. Arnoult, H. Thienpont, K. Panajotov and G. Almuneau, "Oxide-confined VCSELs fabricated with a simple self-aligned process flow", Semiconductor Science and Technology, vol. 32, Number 12, Oct. 2017, https://doi.org/10.1088/1361-6641/aa90ae
  - **paper C: L. Marigo-Lombart**, S. Calvez, A. Arnoult, H. Thienpont, G. Almuneau, K. Panajotov, "Vertical Electro-Absorption Modulator design and its integration in a VCSEL", Journal of Physics D: Applied Physics, 2018, vol. 51, no 14, p. 145101. https://doi.org/10.1088/1361-6463/aab1dc
  - **paper D:** K. Louarn, Y. Claveau, **L. Marigo-Lombart**, C. Fontaine, A. Arnoult, F. Piquemal, A. Bounouh, N. Cavassilas, G.Almuneau, "Effect of low and staggered gap quantum wells inserted in GaAs tunnel junctions", Journal of Physics D: Applied Physics, 2018, vol. 51, no 14, p. 145107. https://doi.org/10.1088/1361-6463/aab1de
- **International peer reviewed journal — On going**
  - **paper E: L. Marigo-Lombart**, C. Viallon, A. Rumeau, L. Mazenq, A. Ghannam, H. Thienpont, K. Panajotov, G. Almuneau, "High-speed electrical injection for Electro-Absorption Modulator vertically integrated on a VCSEL using low permittivity BCB" - Submitted in IEEE Journal of Lightwave Technology
  - **paper F: L. Marigo-Lombart**, C. Viallon, A. Rumeau, H. Thienpont, K. Panajotov, G. Almuneau, "Electro-Absorption Modulator onto VCSEL at 30 GHz for very high-speed data communications" - Submitted in IOP Journal of Physics: Photonics.
  - **paper G: L. Marigo-Lombart**, C. Viallon, A. Rumeau, H. Thienpont, K. Panajotov, G. Almuneau, "Study of a very high-speed III-V Electro-Absorption Modulator to be integrated onto a VCSEL"

- **International conferences**

  1. **L. Marigo-Lombart**, C. Viallon, A. Rumeau, O. Gauthier-Lafaye, A. Monmayrant, H. Thienpont, K. Panajotov and G. Almuneau, "High frequency characterization of a vertical electro-absorption modulator for data communications", IEEE Microwave Photonics, Toulouse, France - 22-25 Oct. 2018 - Poster accepted - **Proceeding**
  2. **L. Marigo-Lombart**, S. Calvez, A. Arnoult, A. Rumeau, C. Viallon, H. Thienpont, K. Panajotov, G. Almuneau, "Design of an Electroabsorption modulator for integration onto a VCSEL", SPIE Photonics Europe, Apr. 22 - 26 2018 - Oral presentation
  3. **L. Marigo-Lombart**, S. Calvez, A. Arnoult, A. Rumeau, C. Viallon, H. Thienpont, K. Panajotov, G. Almuneau, "Integration of Electro-Absorption Modulator in a Vertical-Cavity Surface-Emitting Laser", SPIE Photonics West, Jan. 27 - 01 Feb. 2018 - Oral presentation - **Proceeding**
  4. K. Louarn, C. Fontaine, A. Arnoult, Y. Claveau, **L. Marigo-Lombart**, I. Massiot, J. Colin, C. Cornille, N. Cavassillas, F. Piquemal, A. Bounouh, G. Almuneau, "Pseudomorphic and metamorphic (Al)GaAsSb/(Al)InGaAs MBE grown tunnel junctions for GaAs based Multi-Junction Solar cells", EU PVSEC, Sept. 25-29 2017 Amsterdam, Holland - Poster presentation
  5. **L. Marigo-Lombart**, A. Arnoult, C. Viallon, S. Calvez, A. Lecestre, B. Reig, A. Rumeau, H. Thienpont, K. Panajotov, and G. Almuneau, "Vertical integration of an electro-absorption modulator within a VCSEL device", ICTON July 2-6 2017, Gerona, Spain - doi: 10.1109/ICTON.2017.8024894 - Invited talk - **Proceeding**
  6. **L. Marigo-Lombart**, A. Arnoult, S. Calvez, H. Thienpont, K. Panajotov, and G. Almuneau, "Vertical integration of an Electro-Absorption Modulator on a VCSEL to reach very high modulation frequency", VCSEL day, June 08-09 2017, Cardiff, Wales, UK - Oral presentation
  7. **L. Marigo-Lombart**, L. Mazenq, L. Salvagnac, G. Libaude, B. Rousset, B. Reig, P. Dubreuil, N. Mauran, A. Arnoult, H. Thienpont, K. Panajotov, G. Almuneau, "VCSELs fabricated using self-aligned processing", MNE Sept. 18-22 2016, Vienna, Austria. - Poster presentation
  8. **L. Marigo-Lombart**, A. Arnoult, L. Mazenq, P. Dubreuil, B. Reig, N. Mauran, H. Thienpont, K. Panajotov, G. Almuneau, "VCSELs fabricated using self-aligned processing", VCSEL Day, June 03 2016 Darmstadt, Germany - Oral presentation

9. **L. Marigo-Lombart**, J.-B. Doucet, A. Lecestre, B. Reig, B. Rousset, H. Thienpont, K. Panajotov, G. Almuneau, "Self-aligned BCB planarization method for high-frequency signal injection in a VCSEL with an integrated modulator". Proc. SPIE 9892, Semiconductor Lasers and Laser Dynamics VII, 98921R, April 28, 2016, doi:10.1117/12.2227529 - Poster presentation - **Proceeding**

- **National conferences**

1. **L. Marigo-Lombart**, S. Calvez, O. Gauthier-Lafaye, A. Monmayrant, A. Arnoult, A. Rumeau, C. Viallon, H. Thienpont, K. Panajotov and G. Almuneau, "Optimisation et caractérisation hyper-fréquence d'un modulateur en vue de son intégration verticale sur un VCSEL", JNMO, June 13-15 2018 - cap Esterel, France - Poster presentation
2. K. Louarn, C. Fontaine, A. Arnoult, Y. Claveau, **L. Marigo-Lombart**, I. Massiot, J. Colin, C. Cornille, N. Cavassilas, F. Piquemal, A. Bounouh and G. Almuneau, Journées Nationales du Photovoltaïque, Dec. 5-8 2017, Dourdan, France - Oral presentation
3. K. Louarn, Y. Claveau, A. Arnoult, C. Fontaine, J. Colin, C. Cornille, I. Massiot, **L. Marigo-Lombart**, F. Piquemal, A. Bounouh, N. Cavassilas and G. Almuneau, "Jonctions tunnel AlGaAsSb/AlGaInAs accordées et relaxées sur substrat GaAs pour les applications photovoltaïques", GDR Pulse, Oct. 2-5 2017, Paris, France - Poster presentation
4. A. Arnoult, J. Colin, **L. Marigo-Lombart**, K. Louarn, C. Cornille, C. Fontaine, "De l'intérêt du couplage d'outils de caractérisation in situ pour la croissance de structures complexes", GDR Pulse, Oct. 2-5 2017, Paris, France - Oral presentation
5. **L. Marigo-Lombart**, A. Arnoult, L. Mazenq, P. Dubreuil, B. Reig, J.-B. Doucet, B. Rousset, N. Mauran, H. Thienpont, K. Panajotov, G. Almuneau, "Développement de briques technologiques pour la fabrication d'un VCSEL avec modulateur intégré verticalement", JNMO, May 30 - June 1st 2016 - Les Issambres, France - Poster presentation
6. **L. Marigo-Lombart**, A. Lecestre, P. Dubreuil, B. Reig, G. Almuneau, "Gravure du BCB à la plateforme technologique du LAAS-CNRS", Journée RTB Gravure, Dec. 9, 2015, Toulouse, France - Oral Presentation

LIST OF ACRONYMS

AFM	Atomic Force Microscope
ASFP	Asymetric Fabry-Perot
BCB	Bis-BenzoCyclobuten
CR	Contrast Ratio
DBR	Distributed Bragg Reflector
EA	Electro-Absoption
EAM	Electro-Absorption Modulator
EO	Electro-Optic
ER	Electro-Refractive
FIB	Focus Ion Beam
FOM	Figure of Merit
FP	Fabry-Perot
hh	Heavy-Hole
lh	Light-Hole
MBE	Molecular Beam Epitaxy
MQW	Multiple Quantum Well
OFM	Optical Flux Monitor
PL	Photo-Luminescence
QCSE	Quantum-Confined Stark Effect
QW	Quantum Well
SEM	Scanning Electron Microscope
VCSEL	Vertical-Cavity Surface Emitting Laser

CONTENTS

List of Acronyms vii

1 INTRODUCTION 1
- 1.1 VCSEL for optical communications . . . 3
- 1.2 VCSEL principle and fabrication . . . 4
  - 1.2.1 QW gain region for lasers . . . 5
  - 1.2.2 Threshold gain . . . 6
  - 1.2.3 Mirrors . . . 7
  - 1.2.4 Fabry-Perot cavity . . . 9
  - 1.2.5 Lateral confinement . . . 10
- 1.3 Physical limits of direct modulation and improvements . . . 12
  - 1.3.1 Device improvements . . . 12
  - 1.3.2 Alternatives to direct modulation . . . 12
- 1.4 PhD motivations . . . 14
- 1.5 Structure of the thesis . . . 14

2 ELECTRO-ABSORPTION MODULATOR DESIGN AND INTEGRATION ONTO A VCSEL 17
- 2.1 Absorption effect . . . 18
  - 2.1.1 Semiconductor bulk absorption without electric field . . . 18
  - 2.1.2 Semiconductor bulk absorption with electric field . . . 20
  - 2.1.3 Absorption in a Quantum Well subject to an electric field . . . 20
  - 2.1.4 Excitonic absorption . . . 22
- 2.2 Absorption model . . . 24
- 2.3 Parameter optimization of one single Quantum Well . . . 26
- 2.4 Vertical modulators: state-of-the art and applications . . . 28
- 2.5 Vertical structure of the EAM : MQW embedded in an Asymetric Fabry Perot 30
  - 2.5.1 Cavity design . . . 30
  - 2.5.2 Mirror layers . . . 31
  - 2.5.3 Transfer Matrix Method . . . 32
- 2.6 Vertical integration of the EAM onto the VCSEL . . . 33
- 2.7 Conclusion and perspectives . . . 35

3 FABRICATION AND CHARACTERIZATION IN STATIC OPERATION 37
- 3.1 Epitaxial growth . . . 38

3.1.1 Structures description . . . 39
3.1.2 Particularities of epitaxial growth of EAM-VCSEL . . . 41
3.1.3 Thickness control . . . 45
3.1.4 Epitaxy recipes . . . 50
3.2 Post-growth characterisation . . . 51
3.2.1 FTIR mappings . . . 51
3.2.2 Reflectivity combined with PL . . . 52
3.2.3 Roughness and defects . . . 54
3.3 Fabrication process developments . . . 56
3.4 Self-Aligned process . . . 57
3.4.1 Challenge . . . 57
3.4.2 Air post VCSEL and EAM fabrication . . . 58
3.4.3 Additional step for VCSEL lateral oxidation . . . 62
3.5 Static characterization . . . 66
3.5.1 Electro-Absorption static behavior . . . 66
3.5.2 VCSEL static modulation . . . 80
3.6 Conclusion . . . 82

4 HIGH-FREQUENCY FABRICATION AND DESIGN OPTIMIZATION 85
4.1 BCB planarisation . . . 86
4.1.1 Why BCB and what are the technological challenges ? . . . 86
4.1.2 Planarization process development . . . 88
4.2 High-frequency design and implementation . . . 93
4.2.1 Dielectric Microwave characterization of BCB . . . 93
4.2.2 Extraction of the electrical characteristic of BCB . . . 95
4.2.3 Results . . . 95
4.3 High-frequency injection design . . . 96
4.3.1 Coplanar Waveguide access . . . 97
4.3.2 Process . . . 99
4.3.3 Impact of the substrate doping with the CPW design . . . 99
4.3.4 Microstrip line access . . . 101
4.4 Global Process . . . 103
4.5 Conclusion . . . 108

5 HIGH-FREQUENCY OPERATION 111
5.1 EAM high-frequency characterization . . . 112
5.1.1 Optical alignement . . . 112
5.1.2 Vector Network Analyzer (VNA) implementation . . . 113
5.1.3 RF synthesizer and spectrum analyzer . . . 115

5.1.4 De-embedding . . . 120
5.1.5 Photodiode calibration . . . 121
5.1.6 Results . . . 123
5.2 High-frequency characterization of EAM and EAM-VCSEL — New photodiode . . . 124
5.2.1 Newfocus photodiode response . . . 125
5.2.2 Characterization with the synthesiser set up . . . 125
5.2.3 Characterization with the VNA set up . . . 127
5.2.4 Comparaison VNA - synthesiser . . . 127
5.2.5 Study with several parameters . . . 128
5.2.6 Impedance extraction . . . 130
5.2.7 EAM-VCSEL . . . 136
5.3 Conclusion and possible improvements . . . 139

6 CONCLUSION 141
6.1 Work done and collaborations . . . 141
6.2 Principal results . . . 142
6.2.1 Simulation of EAM and EAM-VCSEL . . . 142
6.2.2 Fabrication of EAM and EAM-VCSEL . . . 143
6.2.3 Characterization of EAM and EAM-VCSEL . . . 143
6.3 Perspectives . . . 145
6.3.1 Design of EAM and EAM-VCSEL . . . 145
6.3.2 Improved epitaxial structures . . . 145
6.3.3 Fabrication . . . 146
6.3.4 Characterization . . . 147

7 APPENDIX A: PROCESSING LIST OF EAM-VCSEL DEVICE 149

8 APPENDIX B 155
8.1 Tips . . . 155
8.2 Mask improvements . . . 157

9 APPENDIX C: EPITAXY RECIPES 159

10 APPENDIX D: METAL THICKNESS 165

BIBLIOGRAPHY 167

1 INTRODUCTION

Vertical-Cavity Surface-Emitting Lasers (VCSEL) are nowadays widely used in many applications such as optical mouse, optical sensors [1] and in our smartphones [2], 3D imaging systems (Project Tango: Princeton Optronics & Google [3]), imaging and gesture recognition (infrared projector in Intel RealSense project [4]) and facial recognition (for the Iphone [5] and Xiaomi [6] and Huawei [7]), LIDAR for future autonomous vehicles [8] and more importantly have replaced edge emitters for short distance optical communications as in data centers [9].

Over the last 20 years more than one billion VCSEL have been produced [10]. Finisar reported their 150 millionth VCSEL shipped in 2013, II-VI reported their 200 millionth VCSEL shipped in the same year and Philips Photonics reported their 100 millionth VCSEL in 2014. This market is expected to grow at a compound annual growth rate (CAGR) of 22% from 2015 to 2020 (see Fig. 1.1), expected to reach USD 2,105.3 million by 2020 [11] [12]. Optical fiber data transmission is expected to record the highest growth within the VCSEL market: $ 615.1 million by 2018, for a CAGR of 31.2 percent during the 2013-2018 period [13]. This increase follows up the data communication and datacenter expansion scheduled in the next years. As an example of the need of very high number of optical transmission flows, optical interconnects number per data center will increase from 10^6 in 2012 to 10^9 in 2020 [14] [15].

Indeed, the constant increase of the data traffic has forced all research groups and industrials to find and explore others solutions than the standard VCSEL technology developed several decades ago to increase the data transfer rate and decrease the energy consumption. To present the topic of this PhD, this introduction chapter is divided as follow:

In the first section we present how and why VCSELs have been widely used for high speed communications. Thanks to the electrical and optical particular properties inherent to the VCSEL devices, they are established as major players in short-haul communica-

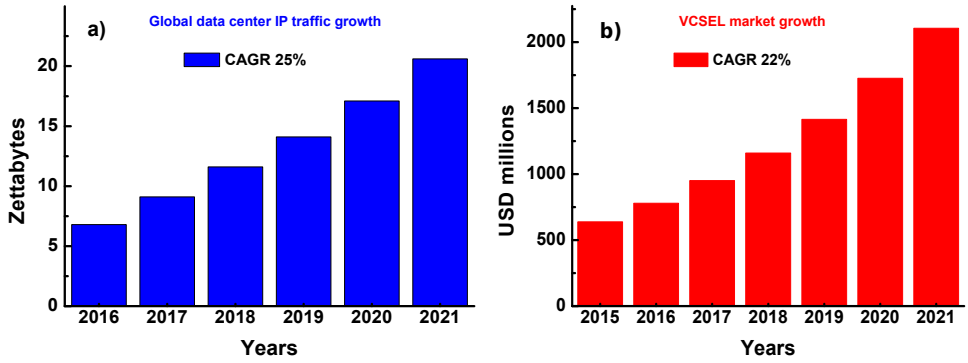

Figure 1.1: (a) Data center traffic growth from 2016 to 2021 with a CAGR of 25 %. (b) VCSEl market growth up to 2021 with a CAGR of 22 %. From cisco

tions links as for example in datacenters.

The second section will focus on semiconductor laser operating principles which are of course valid for VCSELs. We will describe the different losses that occur in this device and how they have to be compensated to reach an optical gain and thus a lasing behavior of the device. Then, we present the Fabry-Perot cavity design to reach the expected emission wavelength. This cavity is embedded between two mirrors that will be described and we will present the different materials that can be used. Finally, we present different configurations to decrease the laser threshold, of lateral confinement such as mesa, lateral oxidation and proton implentation.

The third section will depict the physical limits of the direct modulated VCSEL due to the carrier dynamics limitation that bring us to consider new approaches. We present the different ways to remove this limitation such as the splitting of the modulating and the emitting part and their lateral or vertical integration.

In the forth section we will present the PhD motivation that leads us to work on the vertical integration of an Electro-Absorption Modulator onto a VCSEL. Based on the previous researches, we will describe the different approaches we used to conduct this study.

In the fifth section We will outline the manuscript by describing step by step the reasoning and the key points of the thesis such as the design of the modulator itself, its vertical integration onto the VCSEL, their fabrication and their static and high frequency characterization.

1.1 VCSEL FOR OPTICAL COMMUNICATIONS

With the global data traffic increase due to the explosion of demand for smartphones and connected objects (Internet of Things), data centers are a strategic point for the timely processing of the information. Data centers are more and more present in all countries to decrease the data traffic transport distance and increase the data transmission bandwidth. They are also getting larger and larger and are now huge warehouses of several hundreds of meters long.

To decrease the electrical consumption and increase the frequency bandwidth, copper-based interconnects have been replaced by short-haul optical links. In this financial and electrical consumption race, VCSELs have been prefered to edge emitters. Indeed, their low drive current, circular optical beam which make the fiber coupling easier and more efficient and the possibility to test them directly on the wafers are some of the benefits they offer.

For distance up to 300 m, Multi-Mode (MM) VCSELs are used, while for longer distance, even if the output power is lower, Single Mode (SM) are used to avoid any distorsion and mode competition along the optical fiber.

We can notice in Fig. 1.2 that between 2009 and 2011, 90% of the optical links are less than 100 m where MM VCSEL are predominant sources. Between 2012 and 2014 the trend is exactly the same [16].

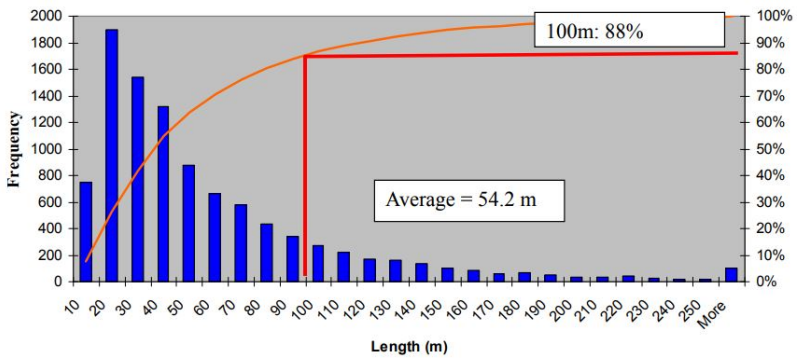

Figure 1.2: Number of manufactured products for data center multimode cable channel distribution communication between 2009 and 2011. Number of devices are plotted as a function of the connection length. In orange is represented the cumulative percentage. Source: Corning Cable Systems

Nowadays, the main challenges of these structures is to provide very high-speed data transmission while decreasing the electrical consumption. Indeed, in 2017, 2% of the global worldwide electricity use was for data centers, and this number is expected to grow to 5% in 2020 [17]. In France around 10 % of the electrical consumption is used for the data centers [18].

It is important to note that between 40 and 50 % of this electricity is used for cooling down the electronics [19] so new solutions need to be found. Indeed, this electricity consumption has to be decreased from 25 mW/Gb to 1 mW/ Gb in 2020 [20]. To this aim, some data centers are built in north countries to take advantage of the low temperature while opening the doors or can be immerged in the sea [21]. Some companies like Facebook [22] and Google [23] declared to use clean data center energy but the electrical consumption still remains a problem. The main solution is to play on both sides of the problem and to decrease the consumption of each electronic component.

This global competition drives a lot of improvements of private and public research institutes. Indeed, to meet the actual and future demand, optical data transmission will have to reach soon 100 Gb/s as shown in Fig. 1.3.

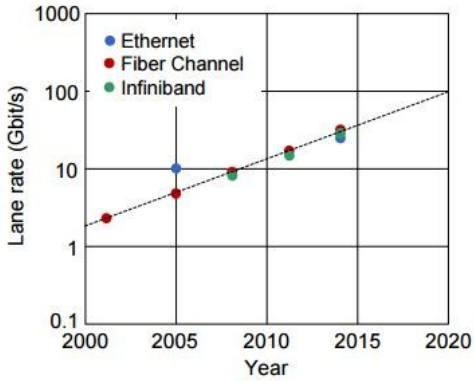

Figure 1.3: Optical bandwidth increase up to 2020

We will discuss in the next sections about the principle of VCSELs and their actual state-of-the art in terms of modulation bandwidth. We will only focus in this manuscript on VCSELs with modulation frequency bandwidth without consideration of all the modulation formats from Non Return to Zero to Phase Amplitude Modulation or Quadratic Amplitude Modulation up to Discrete Multi Tone.

1.2 VCSEL PRINCIPLE AND FABRICATION

We have seen previously why VCSELs have been preferred to edge emitters for short-haul high-speed optical communications in data centers.
We will focus in this section on the physical principles of such devices and how to fabricate them by describing first the implementation of quantum wells in semiconductor lasers, the threshold gain, the mirrors and then the Fabry-Perot cavity to select specific modes. All parts of a VCSEL are represented in Fig. 1.6.

1.2.1 *QW gain region for lasers*

Quantum well lasers are based on quantum confinement effects which allow to improve the current threshold, the adjustment of the emission wavelength and the sensitivity with the current or the temperature.

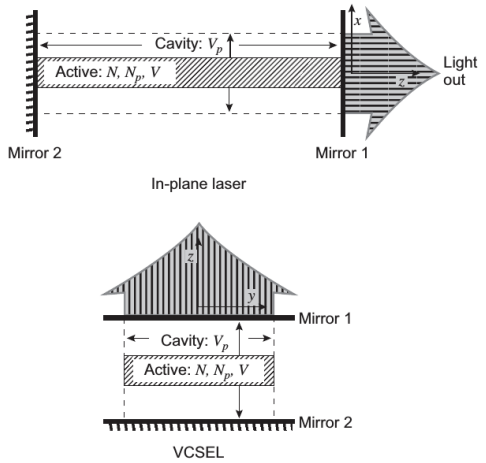

Figure 1.4: Schematic of a edge-emitter laser (top) and a VCSEL (bottom). From [24]

In a laser diode, the current threshold is proportionnal to the active region volume, following the relation [24]

$$I_{th} \approx \frac{qBN_{th}^2 V}{\eta_i} \tag{1.1}$$

where q is the elementary charge, η_i is the current injection efficiency, B is the bimolecular recombination coefficient in III-V material and is about 10^{-10} cm^3/s, N_{th} is the required threshold carrier density and finally, V is the active region volume.

To decrease the current threshold it is thus necessary to decrease the active region volume. In a simple PN junction laser the active region thickness is typically about 1 µm whereas with double heterojunction laser it decreases around 200 nm. Indeed, carriers are confined by the potential barriers due to the gap discontinuity and photons are confined by the optical barriers due to the refractive index variations.

In this cavity configuration, due to the abrupt variation of the refractive index, the photons are very well confined but, to improve both the electrons and holes confinement, quantum wells have to be used. However, photons spread over a much more larger place than the quantum well thickness, of few nanometers, we thus have a decrease of the overlap photons-carriers. This overlap is called confinement factor and is expressed, for a L_{act}-thick active region, as [25]:

$$\Gamma = \int_{-L_{act}/2}^{L_{act}/2} |E|^2(z)dz / \int_{-\infty}^{+\infty} |E|^2(z)dz \tag{1.2}$$

where E(z) is the electric field variation along z axis.

To reach lasing operation, the product confinement factor by the material gain of the active region has to be higher than the absorption losses (α) and the losses due to the external emission.

$$\Gamma g \geqslant \alpha + \frac{1}{L_{act}} \ln(\frac{1}{R}) \tag{1.3}$$

The factor Γg is called modal gain.

It is then possible to extend this expression to consider that the absorption is different inside the cavity (thus called α_i) or outside the cavity (then called α_e), and that both mirrors surrounding the cavity may have different reflectivities (called R_1 and R_2).

$$\Gamma g \geqslant \Gamma\alpha_i + (1-\Gamma)\alpha_e + \frac{1}{2L_{act}} \ln(\frac{1}{R_1 R_2}) \tag{1.4}$$

An approximation can be done to facilitate the numerical calculation of the confinement factor [25]:

$$\Gamma = \frac{D^2}{2+D^2} \quad \text{where D is the normalized active region thickness with} \quad D = \frac{2\pi}{\lambda}(n_i^2 - n_e^2)^{1/2} L_{cav} \tag{1.5}$$

where n_i and n_e are the refractive index respectively inside and outside the cavity. For a standard diode with $\alpha \approx 10$ cm^{-1}, $L_{cav} \approx 300$ µm and $R \approx 0.3$, modal gain is around 50 cm^{-1}. For a double heterostructure of 100 nm, $\Gamma \approx 0.4$ and the volumic gain g has to be $\approx 10^2$ cm^{-1} to reach the same modal gain value. At the opposite, due to the lower overlap in one single quantum well, the volumic gain has to be $\approx 10^3$ cm^{-1} in such a cavity design. It it thus mandatory to use multiple quantum wells structure to improve the modal gain and thus improve the lasing condition.

1.2.2 *Threshold gain*

In the case of VCSEL, the L_{act}-thick active region, composed of multiple quantum wells, has an effective length of $L_{act} = N_{qw} L_{qw}$ where N_{qw} and L_{qw} are respectively the number of quantum wells and their thickness.

In this structure, the threshold relation

$$R_1 R_2 e^{2AL_{cav}} = 1 \tag{1.6}$$

where R_1 and R_2 are the mirror reflectivities, L_{cav} the cavity thickness and A the material amplification coefficient defined as the gain minus the absorption by the free carriers, becomes [25]

$$R_1 R_2 e^{2(\Gamma g L_{eff} - \alpha_i L_{eff} - \alpha_e (L_{cav} - L_{act}))} \geqslant 1 \tag{1.7}$$

If we consider that the absorption is the same inside and outside the cavity then Eq. 1.7 becomes at lasing threshold:

$$\Gamma g_{th} L_{act} = \Gamma g_{th} N_{qw} L_{qw} \approx \alpha L_{cav} + \frac{1}{2} \ln(\frac{1}{R_1 R_2}) \tag{1.8}$$

where the logarithm expression can be developed, as R are close to 1, to 1 - $R_1 R_2$

Let us take the case of a VCSEL with 3 QWs of 8.5 nm. If we assume Γ to be 1 without losses ($\alpha \approx 0$) and while minimizing the threshold gain at 1000 cm^{-1} ; then $R_1 R_2 \approx 0.994 \Leftrightarrow R_1 = R_2 = 99.7$ %

These reflectivities can not be achieved with simple metallic mirrors (where $R \approx 98$ %), we thus have to move to other multilayer designs.

1.2.3 *Mirrors*

To increase the number of path in the active region, mirrors are stacked on each side of the cavity. These mirrors are realized to reach reflectivities of 99.9 % for the bottom one and more than 99.5 % for the top one.
These mirrors can be realized in dielectric, in III-V material or more recently with High Contrast Grading sub-diffractive optical structures. These structures are all based on an alternance of high index - low index layer as described below.

Dielectric or III-V material for Bragg reflections

Mirrors composed of a succession of high and low index layers are called Distributed Bragg Reflector (DBR). Every interface causes the partial reflection of the incident optical wave. In such structure, the layers are $\lambda_0/4n$-thick to obtain constructive interferences at this precise wavelength λ_0. At the interface between low and high refractive index layers, the reflectivity is expressed by [26]

$$R = (n_H - n_L)^2/(n_H + n_L)^2 \tag{1.9}$$

The global reflectivity of the mirror thus increases with the number of stacked periods or by increasing the index contrast.

When the number of periods is increased to N $\lambda_0/4$ optical layers, the stack reflectivity is:

$$R = \left(\frac{1-b}{1+b}\right)^2 \text{ if N is } \begin{cases} \text{even} & b_{even} = \dfrac{n_s}{n_0}\left(\dfrac{n_L}{n_H}\right)^{2N} \\ \text{odd} & b_{odd} = \dfrac{n_L^2}{n_0 \cdot n_S}\left(\dfrac{n_L}{n_H}\right)^{2N} \end{cases} \tag{1.10}$$

Where n_0, n_s, n_L and n_H are respectively the refractive index of the air, substrate, layer of the lower index and the higher one. The stop-band is characterized by its half-width which can be estimated as [26]

$$\Delta\lambda = \frac{\frac{4\lambda_0}{\pi}\sin^{-1}\left(\frac{|n_H - n_L|}{n_H + n_L}\right)}{1 - \left(\frac{4\lambda_0}{\pi}\sin^{-1}\left(\frac{|n_H - n_L|}{n_H + n_L}\right)\right)^2} \tag{1.11}$$

and is thus maximized when the refractive index variation is more significant.

The best contrast is obtained with dielectric layers. At 850 nm, TiO_2 (n = 2.51) / SiO_2 (n = 1.45) pairs can be used as top mirror, deposited upon the epitaxial structure composed by the bottom DBR and the cavity. Their refractive index contrast is Δn = 1.06. The quarterwave thicknesses are 84.7 nm and 146.5 nm respectively. 7.5 pairs are necessary to achieve reflectivity higher than 99.9 %.

Dielectric DBR presents the advantage of making possible the integration of a half-VCSEL structure on Si-wafer and thus integration with silicon photonics [27]. However, in that case, the electrical top contact has to be done intra-cavity since no current injection is possible in this type of mirror. Dielectrics are also very poor thermal conductors, which increases the heating in the structure.

An easier way to fabricate the mirrors is to stack alternatively $Al_xGa_{1-x}As$ / GaAs layers during the same epitaxy growth which makes them simpler to fabricate for industry use. Furthermore, even if the index contrast is lower (Δn = 0.6), it also presents the advantage of being really well controlled and to be, thanks to the bulk crystalline structure, better thermal conductor than with dielectric. However, with III-V material, the required period number is increased up to 25 to reach the same reflectivity value than the above-mentioned one.

HCG structure

To decrease the electrical resistance of the mirrors and to relax the tolerances of the epitaxial growth of a thick DBR stack, High Contrast Grating (HCG) are excellent candidates [28]. A HCG is a lateral difraction grating near wavelength stack above a low refractive index material. The grating bars are composed of alternating of high refractive index material, GaAs, and low refractive index material, namely air. With a tight design

on the bar width and the trenchs depth, very high reflectivity is obtained. HCGs allow to select a precise emission wavelength and to maintain single mode operation.

The lateral patterning in submicron scale can be realized with e-beam lithography or, for lost cost and fast production, by nano imprint.

We can see in Fig. 1.5 a VCSEL composed of a bottom DBR, a cavity, here 4 top DBR stack surrounded by a HCG membrane. The top III-V DBR of 25-30 periods is thus replaced by 4 periods and a GaAs structured layer on top. The mechanical mouvement of this top membrane modifies cavity length and thus the emission wavelength of the VCSEL. We thus obtain a tunable device [29].

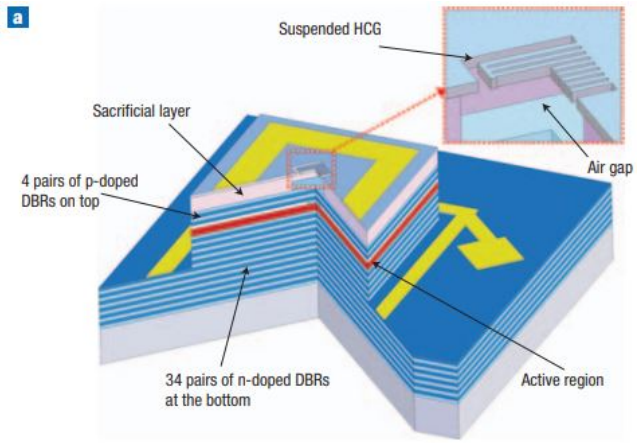

Figure 1.5: HCG membrane on top of a half standard VCSEL structure. Source: [30]

This device makes also possible the integration of a half-VCSEL onto Silicon On Insulator substrate for silicon photonics applications as demonstrated in [31].

However, the very small dimensions required for HCG, typically few hundreds nanometers, and the requirement of lateral and vertical dimensions of the grating make the realization of these HCG structure complicated for large scale use.

1.2.4 *Fabry-Perot cavity*

To create a resonance in the high reflectivity band of the DBR, and then a non-zero transmission, and so generating a longitudinal lasing mode, the mirrors have to be spaced by the cavity region of a length L_{cav} defined to be

$$n_{eff}.L_{cav} = m.\lambda_0/2 \tag{1.12}$$

where n_{eff} is the effective refractive index taken as the average of all the layers in the cavity, m is a positive integer and λ_0 the emission wavelength. For VCSEL, the cavity

is λ_0/n_{eff} thick, meaning, for 3 QWs of 8.5 nm GaAs and 10 nm $Al_{0.3}Ga_{0.7}As$ barriers, cladding plus the gradings for confinement, a thickness of L_{cav} = 255 nm to have a micro cavity resonance at 850 nm.

In the cavity, the QWs are centered and thus correspond spatially with the maximum of the electric field standing wave to have a maximum coverage with the gain region.

To anticipate the temperature increase in the cavity during operation; the cavity resonance position is designed to be red shifted relatively to the QW gain region [32]. Indeed, when the current flows the cavity, the temperature increases, and cavity resonance shifts slower (0.15 nm / °C) than the gain maximum (0.3 nm / °C).

1.2.5 *Lateral confinement*

We have discussed previously about the vertical stacking of the different layers of the cavity and the mirrors forming the micro cavity. Furthermore, to improve the lateral spatial overlap between the gain and the electro-magnetic field, and thus improve the conversion efficiency and decrease the current threshold, it is necessary to decrease as much as possible the lateral dimensions of the VCSEL. We present in this subsection different device designs to realize and combine the electrical and optical confinements in VCSELs.

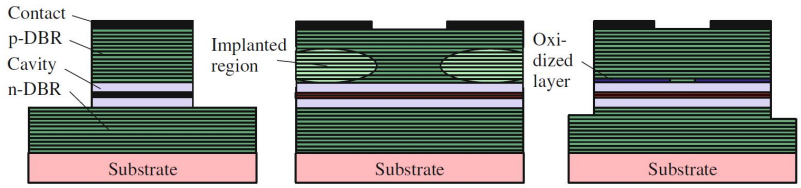

Figure 1.6: Different confinement approaches in a VCSEL. Air-post (left), proton-implanted (center) and oxide-confined VCSEL (right). Source: [33]

Mesa

The first possibility to decrease the active region area in which the current flows is to etch a mesa on top of the VCSEL, see Fig. 1.6 left. Indeed, the standard VCSEL diameter is around 30-40 µm but mesa of 10-15 µm can be etched to decrease the device area. However, decreasing too much the top area clearly complicates the fabrication process since the top electrodes has to be metallized while keeping the emitting window open. The small diameter mesa tends to have poor thermal conductivity which lead to an excess temperature increase in the device and increases the surface recombination.

Proton implanted

While keeping the same mesa diameter or even planar geometries it has been demonstrated that ion implanted VCSEL can be an excellent candidate for the electrical confinement by creating in the implanted zones a highly resistance area. However, here again

the fabrication process is complicated when small apertures are targetted due to the ion diffusion. Furthemore, the resistance of the top DBR is also increased.

Lateral oxidation

To avoid the fabrication process difficulty with small mesa or implantation, it is possible to work with 30-40 μm mesa and add a high-Al-content layer close to the active region. Thanks to a selective oxidation process, with regard to the Al composition, it is possible in a dedicated furnace with H_2O above 400 ° C, to oxidize a high Al-content layer (of 98 or 100 %) in a large depth with respect to the other layers with lower Al-content (90 %).

The resulting oxidation layer (AlOx) provides an electrical and optical lateral confinement with aperture sizes of few micrometers. This method is now widely used for all applications requiring VCSELs with low threshold and highly efficient energy conversion. With an oxide aperture of 4 μm, strictly single mode operation is achieved and can be used for longer communications distances. This process also present the advantage to avoid any surface recombination. Tapered oxides, realized with an Al-content grading, have also been studied to increase the output power and suppress higher modes.

In order to decrease even more the parasitic capacitance of the device and thus to increase the modulation bandwidth, a lot of groups work now with multiple oxide layers where the Al-content is graded in the top DBR close to the active region [34]. Although, it is possible to sandwich the cavity between two deep oxidation layer, this process increases the QW strain, so now, these two oxide layers are preferably placed both above the cavity [35].

Tunnel Junction

To keep the lateral dimension in the range of few micrometers it is possible to bury, between the active region and the top DBR, a localized tunnel junction to have the current only injected in the center. The tunnel junction acts as an optical confinement due to a small resulting index diffrence with the surrounding material. This structure also presents the advantage to work with a N-doped subtrate and to grow all the structure with N-doped DBR where the optical absorption is lower compared to than the P-doped. Single-mode operation is also, thanks to the lateral dimension, obtained with this confinement. This solution has been introduced by the Walter Schottky Institute of Munich Technical University and is mostly used for 1.55 μm and Mid-infrared VCSELs on InP and GaSb substrate.

Photonic Crystal (PhC) structure

A more sophisticated structure is obtained by defining photonic crystal in the top DBR. Etched holes with specific diameters and spacing lead to strong mode discrimination to create a single-mode waveguide in the DBR [36] [37]. However, here again the electrical resistance is increased which lead to higher current threshold and low power efficiency.

PhC can be combined with lateral oxidation or proton implantation to increase the device performances such as lower current threshold and higher efficiency.

1.3 PHYSICAL LIMITS OF DIRECT MODULATION AND IMPROVEMENTS

We will now explain VCSEL perfomances improvement to reach the actual state-of-the-art in terms of high-frequency operation.

1.3.1 *Device improvements*

In 2013, Westbergh and Larsson demonstrated a 40 Gb/s data rate with direct VCSEL modulation up to 85°C [38]. To reach this value they optimized the VCSEL design, first by tailoring the DBR grading and doping and then by decreasing the cavity length. This improvement allows an increase of the longitudinal conductivity around 25% with no increase of the optical absorption. A second improvement was made in 2015 [39] by using five strained InGaAs quantum wells for high differential gain but especially by using an oxide aperture on each side of the active region which improves even more the transverse carrier confinement. Secondary oxide aperture were also introduced above the upper primary oxide to reduce capacitance. With such design it is possible to obtain a 30 GHz bandwidth VCSEL functioning at 50 Gb/s. Another way to increase the VCSEL bandwidth, once it has been optimized to the limit, is to optimize driver and receiver circuits design. By doing so, IBM and Larsson et al. obtained a 50 Gb/s NRZ (None Return to Zero) Error Free component at 90°C [40]. More recently and with a considerable effort on the electronic part they achieved a 64 Gb/s [41] and then 71 Gb/s [42] which is the highest transmission bandwidth performance ever achieved on VCSEL with NRZ format.
More recently, Lott et al. demonstrated the feasability of a very small oxide aperture device about 1 µm to increase the data bandwidth while using a very simple design. They achieved modulation bandwidth higher than 30 GHz at 980 nm [43] [44].

1.3.2 *Alternatives to direct modulation*

To go further in the modulation speed of VCSEL devices for data communications several groups undertaken different approaches to overcome the carrier dynamics limitation. KTH Royal Institute of Technology in Stockholm worked a few years ago on the combination of a transistor and a VCSEL; the so called a T-VCSEL [45]. It presents all the VCSEL advantages and attractive properties of a transistor compared to conventional diode lasers: suppression of relaxation oscillations and reduced turn-on delay. However

at this time, only 7 GHz was achieved so many device improvements have to be done to achieve competing performances.

Chang-Hasnain's team at University of California, Berkeley, incorporated an intra cavity quantum well absorber within the VCSEL structure, more precisely in the top DBR. By applying a voltage, the mirror reflectivity changes and so does the laser output power [46]. However, this technique showed lower modulation speed (9 GHz) than direct VCSEL modulation.

In the same line, the splitting of the modulating and the emitting part could avoid the carrier dynamics limitation. This proposal of a dual-cavity VCSEL is another interesting solution for increasing the modulation bandwidth.

Prof. Koyama demonstrated the efficiency of Transverse-Coupled-Cavity VCSEL [47] where a second cavity, electrically isolated, is set close to the VCSEL to act as a feedback cavity. However, due to the significant feedback in the VCSEL, even if 30 GHz and data transmission of 40 Gb/s was demonstrated, significant extinction ratio cannot be achieved. The main limitation of this device remains the chirp resulting from this feedback injection in the VCSEL cavity. The same group worked with a double identical cavities structure with square shapes. Each structure is independly current driven and separated by a ion implanted area. The global device modulation bandwidth is increased thanks to the appearance of a new resonance that results from the beating between the two compond cavity wavelengths. Here again 29 GHz where achieved with an extinction ratio of 4 dB [48].

Concerning the vertical integration of a modulator onto a VCSEL, as described by Van Eisden in 2008 [49], this method avoids the limits of carrier dynamics on the intrinsic modulation and so will permit higher bandwidth. A modulation at 20 GHz was demonstrated with an electro-absorption (EA) modulator by proper detuning of the resonance. The idea of an external modulation is also interesting to increase the device lifetime which is degraded by the high drive current. Indeed, the actual data bandwidth record are obtained with drive current above 10 mA which decreases the reliability of the VCSEL. However, with an external modulation, this drive current can be decreased to few mA. In 2012, Germann et al [50] worked with another phenomenon about the modulator section, the modification of the refractive index when an electric field is applied perpendicularly to the structure. This Electro-refractive (ER) Modulator on top of the VCSEL, with both cavities having similar resonance wavelengths, demonstrated very high modulation bandwidth of more than 30 GHz and is expected to reach 56 GHz. Moreover, higher bandwidths could be achieved if the parasitic capacitances and resistances are further reduced. Temperature control is also a challenge to preserve low power consumption and a reduced chirp size.

The easier, or at least the quickest, mean to increase bandwidth for data communication is to design VCSEL arrays as done by Larsson et al. [51]. With such a design an aggregate of 6 VCSELs about 40 Gb/s each can reach 240 Gb/s at room temperature but this implies an important work on modulation and multimode interconnects. The actual industrial products are working at 10 Gb/s and arrays of 1x4 reach 25 Gb/s with excellent reliability.

1.4 PHD MOTIVATIONS

Based on previous work described above, I worked in this PhD on the vertical integration of an electro-optic modulator on top of a VCSEL to reach very high-frequency modulation bandwidth. To avoid any chirp phenomenon, as in Coupled-Cavities VCSEL demonstrated by Choquette [52] Germann [50] or more recently by Mateusz [53], we decided to work with an electro-absorption phenomenon. Since the emitting and the modulating sections are, as possible, decoupled, the essential work will be done on the modulator itself. It is therefore mandatory to understand, in such a structure, the variation of the modulation depth, the position of the absorption and resonance as a function of the VCSEL temperature and bias voltage to drive the component. We are talking here of uncoupled cavities when the operation of the top cavity, with an electric field, does not affect the electrical and optical behavior of the VCSEL cavity.
The high-frequency electrical injection in such a structure is also a key parameter to decrease as much as possible the losses. Indeed, this last point suffers from a lack of information on VCSELs devices since all groups use the same electrical design whereas other solutions are available to get free from the substrate doping.

1.5 STRUCTURE OF THE THESIS

To carry out this study, the project is divided in three parts, first the modelling of the EAM and EAM-VCSEL structures, then the fabrication process for static devices and their characterization and finally the high-frequency optimization and characterization of the samples. Thus, the PhD manuscript is written with the objective to retrace chronologically the research project from the EAM design, then its vertical integration onto a VCSEL, next the samples fabrication and finally their characterization.

In the chapter 2, entitled Electro-Absorption Modulator, we describe the physical phenomena involved in this device. We first explain the Franz-Keldysh effect discovered in the 60's, then, when it occurs in a confined structure, the Quantum-Confined Stark Effect (QCSE) enlighted by Miller in 1984, and finally we present the excitonic peak modification which is responsible for the absorption modification and so the modified

transmitted light.
Then, we detailled a simple model to explain and describe the absorption. This model considers transitions between the valence level and the conduction band. It does not implement the tunneling effect and so is valid only for quantum well thicknesses between 5 nm and 20 nm which is our area of interest in EAM devices.
After a description of the state of the art of the vertical modulators, we describe our design optimization with several degrees of freedom such as the period number of DBRs, the number of QWs, the quantum wells and barriers thicknesses and their aluminum content. To perform an optimal design we use a global Figure Of Merit which takes into account of the physical and optical properties necessary to reach very high speed while maintaining a sufficient modulation depth with a low applied electric field. Then, after optimizing the EAM alone, we integrate it onto a VCSEL to decrease as much as possible the coupling between the two cavities and so the chirp which is an unwanted phenomenon for optical communications.

In the chapter 3, the fabrication process for static operation is presented. First we describe the epitaxial growth of the different wafers by Molecular Beam Epitaxy (MBE); as well as the in situ control. We also describe the interest of the digital alloy composition for the barriers and the DBR grading in the VCSEL structure. Then, two technological locks are removed to facilitate the global fabrication of the double mesa structure. An original self-aligned process is presented, without lateral oxidation for a quick and easiest process of the EAMs, and with the lateral oxidation for a simplified VCSEL process. Once the devices were fabricated we characterize them electrically and optically in static operation. The EAM reflectivity spectrum as a function of the voltage and temperature has been measured on a dedicated optical setup, as well as the EAM-VCSEL in operation to demonstrate the feasability of the design.

In the chapter 4, we present the full study of the high-frequency fabrication and design optimization. First by describing a new process development of the BCB planarization with a diverted use of a mechanical press to improve the flatness between the devices. One of the most important points in the achievement of high-speed communication is the optimization of the high-frequency electrical injection in the device. So then, to address this problem we characterize the BCB properties with an efficient deembedding method up to several tens of GHz. We then compare the pro and cons of the coplanar and microstrip design for our devices and finally present the optimum one. Finally, the global process flow of the EAM-VCSEL structure is reported step by step.

In the chapter 5, we present the EAM and EAM-VCSEL characterization in high-frequency regime. First, we describe the electro-optic characterization of the EAM on a set apart bench. Then, the high-frequency operation of the EAM once integrated on the VCSEL is demonstrated. Finally, we studied the electro-optical behavior of the device

with different parameters such as the temperature, the injected light wavelength and the applied voltage to demonstrate its limitation and possible improvements.

To complete the manuscript, we summarize all the work in the conclusion, the technological advances, the remaining problems and we discuss how to solve them. The perspectives for future work are also described.

Two annexes are given useful technical details on the global fabrication process flow with temperatures, spin-coating parameters, and also some tips to improve the realization and reliability of the process.

2 ELECTRO-ABSORPTION MODULATOR DESIGN AND INTEGRATION ONTO A VCSEL

Nowadays a sustainable and already commercial solution for high-speed communication is the use of an edge emitter laser laterally integrated with an external modulator (DFB + EAM) which operates at optical bandwidth higher than 50 GHz. However this high frequency operation is obtained at the expense of a footprint of several hundreds of micrometers which leads to an elevated electrical consumption. The design, the fabrication, the testing and the fiber coupling which require a complex packaging also increase the cost of this approach.
To be a competitive solution, the next generation of devices has to reach optical bandwidth higher than 30 GHz with a sufficient modulation depth while maintaining a drive voltage fo few volts. The vertical integration of an Electro-Optic Modulator onto a VCSEL can meet all these objectives. Of course, in such monolithic integration, the modulator properties have to be adapted to the VCSEL ones. The spectral mutual arrangement has to be carefully studied and it is necessary to minimize the effect of the modulator on the VCSEL intrinsic performances, i.e. the optical cavities have to be slightly coupled. Another problem that arises from this fully integrated structure is thermal management. Indeed, the temperature impact of the VCSEL, operating in a continuous wave (CW), has to be considered and the ratio modulation depth / modulator thickness maximized. Furthermore, to ensure a high frequency operation with all these requirements the modulator resistance and capacitance have to be minimized.

In the first section we will describe the absorption phenomenon of a semiconductor under an electric field which modifies its optical properties and thus leads to a modulation behavior. To increase the modulation efficiency it is of high interest to confine the carriers in quantum wells structure.

In the second section, we will present a model which reports the absorption variation in one quantum well while considering the electric field. We selected a simple model only based on parameters deduced from experimental data and the position of the maximum of absorption in order to be easily implemented in a complex multilayer device within a Fabry Perot cavity. We will thus be able to reproduce the absorption modulation in the EAM-VCSEL device.

In the third section, based on the previous absorption model we present an optimization of a single quantum well with respect to its major parameters as thickness, Al-content in the barrier and applied electric field. To do so, a figure of merit combining the requirement of a modulator such as the modulation depth and the low drive voltage is maximized.

In the fourth section, a state-of-the art of vertical modulator is presented to compare different EAM structures from the literature. On this basis we designed a modulator based on the optimized QW embedded in an Asymetric Fabry Perot cavity for its integration onto a VCSEL. This optimization process has lead to the **paper C**.

In the fifth section, we present the integration of this modulator onto the VCSEL. In particular we studied the effect of spectral detuning between the two cavities and the temperature effect on the absorption phenomenon, as these two aspects are essential for the optimal operation of the final device.

2.1 ABSORPTION EFFECT

The absorption phenomena in a crystal or a quantum well corresponds to the recombination of a photon, which energy is above the band gap of the material, moving a charge from the valence band (VB) to the conduction band (CB). The optical absorption phenomenon is present in all materials and can be influenced when an electric field is applied due to the modification of the band diagram and the envelope functions of the charges.

2.1.1 *Semiconductor bulk absorption without electric field*

Every material is characterized by an intrinsic property, its dielectric constant. This complex number combines the refractive index n, linked to the permittivity ε_r, and the extinction coefficient k of the material. The relation between them is expressed as follows:

$$\begin{aligned} \varepsilon_r^*(\lambda) &= E_1 - iE_2, \\ n^* &= \sqrt{\varepsilon_r^*} = n - ik, \\ \Longrightarrow E_1 &= n^2 - k^2 \text{ and } E_2 = 2nk, \end{aligned} \tag{2.1}$$

With this set of equations, the dielectric or optical behavior of the material can be expressed as a function of E_1 and E_2, or more often by n and k. The optical absorption coefficient α is then characterized by the extinction length l ($l = \lambda/4\pi k$) for which the energy transmitted in the material decreases by a factor e :

$$\alpha = 4\pi k/\lambda \tag{2.2}$$

The absorption spectrum of GaAs has been studied for different doping levels by Casey et al. [54] as shown in Fig. 2.1. Below the energy band gap (1.42 eV) the absorption is very negligible (Fig. 2.1a) but the absorption coefficient varies a lot for energies above the band gap. In (Fig. 2.1b) the importance of the doping level, which modifies the value of the imaginary part of the refractive index is highlighted. It is necessary to consider this variation of absorption since the GaAs material grown by Molecular Beam Epitaxy presents a residual doping (around 10^{15} cm^{-3}), the absorption tail broadening plays an important role in the modulation effect of the EAM. Finally, the reflectivity at the surface interface is directly linked to n and k by :

$$R = \frac{(n-1)^2 + k^2}{(n+1)^2 + k^2} \tag{2.3}$$

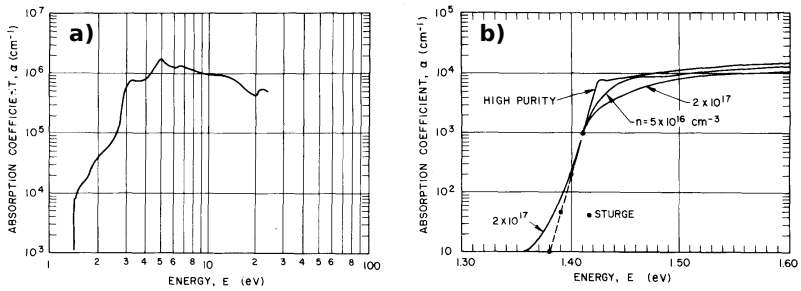

Figure 2.1: Absorption coefficient in GaAs, in bulk (a) and zoomed for different doping levels (b). From [54]

When the temperature increases in the material, its band gap energy is modified following the Varshni law [55]. This variation modifies the absorption spectrum and the slope of the absorption tail as seen in Fig. 2.2. It is thus an important parameter to be

considered in our device since the absorber region of the modulator will be impacted by the VCSEL temperature when operating.

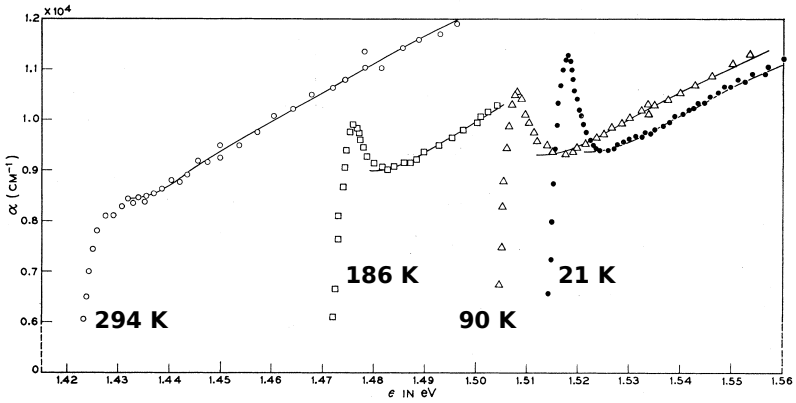

Figure 2.2: Absorption coefficient in GaAs for different temperatures, 294 K, 186 K, 90 K and 21 K. From [56]

To get efficient modulation of the absorption, as expected for opto-electronics devices, playing on the temperature is not a viable solution. It is thus necessary to apply a perpendiculary electric field so called electro-aborption modulation which modifies the band structure and thus facilitates the recombination of the photon into an electron.

2.1.2 *Semiconductor bulk absorption with electric field*

Without electric field the electron and hole wavefunctions are described by the Schrödinger equation whose solution is a plane wave. When an electric field is perpendiculary applied to the material plane, this envelop function becomes an Airy function. The optical absorption phenomenon ensues from the overlap between this Airy function in the forbidden band as described in Fig. 2.3. Obviously, when the electric field increases, the overlap increases too and so does the absorption. The modification of the absorption over energy linked to this effect, called Franz-Keldysh, is represented in Fig. 2.3.

However the Franz-Keldysh effect requires very high voltage to reach a weak absorption variation. It is therefore not possible to use this phenomenon in modern opto-electronic devices.

2.1.3 *Absorption in a Quantum Well subject to an electric field*

The insertion of quantum wells (QW) in the bulk material allows carrier confinement and better overlap of the electron and hole wavefunction. The electronic states are modified and a discretisation of the energy levels occurs. The absorption is thus modified in such

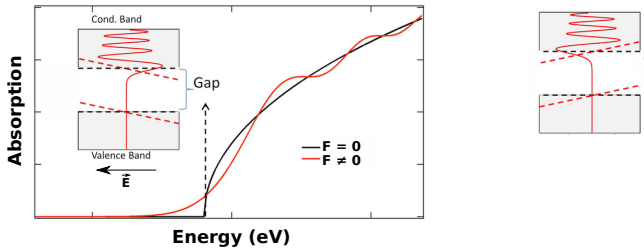

Figure 2.3: Schematic of Franz-Keldysh effect in a bulk semiconductor without (black) and with (red) electric field perpendiculary applied to the material. The variation of the absorption is highlighted and the inset shows the modification of the band diagram and the envelop function. From [57]

structure and the electric field needed to reach high modulation depth is decreased. This splitting in energy levels can be noticed in Fig. 2.4a. When electric field is applied, valence and conduction bands get sloped and the respective envelop functions in CB and VB are pushed to the opposite sides of the QW and thus the overlap between electrons and holes wavefunction is decreased. Due to the spatial confinement in QWs structures, this effect is thus named Quantum Confined Stark Effect (QCSE) and has been calculated for GaAs QW by Miller et al. [58]. The dependance of absorption function on several parameters will be studied in section 2.3.

Miller et al. measured the optical absorption in Multiple Quantum Wells (MQW) structure under an electric field [59]. The result is shown in Fig. 2.4b where a shift of the maximum of absorption to the lower energies (longer wavelengths) and a broadening of the absorption tail can be seen.

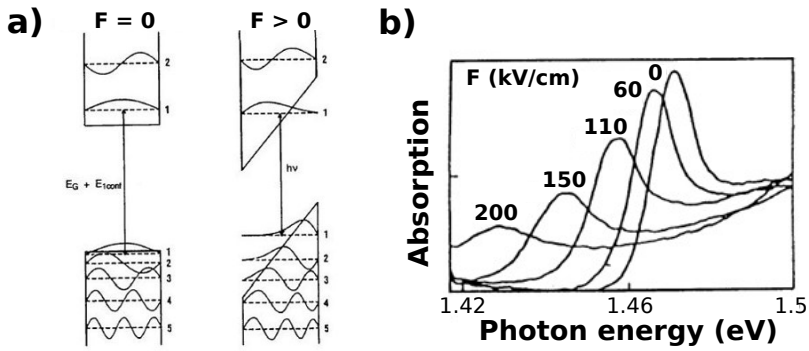

Figure 2.4: Schematic of the Quantum Confined Strak Effect (QCSE) without (a) (from [60] p89 Fig. 46) and with (b) electric field applied perpendicular to the QW (from [60] p90 Fig. 47)

Linked to this absorption phenomena, the electric field also modifies the refractive index of the QW via the Kramers-Krönig equation. The variation of both the absorption and the refractive index are thus linked with the following equation [61]:

$$\Delta n = \frac{c}{\pi} \int_{\omega 1}^{\omega 2} \frac{\Delta\alpha(\omega')d\omega'}{(\omega')^2 - \omega^2} \tag{2.4}$$

The variation of the refractive index with the applied electric field follows the rule:

$$\Delta n = (-1/2)n^3 s E^2 \text{ with } -(1/2)n^3 s = 10^{-13} cm^2/V^2 \text{ from [61]} \tag{2.5}$$

Electro-optic modulators, vertically integrated or not, are therefore based on these two phenomena, the variation of the refractive index, i.e. called Electro-Refractive (ER) modulators or the variation of the absorption, i.e. called Electro-Absorption (EA) modulators. The ER modulation presents the advantage of not being influenced by photocarriers and thus could reach higher modulation frequency compared to EAM. It is also independent on the light intensity and so on the temperature effect which should be an advantage in our vertical integration. However, in the case of ER modulation, the required voltage to change the refractive index and reach an equivalent absorption variation is significantly higher, as demonstrated for GaAs bulk layers [62] and MQWs [61] [63].

The superior efficiency of the EA effect results in a lower sensitivity to electric field non-uniformity. Also, at a given voltage, the modulation spectral window is wider with the EA effect, which relaxes the tolerances on layer thicknesses during the EAM epitaxial growth. As demonstrated by Weiner et al. [61], the chirp, defined as $\alpha_{chirp} = \Delta n/\Delta k$ is lower for EA effect than for ER.

From the above analysis, conclusion may be done that a more attractive solution will be to use a EAM onto a VCSEL. Indeed, working with low drive voltage, wide optical spectrum and furthermore relaxing the constrains on the epitaxial growth of the global Modulator-VCSEL device are key arguments to use EA effect.

2.1.4 *Excitonic absorption*

When an incident photon is absorbed in the QW, the generated electron is excited from the valence band to the conduction band. This electron is attracted with the remaining hole by Coulomb force creating a bound electron-hole pair called an exciton.

In the band diagram E-k the valence band presents a degeneration leading to two distincts bands, the higher, with a lower bending, corresponding to the heavy holes, the lower with a more pronounced bending, corresponding to the light holes. At the Γ-point of these bands, the splitting of the effective mass is given in GaAs by $m_e = 0.067 \cdot m_0, m_{hh} = 0.45 \cdot m_0$ and $m_{lh} = 0.08 \cdot m_0$ with $m_0 = 9.11 \cdot 10^{-31} kg$ is the rest electron mass.

At room temperature, in one single QW, we only identify the heavy hole (hh) peak position. At lower temperature or when the number of QW is significantly increased, a

second peak of higher energy corresponding to the light hole (lh) transition can be seen in Fig. 2.5.

The distance of interaction to form an exciton is about 30 nm, there is thus in a narrow quantum well of around 10 nm a well defined excitonic state from the interaction of the electron-hole pair that survives at room temperature.

The absorption of MQW sandwiched between two contact layers is shown in Fig. 2.5. In that case the MQW are composed of 50 periods of 9.5 nm of GaAs and 9.8 nm of $Al_{0.32}Ga_{0.68}As$.

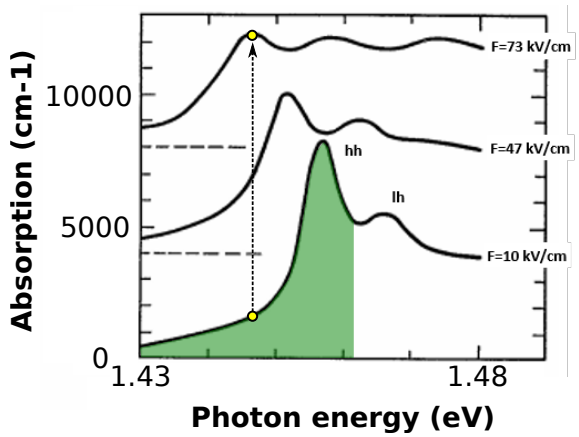

Figure 2.5: Schematic of the Quantum Confined Strak Effect (QCSE) in a MQW structure of 50 QWs under electric field. Light and heavy hole exciton peak position are denoted. The green area corresponds to the higher modulation depth that can be achieved; so it highlights our area of interest. From [59]

We can see that with a low drive voltage the absorption tail is very steep and can thus lead to a significant modulation depth when the electric field is applied as shown in Fig. 2.5 by yellow dots. The maximum of absorption change is reached for the green area, at lower energy (longer wavelength) than the heavy hole position. We also notice that the tail is being broaden when the electric field is increased as described previously. This phenomenon needs to be addressed for the modelling of such a device as described in Section 2.3 since it directly affects the optical properties of the modulator.

When the QW thickness is increased, the confinement is weaker, and the degeneration of the valence band is less important, so the electro-absorption behavior tends to be like in bulk [60] p79 Fig. 38. All QW parameters, such as the barrier level (Al content x_{Al}), the quantum width l_z and the applied electric field F are crucial to maximize the optical absorption in the MQW region and will be discussed in the next subsections.

2.2 ABSORPTION MODEL

In the literature several models, more [59] or less [64] complex, exist to describe precisely the evolution of the excitonic absorption as a function of the applied voltage and the characteristics of the QW.

To have a precise description of the optical absorption around the exciton peak, it is necessary to find the solution Ψ of $H\Psi = E\Psi$ where H is the effective-mass electron-hole Hamiltonian. This Hamiltonian can be written as [65]

$H = H_e + H_h + H_B$ which includes the kinetic operator energy for electron and hole, their effective mass, the built-in rectangular quantum well potential for electron and holes due to the band discontinuity. The exciton resonance is thus given by $E_{exc} = E_{ez} + E_{hz} + E_B$ with E_{ez}, E_{hz} and E_B the first confined electron / hole energy and the binding energy.

To describe precisely the excitonic absorption phenomenon, three mechanisms have to be considered:

- *The shift of the envelope function*: exact solutions for quantum well structure with barriers of infinite height are Airy functions.
- *The binding energy* which correponds to the required energy to split the exciton into two independant particules. As described by Miller et al. [59], when an electric field is applied, the electrons and holes shift on opposite side of the quantum well and the Coulomb attraction between them is reduced leading to a decrease of the binding energy.
- *The tunneling effect* responsible of the broadening of the absorption

The consideration of all these three phenomena really complicates the simulation of the whole absorption spectra and is thus not necessary since the spectral range of interest, in green in Fig. 2.5, only requires the knowledge of the excitonic peak position and the broadening of the absorption.

Furthermore, the tunneling resonance half width below 100 kV/cm is < 1 meV for hh (see Fig. 9 in [59]) which is really low compared to ~ 20 meV of the exciton peak shift position (see Fig. 6 in [59]) for the same electric field. Moreover, as described in [65], for high electric field (higher than 30 kV/cm) the dominant contribution of the exciton energy comes from E_{ez} and E_{hz} meaning tunneling effect and binding energy could be neglected even though they are still strong.

It is thus necessary to have a simpler model that considers the absorption within the green area of Fig. 2.5 as a function of the electric field and the QW properties.

Lengyel's model [64] is so a perfect candidate to complete this study, since there is no consideration in this model of the exciton binding energy neither the tunneling which

becomes important for coupled quantum wells with thickness below 5 nm. For QWs thicknesses above 20 nm the exciton confinement is too weak and electro-absorption tends to be like in bulk GaAs. For these reasons, the Lengyel's model is valid for 5 nm $< l_z <$ 20 nm.

In this model the conduction:valence potential ratio was taken as 60:40. It was demonstrated in [59] (p1053 Fig. 6) that the sum of the electron and the hole energies make the exciton energy insensitive to split ratio (compared 85:15 and 57:43).

The model of Lengyel that we used for our EAM considers a simple transition between the first heavy-hole level of the valence band and the conduction band and their excitons. The solution of these wave functions are given as Airy function for the case of infinite wells while a sophisticated correction has to be applied to consider the QW with finite depth [66]. Alternatively, in the case of finite wells, the electric field contribution is considered as a small perturbation and the solution of the QW perturbed Hamiltonian is expressed as a linear combination of the unperturbed QW solutions [67]. The optical absorption coefficient is then written as

$$\alpha(\epsilon, h\nu, l_z) = \alpha_{hh} \cdot \left(1 + \left[\frac{(E_0 - h\nu)}{\Gamma_{hh}}\right]^2\right)^{-1} \quad \text{for } h\nu < E_0. \tag{2.6}$$

Here, E_0 is the energy of the heavy hole exciton and Γ_{hh} is the Half Width Half Maximum of exciton Lorentzian shape absorption. The coefficient α_{hh} is the peak value of the exciton absorption and can be calculated from first principles as described by Nishi et al. [68]. Alternatively, [64] suggested a phenomenological expression that retains the dependence of α_{hh} on the QW thickness and electron-heavy-hole overlap integral and its dependence on the electric field

$$\alpha_{hh} = \frac{C}{l_z} \cdot \left| \int_{-\infty}^{+\infty} \Psi_e \cdot \Psi_h^* \cdot dz \right|^2 + \alpha_{bulk}. \tag{2.7}$$

The integral incorporates the effect of the electric field on the band diagram since it considers the overlap between the two envelop functions which are shifted when F increases. Here, the term α_{bulk} corresponds to the background absorption level in bulk GaAs for which the electrical dependence is neglected since the major part of the absorption comes from the QCSE in QWs. The C parameter is the product of a material-related constant and the optical matrix element between the s-like spin-1/2 conduction-band wavefunction and the p-like spin-3/2 valence-band wavefunction at the Γ point, which is temperature dependent, as described by Nishi et al. [68]. We use in the following C = 160 000 nm.cm^{-1} and α_{bulk} = 5 500 cm^{-1} [61]. A polynomial expression of Γ_{hh} was

used by Stevens et al. [69] instead of partial derivatives to simplify the calculation (Eq. 2.8), i.e.

$$\begin{gathered}\Gamma_{hh}(l_z, \epsilon) = 7.374 - 0.511 \cdot l_z + 0.0182 \cdot l_z^2 - 0.054 \cdot F + 0.0161 \cdot F^2 \\ \text{for } 5 \text{ nm} \leqslant l_z \leqslant 20 \text{ nm}. \text{ F is the applied electric field (kV/cm)}\end{gathered} \tag{2.8}$$

To enforce the effect of the temperature on the absorption and fit it to our experimental results we consider the temperature dependence of C and Γ_{hh}. Implementation and comparison with experimental results will be discussed in the Section 3.5.1.3.

2.3 PARAMETER OPTIMIZATION OF ONE SINGLE QUANTUM WELL

In this section the optimization of the absorption in one single QW with the Lengyel's model described previously is detailed. To do so, trades-off will be discussed and figures of merit (FOM) incorporating the change of absorption, the applied electric field and the residual absorption (without field) will be considered to design the active region. Finally, we will integrate this MQW active region in an Asymetric Fabry-Perot (ASFP) structure, to improve the modulation depth with a low number of QW, and calculate by the transfer matrix method different FOMs.

The first step to optimize EAM structure is to design the QWs and barriers. In a such optimization various degrees of freedom are available:

- QW thickness l_z (nm),
- Aluminium concentration in the barrier x_{Al} and barrier thickness,
- Applied electric field F.

Susa et al. [70] have done an important modelling work on the design of AlGaAs / GaAs QWs for EAM, in particular about the broadening of the exciton absorption peak due to the electron escape from QW to the barrier which is directly linked to the roughness of the epitaxial layer. This last study however, has considered static modulation only without considering the capacitance of the active region, which is important for high frequency modulation.

Based on the previous works and to illustrate the impact of the different parameters we plotted the absorption shape and its maximum position shift for an Al content between 15 % and 40 %; quantum well thickness between 7.5 nm and 10 nm, and an electric field from 0 kV/cm to 120 kV/cm. Above this field value we explained previously the limitation of the absorption model.
Fig. 2.6 presents the calculated spectral dependence of absorption of a single QW. Fig. 2.6a shows that an increase of Aluminium content in the barriers x_{Al} leads to increase of α and a blue shift of λ_{exc} since it enlarges the energy difference between the well and

the barrier and so decreases the probability of escaping. From Fig. 2.6b we see that an increase of l_z will decrease, at fixed voltage, the overlap between the two wavefunctions and so decrease the absorption coefficient. The same behavior is observed in Fig. 2.6c when the electrical field is increased: the wavefunctions for the heavy holes and for the electrons are shifted on each side of the well and so the overlap integral decreases and so does the absorption.

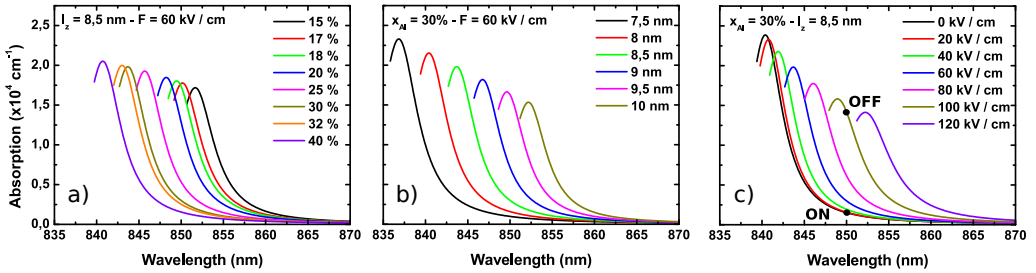

Figure 2.6: Spectral dependence of absorption of a single quantum well for different Al concentration in the barrier (a), quantum well width (b) and the applied electrical field (c).

Here, normally-off modulator is considered exclusively for which the reflectivity is at its minimum R_{off} without bias and increases to reach the ON state, R_{on}, when an electric field is applied.

The first main goal while designing an EAM is to obtain a high modulation depth defined as $\Delta R = R_{on} - R_{off}$ also expressed for the corresponding change in the absorption $\Delta\alpha$, while minimizing the electric field F (in kV/cm).

In our study we only consider standard rectangular shape QW. To find an optimum EAM structure several FOMs have been used in addition to $\Delta\alpha$ or the Contrast Ration (CR): $\Delta\alpha/\alpha_0$ which stresses the importance of the residual absorption α_0, $\Delta\alpha/\Delta F^2$ which considers the importance of the applied electric field or $C \cdot \Delta V^2$ which considers the cut-off frequency via the capacitance. This last FOM has been studied by Chin et al. [71], [72] for InGaAs QWs in waveguide configuration with other criteria as CR, V, optical bandwidth (OBW) and losses. However, these studies were realized for waveguide configuration. Furthermore, all the foregoing studies referenced previously were conducted with thin barriers about 5 - 5.5 nm. Such thicknesses however increase the tunneling effect and so the absorption tail is getting narrow which degrades the optical properties of the device in the 'off' absorption state (without field). Another way to decrease this narrowing is to decrease the roughness of the interface in the superlattice structure. To this aim, we have oriented our work on digital alloy growth of 10 nm thick barriers. Digital alloy are used to provide an average Al content, which should not be reachable with the growth cells at our disposal, by using two others Al contents. PL and AFM measurements that compare both digital and standard barrier are presented in Section 3.1.2.2.

To improve previous studies, introduction and maximization of an alternative FOM, which is a trade-off of all the FOM described previously, $M = (\Delta\alpha/\alpha_0) \cdot (\Delta\alpha/\Delta F^2)$ is adopted in this work. Fig. 2.7 shows a matrix for different "ON" and "OFF" electrical fields with maps of our figure of merit M. For each map, M is plotted as a function of the QW width (x axis) and the barrier Al concentration (y axis). For example the upper left map corresponds to $M = [(\alpha_{60} - \alpha_{20}) / \alpha_{20}] \cdot [(\alpha_{60} - \alpha_{20}) / (60^2 - 20^2)]$. The blanked areas correspond to an exciton absorption peak red shifted beyond 850 nm, which is our area of interest, and so the absorption value is not extracted. As we can see for each map M is maximum along the diagonal: for a given l_z if x_{Al} increases, the absorption increases up to a maximum and then decreases. The area of interest, where M is maximum, is obtained for l_z = 8.5 nm and x_{Al} = 30% for a ΔF of 40 kV / cm between 100 and 60 kV / cm.

Simulation of this FOM has been done at precise values of x_{Al} and l_z that is why discretization of the mapping can be observed and result is islands shape.

The same matrix mapping has been done with another FOM which corresponds to the diminution of the optical intensity in an absorber cavity $M' = (\Delta\alpha) \cdot l_z$ (not shown). The maximum of M' is obtained for the same QW parameters as for M which supports our result.

2.4 VERTICAL MODULATORS: STATE-OF-THE ART AND APPLICATIONS

We have described in the previous section the optimization of a single quantum well while considering its thickness and the Al content in the barrier with a low ΔF drive voltage. We will now describe briefly the state-of-the-art results on vertical modulators and more precisely how to optimize the global design to obtain a high modulation depth of the VCSEL output light while maintaning a low drive voltage and considering the high frequency operation.

The high modulation depth, meaning a large absorption variation, can simply be achieved by increasing the number of quantum wells (n_{QW}) [73] of several tens of QWs but this leads to an unwanted excess of the applied voltage V, an inhomogeneity of F in the superlattice structure and a non-uniformity in the epitaxial growth [74]. For this last reason, the Asymetric Fabry Perot (ASFP) scheme is preferable to a high number of quantum wells (70 - 100) stacked on top of a single DBR [63].

Furthermore, even if the increase of n_{QW} leads to a higher bit rate, the dissipated power in the device also increases [75]. On the other hand, larger cavity thickness will decrease the capacitance C ($\propto$ 1/thickness) and so increase the electrical cut-off frequency f_{-3dB} which is $\propto 1/RC$.

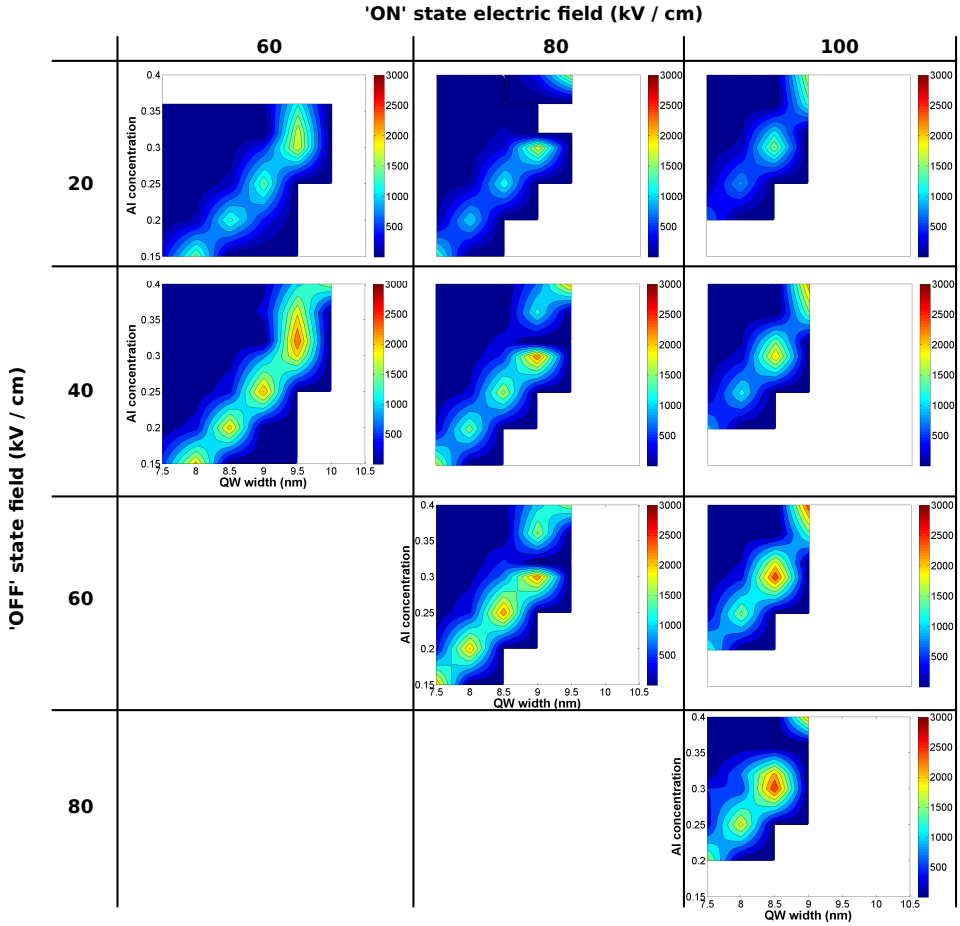

Figure 2.7: Maps of the electro-absorption modulator figure of merit $M = (\Delta\alpha/\alpha_0) \cdot (\Delta\alpha/\Delta F^2)$ plotted for different On and Off levels of the applied electric field

To overcome the problem of the high applied voltage V while keeping a satisfying CR, the reflectivity ratio of the 'on' state on the 'off' state, two solutions are applicables:

1. Decreasing n_{QW} and increasing the top mirror reflectivity (R_T) [76] up to 0.76 (by exceeding this value, Yan et al. demonstrated that V increases again [77]). However, this approach leads to increasing the capacitance and so reduces the electrical cut-off frequency f_{-3dB} [78],
2. Getting the excitonic peak position (λ_{hh}) closer to the wavelength resonance of the ASFP cavity (λ_{FP}). In that case weaker electrical field is necessary to reach the same transitions level; i.e. lower V. However, residual losses at zero-bias will increase, which is undesirable for normally-off modulators.

Another approach to increase $\Delta\alpha$ while maintaining a sufficiently low V is to modifiy the rectangular shape of the QWs by grading the Aluminum content. Based on Hiroshima model [79], Ishikawa et al. demonstrated its advantage on the energy shift under an applied voltage with a grading in the QW from 0% of Al content to 30% [80]. The barrier concentration can also be modified to play the same role [81] however these two approaches clearly complicate the epitaxial growth of MQWs. A simpler proposal is to incorporate a very thin barrier in the QW to split apart the wavefunctions of the heavy holes and the electrons on each side and so decrease its overlap. It has been demonstrated that in coupled QWs λ_{exc} shifts more quickly with lower voltage [82]. This has also been calculated by Zouganeli et al. [83] and demonstrated for imaging applications [84]. Unfortunately this approach complicates even more the epitaxial growth of the whole stack.

2.5 VERTICAL STRUCTURE OF THE EAM : MQW EMBEDDED IN AN ASYMETRIC FABRY PEROT

In this section we will describe the integration of the optimized QW sandwiched between two mirrors. We will first describe the design of the cavity, then the mirrors and finally the complete integration.

2.5.1 *Cavity design*

To satisfy the need of high-speed operation, the cavity must be as thick as possible. Indeed, the cut-off frequency of the device is inversely proportionnal to its capacitance which is linked to the modulator area (A) and the thickness (t) of the undoped region by the formula $C = \varepsilon_r \varepsilon_0 A/t$.
However a thicker cavity means a higher bias voltage to achieve the same modulation depth. We opted, to reach the objective of high-speed operation with low drive voltage and high modulation depth, to work with a 2λ-thick cavity. This dimension allows the incorporation of 25 QWs which is, compared to the previous studies [126], optimal for our application.

As described in the introduction of this manuscript, the FP resonance wavelength is directly linked to the thickness of the cavity itself. To have a resonance at 850 nm it is thus necessary to design the cavity with a thickness which is proportionnal to $\lambda_{opt}/2$ with $\lambda_{opt} = \lambda_{FP} \ / \ n_{eff}$ where the effective refractive index of the cavity is taken as the average on the whole thickness.

The 25 QWs and barriers are 25*8.5 + 26*10 = 472.5 nm thick. Regarding the refractive index of both layers of GaAs (3.6417) and $Al_{0.3}Ga_{0.7}As$ (3.3793), the effective value on this stack is 3.497 which, without any other layers, corresponds to an optical cavity lo-

cated at 810 nm. To reach the expected wavelength of 850 nm for data communications, an optical thickness of 495.41 nm is required. To do so, $Al_{0.3}Ga_{0.7}As$ cladding layer has to be implemented on both side of the MQW. We thus added 7 nm of cladding layers on both sides of the QW stack.

This cavity has now to be implemented in the Asymetric Fabry Perot structure to improve the modulation depth.

2.5.2 *Mirror layers*

In this subsection we describe the design of the ASFP structure by optimizing the periods number of the top DBR and for the shared DBR while considering the vertical integration of the modulator onto the VCSEL. We will thus describe first the refractive index of each layer, then the reflectivity at the interface between them. The reflectivity of the stack is then presented and in the next subsection implemented with the transfert matrix method to calculate the absorption as a function of the applied voltage.

Each layer of the structure is parametrized with its thickness, which is a quarter-wavelength thick as described in Section 1.2, and its complex refractive index with:

$$\begin{aligned} &n_j = n_i - i \cdot k \text{ with } k = \alpha_{n,p} \cdot 10^{-4} \cdot \lambda_0/4\pi \\ &\alpha_{n,p} \text{ is linked, for GaAs, to the doping level by } \alpha_n = 5 \cdot 10^{-18} \cdot N \text{ and } \alpha_p = 11.5 \cdot 10^{-18} \cdot P \end{aligned} \tag{2.9}$$

where N and P are the doping levels in the N and P regions. The real part of the refractive index are taken from Afromovitz [85] where

$$n^2 - 1 = \frac{E_0 E_d}{E_0^2 - E^2} \quad \text{with} \quad \begin{cases} E_0 = 3.65 + 0.871x + 0.179x^2 \approx 2.6 + 3/4E_g \\ E_d = 36.1 - 2.45x \\ E_g = 1.424 + 1.266x + 0.26x^2 \end{cases} \tag{2.10}$$

We set n_H and n_L as the refractive index of the high and low index layers, in our case the real part are given by $n_H = n(Al_{0.15}Ga_{0.85}As) = 3.499$ and $n_L = n(Al_{0.9}Ga_{0.1}As) = 3.031$.

As described in the previous chapter, in most cases, the lateral electrical and optical confinement is done with a highly doped Al-content layer. For this layer, $Al_{0.98}Ga_{0.02}As$ is prefered to AlAs due to the more stable oxide formed from this alloy.

It is therefore not possible to use so high Al-content layers for the DBR to prevent any oxidation of the mirror. We thus work with Al-content of 90 %. Furthermore, this value is a good compromise between sufficient contrast Δn between both high low index

layers (around 0.5) while maintaining a lattice missmatch of 0.1 % and not too aburpt band discontinuity as for AlAs / GaAs which could increase the electrical resistance of the mirror.

For the lower Al-content layer, we selected sufficiently high Al-content to avoid any optical absorption in these layers. 15 % is thus a good choice and allows sufficient index variation between both layers.

We have discussed about the calculation of the reflectivity of such a stack structure in Section 1.2.3.

We plot in Fig. 2.8 the reflectivity of the whole stack as a function of the number of periods for three materials combinations.

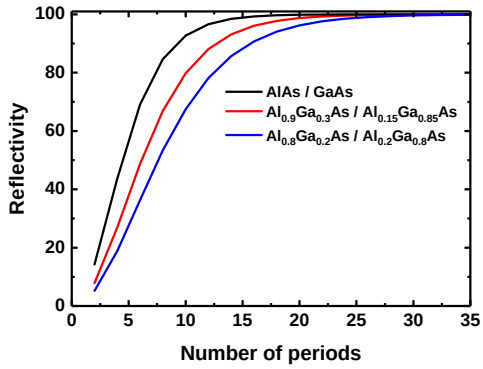

Figure 2.8: Reflectivity maximum of the DBR stack with three Al-content combinations

We thus work, for the next calculations, with DBR stack consisting of $Al_{0.9}Ga_{0.1}As$ / $Al_{0.15}Ga_{0.85}As$ layers.

2.5.3 *Transfer Matrix Method*

In this subsection we optimize the DBR period number by modeling the multiple quantum well structure embedded in the Asymetric Fabry-Perot cavity.

To do so, we used the Transfer Matrix Method [86] which considers each layer as a matrix of reflected and transmitted electromagnetic waves. The wave propagation through N layers under normal incidence is described as a product of each interface contribution. We can thus simulate the global reflectivity of the device with the 2-λ thick cavity sandwiched between the two mirrors.

In Fig. 2.9b we plot the reflectivity of the stack composed of 25 QWs embedded in 6 and 10 DBR periods without consideration of the absorption in the QW. The cladding layers, as explain previously, allow to tune the FP resonance position. In Fig. 2.9 a) we present the refractive index variation along the thickness of the device. DBR and MQW

cavity are shown respectively in green and red. In Fig. 2.9c we illustrate the influence of the top and bottom DBR period number on the FP resonance. Indeed, when the period numer is increased, the FP peak and the plateau on each side, increase too. We can also notice that smaller period number provides broader resonance meaning larger spectral operation bandwidth.

To reach the maximum contrast ratio and reflectivity change it is necessary to have, without modulation, a low reflectivity at the FP position and a high reflectivity at the excitonic peak position. For this reason we selected the 6/10 couple for the DBR periods.

Of course, without top DBR, we would not have any cavity and so no Fabry-Perot resonance would be observed.

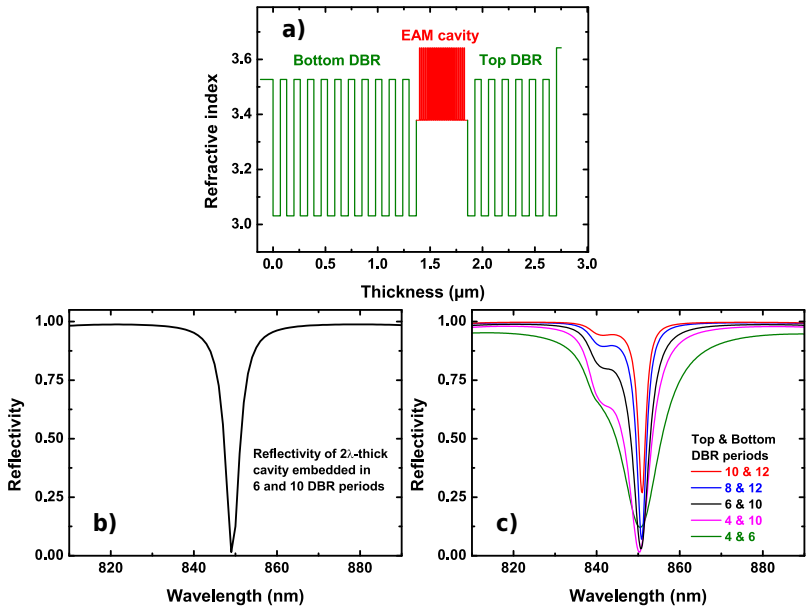

Figure 2.9: MQW embedded in an Asymetric Fabry-Perot strucutre. a) Refractive index variation along the structure, b) reflectivity of an ASFP of 6 and 10 DBR periods without consideration of the absorption phenomena c) Reflectivity with the absorption for different couples of parameters

2.6 VERTICAL INTEGRATION OF THE EAM ONTO THE VCSEL

We have carried out so far the design of the multiple quantum wells cavity, the $\lambda/4$-thick layers for the DBR and the selection of the DBR periods number. We discuss in this last section the integration of a such structure onto a VCSEL.

We considered a standard structure for the VCSEL device. In the literature, most of the devices have top and bottom DBR period of 20-25 and 30-35 pairs respectively. The VC-

SEL cavity is λ/2-thick with a high Al-content layer for the oxidation, and 3 QWs. In the VCSEL, the DBRs are realized with Al grading, as explained in the next chapter, to decrease their electrical resistance.
Considering so far the vertical integration of the EAM onto the VCSEL, in order to have a slight decoupling of cavities Van Eisden et al. [87] have demontrasted that it is mandatory to provide a large number of periods of the middle DBR to decrease as possible the optical feedback of the EAM section into the VCSEL cavity. They worked with an intermediate DBR of 33 periods and a bottom one of 35. The too small difference of reflectivity between these mirrors could have been an obstacle for high power efficiency of the VCSEL. Especially when we consider the EAM top DBR which increases furthermore the top reflectivity seen by the VCSEL cavity.

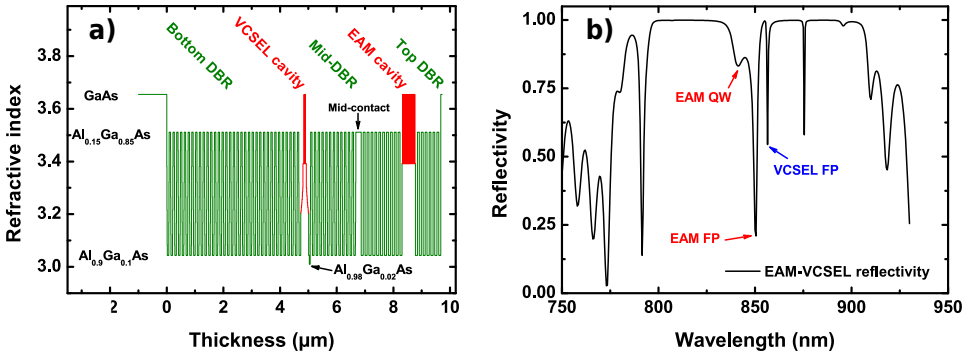

Figure 2.10: EAM-VCSEL refractive index along the strucutre (a) and the simulated reflectivity (b)

We thus worked with a VCSEL structure of 22 and 35 DBR periods. We EAM cavity is added on top of this structure. 10 periods below the MQW we increased the λ/4-thick $Al_{0.15}Ga_{0.85}As$ layer to 3λ/4 to provide the electrical mid contact as shown in Fig. 2.10a. The EAM cavity is then topped by 6-period DBR. By adjusting the cladding layers of the VCSEL, we can reach the expected detuning of 5 nm between the two cavities to decouple them. This detuning is mandatory to provide a decoupled operation of the EAM-VCSEL otherwise the optical behavior would be the same than a ER Modulator where the electric field modifies the top DBR reflectivity and thus the FP resonance. The reflectivity spectrum of this EAM-VCSEL structure is shown in Fig. 2.10b.
This structure is, at this moment, optimized for room temperature operation and could be improved after the first fabrication and characterization run, considering the temperature effect on all the parameters. Indeed, the detuning between the EAM QW and the EAM FP may be enhanced. This work will be described in the next chapter.

2.7 CONCLUSION AND PERSPECTIVES

Based on a simple absorption model we optimized the QW design of the absorber region, namely its thickness (8.5 nm) and the Al-content (30%) of the barrier to reach high modulation depth while maintaining a low drive voltage. Then, this 2-λ thick multiple quantum well cavity has been embedded in an Asymetric Fabry Perot to increase the number of paths the light traverses the absorber region and thus to decrease the required quantum wells number and thus relax the tolerances on the epitaxy growth.

With the Transfer Matrix Method we designed this EAM structure centered at 850 nm with 6 and 10 DBR periods with $\lambda/4$ layers of $Al_{0.9}Ga_{0.1}As$ and $Al_{0.15}Ga_{0.85}As$ to reach the higher optical contrast without absorption phenomena.

About the emitting section we considered a standard VCSEL structure composed of 3 QWs, one high-Al-content layer and 22 and 35 DBR periods. The EAM structure is thus embedded within the VCSEL, its bottom DBR coincides with the top VCSEL DBR which is surrounded by the absorber cavity and the top EAM DBR.

The properties of both EAM and VCSEL QWs have been designed to be the same. We only modified the cavity lengths to decoupled them. We designed the device to have a blue shift of the EAM FP resonance compared to the VCSEL one.

To go further with this simulation work, it would be interesting to study the impact of the top DBR on the VCSEL emission properties. Indeed, an increase of the top mirror reflectivity seen by the VCSEL cavity will decrease the output power.
Another work would consist in the modelling of the feedback light from the modulator to the VCSEL and to simulate the induced modifications on the ouput emission.

The next chapter will describe the fabrication process of such integrated EAM-VCSEL with different technological developments to achieve a reliable process on the double mesa structure and the static characterization.

3 FABRICATION AND CHARACTERIZATION IN STATIC OPERATION

Vertical-Cavity Surface-Emitting Lasers (VCSELs) are now widely used and commercialized. Their fabrication is thus standard and well known, nonetheless VCSEL complex and multilayered structure remains a challenge. Indeed, the epitaxial growth of hundreds of thin layers requires precise calibration and in situ or ex situ monitoring tools. About the fabrication process, a perfect alignment between the emitting window, formed by the passivation layer and the metallization, and the lateral confinement is required. In the case of high speed operation both contacts are located on top and separated by a polyimide based insulator to decrease the parasitics capacitance.
In our device, the VCSEL is integrated with an electro-absorption modulator (EAM) which complicates even more the fabrication. Actually, we have a double cavity and a thicker device which increases the complexity of the epitaxial growth. Regarding the fabrication process of the devices, this configuration has three electrodes and, passivation and metallization are deposited upon an important surface relief of several micrometers. To realize such a EAM-VCSEL, technological developments have to be done on the epitaxial process itself and then on the fabrication process to realize a functional device for high frequency operation.

In the first section of this chapter we will describe the epitaxial growth of the designed structures. We will detail the grown structures with the associated challenges such as the control of the aluminum content gradings in the Distributed Bragg Mirrors (DBRs), the use of digital alloy for quantum wells barriers and the control of the layer thicknesses.

The second section will focus on the post-growth study with reflectivity wafer mappings and photoluminescence measurements to check the properties of the wafers. Measurements of surface roughness and defects will also be reported.

The third section will present the fabrication key aspects. This complicated structure composed of two mesas, three electrodes and a high frequency injection scheme requires several technological developments that will be summarized.

Indeed, one difficulty of such process is to realize passivation and metallization on a structured pattern of few micrometers. To this aim, a novel recipe based on a double resist stack is used to realize, with one photolithography step, two successive lift-offs of the dielectric layer as well as the metal deposition on the EAM and VCSEL sidewalls. This technological development has been also applied to oxide-confined VCSEL, which is the most used confinement method for VCSEL and will be described **in the fourth section**. These two technological developments have been published in **paper A and B**.

Based on these developements, we present **in the fifth section** the static characterization of the stand-alone modulator; namely reflectivity and photocurrent measurements, as a function of the temperature and the applied voltage. A comparison with our model described in Chapter 2 is realized and shows very good agreement which will be useful to provide a feedback on the design and so further optimize it.
EAM-VCSEL has also been characterized to check the proper static operation of the modulator when it is integrated onto the VCSEL.

3.1 EPITAXIAL GROWTH

The term epitaxy litteraly means the process of the deposition of a crystal layer atomically arranged on a substrate layer. This perfect arrangement of the deposited atoms onto the substrate surface leads to high purity films for opto-electronics devices such as lasers, modulators, tunnel junctions etc. The molecular growth of very thin layers of III-V materials can be done by Molecular Organic Chemical Vapor Deposition (MOCVD), also called Metal Organic Vapor Phase Epitaxy (MOVPE), or by Molecular Beam Epitaxy (MBE). The MBE presents several advantages compared to MOCVD such as better interface quality, easy addition of new materials and lower risk with very dangerous gases as it is the case of MOCVD. However, the cells flow variation in time, the low growth rate, the frequent need to change the evaporating sources to fill them and the difficulty to obtain good gradings make the MOCVD technique the more attractive for industrial use.

In our project we need a good interface quality in order to reach high modulation depth and so we worked with a MBE 412 equipment from the manufacturer Riber.

To realize the DBR doping we used Si for N-dopant and C for P-dopant. The C dopants can be easily controlled in thin layers with the CBr4 flow thanks to the travel speed of the baratron for the CBr_4 evaporation. Furthermore very high dopant concentration can

be reached with carbon for electrical contacts in constrast to Zn, Be or Mg, which present disadvantage of having an enhanced diffusion in the structure.

In this section the epitaxial growth of EAM and EAM-VCSEL devices is explained and the needed improvements in order to reach high modulation depth with low drive voltage with high modulation bandwidth are described.

3.1.1 *Structures description*

Five different structures have been grown: 3 EAM (called A, B and C) and 2 EAM-VCSEL (called D and E). This allows to study the impact of the DBR doping on the applied electric field needed for the modulation (EAM (A) and (B) in Table 3.1), the impact of the substrate doping on the high-frequency properties (EAM (B) and (C)) and finally the optimum detuning between the two cavities with EAM-VCSEL (D) and EAM-VCSEL (E).

Doped Substrate	**Doped DBR**	**Wafer structure**
Yes	**No**	EAM (A)
Yes	Yes	EAM (B)
No	Yes	EAM (C)
Yes	Yes	EAM-VCSEL (D)
Yes	Yes	EAM-VCSEL (E)

Table 3.1: Detail of the five grown wafers

The full description of the device structure is reported in the table below. Different sections as the EAM and VCSEL DBR, their cavities and the highly doped layer are presented. Remarks about the grading for the VCSEL DBR and the realization of the different Al content layers are provided in the same table.

Section	Repetition	Layer x_{Al}	Remark	Doping (P/N)	Thickness (nm)
Top contact	1	GaAs	-	N 5e18	50
Top DBR	1	AlGaAs 90	Abrupt interface	N 2e18	69.1
	6	AlGaAs 15	Abrupt interface	N 2e18	61.3
	6	AlGaAs 90	Abrupt interface	N 2e18	69.1
Clading	1	AlGaAs 30	Digital	-	7
EAM QW	1	AlGaAs 30	Digital	-	10
	25	GaAs	-	-	8.5
	25	AlGaAs 30	-	-	10
Clading	1	AlGaAs 30	Digital	-	7
Top shared DBR	1	AlGaAs 90	Abrupt interface	P 2e18	69.1
	10	AlGaAs 15	Abrupt interface	P 2e18	61.3
	10	AlGaAs 90	Abrupt interface	P 2e18	69.1
Middle contact	1	AlGaAs 15	-	P 5e18	181
Bottom shared DBR	1	AlGaAs 90 - 15	-	P 2e18	20
	12	AlGaAs 90	-	P 2e18	49.1
	12	AlGaAs 15 - 90	Grading	P 2e18	20
	12	AlGaAs 15	-	P 2e18	41.3
	12	AlGaAs 90 - 15	Grading	P 2e18	20
AlOx	1	AlGaAs 98	Digital	P 2e18	30
	1	AlGaAs 90	-	P 2e18	55
VCSEL cavity	1	AlGaAs 30 - 60	Grading	-	90
	1	AlGaAs 30	Digital	-	15
	1	GaAs	-	-	8.5
	2	AlGaAs 30	Digital	-	10
	2	GaAs	-	-	8.5
	1	AlGaAs 30	-	-	15
	1	AlGaAs 60 - 30	Grading	-	90
Bottom DBR	1	AlGaAs 90	-	N 2e18	49.1
	1	AlGaAs 15 - 90	Grading	N 2e18	20
	35	AlGaAs 15	-	N 2e18	41.3
	35	AlGaAs 90 - 15	Grading	N 2e18	20
	35	AlGaAs 90	-	N 2e18	49.1
	35	AlGaAs 15 - 90	Grading	N 2e18	20
Buffer	1	GaAs	-	N 2e18	1000
Substrate	-	GaAs	-	N 2e18	-

Fig. 3.1 shows the different epitaxial layers: in yellow the highly doped layers for the electrical contacts, in green the DBR and in red the two active regions. A) is a Scanning Electron Microscope (SEM) view of the EAM after epitaxy and mesa etch and b) is a zoom on the active region showing the 25 QWs in the EAM cavity. C) is a SEM picture of a Focus Ion Beam (FIB) cut of the whole EAM-VCSEL structure. In d) the corresponding standing wave electric field, calculated with the Transfer Matrix Method at 870 nm, is plotted and highlights the importance of the design and the good control of the very thin layers.

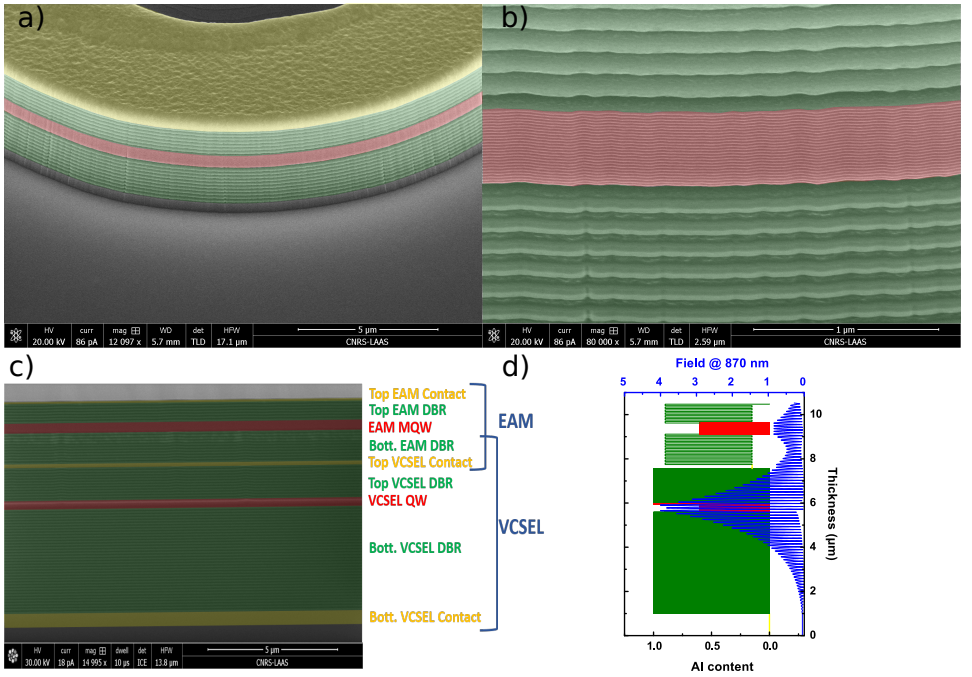

Figure 3.1: SEM pictures of the grown structures. a) EAM mesa after etching, b) zoom on the MQW region and c) FIB cut of the global EAM-VCSEL stack. Highly doped regions for electrical contacts (yellow); DBR (green) and active regions (red) are colorized.

3.1.2 *Particularities of epitaxial growth of EAM-VCSEL*

The epitaxial growth of the structures has been done in a Riber 412 MBE reactor. Based on previous studies, the substrate temperature was set at 550°C and the V/III ratio for AlGaAs at 3.2 was used and maintained during the entire growth of the structure to ensure very low surface roughness. In this vaccum reactor, the cell flow is linked to the temperature following Clausius-Clapeyron law which is a way of characterizing a discontinuous phase transition between two phases of matter of a single constituent. Nevertheless after the cell temperature is decreased and then increased again, a variation

of 10 % on the evaporated flow can be observed for the same cell temperature. New cells calibration are thus required before each growth. Indeed, this structure is composed of 3000 layers and the epitaxial growth lasts more than 17 hours which increases the required precision of the callibration.
In this reactor, the following cells have been used for the growth: 2 x Ga, 2 x Al and 1 x As cracker. Cell evaporation rates were choosen accordingly in order to provide a growth rate of 1 µm/h for both $Al_{0.9}Ga_{0.1}As$ and $Al_{0.15}Ga_{0.85}As$. In order to realize the different compositions required in the stack for Al_xGaAs, and this without changing the cell temperature, a "slow" and a "fast" rates from two cells were combined for each material leading to 0.1 and 0.85 µm/h for Ga and 0.9 and 0.15 µm/h for Al. These compositions are summarized in table 3.2 About the dopant cells, Si and C were used for N and P doping of the DBR and the contact layers of the structure.

Effusion cell	Growth rate (µm/h)	$Al_{0.15}Ga_{0.85}As$	$Al_{0.9}Ga_{0.1}As$	$Al_{0.3}Ga_{0.7}As$		DBR grading	
Ga1	0.1	-	X	X	X	-	X
Ga2	0.85	X	-	-	-	-	-
Al1	0.15	X	-	X	-	-	-
Al2	0.9	-	X	-	-	X	-

Table 3.2: Cells use for different Al-content layers, for barriers and DBR gradings.

The epitaxial growth of such a stack involves some challenges such as the DBR grading, the digital alloy composition for barriers and the high Al-content layer. These particularities are described in the next subsections.

3.1.2.1 *DBR grading*

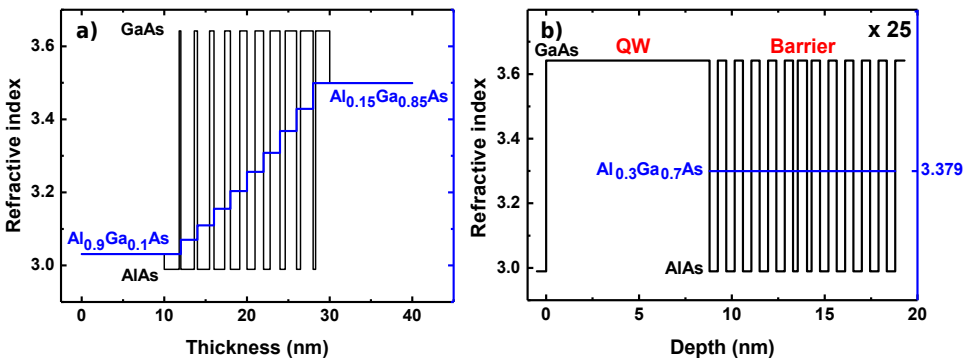

Figure 3.2: Refractive index variation along the QW and barrier with digital alloy

The abrupt shift in Al-content heterostructure in a DBR from the high bandgap (low index) ($Al_{0.9}Ga_{0.1}As$) to the low bandgap (high index) ($Al_{0.15}Ga_{0.85}As$) layer introduces a series resistance which increases the applied voltage in the structure and thus leads to a higher internal temperature through Joule effect and finally a faster deterioration of the device. To avoid this effect, discretized superlattice can replace the abrupt interface to decrease in gradual steps the Al-content from 90 % to 15 %. To realize these graded values of Al-content one solution consists in modifying the cell temperature. However, as the temperature change is not reliable to retrieve the same flows, this method cannot be used. We thus grow alternatively layers with high and low Al-content for which the ratio between the respective thicknesses corresponds to the expected Al-content.

In the case of the VCSEL structure, DBRs are usually grown using a 20nm-thick region at the interfaces to decrease the electrical resistance [88] [89]. We then implemented this approach in our VCSEL device.

The $\lambda/4$-layers thickness of 69.1 nm and 61.3 nm of respectively $Al_{0.9}Ga_{0.1}As$ and $Al_{0.15}Ga_{0.85}As$ are replaced by 49.1 nm and 41.3 nm plus 20 nm of grading at their mutual interfaces. This grading part is divided in 10 steps of 2 nm of an Al-content of 7.2 or 7.65 %. To reach of the Al-content of each layer we have to consider its average since, with our 4 cells (2 Ga and 2 Al) we can not reach all the values without modifying the cells temperature. For example, the 2 nm-thick layer of 40 % is divided in 0.8 nm of AlAs and 1.2 nm of GaAs which gives an Al-content average of x_{Al} = (0.8 * 100) + (1.2 * 0) / (0.8 + 1.2) = 40 %.
In Figure 3.2a we present an evolution of the refractive index in the DBR grading from 90 % to 15 %.

This grading was used for the N-doped bottom VCSEL DBR and the P-doped top VCSEL DBR. Since there is no current flowing in static operation in the EAM region it was not necessary to complicate furhter the structure and so no grading was used.

Unfortunately this Al-content grading presents the disadvantage of considerably modifying the band structure of the layer and so the continuity of the doping as described in [24]. To compensate it, and so decrease the DBR resistance this grading section need to be overdoped.

3.1.2.2 *Digital alloy for barriers*

As for the DBR grading, the 30% Al-content (which has been demonstrated to be optimum in Chap 2 for the absorption) can not be done with the 2 Al-cells in the MBE reactor. Two solutions are praticable:

- Stop the epitaxial growth and modify the cell temperature as described previously, however this solution is not feasible for DBR grading.

- As for the DBR intermediate layers, consider the average of the Al content. $Al_{0.3}Ga_{0.7}As$ is in that case replaced by equal alternance of $Al_{0.6}Ga_{0.4}As$ and GaAs layers. In that case the 60 % of aluminum is obtained with the slow Al (0.15 µm/h) and Ga (0.1 µm/h) cells. Indeed with these two cells simultaneously opened we get an Al-content of 0.15 / (0.1 + 0.15) = 60 %.

We select the second option for the realization of the QW barriers. Furthermore, the quality of the QW / barrier interface plays an important role in the absorption tail shape and in the recombination process. Indeed, an interface with a lot of defects will decrease the photon escape time and so increase the modulation speed of the EAM device, however it will degrade the absorption properties of the component. To validate the use of this digital alloy for the studied structure, samples with 5 and 25 multi-QW (same configuration than the expected EAM stack) were grown with classical bulk barriers and digital alloy barriers. The barrier, with digital alloy, of 10 nm was realized by using $(GaAs)_{5nm}$ and $(Al_{0.6}Ga_{0.4}As)_{5nm}$ with a perfect symmetry as described in Figure 3.2 b). The thicknesses of the different layers are in good agreement with Kaspi et al. [90].

Photoluminescence (PL) were carried out to study the electro-optical properties of such a structure. As shown in Fig. 3.3a, the digital alloys barriers exibit better PL response at room temperature but, as predicted in Chapter 2, the photon lifetime is more important leading, due to minor impurities at the interface, to a smaller electrical bandwidth. However, as demonstrated by previous studies, the first physical limitation of such devices would come from the parasitics elements. As absorption modulation is the topic of this project, the epitaxial growths were therefore realized with digital alloy.

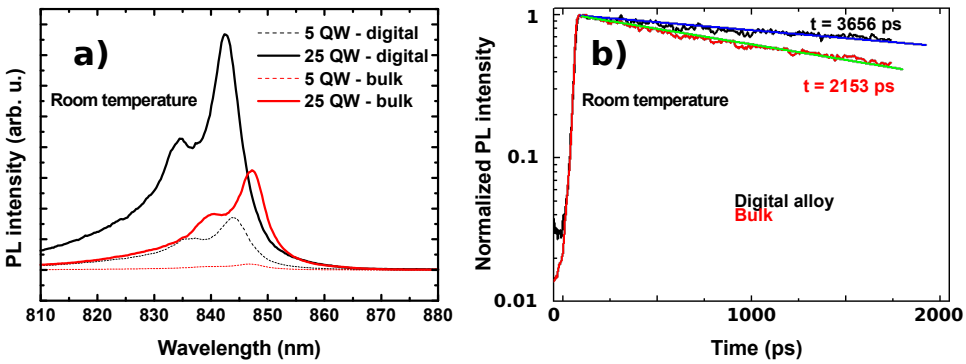

Figure 3.3: Room temperature PL of 5 and 25 QWs separated by digital alloy or bulk barriers a) Wavelength characterization, b) timely response.

3.1.2.3 *Oxide confinement*

As described in the section 1.2.5, the electrical and optical confinement in VCSEL is now generally realized with a high aluminum content layer which is oxidized with a water gas flow at high temperature (> 400°C). This Al-content has to be high enough to be oxidized selectively compared to other Al compositions (which are 90%) in a convenient time (the oxidation rate varies exponentially with the Al content). The layer can not be pure AlAs due to the strain induced by the oxidation since a shrinkage of 10 % is observed for the oxide layer. Thus, a composition of $Al_{0.98}Ga_{0.02}As$ is prefered to reduce this oxide-related strain. As for the DBR grading and for the barriers, a digital composition has to be considered to perform the 98% of aluminum. To this aim, the 30 nm of $Al_{0.98}Ga_{0.02}As$ are obtained by repeating 10 x (1.2 nm AlAs - 0.6 nm $Al_{0.9}Ga_{0.1}As$ - 1.2 nm AlAs). In an industrial context this concentration has to be very well controlled since it is linked with the oxidation rate and thus the repeatability of the oxidation.

3.1.3 *Thickness control*

The previous chapter and the previous section has demonstrated the tight precision required in such an electro-optic component. The modulation properties of the device are closely linked with the layer thicknesses as seen in the mapping of the FOM in section Chap 2, 2.3. Indeed, a variation of less than 1 nm (10 %) is sufficient to degrade considerably the properties. The gain-resonance wavelength detuning is also very important and a poor control of the epitaxial growth could lead to the non-operation of the VCSEL (as explained in Intro) or its modulation by the EAM (as described in Chap 2). In addition to the absorption or detuning position, very thin layers are needed to achieve the DBR grading and the QW barriers which also demonstrate the complexity of the thickness control.
For thoses reasons, a precise and systematic calibration of the cell flows is mandatory before the long-time epitaxy growth of the structure for both thinner layers as QW and barriers and thicker layers as the DBRs and intermediate contact layers.

Before or during the epitaxial growth several in-situ instruments are available to perform the cells flow calibration to ensure the expected optical and physical properties of the stacked layers. In the following section we describe the burst transient from the cell flux just after the shutter opening monitored in real-time by flux gauge measurement and then with an atomic absorption setup. Then, we present the reflectometry measurement during the growth of $\lambda/4$ layers deposited by each individual cell and how to apply an experimental fit providing a feedback on the precise temperature to get the expected flow rates.

3.1.3.1 *Flux gauge*

The flux gauge is an equipment comprised of a filament acting like an electron source (Bayard-Alpert gauge), a grid which accelerates the electrons and a collectors that detects the ionized element. The measurement of the collisions between the electrons and atoms in the grid gives a good estimation of the evaporated flows.
In particular, the flux gauge measurement highlights the cells overflow burst when its shutter is opened, as seen in Figure 3.4, a transient overpressure implying the variation of the growth rate. Indeed it is of high interest to consider this cell burst, mainly with thin layers (in DBR grading, digital alloy for the barriers) where the burst duration is of the same magnitude as the shutter opening time.

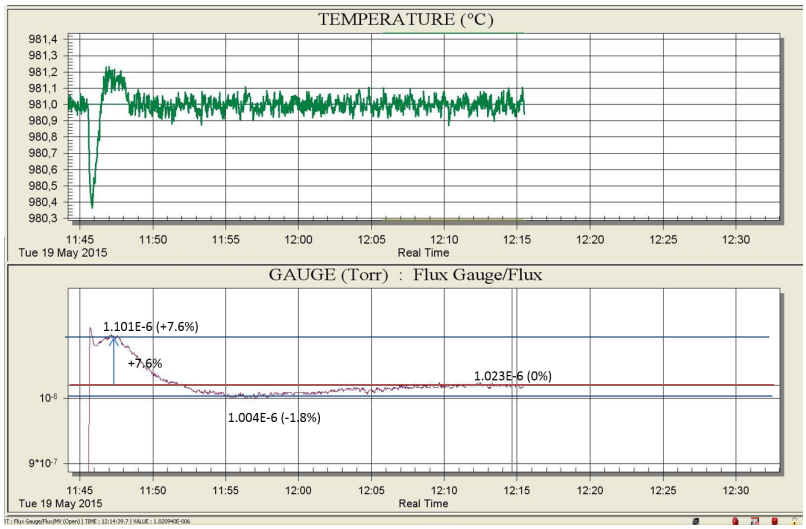

Figure 3.4: Measurement of the burst effect when the shutter is opened at 11:45:30. Temperature is plotted on top and below the flow measurement by the flux gauge

This estimation is however not very accurate and can vary with several parameters. Furthermore, as it can be seen in Fig. 3.5 a) the flux gauge can not be used during growth since it is in front of the wafer for measurement and has to be retracted for the growth. Thus, for the real-time monitoring of fluxes during the growth another method based on the atomic absorption is employed.

3.1.3.2 *Optical Flux Monitoring*

The atomic absorption, linked to the variation of the beam flux density, of a chemical species of the III column can be linked with the resulting growth rate following a Beer's law as demonstrated by Pinsukanjana [91].

$$\alpha_i = 1 - \exp[-A_i r_i (1 + B_i r_i)] \tag{3.1}$$

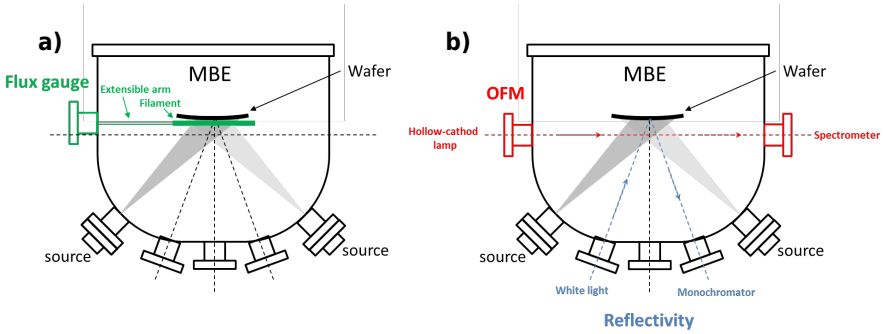

Figure 3.5: Schematic of the MBE reactor with the flux gauge equipment (a) and the Optical Flux Monitoring and Reflectivity (b)

α_i and r_i are respectively the atomic absorption of the material and the growth rate. The A_i and B_i parameters given are reactor dependent but it the area of interest a linear regression can be roughly done to have an idea of the phenomenon. In addition to the flux measurement, the Optical Flux Monitor (OFM) is an essential measurement to know precisely the burst amplitude and its duration for each cell. For the Ga one, an hollow-cathod lamp beam go through the MBE chamber and the transmitted signal is measured by a spectrometer as shown in Fig. 3.5b. The measurement could be even more accurate by using a mirror and thus measure the reflected signal which is absorbed twice.
The OFM measurement was done along all the epitaxial growth of the structure and an example is given in Fig. 3.6a. The positions of the two cavities are clearly visible by the low Ga absorption, and also the slight variation of the cell flow over the time. This variation is due to the amplitude variation of the light and the slight movement of the reactor in time. In Fig. 3.6b a zoom is shown on two DBR periods which highlights the cell burst in the 49 and 41 nm layers. In Fig. 3.6c is a more important zoom on the DBR grading. We clearly identify the digital alloy grading described in Fig. 3.2a.

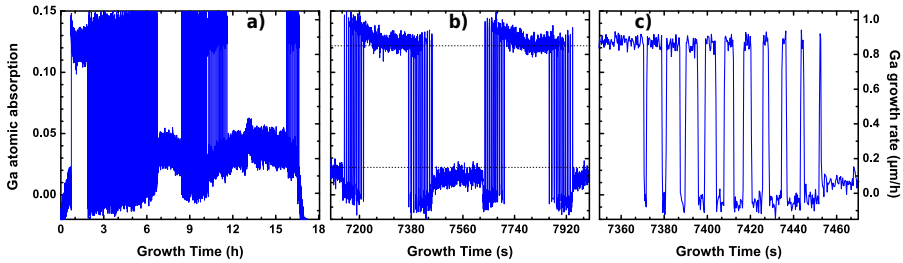

Figure 3.6: OFM measurement of the Ga absorption during the whole EAM-VCSEL growth (a), zoomed on a two DBR periods (b) and zoomed on the DBR grading (c)

To compensate the cell burst effect (shown in Fig. 3.6 b)) we intentionally slightly decrease the cell temperature to get the aimed growth rate considering an averaged value integrated over the shutter opening duration. However this technique is only valid for

thick layers and not for thin ones (QW or DBR gradings). We thus moved to a reflectivity measurement of fast and slow growth rate cells to adapt the cell temperature to achieve the expected growth rate for each layer of the device.

3.1.3.3 *Optical reflectometry*

Once the burst effect has been identified, it is necessary to measure the cells flow and adapt the temperature to reach our expected stable rates. A reflectivity measurement is realized to have a cell flow calibration. To do so we use a low-angled (20°C) white light which is reflected at the surface of the wafer and collected in a DK480 monochromator as presented in Fig. 3.5b. In this configuration we measure the reflectivity of the wafer at 840 nm below the energy gap in the transparency window of the material. We grow $\lambda/4$-layers of GaAs at 0.1 µm/h, GaAs at 0.85 µm/h, AlAs at 0.15 µm/h, AlAs at 0.9 µm/h corresponding to the four cells at our disposal, as described in Fig. 3.7.

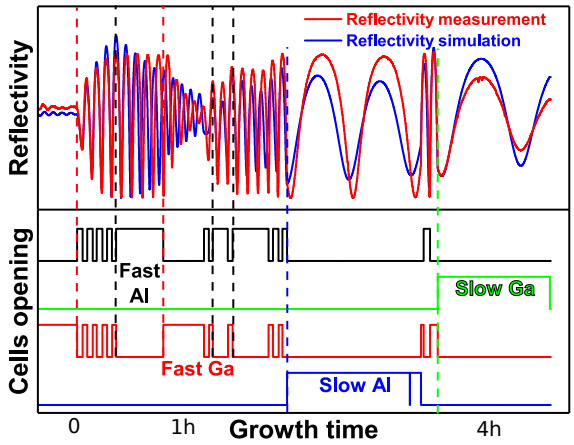

T0	T1	V1	V Expected
45.16	1245.1	1	0.9
51	861.3	0.097	0.1
92.76	1009.9	0.87	0.85
70	1139.7	0.151	0.15

Figure 3.7: Cells calibration by reflectivity fit. Fit are done on $\lambda/4$-layers of GaAs and AlGaAs to match the growth rate. In green the reflectivity at 600nm is plotted and in blue the simulation.

We then compare this measurement to the simulated reflectivity, of such layer structure, using the Transfer Matrix Method. By adjusting the values of the parameters, specifically the cells flow rates, we fit the blue curve (simulation) with the red one (measurement) and so we deduce the crucible temperature giving the expected growth rate. Indeed, the growth rate (V) varies exponentially with the temperature with $V_2 = V_1.exp((T_2 - T_1)/T_0)$, knowing T_1 and V_1 (from the current growth rate), and the parameter T_0 which is intrinsic to the cell, we adjust T_2 to reach the aimed flux V_2. The amplitude of the simulated and measured reflectivity are due to the refractive index considered for the modelling but do not affect the calibration. Only the peaks and valleys positions are important.

We also acquired this measurement during the whole EAM-VCSEL growth, as shown in Fig. 3.8. In particular, a very good agreement is obtained with the simulated reflectivity along the whole structure growth time. We can see in this figure the different cells opening. The fast Al and Ga cells are used for the thicker layers as the DBR periods while, to increase the precision, the slow Al and Ga are preferred for the cavity regions.

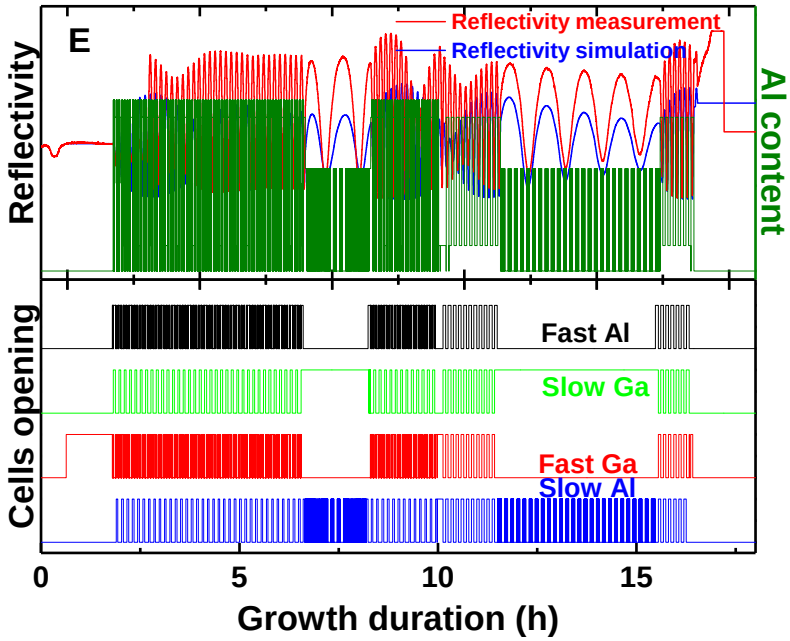

Figure 3.8: Reflectivity measurement of the global structure at 840 nm with a white light source reflected at the surface of the wafer E.

With this calibration and monitoring routines, we demonstrated reliable way to grow complex stacks such as our EAM-VCSEL structure.

3.1.3.4 *Structure for X-ray diffractometry calibration*

To further improve the calibration method, we implemented another way to provide a better calibration of the cell flux.

It is possible to grow on the same wafer a double superlattice stack comprising, from bottom to top, alternating Ga_1As (at 0.15 µm/h) and Al_1As (at 0.1 µm/h) thin layers (10 nm) and then an alternating Ga_2As (at 0.85 µm/h) and Al_2As (at 0.9 µm/h) thicker layers (120 nm).

With the X-ray diffractometry measurement, which reveals information about the crystal structure, the two spatial frequency give two distinct angular frequencies. We thus obtain specific peaks corresponding to each superlattice. The small peaks periodicity is linked to the important superlattice (fast cells growth) while, with the low thicknesses superlat-

tice, we obtain more widely spaced peaks. Thanks to this distinction it is possible to fit both superlattices and thus extract the precise thicknesses of each layer and so obtain an information about the four cell flux rates. We can then adjust the temperature to reach the expected flux rate as described previously.
Unfortunatelly this method has been developed posteriorly to the growth of the structures described in 3.1.1. Nevertheless, it has been used for the growth of a half-VCSEL structure at 1550 nm and has proven to be very effective, and will be very helpful for the next growths of EAM-VCSEL structures.

3.1.4 *Epitaxy recipes*

The MBE equipment is controlled and monitored by a software named Crystal XE which controls the cells temperature, the opening and closing of the cells shutters and the degree of openness of the valves. Considering the expected layers thicknesses (in Table 3.1.1) we adjusted the cells temperature with the calibration previously described.

A main recipe is created for the whole structure and enables to call subrecipes as for the DBR grading or digital barrier.

To check that the recipe is error free, a labview program interprets the programmed growth recipe and simulate the reflectivity spectrum all over the epitaxial growth. An example of simulation for our structure is shown in Fig. 3.9.

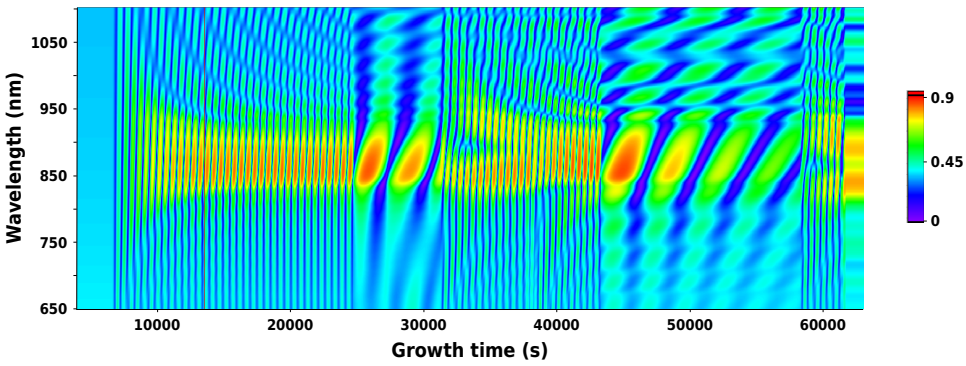

Figure 3.9: Reflectivity simulation of the EAM-VCSEL all over the growth time, calculated from the Crystal XE structure recipe

We describe in Annex C the global EAM-VCSEL routine and the associated subrecipes such as DBR grading, QW and barrier.

3.2 POST-GROWTH CHARACTERISATION

3.2.1 *FTIR mappings*

After the epitaxial growth of the wafers it is of high interest to measure the main characteristic of the EAM and the EAM-VCSEL structure such as:

- FP resonance wavelength of the EAM, which is directly correlated to the cavity thickness
- Excitonic absorption peak position (λ_{hh}), which is linked to the QW properties
- FP resonance wavelength of the VCSEL
- Photoluminescence of the QW of the VCSEL

To do so, a reflectivity mapping with FTIR (Fourier Transform InfraRed spectroscopy) was done on all wafers at the center, at 10 mm, 25 mm and 40 mm of the center to check the uniformity along the radius. Results are presented in Fig. 3.10.

This reflectivity measurement is useful, for the EAM structures, to know precisely the position of the excitonic absorption peak. Indeed, the heavy hole position, as denoted in Fig. 3.10, can be seen at respectively 836.7 nm, 837.15 nm and 835.03 nm and the FP resonance at 850.5 nm, 831.25 nm and 843.81 nm for the samples A, B and C. Here we can also clearly identify the position of the light hole position at 10 nm below the heavy hole one. For the sample B, the exciton position and the FP are convolved leading to a high value of the reflectivity at this wavelength. However for wafers D and E it is impossible to identify neither the position of the excitonic peak nor the Fabry Perot corresponding to the EAM cavity and nor the VCSEL one. Each part, EAM DBR, shared DBR and bottom DBR has its own reflectivity characteristic which contributes to the global spectrum and so complicates the extraction, of individual resonnnce wavelength.

About uniformity, a shift of the FP resonance wavelength ($\Delta\lambda_{FP}$) of 2.4 nm and 1.82 nm for respectively sample A and C corresponding to a $\Delta\lambda_{FP}$ / λ_{FP} of 0.28 % and 0.22 % can be noticed, which is an excellent result on 4 inches wafers.

The maximum reflectivity values differences are due to the FTIR calibration itself. Indeed, to provide the calibration a gold wafer is inserted on a mechanical arm which loads it and provides the measurement. Then the wafer to be measured is positioned but the flatness is not ensured which can lead to maximum amplitude variations. The FTIR is thus not a precise equipment for reflectivity values and can not be used for the EAM characterizations but is useful for the position of the FP and the excitonic peak position.

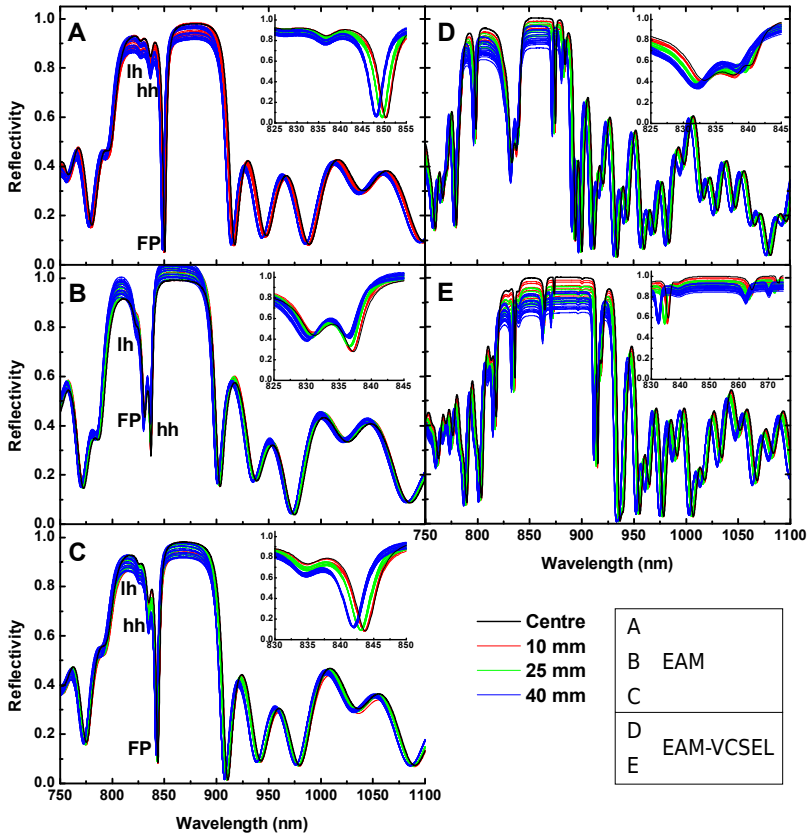

Figure 3.10: FTIR mappings of the five wafers at the center (black), at 10 mm from the center (red), 25 mm(green) and 40 mm (blue). For the EAM wafers, the excitonic and the Fabry-Perot positions are labelled. Zooms on the zones of interest are plotted in the insets.

3.2.2 *Reflectivity combined with PL*

For the EAM-VCSEL structures (D and E) we can notice two resonances. Due to the differences between the EAM and the VCSEL cavities, i.e. the thickness $\lambda/2$ compared to 2λ and the number of QWs (3 versus 25), it is not possible to distinguish which cavity corresponds to the EAM or to the VCSEL. To do so, it is necessary to move forward to another method described here after.

After the global reflectivity measurement presented previously (and also by black arrow in the inset in Fig. 3.11) we dry etched the top DBR to reach the EAM cavity, thanks to an end-point detection system installed on the ICP-RIE reactor. We thus measured the photoluminescence of the EAM QWs (Fig. 3.11 red arrow). Subsequently we etched this cavity and measured the reflectivity of the VCSEL itself (blue left arrow). Finally, after etching the whole shared DBR and stopping in the VCSEL cavity, we measured

the photoluminescence of the VCSEL QW (Fig. 3.11 blue right arrow). Results of these successives etchings and measurements as presented in Fig. 3.11 are discussed here after.

Wafer D

About the wafer D, the reflectivity spectrum presents a very broad peak around 836 nm which is a convolution between the EAM excitonic peak and the VCSEL FP resonance.
The PL maximum intensity of the EAM QW is located at 848 nm and for the VCSEL between 830 and 840 nm. The exact position can not be determined due to the convolution with the FP resonance.

The configuration of the wafer D is adverse since the QW PL is red shifted in regards to the FP and so no lasing operation is possible as seen in the Introduction.

Wafer E

At the opposite, in the configuration of the wafer E, the wavelength of the QW PL is shorter than the FP resonance of about 23 nm which is perfect for lasing operation and potential EA modulation as described in Chap 2. Indeed, the PL of the EAM QW are located at 843, here again a shoulder appears due to the stop band of the below DBRs. The PL for VCSEL QW is at 847 and will thus, with the rising internal temperature, move closer to VCSEL FP resonance at 870 nm. The EAM FP resonance is found 5 nm below at 865 nm.
All the PL and reflectivity properties of the wafers are summarized in Table 3.3.

		A	B	C	D	E
PL	EAM	837	836	835	848	843
	VCSEL	-	-	-	850	847
FP resonance	EAM	850	831	844	836	865
	VCSEL	-	-	-	836	870

Table 3.3: Wavelength positions of the QW and the FP resonance of each grown structure

Another way to obtain the same information is to use a lateral high resolution PL measurement. In that case a very localized laser spot is needed to not measure both EAM and VCSEL cavity since they are only distant of 3 µm.

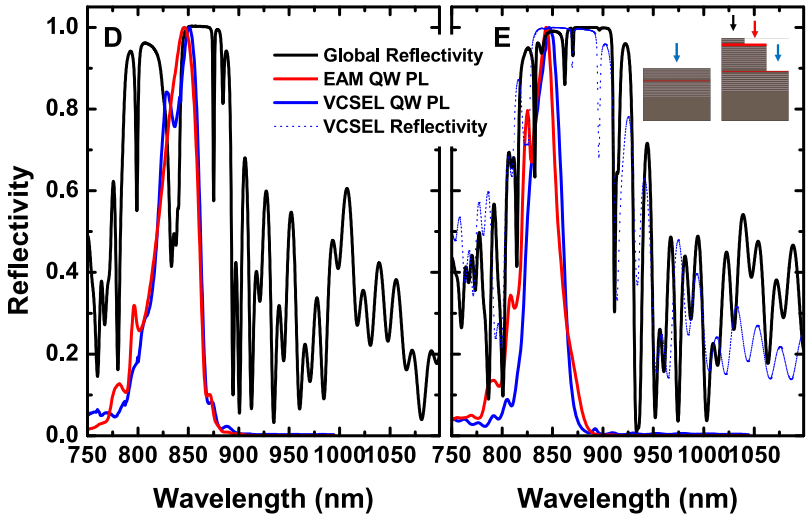

Figure 3.11: Relectivity and Photoluminescence of the QWs of the EAM-VCSEL structures. Global reflectivity (black), PL of the EAM QW (red), PL of the VCSEL QW (blue) and for the wafer E, VCSEL reflectivity (dashed blue).

3.2.3 *Roughness and defects*

In addition to these reflectivity and PL measurements, Atomic Force Microscope (AFM) characterization of the samples surface has been done to evaluate the surface morphology of the grown structure. AFM results are shown in Fig. 3.12. On the left, oval defects are identifiable and crosshatch due to strain relaxation appears along diagonals. In b) the phase of the signal collected by the probe is shown and the step benching can be observed. Surface roughness measurements of 25 QWs grown with digital alloy barriers or bulk, and wafers A and B itself are summarized in Table 3.4.

Two averages are given, R_a and R_q (also called Root Mean Square, RMS) which represent respectively the arithmetic mean and the mean square deviation and are given by:

$$R_a = \frac{1}{l}\int_0^l |z(x)| \cdot dx \quad \text{and} \quad R_q = \sqrt{\frac{1}{l}\int_0^l |z^2(x)| \cdot dx} \tag{3.2}$$

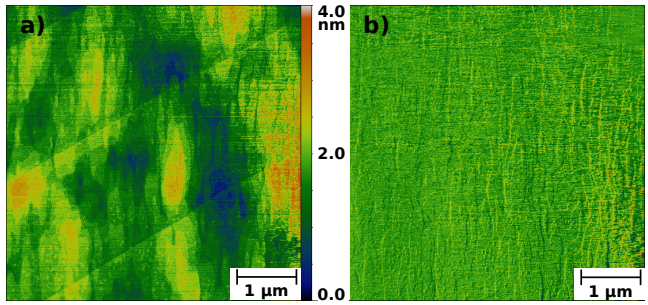

Figure 3.12: AFM measurement of the surface of the sample A. a) amplitude b) phase

Sample	R_a (nm)	R_q (nm)	Scanned distance
25 QW with digital alloys	0.248	0.317	500 nm
	0.296	0.369	5 µm
25 QW with bulk	0.211	0.258	500 nm
	0.369	0.473	5 µm
Wafer A	0.177	0.22	500 nm
	0.419	0.527	5 µm
Wafer B	0.237	0.292	500 nm
	0.431	0.531	5 µm

Table 3.4: AFM measurement of the surface roughness of MQW with digital alloys or bulk barriers, and wafers A and B. Arithmetic mean (R_a) and mean square deviation (R_q) results are given for two scan lengths

It is important to note that one single atom layer corresponds to 0.1 nm meaning that R_a is really close to this value and to the detection limit of the equipment. By comparing the surface roughness of the studied samples, no evident difference can be found since the results are really close to the noise measurement meaning the quality of the surface is good enough for the devices. Indeed, the very small variation are maybe only due to the measurement location where a small defect can appear. No improvement can be noticed for the digital alloy of the barrier compared to the bulk one with the AFM characterization.

We have described in this section the epitaxy of complicated structures of several hundreds of layers during 8h for the VCSEL and 17h for the EAM-VCSEL. To reach the expected characteristics, we measure the cell burst due to the temperature stabilisation. Then, despite a precise measurement with the OFM, we moved to a reflectivity measurement, during the growth of simple GaAs and AlAs layers, that we compared to a simulation curve to calibrate the require temperatures to achieve the expected growth

rates. We have grown 5 wafers, 3 EAM and 2 EAM-VCSEL, and measured their main characteristics as the QW PL and the FP resonance position.

3.3 FABRICATION PROCESS DEVELOPMENTS

The epitaxial growth of the five structures including EAM and EAM-VCSEL has been presented. In this section, the fabrication process will be described and more precisely two developments of technological bricks essential to make the realization of the double mesa structure easier. Indeed this device requires precise alignments conjointly, passivation on important relief of few micrometers and planarization for high speed injection.

As shown in Fig. 3.13, the fabrication of the EAM-VCSEL requires the development of the following technological bricks:

- *EAM and VCSEL passivation with dielectric.* This step is realized by lift-off to reduce the number of photolithography and dry etch steps and thus reduce the misalignment and overetch errors. Furhermore, for the passivation of both EAM and VCSEL sidewall, the photolithography is done on a relief of several micrometers with a high height/width aspect ratio which complicates the resist deposition and the lift-off itself. Moreover, as the SiO_x thickness used here is about several hundreds of nanometers to be used as hard mask, it is necessary to develop a reliable process which takes into account these constraints.
- *Top and middle metal contacts.* The required metal thickness (several hundreds of nanometers) is also important to ensure good electrical properties at high frequency (as described in Chapter 5) which also requires a thick resist for the lift-off. About the top contact, the difficulty, besides the thickness, resides in the depth of the opened hole in the BCB.
- *BCB planarization.* Even if the degree of planarization of the BCB is pretty good for small reliefs and spaced devices around 400-500 µm, it is still complicated to achieve a perfectly flat surface on a more dense device sample or with substantial reliefs and different heights. Then, BCB has to be etched to reach the top EAM surface without damaging it which requires a stop etch layer and a monitoring by an end-point detection system. The surface has also to be smooth enough to decrease the injection loss at high frequency while providing good metal adhesion for probing and bonding.

Based on these observations the dielectric lift-off on top of the mesa has been first developed and implemented as a self-aligned process for EAM fabrication. This innovative process (described in 3.4.2) combines, thanks to a double resist stack, the mesa etch, the sidewalls passivation and the metallization. Its feasability has been demonstrated for the fabrication of an air-post VCSEL device and oxide confined VCSELs.

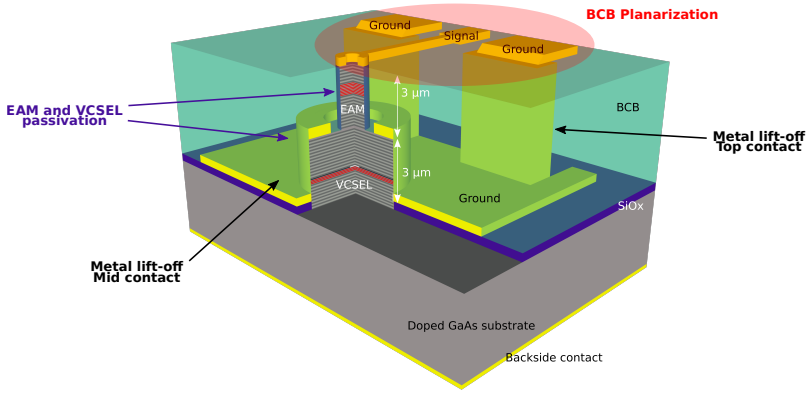

Figure 3.13: Global view of the EAM-VCSEL device. Technological difficulties are highlithed around the schematic.

These developments will be described in the next sections.
Finally, an innovative technique using a mechanical press under high pressure and temperature, by using nanoimprint tool, will be presented to make the BCB surface perfectly flat, indepently on the relief and pattern distribution. This planarization is followed by the etching down step for the electrical contact fabrication.
This planarization technique will be subject to a section in the next chapter focused on high-frequency devices.

3.4 SELF-ALIGNED PROCESS

3.4.1 *Challenge*

In the fabrication process of a standard passivated and metallized mesa with a top opened window, four lithography steps with precise mask alignments between them are required consisting of the following main stages:

- First, an annular top contact is defined by a metal lift-off
- Then, a first lithographic alignment is done to form an etching mask for the mesa definition [92];
- Next, surface passivation is realized on the whole wafer by a plasma-assisted dielectric deposition, followed by a new tight mask alignment [93] to define the transparent emission window. This window opening is done by etching the passivation layer with a chemical solution or by dry etch. Besides the risk of lateral misalignment, both selective etching methods can be problematic with a possible under-etch of the passivation layer with the chemical method, or damaging the top VCSEL

semiconductor layers because of the lack of selectivity for the dry etch [93] [94], resulting in deteriorated VCSEL performances;

- Finally, the last lithography step and alignment is realized for the lift-off of the metallic top contact-pad.

The development of a self-aligned process is of great interest as already demonstrated for the fabrication of high performance HBT transistors or ridge lasers [93] [95]. To that extent, Al-Omari [92] used a top metallic contact deposited over a photoresist layer as a hard mask to dry-etch the VCSEL mesa. Chua [96] developed a pseudo-planar approach by opening via holes down to the AlAs layer to carry out the lateral oxidation. This process has subsequently been improved by Strzelecka [97] to increase the device density. Recently, we have shown that air-post VCSELs could be created using an innovative self-aligned process, which combined several masking and lift-off steps defined by a single lithographic step [98].

This process flow, most suitable for 3D imaging and sensing applications, can also be easily implemented for the fabrication of other optoelectronic devices such as modulators, ridge waveguide lasers, detectors, solar cells or any process combining dry etch, passivation and metallization.

3.4.2 *Air post VCSEL and EAM fabrication*

As described above, the first development was to fix the issue of the lift-off on a surface vertical relief of several micrometers. The feasability demonstration of the process developed here has been done on air-post VCSEL (without lateral oxidation) and will be then very usefull for EAM devices fabrication.

The solution proposed here consists in drastically simplifying the above process flow by performing all of the steps by applying only one lithographic step instead of four, and thus without any required mask alignment. To do so, a suitable T-shaped double-layer photoresist is used for successively achieving the VCSEL mesas etching by Induced Coupled Plasma-Reactive Ion Etching (ICP-RIE), the sidewalls passivation with SiO_x layer by PECVD and emission window opening by a first lift-off, and finally, completing the process by the top metal contact lift-off. This innovative self-aligned process enables a very fast and straightforward process flow. In addition, the metal overlap on the top-mesa emitting window is easily controlled during the process. This sequence of processing steps is greatly facilitated by low-temperature plasma-assisted deposition of the passivating dielectric layer (SiO_x or Si_xN_y), since a lift-off technique can be used for releasing the emission opening window on top of the mesa.

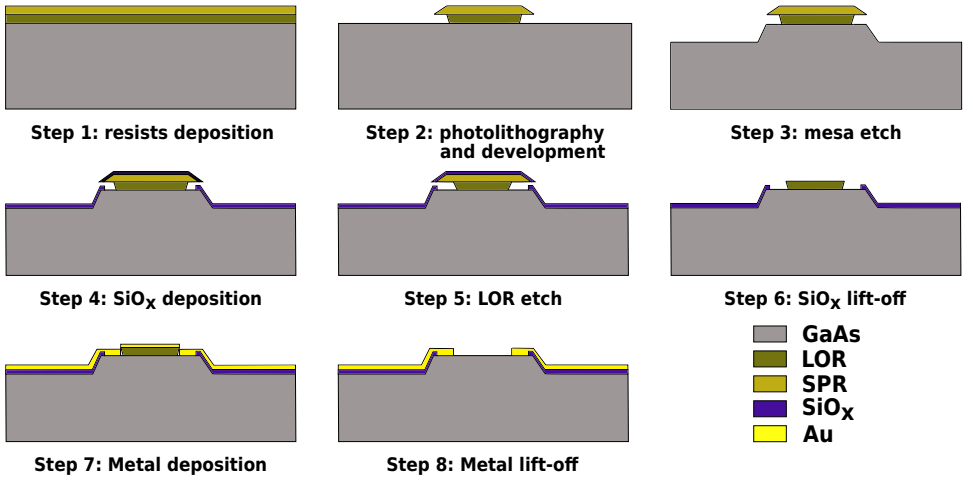

Figure 3.14: Schematic of the self-aligned process flow for EAM or VCSEL without lateral confinement

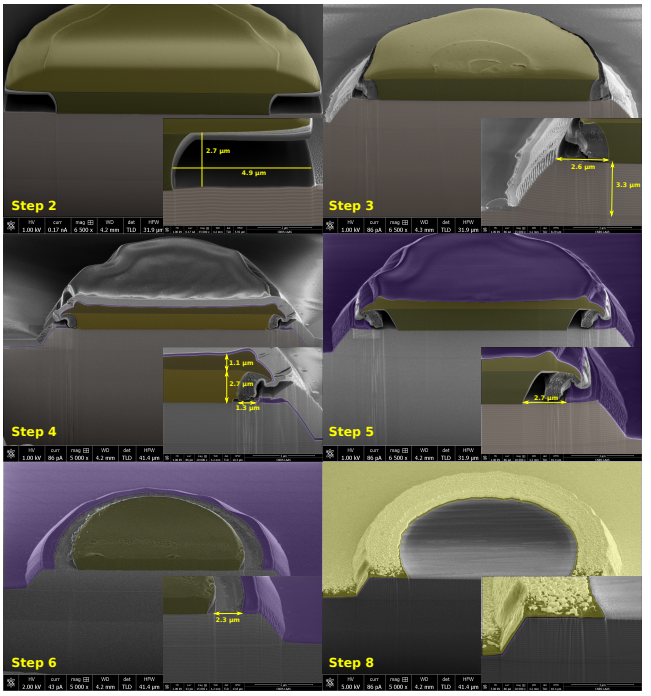

Figure 3.15: SEM pictures of a VCSEL at different stages of the self-aligned process flow

3.4.2.1 *Sample description*

The studied 980 nm VCSEL structure was grown by MBE with a Riber 412 reactor on a GaAs Si-doped substrate. It is composed of a 30.5 period $Al_{0.9}Ga_{0.1}As$/GaAs bottom N-doped Bragg reflector (DBR), a λ-thick active region consisting of 3 InGaAs/GaAs

quantum wells surrounded by $Al_{0.2}Ga_{0.8}As$ cladding layers, a 30 nm $Al_{0.98}Ga_{0.02}As$ layer located in the first top-DBR period which embeds the oxide confined aperture, a 19.5 periods P-doped DBR and a GaAs top heavily P-doped contact layer.

3.4.2.2 *Process description*

The process, described in Fig. 3.14 starts by spin-coating the LOR30B to a thickness of 2.7 µm, to enable the lift-off of sufficiently thick (typically more than 500 nm as described in Section 3.3) layers, and the SPR700 photoresist to a thickness of 2.3 µm to ensure GaAs etching step of 3 µm. After photolithography and development (step 2), suitable T-shaped disks are obtained as shown in Fig. 3.16. We get an undercut recess of 4.9 µm necessary for the future lift off. This undercut recess can be adjusted by varying the development time and by modifying the LOR soft bake temperature: etch rate is divided by a factor of 2 between 170°C and 200 °C. Our process drastically increases the undercut dimension with respect to [99] where maximum 1 µm wide undercut has been achieved due to limitation of the mechanical strength of the SPR and the strain induced by the dielectric layer. In the specific device described here the undercut length is not an essential parameter but if we want to considerably decrease the mesa diameter, the undercut has to be reduced, too. VCSEL airpost or modulator of 10 µm aperture can be easily fabricated using our method. If we want to decrease aperture diameter beyond 10 µm we have to decrease the undercut to 1 µm as well as to modify the dielectric deposition recipe to avoid any deposition on the SPR photoresist sidewalls that will prevent the lift-off. This procedure will not affect the metal deposition and its lift-off since it is only realized by the LOR resist.

Due to the over-development, mandatory to obtain the LOR under-etch, the SPR shows angled slope sidewalls, shape that will be transferred to the mesa sidewalls after dry etch. This mesa angled slope ensures conformal deposition of the passivation film and later on of the top-contact metal deposition. Dry etch by ICP-RIE of the mesas across the top DBR is performed under Cl_2-based chemistry and is controlled by an in-situ laser reflectometry monitoring system. As shown in Fig. 3.15 (step 3), an etch depth of 3.3 µm has been aimed in order to stop the etching within the intrinsic active region and so to confine the current in a smaller diameter cavity. During this step, the SPR topmost photoresist layer is also etched but with a rate about three times slower than the AlGaAs semiconductor. After the mesa etch, the remaining thickness of the SPR photoresist is 1.1 µm, which is sufficient to achieve the subsequent SiO_x passivation lift-off. Furthermore, this plasma etch also reduces the LOR undercut recess from 4.9 µm to 2.6 µm, a size which remains sufficient for the SiO_x lift-off. As depicted in Fig. 3.15, after step 4, a Pt thin layer is locally deposited with the FIB ionic column system (appearing in grey on top of the mesa); this metallic layer does not play any role in the VCSEL process, but

is used to increase the contrast of the SEM images and thus to measure more easily the SiO_x and SPR thicknesses. The maximum thickness of the SiOx that can be deposited is, strictly speaking, limited by the initial LOR resist thickness, but, in reality, the SPR could break-off under the accumulated strain of the thick SiO_x layer. For this reason, a post exposure bake (PEB) is applied to harden the photoresist layer, while the ICP-PECVD deposition has to be performed at a lower temperature than the PEB.
The 200 nm SiO_x passivation layer is deposited at 100°C under SiH_4 / N_2O gas flow at RF power of 150 W and at 5 mTorr pressure which leads to a 85 Å/min deposition rate. This layer presents a continuous conformal deposition on the VCSEL sidewalls. At this stage, the lateral spacing between the base of the LOR layer and the edge of the SiO_x layer is only 1.3 µm, which is not sufficiently large to proceed with the metal deposition and its lift-off. Therefore, the LOR resist layer is selectively further under-etched to increase the undercut recess to adjust the overlap between the metal contact and the GaAs surface to a width of 2.7 µm (step 5). Thanks to this lateral etching with this second development step, the final width of the contact annular ring can be tuned, and it will then control the electrical injection efficiency in the VCSEL structure. Also, it is important to note that this etch preserves the reverse inclined sidewalls of the LOR necessary for the next metal lift-off. Then, the SPR photoresist is selectively removed in acetone. As we can see from Fig. 3.15 (step 6) the semiconductor surface is revealed over a width of 2.3 µm between the edges of the LOR and the silicon dioxide layer that will set the contact pad width of the final VCSEL device. Metal contact, consisting of 50 nm Ti and 200 nm Au, is e-beam evaporated in an EVA600 chamber on the sample, after which the LOR is finally lifted-off in a DMSO chemical solution.

3.4.2.3 *Sample characterization*

In order to demonstrate the effectiveness of this self-aligned process requiring only one single lithography step, the VCSEL wafer was characterized in a Karl Suss PA200 probe station at room temperature under continuous wave electrical injection with a large area PIN-25DP Si photodiode. Typical light-current-voltage (LIV) characteristics are shown in Fig. 3.16. It is important to note here that these devices do not include oxide lateral confinement, and are only "air-post" confined by the mesa structure. The LIV curves show that the electrical injection is efficient in the VCSEL structure despite the high series resistance which is due to a low doping level in the N-DBR. The laser threshold around 20 mA (2 kA/cm^2) is consistent with the air-post configuration. The implementation of smaller oxide-aperture, compatible with this process will of course reduce the laser threshold to a few mA.

We can also notice that the VCSEL is not single mode due to the too large confinement inherent to airpost configuration.

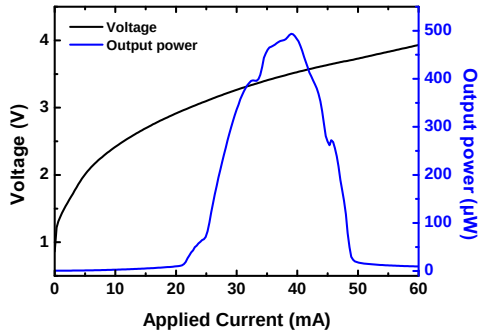

Figure 3.16: LIV characteristic of a VCSEL after the self-aligned process without oxide confinement

The feasability of this resist double stack as an efficient process has therefore been demonstrated for the sidewalls passivation and the metal lift-off of a structured device. This will be thus implemented in the global process flow.

3.4.3 *Additional step for VCSEL lateral oxidation*

To go further in the process described above for single mode operation VCSEL devices it is necessary to add an electrical and optical confinement. As seen in Introduction the lateral oxidation of a high aluminum content layer is more often used for VCSEL industrial manufacturing.

3.4.3.1 *Improvement interest*

We extend this work and propose a new process flow to fabricate, in a very simple and straightforward way, the widely-used oxide-confined VCSELs. The demonstrated process drastically simplifies the oxide-confined VCSEL fabrication as demonstrated previously on air post geometry by reducing the total number of lithographic alignment steps from four or more to only one alignment, with the additional advantage of relieving the required tolerances.

3.4.3.2 *Process description*

The fabrication process is schematically shown in Fig. 3.17. The first step is to etch four 3-µm-wide 37µm-diameter curved trenches of 26.5 µm length to open an access to the buried $Al_{0.98}Ga_{0.02}As$ layer, which, upon wet thermal oxidation, will lead to the definition of the lateral confinement aperture. To do so, a 2.3 µm-thick SPR700 photoresist mask is applied in a first photolithography step (a), followed by the inductively coupled plasma etching (ICP-RIE) with a Cl2/N2 gas mixture of the top DBR and active region (b). Then, a selective oxidation (c) of the $Al_{0.98}Ga_{0.02}As$ layer is realized in a dedicated

oven (AET Technologies) under $N_2/H_2/H_2O$ gas moisture at 410°C, reaching a 28-µm size of the oxidized region after 70 minutes. The resulting oxide aperture is observed by near-infrared microscopy and is shown in Fig. 3.18b. It exhibits an asymmetric shape of 4 µm by 7 µm, resulting from a non-uniformity of the etching step across the different trenches. After this first sequence, a double-layer stack of LOR 30B light-insensitive resist and SPR700 positive resist is spin-coated. Then, the only non-critical mask alignment of our method is performed on a MJB3 mask aligner (c). A circular mesa wider than the already etched patterns is then etched under the previous ICP-RIE conditions to obtain steeply inclined sidewalls, which ensure the continuity of the following passivating and metallic depositions. After etching, a 300 nm SiOx passivation layer is coated by Inductively-Coupled Plasma-Enhanced Deposition at 100°C (d). In order to promote the subsequent lift-off of the metal layer on top of the mesa, the LOR recess is slightly widened thanks to a short dip of 10 seconds in the resist developer that leads to a 2.5 µm recess. This recess can be proportionally extended with longer development time. Then, the SPR700 cap resist and the above-mentioned SiO_x layers are selectively lifted off in acetone. Afterwards, a 50 nm Ti/ 200 nm Au contact is deposited by e-beam evaporation above the remaining LOR layer (still with inverted edge profiles) and the unprotected GaAs surfaces (e). The LOR resist is finally removed in a dimethylsulfoxyde (DMSO) solution heated at 80°C, resulting in the final metal lift-off (f). Fig. 3.18a shows a scanning electron microscopy cross-section view of the final device. The contact pad width is currently 2.5 µm, which might be sufficient for low resistance access considering the high doping level of the GaAs cap layer. Thanks to this method oxide-confined VCSELs have been fabricated by combining the required lateral oxide confinement, mesa etch, sidewall passivation and top contact metallization steps using only two photolithography steps, and this without any critical alignment. Indeed, the mask alignment illustrated in the third scheme presented in Fig. 3.17 does not require an accurate lateral positioning, since the external lateral oxidation extent, of several tens of micrometres, enables to place the outer mesa edge anywhere on this oxide layer.

3.4.3.3 *Sample Characterization*

The fabricated oxide-confined VCSELs were electrically characterized, as previously described. Fig. 3.19 shows the Light-Current-Voltage characteristics of the VCSEL device illustrated in Fig. 3.18b. A threshold current of 3 mA is obtained and a maximum optical power at rollover is 1.6 mW. These performances are equivalent to the standardly processed oxide-aperture VCSELs. With this same vertical structure, laser performances are very similar whether a standard VCSEL process or our self-aligned process is applied.

The VCSEL devices were also optically characterized to extract the spectral properties of the output beam, in particular to check their modal content. An optical spectrum

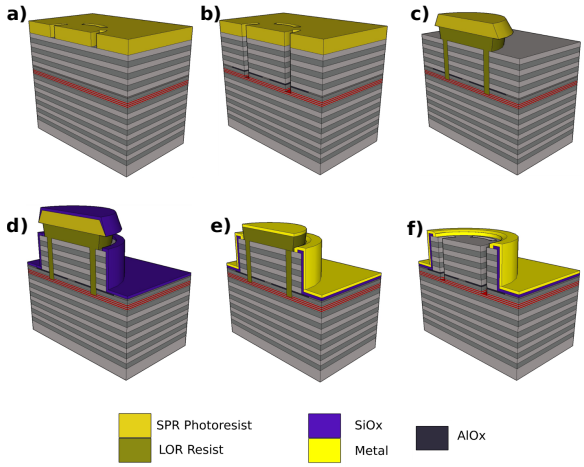

Figure 3.17: Process flow of the self-aligned VCSEL process including the following steps: via-trench etch (b), lateral selective oxidation (c), isolation mesa etch and SiOx passivation (d) and top-contact metallization(e).

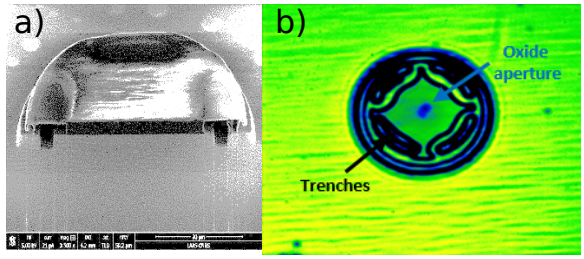

Figure 3.18: Self-aligned oxide-confined VCSEL at different processing stages a) Focus Ion Beam cross-view of the VCSEL after the SiOx passivation b) Top view of the final device with the oxide aperture visible.

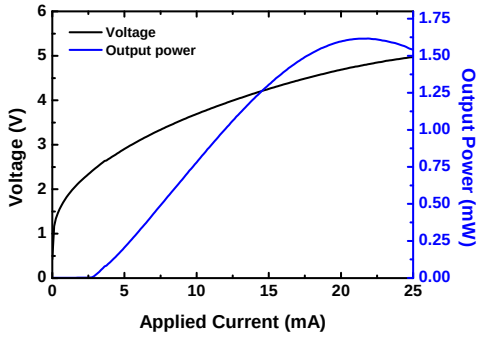

Figure 3.19: L-I-V curve of our self-aligned device.

analyzer was used (ANDO AQ-6315-A) with a wavelength resolution of 0.1 nm. The laser spontaneous emission was also imaged below the laser threshold which enables to confirm the previously-measured (see Fig. 3.18b) oxide aperture size and shape.

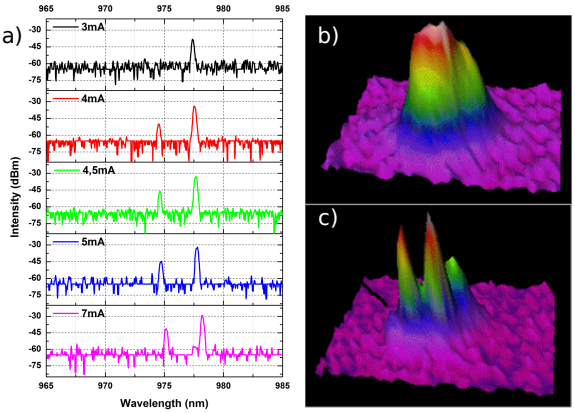

Figure 3.20: a) spectral characteristics of the fabricated VCSEL for various injection currents (3, 4, 4.5, 5 and 7mA). On the right, modes images b) at 3 mA (nearly single mode) with an OD1 filter (transmission=10%) and c) above the threshold at 7 mA (multi mode) with an OD3 filter (transmission=0.1%).

In Figure 3.20, the spectrum of the output signal of the same VCSEL is presented at different levels of injection current. The laser appears to be quasi single-mode only just above threshold, since a second lateral mode appears at 4 mA. The non single mode operation is due to the potato shape of the oxide aperture which can be avoid with a better etching process. This second mode is certainly due to the largely asymmetric oxide shape mentioned above. As it can be seen on the modes images the second mode appears along the long axis of the oxide aperture. The mode profile image above threshold (Fig. 3.20c), taken with a pump current of 7 mA with an OD3 attenuation filter, has actually an absolute amplitude enhanced by a factor 100 compared to the one taken under 3 mA (Fig. 3.20b). Therefore, this multimode behaviour is not an inherent property of the auto-aligned process, but originates from a slightly-not-uniform etch of the oxidation access trenches which, in turn, has led to an asymmetric oxidation from the four etched trenches.

This process has been done on a very standard and basic vertical VCSEL structure. In particular, the electrical and the optical characteristics of this epitaxial VCSEL structure have not been optimized. Improvements of the electrical and optical performances can be demonstrated with more elaborated vertical VCSEL structures, by using for example multiple oxide layers and optimized doping profiles in the top mirror to improve current injection and optical lateral confinement.

In conclusion, an innovative technological process to fabricate oxide-confined VCSELs, based on carefully sequenced set of self-aligned technological steps including a mesa etching, a surface passivation, and a top annular contact metallization has been demonstrated. This process flow has been applied to oxide-confined VCSELs which are very largely deployed in many different applications. This self-aligned process presents a

much easier fabrication flow, and hence largely simplifies the device manufacturing, without any penalty on the final performances of the laser. Finally, this self-aligned process can also be adapted to other optoelectronic components as modulators, detectors, or solar cells, to mention a few.

3.5 STATIC CHARACTERIZATION

3.5.1 *Electro-Absorption static behavior*

The objectives of this section are to verify the EAM optical design while validating the self-aligned process described in the previous section. To do so it is necessary to evaluate the electro-optical properties of the modulator as the reflectivity modification with the temperature, in accordance with the operating conditions, under different voltage bias. Furthermore, these measurements will give a feedback on the optical model and so will enable prediction of the performance when the EAM is integrated onto a VCSEL.

We describe first the optical bench used for this characterization, then we measure the effects of the voltage and temperature on the reflectivity spectrum. Later, we provide a comparison between these measurements on samples A (non-doped DBR) and B (doped DBR) with the absorption model combined with the Transfer matrix Method as decribed in the previous chapter. Finally, the photocurrent measurement of the device give us more precise information on the excitonic position and so improve the model to have a better feedback and prediction of the EAM properties once integrated onto the VCSEL.

3.5.1.1 *Optical bench characterization*

An electro-optical setup was built in order to measure the reflectivity modulation properties at adjustable wavelengths around Fabry-Perot resonance. This reflective configuration for measuring modulation static performance is mandatory since the strong absorption of the GaAs substrate in the 880 nm range does not allow to do transmission characterizations.

The measurement setup is schematized in Fig. 3.21. Our sample is positionned horizontally on a temperature controlled Peltier module driven by a Keithley 2510-AT TEC SourceMeter between room temperature (RT) and RT + 60°C. The backside contact is directly taken on this Peltier module, with thermally and electrically conductive glue, and top electrode is contacted with a manual probe manipulator. A Keithley 2601 SourceMeter is used to both apply voltage and measure the photocurrent. We inject white light (WL) through a lens system (in red in Fig. 3.21) to be vertically incident on the top of the modulator. The back reflected signal is deflected by a beam splitter (BS) towards a spectrometer (SR500I Andor) with a Newton CCD camera. With the horizontal movement

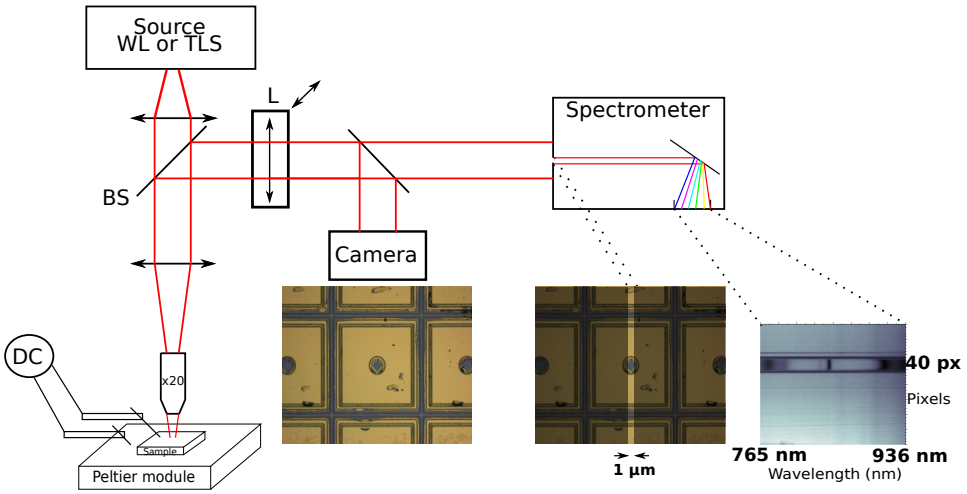

Figure 3.21: Schematic of the optical setup

of the lens (L) in front of the 1200 grooves/nm grating we are able to acquire a hyperspectral image of the surface device as described in [100]. Indeed, the spectrometer slot filters a thin area (around 1 µm) of the modulator as shown in Fig.3.21 and this image associated with the lens movement gives the bottom right hyperspectral image with the signal amplitude plotted as a function of the wavelength in X axis and the position of the slot in the Y axis in pixel.

It is necessary in this configuration to measure both the reflectivity of a gold wafer with and without light for dark measurement and then provide a normalization.

With this setup configuration we have a measurement comprising:

- Spectral range, determined by the spectrometer grating, of 171 nm centered at 850 nm
- good signal over noise ratio (dark level of 600 shots / maximum amplitude of 60 000 shots on each pixel)
- 40 pixels covering the modulator area, around 1 pixel for 1 µm

We thus do an average on the 40 pixels corresponding to the EAM opened window (Fig. 3.21 bottom right) to have the reflectivity of the modulator as a function of the applied voltage for different temperatures.

It addition to this measurement, it is also possible to use a tunable laser source (TLS) instead of the white light to measure the electrical and optical response of the modulator between 820 nm and 870 nm and thus plot the photocurrent (which is related to the absorption) of our device at different temperatures. Indeed, the photons with the energy which corresponds to λ_{laser} will be recombined in the active region and thus a charge will move from the valence to the conduction band leading to a current. This current measurement is useful to know the absorption value at the precise wavelength of the TLS.

In this last configuration it is also possible to add a photodiode before the spectrometer used for reflectivity and so to measure the voltage response to obtain an alternative reflectivity measurement without using a spectrometer.

3.5.1.2 *Impact of the voltage bias and temperature on the reflectivity spectrum*

We present in Fig. 3.22 the reflectivity spectrum of the sample A taken at room temperature without electric field. The position of the excitonic peak and the FP resonance are shown respectively with red and green squares. The impact of the electric field and the temperature on this spectrum are shown on right and left and the new reflectivity spectra is plotted in dashed black line.
To understand properly the effect of both voltage and temperature it is necessary to recall the formulas of the absorption model of eq. 2.6, eq. 2.7 and eq. 2.8 described in detail in Chapter 2:

$$\alpha(\epsilon, h\nu, l_z) = \alpha_{hh} \cdot \left(1 + \left[\frac{(E_0 - h\nu)}{\Gamma_{hh}}\right]^2\right)^{-1} \tag{3.3}$$

$$\alpha_{hh} = \frac{C}{l_z} \cdot \left|\int_{-\infty}^{+\infty} \Psi_e \cdot \Psi_h^* \cdot dz\right|^2 + \alpha_{bulk}. \tag{3.4}$$

$$\Gamma_{hh}(l_z, \epsilon) = 7.374 - 0.511 \cdot l_z + 0.0182 \cdot l_z^2 - 0.054 \cdot F + 0.0161 \cdot F^2 \tag{3.5}$$

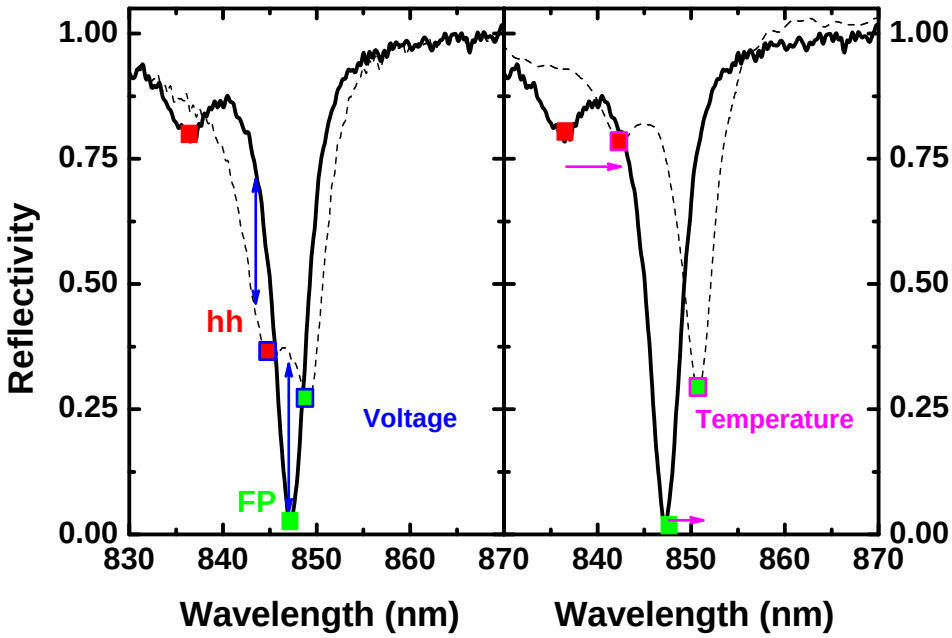

Figure 3.22: Impact of the voltage (left) and temperature (right) on the reflectivity spectrum of sample A. Solid and dashed line curves correspond to U = 0 V and U = 50 V in the left figure and T = 23°C T = 43°C in the right figure.

Electric field

As noticed in Fig. 3.22 a) when an electric field is applied to the EAM structure the reflectivity spectrum is modified by a:

- Red shift of the FP resonance (highlighted in green) due to the modification of the refractive index via Kramers-Krönig as described in Section 2.1.3.
- Red shift of the excitonic position (highlighted in red)
- Broadening of the reflectivity linked to absorption tail with the Γ_{hh} parameter
- Decrease of the absorption (α_{hh}) due to a lower overlap between electrons and holes envelop functions.

The two last modifications lead to an increase of the reflectivity and thus to a modulation phenomenon, highlighted with blue arrows in Fig. 3.22.

Temperature

The temperature plays also an important role in the reflectivity spectrum. Indeed it is modified by a:

- Red shift of the FP resonance due to the modification of the **refractive index**:

$$n = 3.255 + A \cdot 10^{-4}\ T \quad \text{with T in K} \tag{3.6}$$

  where the thermooptic coefficient A is measured at 850 nm as 3.23 by Kisting et al. [101] and at 1.5 µm as 2.34 by Skauli et al. [102].

- Increase of the minimum of the FP resonance due to the modification of the absorption value with **C and** Γ_{hh}
  The variation of the $\boldsymbol{\Gamma_{hh}}$ **parameter** (Eq. 3.5) that corresponds to the broadening of the heavy hole peak has already been reported and different values were obtained for GaAs QWs. 1.7 ($\pm$ 0.5) µeV/K for a 15-nm thick QW [103] up to 10 µeV/K [104] in the case of coupled quantum wells with 9.5-nm thick QW and 2.9-nm thick barrier.

- Red shift of the excitonic peak position due to the **variation of the energy band gap** (note that E_g (in eV)= hc/λ_g (in µm)) of the GaAs as a function of the temperature with the following Varshni law [55]:

$$E_g(T) = E_0 - \frac{\alpha \cdot T^2}{T + \beta} \quad \text{with} \quad \begin{cases} E_0 = 1.5216\ eV, \\ \alpha = 8.871 \cdot 10^{-4}, \\ \beta = 572. \end{cases} \tag{3.7}$$

The parameters given in Eq. 3.7 give a $\Delta\lambda_{exc}$ of 19.7 nm for a $\Delta T = 60°C$.

The quantitative comparison analysis of these variations will be done in the next subsection. Indeed, we measured reflectivity and photocurrent of samples A and B under several electric field and with different temperatures to extract the impact of each parameter on the reflectivity spectrum.

3.5.1.3 *Comparison between reflectivity measurement and model calculations*

The model presented previously was only valid at room temperature but once integrated onto the VCSEL, the EAM device will be subject to a temperature rise of about 50-60 °C. It is thus absolutely necessary to complete the model to understand the variation of each parameter with the temperature and the voltage and be able to predict the modulation behavior before its integration.

To this aim, the reflectivity and the photocurrent of the EAM structure under electric field at different temperatures have been studied and results are described in this section.

For both samples, mesa diameters about 35 µm are measured. For the sample A (non doped DBR) voltage from 0 V to 50 V, corresponding to 185 kV / cm for the undoped 2.7 µm thickness is applied whereas for the sample B (doped DBR) voltage from 0 V to 6 V, corresponding to 104 kV / cm for the active region of 485 nm thickness, is enough to ensure a very good modulation behavior. The electric field considered here corresponds to the voltage applied divided by the undoped thickness region of the device and is found to be in a very good agreement with our first simulations of a single QW (Fig. 2.6 c).

Sample A - Reflectivity

Fig. 3.23 shows the reflectivity spectrum measured with the setup previously described for sample A. Results of measurements (on top) and of corresponding simulations (below), obtained with the Transfer Matrix Method combined with our model, are presented for four temperatures, from room temperature (RT) to RT + 60°C. This last temperature corresponds to 85°C which is a standard value for electronic devices in operation.

We can see that when we apply an electrical field the excitonic peak is red shifted by several nanometers. At room temperature λ_{hh} red-shifts from 836 nm to 844 nm (so 0.04 nm / (kV/cm)) and the reflectivity of the global structure, which is here a convolution between the Fabry-Pérot resonance and the absorption in the MQWs, decreases. So we have, at 847 nm a modification of the FP resonance amplitude by the excitonic absorption, which is exactly the electro-absorption phenomenon we are interested in [63] [76].

Between room temperature and RT + 60°C the excitonic peak shifts from 836 nm to 857 nm (21 nm) which is in very good agreement with the Varshni law (Eq. 3.7).

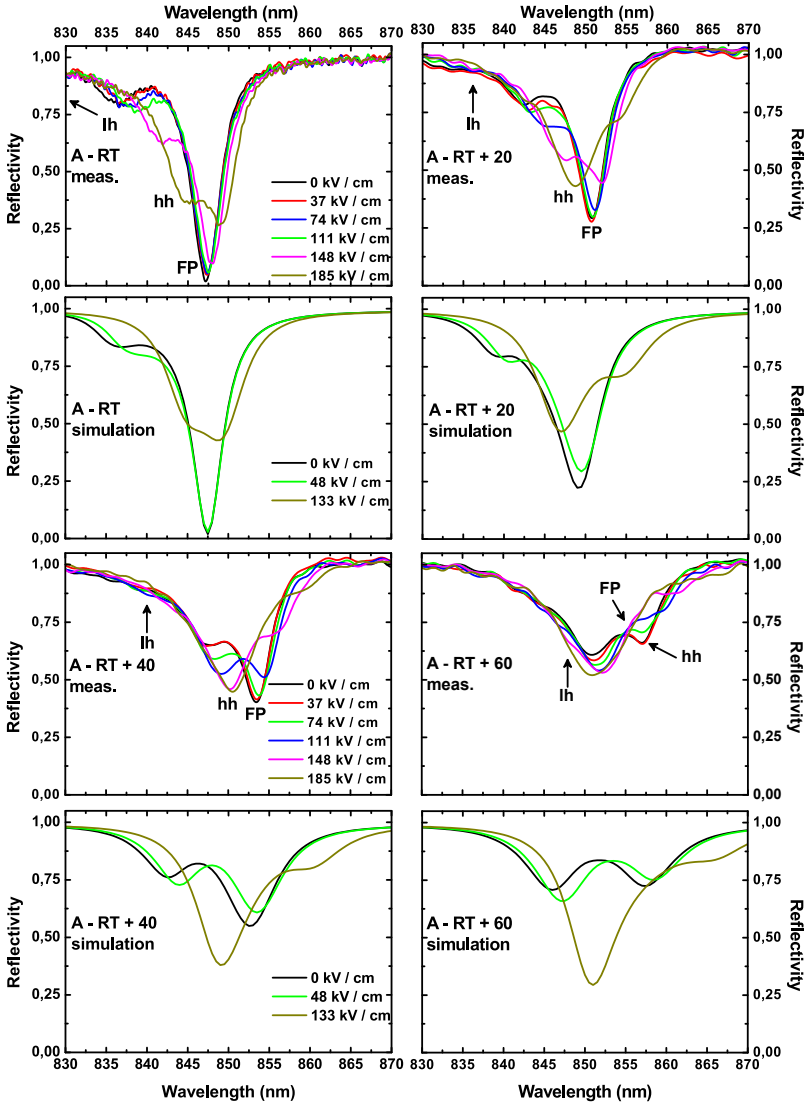

Figure 3.23: Reflectivity measurements of sample A (non doped DBR) as a function of the wavelength at different applied voltages of 0, 10, 20, 30, 40 and 50 V, and at different temperatures from room temperature to RT + 60°C. On rows 1 and 3 are plotted the experimental results and on rows 2 and 4 the corresponding simulations according to our model.

We modified our model, in addition of this band gap variation, by introducing the three parameters described previously in order to implement the effect of the temperature. We found that:

1. the **refractive indices** of all the layers varies with the following relation:

$$n = 3.255 + 3.1 \cdot 10^{-4}\ T \quad \text{with T in K} \tag{3.8}$$

which is in a very good agreement with the literature.

2. the **C coefficient** in Eq. 2.7 which is an experimental parameter is set to be linearly dependent on the temperature with a factor of 16000 cm^{-1}/K. An increase of the C value moves away the heavy hole transition from the FP resonance and increases its FWHM.
3. the Γ_{hh} **parameter** (Eq. 3.5) varies with $d\Gamma_{hh}/dT$ taken as 1 $\mu eV/K$ for the 8.5-nm thick QW in our superlattice which is also in good agreement with previous works.

Keeping these three parameters fixed we obtain a very good agreement between our simulations and the experimental results for different applied voltages and the four studied temperatures, see Fig. 3.23. The small residual differences between the calculated and measured reflectivity curves can be explained by the fact that we consider only one QW transition level and that the refractive index is supposed to be insensitive within the applied field F range around room temperature. The slightly higher mismatch at the more elevated temperature would rather indicate a non-linear evolution of the parameter C with temperature what could be more carefully defined by studying MQWs without any DBRs.

The variation of the refractive index with the electric field can also be seen here as the red shift of the λ_{FP}, going from 847.22 nm to 848.71 nm (8.10^{-3} nm / (kV/cm)) but this value, linked with the absorption tail in that case, is very dependent on the temperature. The variation of the refractive index is actually linked to the electric field with the relation: $\Delta n = -(1/2)n^3 s E^2$ with $(-1/2)n^3 s = 10^{-13}$ cm^2/V^2 [61]. This variation of the refractive index in our structure would result in much smaller change of the absorption compared to the electro-absorption change itself.

Sample A - Contrast Ratio

The measured contrast ratios (CR) and the reflectivity change (ΔR) between zero-bias and a given field of 133 kV/cm are presented in Fig. 3.24 for the different temperatures.

At room temperature a contrast ratio of 19 is measured at 847 nm with a FWHM value of 0.5 nm. The reflectivity change is 34%. Such a contrast ratio can only be obtained at a very low reflectivity R_{off} when the MQWs are not subject to high electric field, otherwise, as it is the case for high temperature, CR decreases very quickly even if ΔR remains susbtantially large. Indeed, CR can also be written as $\Delta R/R_{off} + 1$ and so it decreases very fast when temperature is increased since R_{off} dramatically increases.

The same measurement was done on the third EAM structure where DBR are doped but not the substrate. This sample was processed like the double mesa structure since not backside contact is possible. Fig. 3.25 presents the reflectivity spectrum as a function

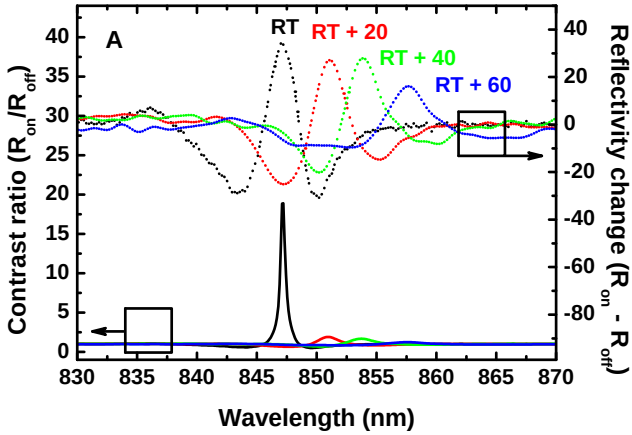

Figure 3.24: Contrast ratio corresponding to high electrical field (133 kV/cm) reflectivity divided by the reflectivity without field (solid lines) and change of reflectivity (dashed lines) plotted for room temperature (black), Rt + 20°C (red), RT + 40°C (green) and RT + 60°C (blue)

of the applied voltage at room temperature. The reflectivity normalization, even with the gold wafer and the substraction of the dark level of the camera, is not perfect and is thus taken at the reflectivity amplitude at the excitonic peak position and the FP position. The fact that the reflectivity at higher wavelengths is higher than 1 is only an artefact of the measurement and its normalization but does not affect the reflectivity value between 830 nm and 840 nm.

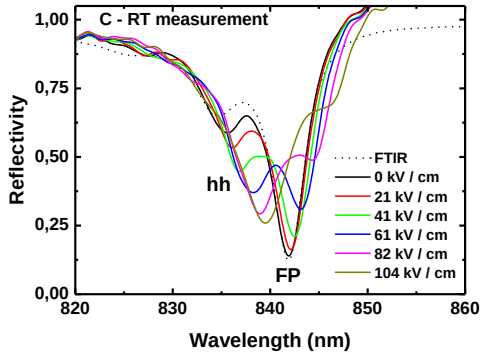

Figure 3.25: Reflectivity measurements of sample C function of the wavelength at different applied voltage corresponding to 0, 1, 2, 3, 4 and 5 V at room temperature. Dashed line corresponds to the FTIR measurement.

The configuration of this sample (excitonic peak position to FP resonance) is the same as sample A. The excitonic peak position shifts from 836 nm at 0 kV/cm to 840 nm under 5 V (104 kV/cm) which corresponds to a variation of 0.038 nm / (kV/cm) in excellent agreement with the value obtained for sample A. The variation of the Contrast Ratio and Reflectivity change as a function of the applied voltage has also been studied and

we found at 842 nm a modulation depth of 37 % with a CR of only 3.5 due to the high reflectivity (14 %) without bias.

This last sample is obviously a good configuration in terms of FP position compared to the absorption position and presents a low drive voltage to reach almost 40 % of modulation depth. However the achieved result was obtained at room temperature and we clearly see that if the temperature increases the performances will be deteriorated. The excitonic peak position has to be more blue shifted.

Sample B - Reflectivity

Fig. 3.26 presents reflectivity measurements for sample B for a reverse voltage ranging from 0 V to 5 V. The λ_{hh} is red-shifted compared to the λ_{FP} at RT and zero-bias, which means that the reflectivity at the FP cavity resonance is in fact a convolution between the curves of lh and hh absorption and the resonance response of the FP structure. This explains the high level of reflectivity (more than 25%). This convolution makes difficult the precise extraction of the variation of $\lambda_{FP}(T, V)$. Indeed, based on our calculation fitting closely the experimental curves, we can deduce that when the FP is between the lh and hh positions at RT, $\Delta\lambda_{FP}(F)$ = 0.3 nm / V (14.10^{-3} nm / (kV/cm)) whereas when it is blue shifted to the lh position at RT + 40°C, $\Delta\lambda_{FP}(F)$ = 0.2 nm / V (9.10^{-3} nm / (kV/cm)).

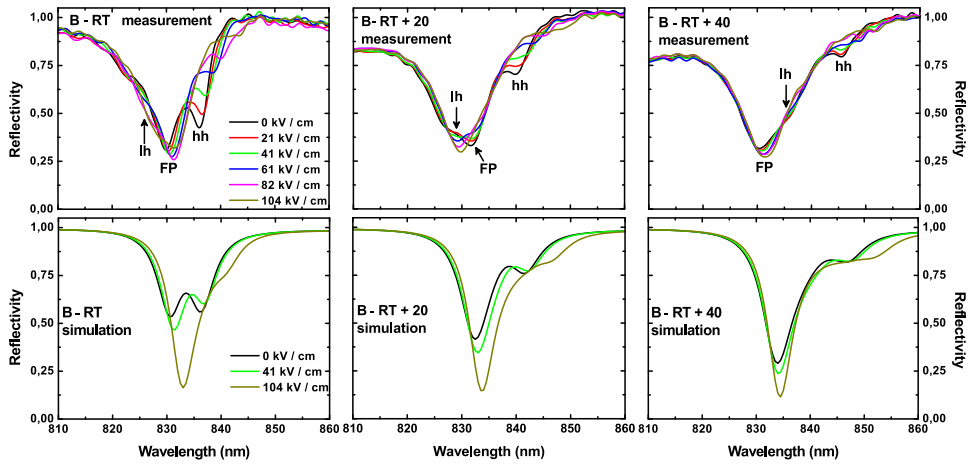

Figure 3.26: Reflectivity measurements of sample B as a function of the wavelength at different applied voltages of 0, 1, 2, 3, 4 and 5 V, and at different temperatures from room temperature to RT + 40°C. On top, measurements are plotted and below the simulations according to our model

The modulation in this sample is obtained at higher wavelength than λ_{FP} and a ΔR of 30% can be achieved at 836.1 nm but the CR is only of 1.7 limited by the very high R_{off}. As for the sample A, the modulation depth decreases as the temperature increases. It is

obvious that this configuration is not appropriate for our application but, as shown by our calculation, could be more efficient if the device would be cooled down to -15°C to achieve a perfect match of λ_{FP} and λ_{hh} and so a very high CR. As we can see from both Fig. 3.23 and Fig. 3.26, the temperature degrades the optical properties of the modulator if a proper detuning is not considered.

We summarize all the results in Table 3.5 and conclude this work by the following variations:

Wavelength \ Sample	A	B	C
λ_{exc} (nm)	836	836	835.6
λ_{FP} (nm)	847	831	842
$\Delta\,\lambda_{exc}$ (F) (nm / (kV/cm))	0.034	0.033	0.0375
$\Delta\,\lambda_{FP}$ (F) (nm / (kV/cm))	8.10^{-3}	14 and 9.10^{-3}	20.10^{-3}
$\Delta\,\lambda_{exc}$ (T) (nm / °C)	0.35	0.25 (hh) and 0.3 (lh)	-
$\Delta\,\lambda_{FP}$ (T) (nm / °C)	0.155	0.15 (hh) and 0.125 (lh)	-

Table 3.5: Excitonic peak and FP resonance wavelengthes shifts for samples A, B and C with the applied voltage and with temperature

- **Excitonic peak shifts about 0.035 nm / (kV/cm) and 0.3 nm / °C**
- **FP resonance shifts about 0.010 - 0.020 nm / (kV/cm) and 0.15 nm / °C**

Sample E - Reflectivity

To conclude these reflectivity measurements we also measured the reflectivity of the modulator from sample E (EAM-VCSEL with the good cavity detuning). This measurement gives an additional information about the optimum detuning of the absorber position to the EAM and VCSEL resonances.

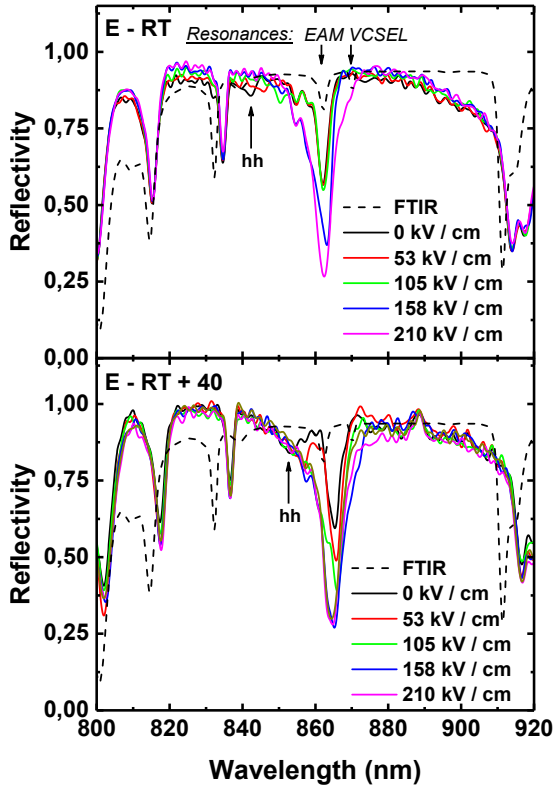

Figure 3.27: Reflectivity measurement of the modulateur on top of the VCSEL on sample E at RT (top) and RT + 40 °C (bottom)

Measurements were done at RT up to RT + 40 °C. We can see in Fig. 3.27 the shift of the excitonic peak position with the temperature and the voltage. Here, we applied up to 10 V (210 kV/cm) on the EAM section.

Thanks to the substantial detuning at RT the exciton peak is still well placed at high temperature and modifies the reflectivity of the EAM resonance and also of the VCSEL resonance under an electric field as expected.

3.5.1.4 *Photocurrent with temperature and voltage*

In addition of reflectivity measurements, we measured the photocurrent of our two structures at different temperatures and under applied electric field. Room temperature results of sample B are shown in Fig. 3.28 (a) for 0 to 6 V applied reverse bias. We can see the FP resonance at 829 nm and, red shifted, the excitonic peak. Black and red curves, for 0 and 1 V respectively, are lower than the rest of the curves in Fig. 3.28a because the absorption is weaker. When the voltage increases the electro-absorption, thanks to the Fabry-Perot cavity, the overall absorption is enhanced. The QCSE is clearly identifiable here with the red shift of the right side peak and the decrease of its amplitude.

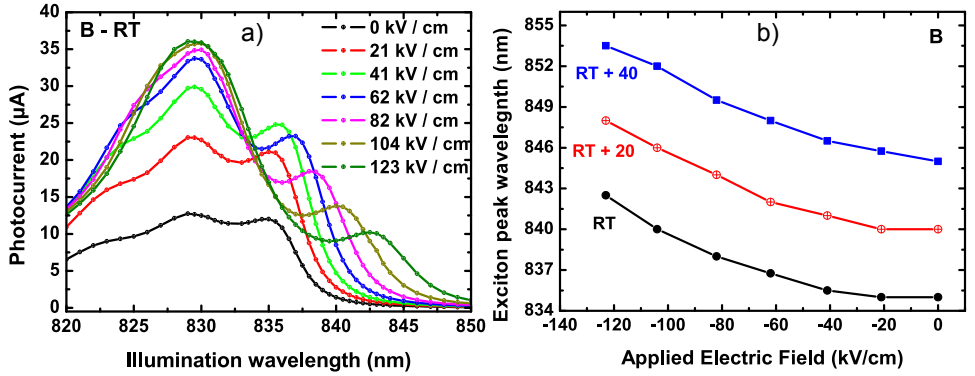

Figure 3.28: (a) Photocurrent of sample B as a function of the TLS illumination wavelength with an applied voltage from 0 V to 6 V (123 kV / cm) at RT. (b) Excitonic peak position function of the applied voltage at RT, RT + 20°C and RT + 40°C

In Fig.3.28 (b), the evolution of the excitonic peak is plotted as a function of the applied voltage at room temperature (black), RT + 20°C (red) and RT + 40°C (blue). The $\Delta\lambda_{exc}$ variation as a function of the temperature is nearly linear with a slope of 0.28 nm/°C in average over all temperatures and voltages, in perfect agreement with our previous measurement, and still in good agreement with the litterature [63] and with our estimation from Eq. 3.7.

We fitted the electrical dependence of λ_{hh}, whatever the temperature, with the following expression:

$$\lambda_{hh}(V) = \lambda_{hh_0} - 9.23 \cdot 10^{-3} \cdot F + 4.04 \cdot 10^{-4} \cdot F^2 \tag{3.9}$$

with λ_{hh_0} the excitonic peak position without electric field, and F the applied electric field (in kV/cm). Up to 60 kV/cm (3 V here) this relation is in good agreement with Zouganeli et al. [83] but above this value, the thickness of the QW barriers begins to play an important role in the carrier escape from the QWs and, since these authors worked with thinner barriers of 6 nm instead of 10 nm, the coefficient in the square term in their case is higher.

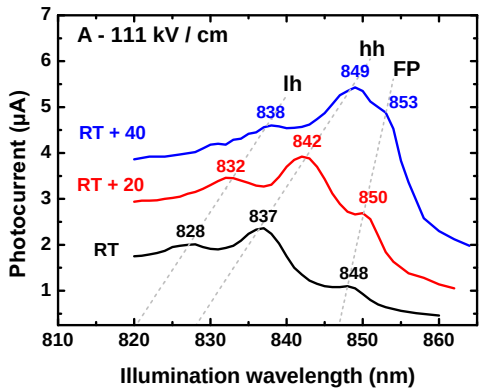

Figure 3.29: Photocurrent of sample A as a function of the TLS illumination wavelength with an applied voltage of 30 V (111 kV / cm) at RT, RT + 20°C and RT + 40°C. Light hole, heavy hole and Fabry Perot position are denoted on top.

The same measurement has been done for sample A, the results are shown in Fig. 3.29 where the photocurrent is plotted for three temperatures under 30 V (111 kV / cm). For readability, light hole, heavy hole and Fabry-Pérot positions are denoted with dashed lines with the corresponding transitions on top of them. These measurements clearly show that the λ_{hh} get closer to λ_{FP} when the temperature increases. As demonstrated for sample B, the excitonic peak shifts by 0.25 nm / °C for the lh and by 0.3 nm / °C for the hh. The small difference between lh and hh comes from the measurement accuracy. The λ_{FP} shifts by 0.15 nm / °C and 0.125 nm / °C respectively under 0 and 30 V. This shift has also been seen in Fig. 3.23.

Thanks to our simulation model and the good agreement with our experimental results we are able to predict the transmission value of the design without substrate (as in a EAM-VCSEL structure described in Section 2.6). In the case of the sample A, a transmission change of more than 40 % is calculated.

3.5.2 *VCSEL static modulation*

We have seen in the previous section the characterization of the stand-alone EAM, first in static with reflectivity and photocurrent measurements as a function of the applied voltage and of the temperature. We will now discuss the static characterization of the EAM-VCSEL device.

Fig. 3.30 presents our results of the VCSEL output power at room temperature for different applied voltages on the EAM cavity. The VCSEL voltage is relatively high and output power pretty low compared to standard VCSEL due to unexpected very small ($< 1\mu m$) oxide aperture leading to a high resistance and so to high internal temperature of the device.

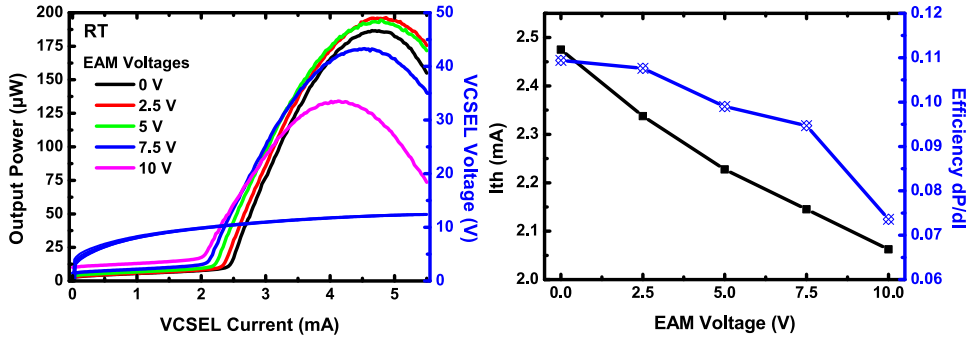

Figure 3.30: (a) L-I-V curve of the EAM-VCSEL structure. The output power is plotted for different EAM voltages. (b) Evolution of the VCSEL threshold and efficiency.

At 5.5 mA and for 5 V, the output power is 172 µW and decreases to 73.5 µW for 10 V, leading to a modulation of 57% (11.4 %/V). If we just compare the maximum output power, whatever the VCSEL current, the total modulation is about 31%. This value is in good agreement with the transmission change simulation that we have done for the EAM sample A, for which one the configuration was the same (exciton blue shifted to the resonance). Through the shift of the top structure reflectivity that modifies the behavior of the device even at the threshold, a change of the output power also occurs at the threshold current of 2.5 mA. Without voltage bias, the output power is 17.2 µW and increases to 54.5 µW for 7.5 V. Modulation depth of 68 % corresdonding to 9 %/V is achieved.

Above 2.5 V, as in can be seen in Fig. 3.30 (b), the output power, the VCSEL threshold and the slope efficiency decrease because when the EAM voltage increases the top DBR reflectivity (seen by the VCSEL) also increases and so less photons are generated and escaped.

Figure 3.31 presents the LIV characteristic of an other EAM-VCSEL device.

On top of this Figure we present the LIV curve showing here again a modulation of more than 70 % at threeshold and around 40 % just before the thermal roll-over.

With an Optical Spectrum Analyzer (OSA) we measured the emission wavelength of the device as a function of the VCSEL drive current and the EAM bias voltage. Results are shown in (b) and the extraction of the wavelength shift in (c). As we can see, the device exhibits a wavelength shift of 0.08 nm even for the modulation depth of 70 %. This parameter is crucial for optical communications and demonstrate once again the efficiency of our device.

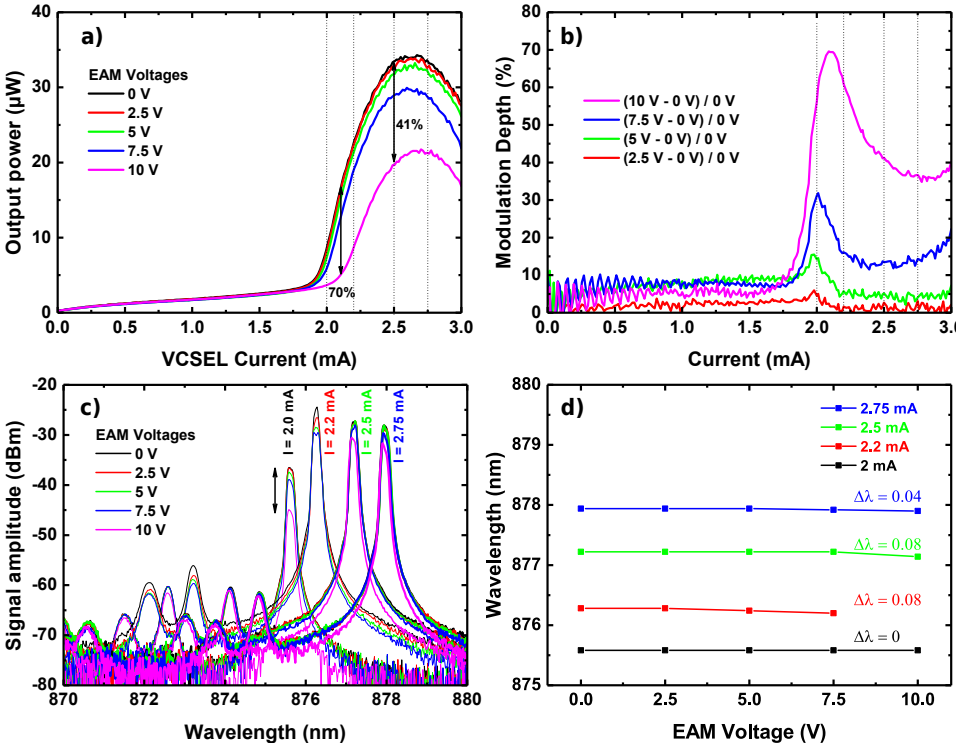

Figure 3.31: (a) L-I-V curve of the EAM-VCSEL structure. The output power is plotted for different EAM voltages. (b) Spectrum measurement of the device under different EAM bias voltages. (c) Extraction of the wavelength shift when the VCSEL is modulated

3.6 CONCLUSION

In this chapter the fabrication of EAM and EAM-VCSEL devices has been described from the MBE growth to the whole fabrication process based on technological locks. Five different structures including stand-alone EAM and EAM-VCSEL devices have been grown considering the constraints of the molecular beam epitaxy of such a complexe stack including the tigth control of numerous parameters such as the temperature growth, the cells flow and their calibration, the V/III ratio, the inherent difficulties for VCSEL growth as DBR gradings, and then the digital alloy composition for the barriers. We improved the calibration and monitoring methodology to increase the chance of success. Then, the samples reflectivity has been characterized with FTIR reflectivity mappings to verify the optical properties and successive etchings, and photoluminescence were used to clearly identify the exciton peak wavelength and the Fabry-Perot resonance for each device. Later, the development of a first self-aligned process useful for the efficient and fast fabrication of a single mesa with etching, sidewalls passivation and metallization was presented. The feasability of this process was demonstrated on a air-post VCSEL

and then implemented for oxide confined VCSEL. This process has been used for EAM fabrication and the acquired know-how useful for the global process.

We then measured the static behavior of samples A, B and C (respectively undoped and doped DBR and undoped substrate). We achieved modulation depths of 40 % for less than 5 volts. We studied the influence of the temperature and the voltage on the exciton peak and the Fabry-Perot resonance positions. Thanks to these measurements we improved the electro-absorption model and are now able to optimize the design of the modulator. After integration onto the VCSEL, the EAM exibited once again more than 70 % of modulation just above lasing threshold and 40 % along the LIV curve.

However, it is still possible to increase furthermore the performances of our device.
First, about the design itself. We have seen that, even if the non-doped DBR could lead to high-frequency operation, the required voltage is too high to be integrated with electronics. To decrease the VCSEL DBR resistance we have to over-dope the P gradings layers and maybe use only 3 or 4 steps instead of 10. We can also work with a P-N-P device (instead of N-P-N here) and thus have only 6 P-doped DBR periods on top of the emitting region. It will decrease the optical absorption of the emitting light.
Another improvement to decrease the required voltage is to use the Coupled Quantum Wells instead of the classical rectangular QW. Indeed, the insertion of a very thin barrier in the QW allows a faster modification of the carrier envelop function on each side of the QW and thus a fast modification of the absorption.
About the epitaxy, we recommend to use for the next runs, the superlattice method for the cells calibration and to simulate and measure in real-time the reflectivity spectrum of the structure. We will thus be able to adjust the cells flow if we notice any shift.

Second, to improve furthermore the performances we can also improve the fabrication process. Of course we have to have a better control of the oxidation by using test structures to benefit from the monitoring available in our lab [105]. We can also increase the intermediate contact ring thickness to have a more uniform current injection in the VCSEL.

All these improvements will be done in future expitaxial growth and process run.

The next chapter will focus on the global process fabrication with another development about the BCB planarization for high-speed operation. It will also discuss about the electro-optical high-frequency characterization of the EAM and EAM-VCSEL.

4 HIGH-FREQUENCY FABRICATION AND DESIGN OPTIMIZATION

We have described in the previous chapter the design of the EAM and its integration onto the VCSEL from an optical point of view. We have also described the fabrication of EAM for static operation and the electro-optical characterization of the EAM and EAM-VCSEL.

This chapter will now focus on the high frequency design, device fabrication and the characterization under high-frequency modulation up to 40 GHz.

The first section will be dedicated to the efficient planarization of the BCB on top of the device to decrease the parasitic capacitance with a low permittivity material. Indeed, to have a perfect continuity of a smooth metal contact and so ensure an optimal electrical injection we developed an original process method. Then, we implemented a dry etch recipe to reduce as much as possible the roughness of the BCB surface which is detrimental for the high-frequency properties.

Based on this technological implementation and with the help of the previous process development presented in Chapter 3, the fabrication of the whole EAM-VCSEL device with reliable methods will be presented **in the second section** for its electrical and optical high-frequency characterization.

In the third section we will describe the optimization of the applied high-frequency modulation signal. Indeed, the BCB has been chosen for its physical properties and its simple application. However, even if it is now widely used, few experimental datas about its characteristics above 40 GHz are available in the literature which is essential to realize an optimal design. We first extracted the permittivity value ε_r from lines measurement and then optimized the RF pads to decrease the capacitance and losses as much as possible. This work has been published in **paper E**

4.1 BCB PLANARISATION

The technological developments described in the previous chapter are not sufficient to reach ultra high-frequency operation of several tens of GHz. To go further and increase the electrical bandwidth, as needed in this project, it is necessary to have an optimal design for both electrodes pads on top, separated by a low permittivity material. Indeed, the addition of this layer decreases the capacitance between the two electrodes and so increases the possible maximum modulation frequency of the device.

4.1.1 *Why BCB and what are the technological challenges ?*

Several approaches can be used to reach high-frequency operation by decreasing the electrical parasitics. First, one can use a metal pad upon an air bridge but the process flow is even more complicated since it involves multiple photolithography steps, and large footprint and the reliability of the device in the time can be altered.

Alternatively, a very thick dielectric layer can be deposited but its structuration is quite complicated since it required an additional photolithography step with a tight alignement and a wet or dry etch to open the emitting window. But this selective etch step is critical since it can modify the resonance wavelength of the microcavity. This etch step can also lead to an undesired underetch of the Al-containing layers. This method also present the disadvantage of reproducing the relief during the deposition so no perfect planarisation can be achieved. Indeed, the planarization presents the advantage to provide the same insulator thickness on all the wafer for all the devices. Finally, low permittivity spin-coattable polyimide are very good candidates and are most often used to overcome these last issues. Even if its thermal conductibity and thermal expansion is lower compared to SiO_x or Si_xN_y, as described in Table 4.1, its dielectric constant is lower and the reliability is better as shown by Garrou et al. [106].

Physical property	**BCB**	**SiO_x**	**Si_xN_y**
Dielectric constant	2.65	3.9	7.5
Volume resistivity (Ω.cm)	1e19	1e15	1e14
Breakdown Voltage (MV/cm)	5.3	10	10
Thermal conductivity (W/m.K)	0.29	1.4	> 30
Coefficient of Thermal Expansion ($.10^{-6}$ / °C)	52	0.5	3.3
Tmax (°C)	350	1600	> 1000

Table 4.1: BCB properties compared to SiO_x and Si_xN_y

BCB (Bis-benzocyclobuten Cyclotene™4026-46) is deposited by spin-coating and as described by Burdeaux et al. [107] with a degree of planarization (DOP) of about 95% achievable whatever the device thickness. This degree of planarization is even improved when devices are separated by a distance of 400 or 500 µm but at the expense of the low device density on the wafer. Indeed the actual industrial VCSEL pitch is about 150-200 µm.

Nevertheless the BCB process requires an additional photolithography step in order to open a via to the mesa surface, thus involving a tight mask alignment and thus degrading the planarization.

On the one hand, the development of this photoresist is an advantage since it offers slightly inclined flank (around 45 °) which favorises the metal deposition and its continuity, but on the other hand it really complicates the process because it is necessary to anticipate the angled sidewalls lateral extension to have a perfect alignement at the top of the device.

To overcome this problem, it is possible to planarize polyimide between the mesas, i.e. bring the BCB surface at the same height level than the device top surface. After spin-coating, the BCB is significantly thicker than the device so it is necessary to etch it to reach the top mesa surface. To do so, two ways are possible: first by Chemical Mechanical Polishing (CMP) which is the faster way to decrease the BCB thickness after thermal curing but this process is difficult to apply and may lead to unsatisfying results [108] and to unwanted contamination by the polishing residus. The second one is to dry etch the BCB in a controlled way. However, even if the degree of planarization of the BCB is acceptable for some applications such as bonding, in the case of planarization for electrical contacts, it creates a slight bump relief on the border of the mesa after spin-coating. After etching this relief is replicated and a short-circuit can be seen at the top corner of the mesa as shown in Fig. 4.2.

Finally, mechanical pressing techniques such as for nano-imprint process, can be advantageously and reliably used for polymer planarization as demonstrated for other polymers, like SU-8, by Shih et al. [109] and Abada et al. [110]. After obtaining the required BCB flatness, Yang et al. [111] reported a study about the reactive ion etching (RIE) conditions for BCB etching with SF_6-based gas mixtures. To have a strictly selective etch of the BCB layer, a stop layer (for example, Si_3N_4) can be used as shown by Demir et al. [112].

In the following, we present an innovative process combining press step to make the BCB surface flat and the development of a reproducible dry etch recipe to etch to finalize the planarization while keeping the surface smooth enough for high speed injection.

4.1.2 *Planarization process development*

4.1.2.1 *Spin-coating of BCB*

Adhesion promoter, AP300, have been used prior to the spin coating of BCB 4046-26 resist [113]. BCB is deposited with a speed ramp up to improve its flatness. BCB is then soft baked at 80 °C during 90 seconds to evaporate part of the solvent. After this step the BCB layer resulting thickness is 10.6 µm overpassing the 3.5 µm VCSEL mesa heigth. Dow Chemical studied BCB adhesion on metal and on top of inorganic materials [113] but not the adhesion on Silicon or GaAs substrate. A test sample was processed without SiO_x catch layer but with an AP3000 promoter layer on top of the GaAs substrate in order to test the adhesion properties. After Hard Cure, BCB tenses up and can peel off in some places as shown in Fig. 4.1.

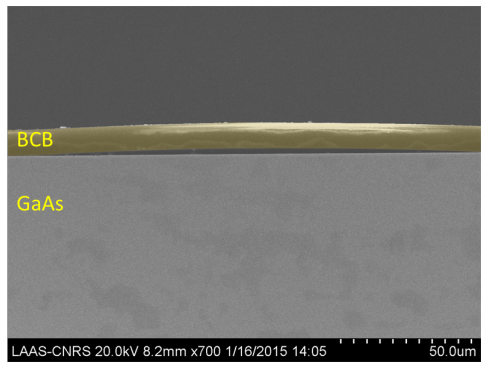

Figure 4.1: SEM cross view of the bad grip of the BCB on GaAs substrate in the absence of inorganic layer

For all the other samples, 100 nm thick SiO_x layer were deposited by ICPECVD after a short HCl cleaning of the GaAs substrate to avoid peeling.

4.1.2.2 *Planarization of BCB by nanoimprint-based pressing method*

After this step, BCB has not yet received any high temperature treatment and it is still possible to thermally reflow it by applying a high pressure. Indeed, after spin-coating, the BCB is heated at 80 °C so spreading will occur at higher temperature since all the solvent have not been removed yet. After several tests it was found that above 100 °C, the reflow phenomenon stops and no notable change is seen between 5 minutes or 10 nor 15 minutes.

The sample is thus placed on the thermocouple and is covered by a Si wafer. This wafer received a FDTS (Perfluorodecyltrichlorosilane) treatment, to make it hydrophobic and thus facilitate the separation between the sample and the wafer after this process. The sample and the Si wafer are sandwiched between two membranes (see step 2 Figure

4.2) and the sample is heated at 100 °C for 5 minutes to reduce the BCB viscosity and to improve its flowing.

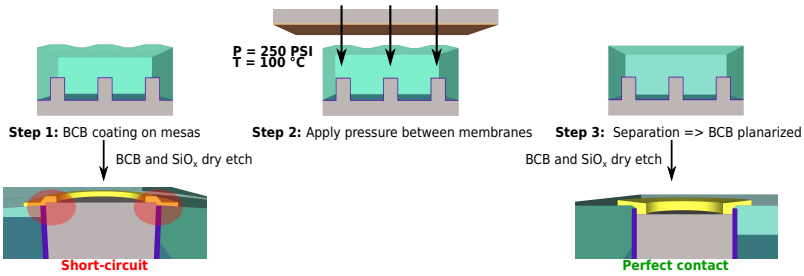

Figure 4.2: Process flow of the self-aligned process including mechanical press step and ICP-RIE dry etch

Three pressures were studied: 120 PSI, 250 PSI and 450 PSI (resp. 8.3, 17.2 and 31 bars). Top picture of the sample after separation is shown in Fig. 4.3. The higher pressure tends to rip the BCB layer from the dielectric. To ensure a perfect planarization without damaging the BCB film, an applied pressure of 250 PSI was optimum and demonstrated very good reproducibility.

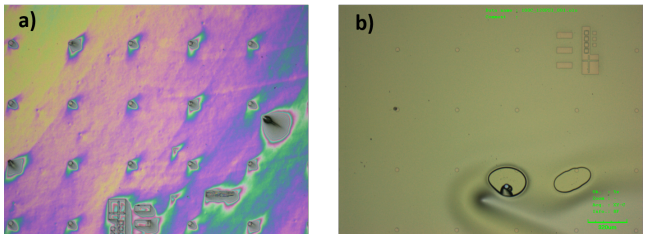

Figure 4.3: Microscope top views of sample surface after separation at 450 PSI (a) and 120 or 250 PSI (b)

4.1.2.3 *BCB Hard cure - thermal treatment*

After the planarization and before the dry etch it is mandatory to anneal the BCB to remove most of the solvent that constitute it and thus improve its mechanical strength and electrical properties. To this aim, it is annealed up to 250 °C in a furnace, in N_2 atmosphere to prevent any oxygen contamination. Furthermore, to avoid temperature overshoot when reaching this setpoint it is necessary to apply stages as described in Fig. 4.4. When decreasing the temperature, care has to be taken to not stress the BCB film and so a slow ramp down must be done.

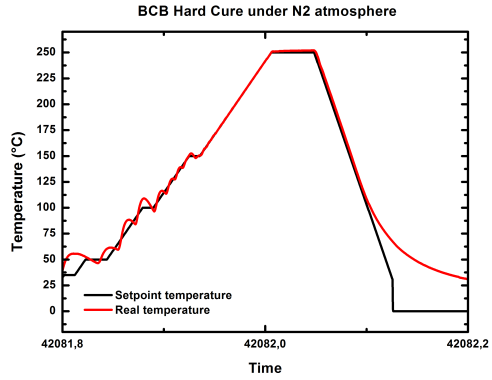

Figure 4.4: BCB Hard Cure treatment between planarization and plasma etch

4.1.2.4 *BCB thickness final adjustment*

The final step of the BCB planarization is the thickness readjustment in order to strictly level the BCB at the mesa top surface, thus resulting in a prefect planarized geometry. This etching step, is realized in our case by dry etching the total surface of the sample without the need of masking materials. Different conditions have been tested for the dry etching of the BCB layer. Inductively coupled plasma reactive ion etching (ICP-RIE) has been used with a TRIKON Omega 201 reactor, with a mixture of $SF_6/O_2/Ar/N_2$ injected gas. Also, the temperature stability has been demonstrated to be utmost to achieve the best results in term of surface roughness and good process repeatability. Samples are thus bonded with Fomblin® oil on the Si 6 inches succeptor to ensure a perfect themalization and repeatability. The results of this study are reported in the Table 4.2, where the roughness of the two last recipes (A and B) are given.

Other plasma reactors have been studied, such as P1, Tepla, without convincing results either by too fast etching rate or by non reproducibility of the plasma etch.

	O2 (sccm)	SF6 (sccm)	N2 (sccm)	Ar (sccm)	Picp (W)	Pbias (W)	Pressure (mTorr)	Temp (°C)	Results RMS	Etch rate (nm/min)
	50	5	0	0	500	80	20	17	rough	-
	50	5	0	0	500	8	80	17	rough	-
	50	5	0	50	500	10	20	17	rough	-
	50	5	50	0	500	10	80	17	rough	-
A	50	5	50	0	500	40	80	17	100 nm	460
B	98	2	0	0	500	40	70	17	10 nm	350

Table 4.2: Etching parameters to decrease the BCB thickness

The second last and the last recipes, called A and B for the next subsection, gave the most satisfactory results in terms of reproducibility and roughness, whereas the previous experiments have resulted in very rough etched surfaces and problem with the pressure stability. The roughness of the BCB surface is an important parameter since it will directly influence the quality of the Au top contact and so the high frequency performances. Small roughness is also mandatory to ensure a good adhesion of the metal on the BCB. Indeed, without any dry etch this adhesion is really bad and delamination occurs. Furthermore, the last recipe enables an etching rate of 350 nm/min which is a good trade-off between a fast etch and an enough slow rate to provide an excellent etch stop thanks to the end-point detection system.

The in-situ real time reflectometry signals in the cases of recipes A and B measured during the dry etch step are reported in Fig. 4.5. This monitoring enables to follow the surface morphology and is used as an end-point detection.

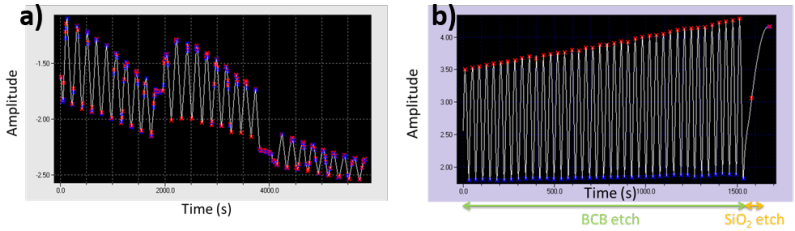

Figure 4.5: End Point Detection Laser signal during recipe A (a) and B (b)

The decrease of the reflected laser signal during recipe A in Figure 4.5 on the left is due to a degradation of the surface roughness during the etching time. On the contrary, on the right, the reflectivity amplitude increases while the BCB layer is etched since the total light absorption decreases within the thinner and thinner BCB layer, at 670 nm wavelength. Furthermore, the periodicity remains identical throughout the whole etch run which reveals that the process remains stable over time and reproducible.

To confirm this observation during the dry etch, AFM measurements are done on metal deposited on BCB after dry etch and the results are shown in Fig. 4.6. Roughness of more than 100 nm peak to peak is measured with recipe A whereas only 10 nm with recipe B.

The recipe B, with 98 sccm of O_2 and 2 sccm of SF_6 was thus prefered and used for the global process.

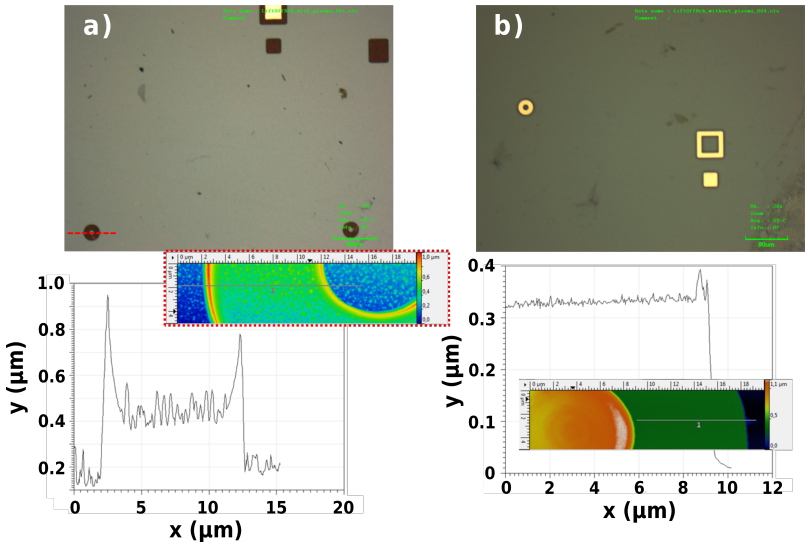

Figure 4.6: AFM measurement after metal deposition on BCB dry etched with recipe A (a) and B (b)

4.1.2.5 *Planarization result on a VCSEL mesa*

To validate the self-aligned planarization technique an VCSEL mesa was realized. The SEM view after FIB cut is presented in Fig. 4.7. We clearly see that the top contact is very well planarized and no short-circuit occurs at the edges of the devices.

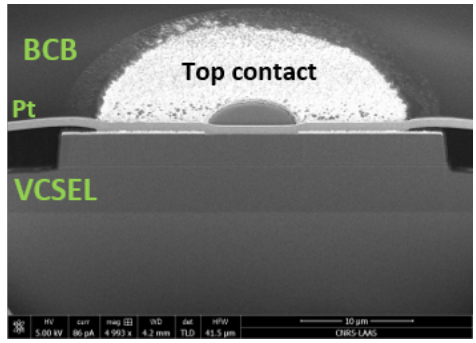

Figure 4.7: SEM view of a planarized VCSEL after FIB cut. Pt is deposited to clearly see the BCB surface

This technique, fully described in [114], also ensures an efficient planarization undependently of the pitch between the devices of that dimension (3-4 µm height) and can be used with device pitch as low as 150 or 200 µm. However this planarization has only been demonstrated with samples of 2 x 2cm and still has to be implemented for full wafers processes.

4.2 HIGH-FREQUENCY DESIGN AND IMPLEMENTATION

We have described in the previous chapter the static characterization of the EAM and EAM-VCSEL devices. These results are very good in terms of drive voltage and modulation depth compared to the actual state-of-the-art and have now to be validated at high frequencies. To reach the target of modulation at several tens of GHz the optical design is not the only key point, the efficient injection of the HF signal is also very important, which requires decreasing of the coupling with the substrate and reducing the losses due to the parasitics capacitance.

We will explain in this section the BCB characterization method developed to extract its relative permittivity and tangent losses. Then, based on this value we designed with High Frequency Structure Simulator (HFSS) software a commonly used Coplanar Waveguide (CPW) access but demonstrated its limit for our three electrodes device. We thus moved to a microstrip line configuration and designed and optimum structure for high-frequency injection while minimizing the losses.

All the work described in this section has been realized in collaboration with Dr. Christophe Viallon for the simulation part and de-embedding calculations.

4.2.1 *Dielectric Microwave characterization of BCB*

The usual methods employed to extract the dielectric characteristics of insulating materials at microwave frequencies involve inserting the studied material into a waveguide or a transverse electric and magnetic (TEM) transmission line. Complex dielectric constant and permeability is extracted from the measured scattering matrix all over the frequency range as in [115].

In our case, only a thin layer of BCB can be deposited over a substrate of different nature, which makes it virtually impossible to design a purely TEM structure. We chose here to focus on the microstrip transmission line for its simplicity of fabrication: the layer of BCB is placed between the signal path and the lower ground plane. The microstrip line supports a quasi-TEM propagation mode. Since the electromagnetic wave propagates partly in the air and partly in the material to be characterized, measurements give only access to an effective permittivity. Fortunately, proven analytical models exist in the case of the microstrip line. They are used to retreive the relative dielectric permittivity from measured effective permittivity.

Before discussing the measurement technique in detail, let's see how the test structures are fabricated.

4.2.1.1 *Wafer fabrication*

Only few steps are required to fabricate microstrip lines structures for BCB characterization. First, the ground plane located under the BCB is deposited on the whole sample. Then, BCB is spin-coated and an additional photolithography step is employed to form the openings used to electrically connect the ground plane to the ground pads located on top of BCB layer. Finally, after the heating treatment, a lift-off is performed to fabricate RF pads, vias and the transmission line.

In the case of an EAM vertically integrated onto a VCSEL, the first mesa is 3 µm thick and another etch step is required to reach the active region of the VCSEL to provide the lateral electrical and optical confinement. That corresponds to a global thickness of 6 µm.

About the top access lines, based on a standard value given by Cyclotene™of 2.65 (at low frequency), we designed line access of 14 µm width, corresponding to an impedance of around 53 Ω, with different lengths, 200, 300, 700 and 1200 µm, as done(ou described) by Ghanam et al. [116].

Coplanar RF pads are added to the ends of microstrip lines for Ground-Signal-Ground (GSG) RF probes contacts to land on. These square pads are 60 µm large.

4.2.1.2 *Access pads de-embedding*

The first step is to remove the contribution of the RF pads from raw measured data. Usually, the electrical equivalent lumped model of the pad is retrieved from dedicated Short, Open and/or Thru dummies structures [117]. Open and Short patterns are both used to calculate the equivalent parallel capacitance and series inductance of the pad, respectively. This technique is rapidly problematic with increasing frequency due to the non-ideality of corresponding terminations [118]. These problems are avoided if both Open and Short devices are replaced by using only one thru pattern to determine the same model of the pad, but this technique introduces new issues [118,119]. Indeed, since the pad is modeled by lumped elements, all these methods are valid only for access dimensions much smaller than the wavelength (i.e. λ_g / 20) of the highest test frequency. A short thru pattern is then desirable but the close proximity of both signal pads and probes introduces some cross-talk that again lead to an incorrect pad modeling [119].

The technique we developed avoids all previously mentioned issues. Two transmission lines of different lengths are used to extract the propagation constant γ from which the electrical model of the pad and the transmission line characteristics impedance Z_c are assessed. Open/Short or Thru dummies structures are no longer required.

Full details of this method developed by Dr. Christophe Viallon can be found in our **paper E**.

4.2.2 *Extraction of the electrical characteristic of BCB*

The extraction process of the electrical characteristic of BCB material is summarized by Fig. 4.8. First, the complex effective permittivity $\overline{\epsilon_{eff}}$ is calculated from the de-embedded measurement data of one of the two transmission lines. The Transmission-reflection method, introduced in [115] and modified in [116], is used to extract $\overline{\epsilon_{eff}}$. The relative permittivity ϵ_r as well as the loss tangent term $\tan\delta$ are then determined either by a direct computation carried out by using analytic equations derived from Bahl's model (method 1) [120], or by using an iterative calculation algorithm based on the Jensen-Hammerstad model (method 2) [121]. The choice between these methods is dictated by the validity range of each model regarding microstrip line geometry. It mainly depends on the thickness over height t/h ratio of the analyzed microstrip line. Theses two techniques as well as form factor validity ranges are developped in [116]. Accurately measured geometric data of the line are also required to insure the best possible accuracy of the extraction.

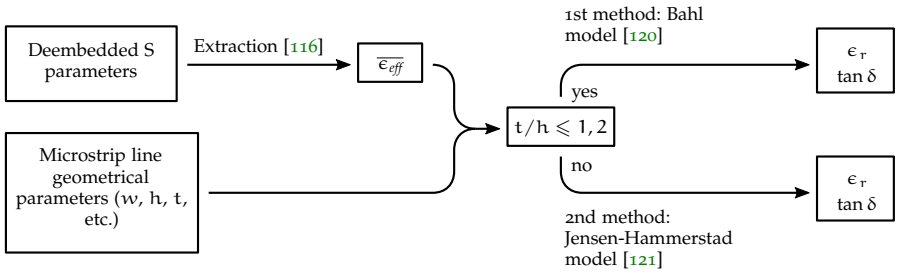

Figure 4.8: Illustration of the operation of the two extraction methods of electrical characteristic of the dielectric used inside a microstrip line.

4.2.3 *Results*

We present in Fig. 4.9 the thru measurements with an Anritsu Vectorstar in complement of a Broadband Test Set 3738A for higher frequencies with Cascade Infinity 110 GSG 150 probes on microstrip access lines on 6 µm-thick BCB layer. Based on the method previously described we extracted the BCB permittivity and $\tan\delta$. Results are shown in Fig. 4.10. As we can see, both methods reach the same outcome. At low frequency, a permittivity of 2.62 is measured and descreases to 2.5 at 60 GHz. After 67 GHz, the RF source switch which explains the abrupt change in slope.

About the $\tan\delta$, which can be defined as ϵ''/ϵ', from the phase measurement we extracted a value comprised between 0.01 and 0.03 in the 0 - 60 GHz range.

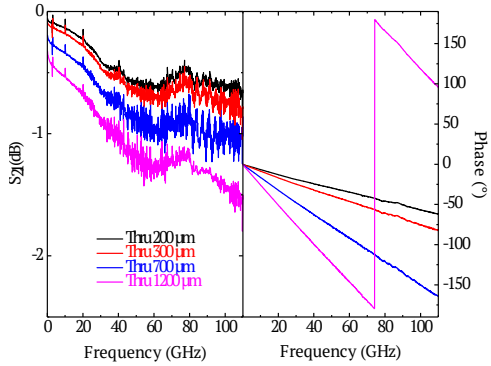

Figure 4.9: Measurement of thru designs of 200 µm (black), 300 µm (red), 700 µm (blue) and 1200 µm (magenta)

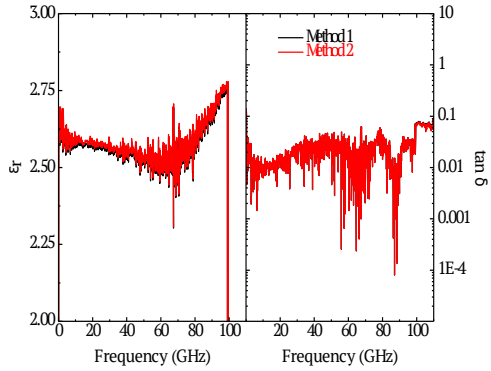

Figure 4.10: BCB permittivity extracted from both method 1 and 2 from different lines lengths

The method developed here to extract the BCB permittivity from microstrip line access measurement will be re-used to carry out the de-embedding of the access impendance on the modulator impedance itself in Section 5.2.6.

4.3 HIGH-FREQUENCY INJECTION DESIGN

Once we have characterized the BCB permittivity, we are now able to provide an optimum high-frequency injection design to decrease the electrical losses and thus reach the very fast operation of the modulator.

We compare in this section two RF access designs, a commonly used CPW in VCSEL community, and a microstrip line access.

4.3.1 *Coplanar Waveguide access*

For high frequency injection signal several probe configuration are available, for a single signal probe: Gound-Signal (GS) or GSG, and for a dual signal injection: GSGSG or GSSG. For device modeling and characterization Cascade Infinity Single is an excellent candidate [122]. For those probes, the minimum pad size is 25 x 35 µm and pitch (spacing between probes) of 50 to 250 µm. We worked in this section with a pitch of 150 µm.

To increase the accuracy of the very small voltage difference measurement, we used two probes as ground and a third one for the signal injection, corresponding to GSG configuration.

To couple high microwave frequency signal, different types of structures exist. The Coplanar waveguide (CPW) and the microstrip line access and a third one which is a combination of both, Coplanar Grounded (CPWG).

In the case of CPW the ground plane is at the same height than the signal line as shown in Fig. 4.11 and 4.12. Coplanar waveguide (CPW) access are commonly used for high frequency injection in VCSEL. Even if here we do not inject current but we only apply an electrical potential difference, we decided to keep this configuration.

Indeed, in the VCSEL community all the groups, of Coldren [24], of Larsson [123], of Lott [124], work with a similar coplanar access design. However, the issue due to the substrate doping on high-frequency performances is well know since to avoid any coupling with the highly doped bottom N-contact layer close to the active region, they etch the N-layer under the pad line which provides an additionnal process step. This approach is only possible for VCSEL stand-alone device. To increase the optical bandwidth, the vertical integration of an electro-optic modulator onto a VCSEL has already demonstrated to be a competitive device [50, 125, 126]. In that case a double mesa structure is required with three electrodes contact. Two on top for the small signal injection in the modulator and the shared ground, and one at the bottom for the VCSEL drive current injection. This approach requires necessarily a highly doped substrate. To this aim, we propose in this paper to compare coplanar waveguide (CPW) access and microstrip lines access for this kind of structure to decrease the parasitics capacitance and thus the inherent losses. Indeed, all the groups who already worked with this vertical integration of an electro-optical modulator onto a VCSEL used highly doped substrate for the current injection in the VCSEL without consideration, to our knowledge, about the induced losses. Paraskevopoulos et al. [127] used a CPW access with a very large spacing between the access line and the ground plane, Chen et al. [128] worked with a GSSG access presenting the advantage to provide all the access on the same level but the substrate doping remains an issue. Finally, Yakimov et al. [87] even if they do not describe precisely the RF injection, used a doped substrate with a CPW access.

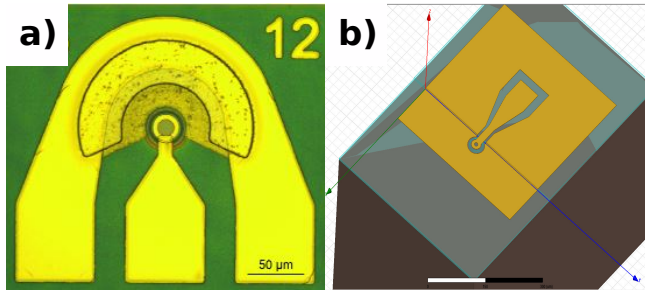

Figure 4.11: a) Top view of a VCSEL powered by a CPW (from [27]), b) 3D schematic of the HFSS simulation of the CPW access for the EAM-VCSEL device.

The spacing between signal and ground (gap illustrated in Fig. 4.12 b)) allows to tune the impedance of the access

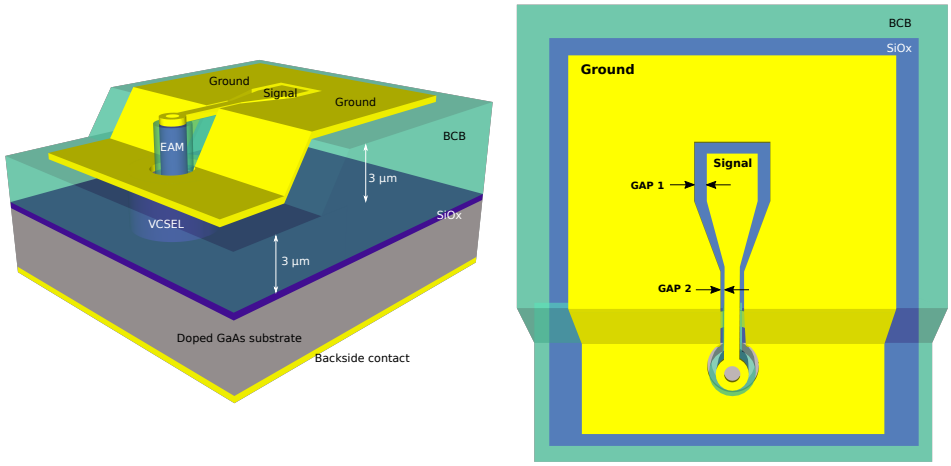

Figure 4.12: CPW design for EAM-VCSEL device. On the left, tilted view, on the right, top view.

The distances shown in Fig. 4.12b between ground plane and signal pad line are called *Gap 1* and *Gap 2*, respectively.

To improve the EM wave confinement in the CPW structure, since the BCB thickness is of only 6 µm, it is necessary to bring the ground plane close to the access line. To this aim, gaps 1 and 2 (as shown in Fig. 4.12) were designed with HFSS (High Frequency Structure Simulator) software and set at 15 µm and 5 µm respectively. This last dimension allows to decrease as much as possible the penetration depth of the magnetic field in the substrate while considering the fabrication process difficulties for the metal lift-off.

Furthermore, in this configuration, few micrometers before the EAM mesa, the BCB thickness is decreased to reach the top VSCEL mesa and thus the intermediate contact. This last dimension is crucial and present a very difficult process step since it is necessary to control the sidewall inclination to reach the VCSEL contact. Indeed, the VCSEL mesa

diameter can not be too large to avoid oxidation problem like non reproducibility or non linear oxidation rate.

4.3.2 *Process*

We worked with three different substrates: a N-doped, a P-doped and a Not Intentionally Doped (NID).

After cleaning, 100 nm-thick SiO_x layer is deposited by PECVD at the surface to ensure a good adhesion of the BCB. BCB is spin-coated to reach 10.5 µm and then hard-cured to remove most of the solvent.

We also etched one NID sample with the dry etch recipe described previsouly to reach 5 µm and thus study the impact of the BCB thickness on the high frequency properties and misadaptation.

Finally, the Ti/Au 50 / 200 nm metal pads, defined by lift-off, was evaporated with the dimensions above described.

4.3.3 *Impact of the substrate doping with the CPW design*

Open, short and thru structures are measured up to 110 GHz with the same equipment than in Section 4.2.3. We present in Fig. 4.13 the S_{11} and S_{21} parameters obtained on thru lines with the three different substrates doping.

The doped substrates present lower insertion losses. S_{21} is strongly related to propagation losses but it also depends on the amount of wave reflected at the input, represented by S_{11}. Since S_{11} is high for the device fabricated on P-doped substrate, it is quite hard to conclude on the substrate contribution on insertion losses. In addition, N-doped behavior is somewhat different than P-based one, probably due to the difference in doping concentration between both samples, such data being not very accurate from the supplier

However, we can better understand what is happening in these samples by extracting an equivalent electrical model. The Π-model illustrated in fig.4.14 is used here. The extracted R_s, L_s, R_p and C_p are plotted in 4.15 and 4.16.

As seen in Fig. 4.15, on NID substrat, below 60 GHz the line access exhibits a very small resistance of 1 Ω which is increased to 2 to 4 with doped samples. With doped substrates, an important part of the return current goes through the substrate. This negative magnetic coupling effect induces extra losses and slightly decreases the inductance values L_s. This effect changes the magnetic field distribution as seen in Fig. 4.17.

The other consequence of this highly doped substrate is the shielding effect seen in Fig. 4.17. It increases the equivalent capacitors C_p of the thru device compared to NID-

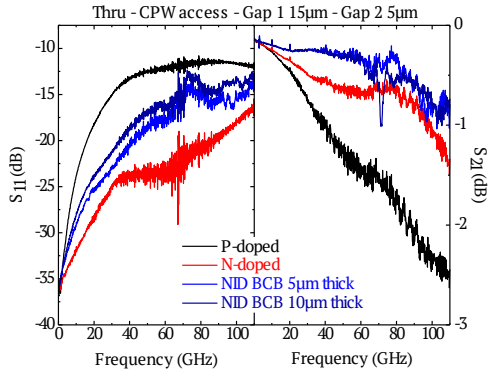

Figure 4.13: S_{11} and S_{21} parameters on Thru designs for P-doped (black), N-doped (red) and Not Intentionally Doped (blue) substrates.

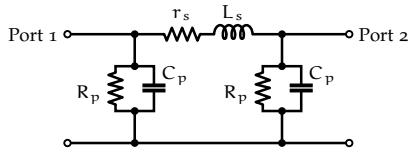

Figure 4.14: Π equivalent lumped network used to model Thru structures.

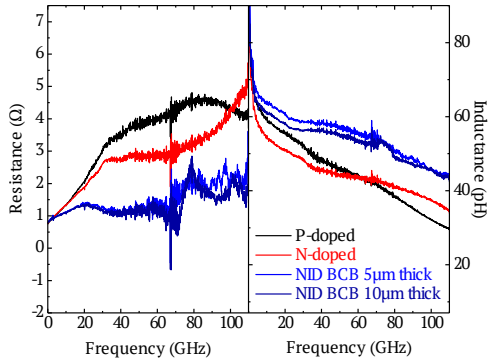

Figure 4.15: Resistance and Inductance extracted from the CPW access measurements

substrate devices (Fig. 4.16). The lower resistivity of doped substrates also lowers the equivalent parallel resistor R_p compared with NID substrates.

As expected, a coplanar access line suffers from substrate conductivity and when doped substrates are placed underneath, the increase in access resistance (R_s) becomes unacceptable given the moderate impedance, around 600 Ω at 40 GHz, presented by the modulator at very high frequencies. For this reason, microstrip line is now investigated.

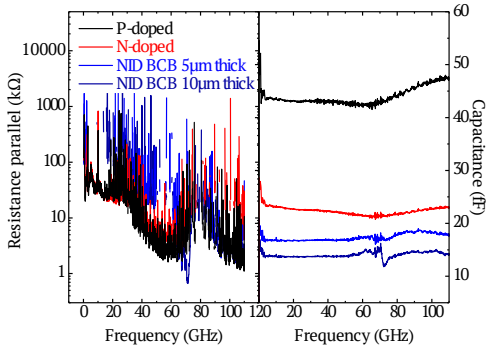

Figure 4.16: Resistance parallel and capacitance extracted from the CPW access measurements

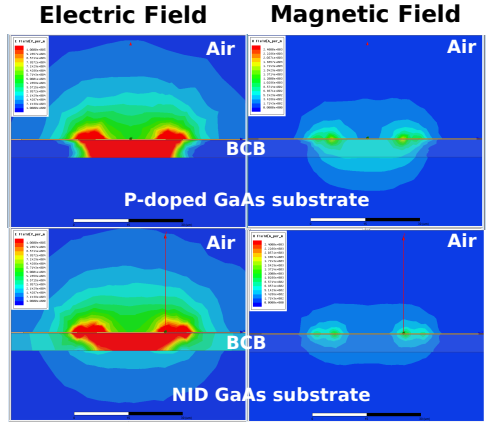

Figure 4.17: Electric and Magnetic fields for CPW access with P-doped substrate (top) and Not Intentionally Doped substrate (bottom).

4.3.4 *Microstrip line access*

The microstrip line appears as an alternative to avoid the previously described substrate-induced losses. The electric contact required between EAM and VCSEL to bring bias voltage is used as the microscrip line ground plane to shield the underlying doped substrate. The RF performances of this solution is compared with the previously studied CPW line

it is possible to work with microstrip design where the ground plane allows to remove the accumulation charges in the substrate as seen in Fig. 4.18.

In this configuration, the ground shared contact is transfered on the substrate, 6 µm below the access line so no complicated angled photolithography step is required. However, it is still necessary to have both contacts on top so an opening is done in the BCB layer to take the contact as done in Section 4.2.1.1. Dimensions about this microstrip line design will be discussed in the next section.

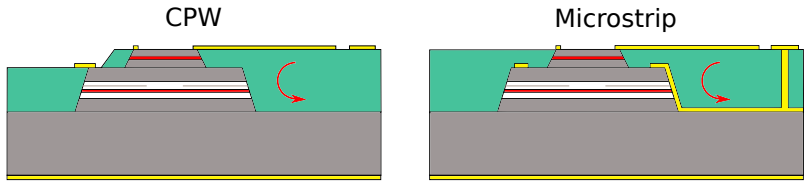

Figure 4.18: Schematic crossview of the EAM-VCSEL with CPW access (left) or Microstrip line (right). The coupling is represented by the red arrow

Another advantage of the microstrip configuration is about its simulation. Indeed, physical line models already exists in softwares and are easily implementable.

We compare in Fig. 4.19 the CPW access and the microstrip access lines on P substrate (which is here the worst case).

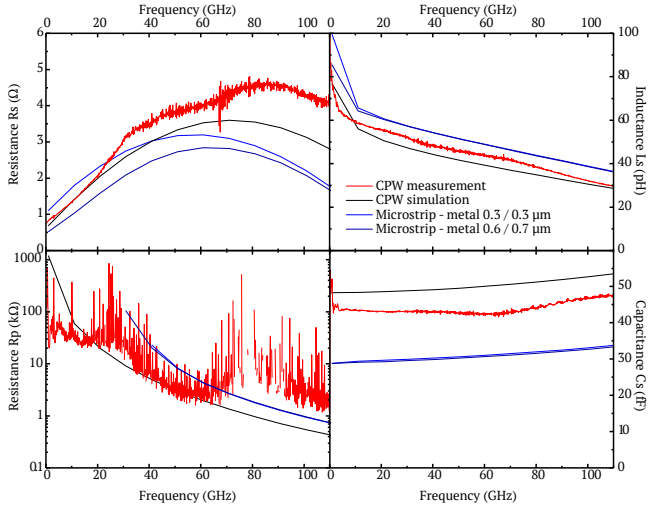

Figure 4.19: Electrical parameters, Rs, Ls, Rp and Cs, of measured (red) and simulated (black) CPW access comapred to microstrip line with thin metal deposition (blue) and thicker metal (dark blue).

.

As we can see, the simulation (black) is in good agreement with our measurement on CPW (red). The CPW presents higher resistance due to the substrate doping as explained previosuly. Thanks to the more significant penetration of the magnetic field with CPW, the inductance is lower than microstrip but as expected its capacitance is, in simulation, 40 % higher. These results can be easily correlated with the electric and magnetic field simulation shown in Fig. 4.17.

At high frequency, due to the skin depth, the EM wave is confined in a very thin metal layer, below 300 nm, for this reason no difference can be observed between both serie resistance.

Even if the gain with the microstrip is not so significant, thanks to its advantage to be used with doped substrated we will thus prefer it for our application.

4.4 GLOBAL PROCESS

Previously, two technological locks useful to fabricate the global device, see Fig. 3.13, with a double mesa structure with planarized electrodes on top has been demonstrated. The whole process flow with the different photolithographies, dielectric passivation, metallization, etchings and oxidation will be described now.

The process flow is described step by step in Fig. 4.21 and below. Note that only the full description of the key process steps will be done, the complete and detailled process flow will be described in Annex A.

To reach very high speed operation for both the EAM and the EAM-VCSEL, both samples were processed with the same steps to achieve a total thickness of 6 µm of BCB. Furthermore, having the same thickness of dielectric will allow the direct comparison of the high frequency properties of the devices.

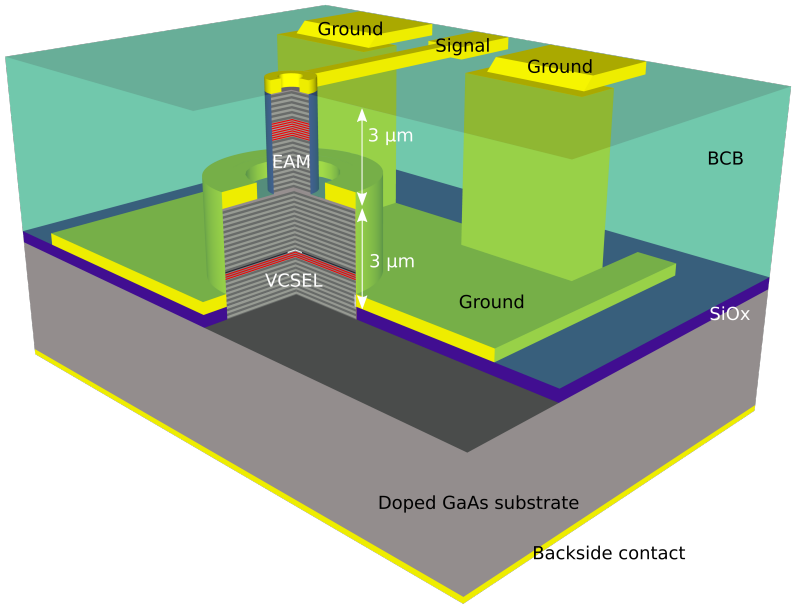

Figure 4.20: Global view of the EAM-VCSEL device

To realize this process flow, its implementation on a dedicated software to write the different mask levels is necessary. The software used here is Clewin which has been prefered to Cadence or Klayout for its ease of use in our specific case. To ensure a good oxide aperture for the VCSEL confinement five diameter were designed as shown in Fig.

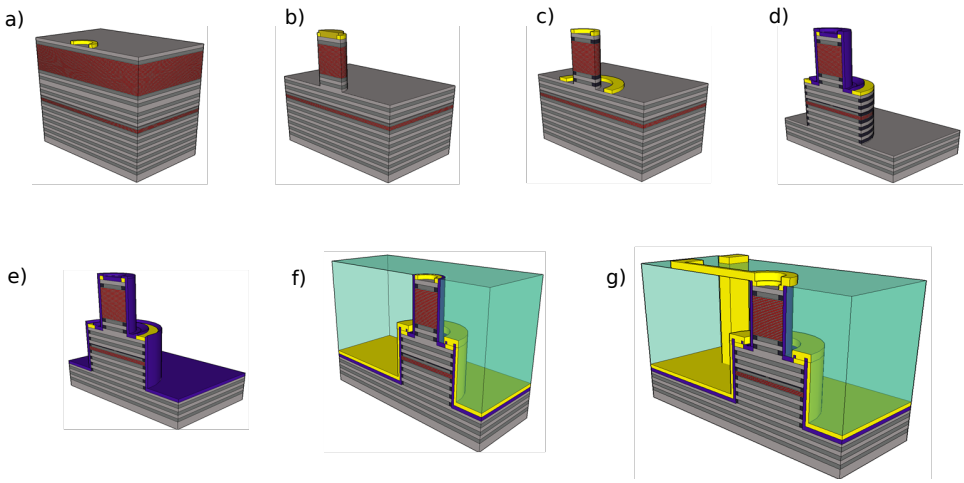

Figure 4.21: Global process of EAM and EAM-VCSEL for high-speed operation

4.22, Y axis. The EAM mesa diameter plays an important role in the electrical limitation so we processed ten diameters from 18 µm to 27 µm (X axis in Fig. 4.22).

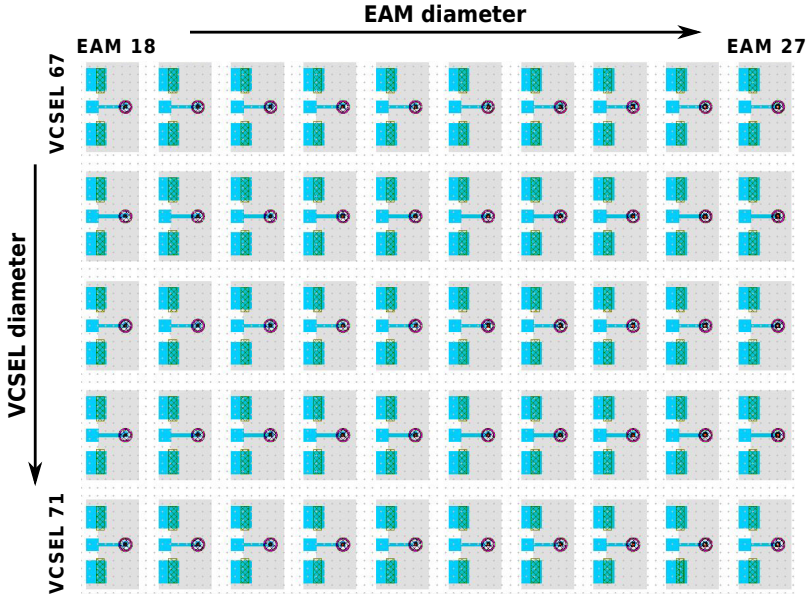

Figure 4.22: Unitary block of devices. EAM diameters are between 18 µm and 27 µm and VCSEL mesa diameters between 67 µm and 71 µm. This block is then repeated with different line lengthe and pad areas.

To decrease the losses in the dielectric at high frequency it is necessary to minimize the surface of the gold area on top of the BCB. The mask design is formed by three blocks, each of 10 x 5 devices, with micro strip line length of 50, 100 and 150 µm in order to tune the impact impedance as described in the next section of this chapter.

To decrease furthermore the capacitance due to the pad area we reduced the signal pad area from from 3600 μm^2 to 2300 μm^2 as described in Fig. 4.23b. This produces another set of block.

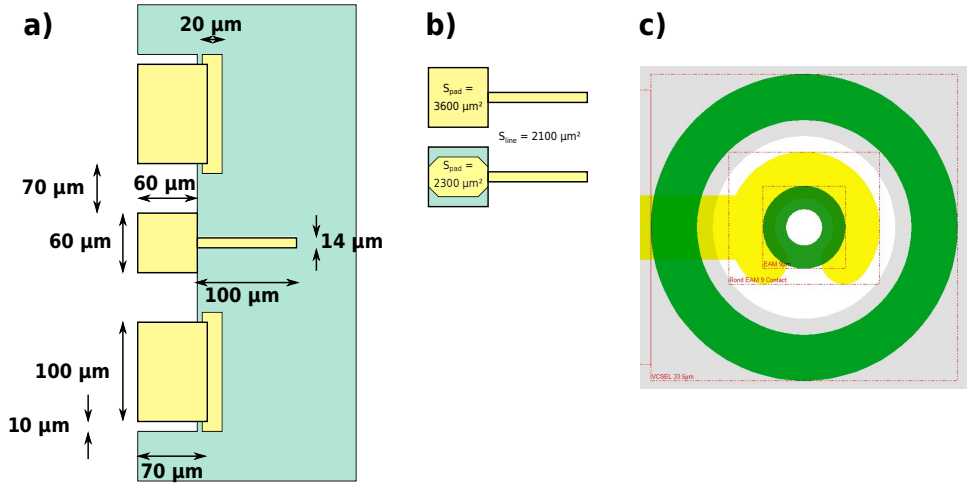

Figure 4.23: a)Dimension of a standard pad with the GSG pads (yellow) and the bottom ground plane under the BCB (green). b) is a description of the reduced pad area. c) is top view of the mask. In green the EAM and middle contacts, in yellow the electrical top contact and in grey the bottom ground plane.

- **Step 1: EAM top contact**
  - *Sample cleaning*

    Before every resist deposition it is necessary to remove organic particules. Aceton is used to this aim, then Isopropanol dilutes the aceton to avoid any traces and finally, deionised water is recommanded before nitrogen drying. This last step avoids the removed particules to get stuck between the drop and the sample surface.

    Heat at 110°C for 2 mintues.
  - 1^{st} *Photolithography*

    Spin-coating of LOR and SPR resists Insulation with MJB3 to define 5 µm large rings and of different diameters between 18 µm and 27 µm. Such diameters were choosen to measure the impact of the diameter on the capacitance (proportional to r^2) but not being too small to not complicate too much the process. Development with MFCD26 and rinse with deionised water for 1 minute and nitrogen drying.
  - *Desoxidation*

    Before each metal deposition step it is mandatory to remove the native oxide at the surface of the III-V material which could introduce a resistance and

so increase the applied voltage. In this regard the sample is immerged in a chemical solution of HCl / H2O2 1:5 for 30 seconds.

- *Metal deposition*
  Metal is then deposited by e-beam evaporation. Here 50 nm of Ti is first deposited as an adhesion layer, and 600 nm of Au to decrease the losses in the metal at high frequency as described in next section. Au/Ge/Ni/Au would have been a better metal stack for the N-doped contact but the deposition equipment was not available. Nevertheless, since we are not looking for high drive current, the metal material is not so crucial.
- *Lift-off*
  The resist and non desired metal are then lifted off in a chemical bath of DMSO or remover PG heated at 80°C. The second one, even if it is more efficient, has to be used carefully due to its CMR (carcinogenic, mutagenic or toxic for reproduction) risk.

- **Step 2: EAM mesa etch**
  - *Sample cleaning*
  - 2^{nd} *Photolithography*
    Spin coating of 2.3 µm SPR resist.
    insulation MJB3 to define circle smaller than the top contact ring which will be used as a hard mask for etching.
    Development
  - *Dry etch*
    The EAM mesa is etched by ICP-RIE in an Technology Omega 201 reactor. The physical and chemical parameters are given in Annex A. A laser End Point Detection is used to control the etch and stop in the middle contact layer precisely. An example of this in situ real time reflectometry is given in Annex A.
  - *Optional oxidation*
    To decrease the electrical capacitance of the modulator it is possible to oxidize the high Al content layers in an oxidation furnace. This will lead to a smaller active region diameter seen by the current at high frequency and so could increase the cut-off frequency. However, this will increase the strain in the vertical structure of the modulator and the aperture can not be too small to not impact the output beam of the VCSEL.

- **Step 3: VCSEL top contact**
  - *Sample cleaning*

- 3^{rd} *Photolithography*
  Spin-coating of LOR and SPR resists
  Insulation of 5 µm large rings and of different diameters between 67 µm and 71 µm. Five diameters are considered here to try to reach the perfect oxide aperture.
- *Desoxidation*
- *Metal deposition*
  Here again 50 nm Ti/ 600 nm Au metal are deposited for the middle P-contact.
- *Lift-off*

- **Step 4: EAM passivation, VCSEL etch and oxidation**
  - 4^{th}*Photolithography*
    Spin-coating of LOR and SPR resists
    Insulation to open circles around 65 µm
    Development
  - SiO_x *deposition*
    Deposition of 400 nm of SiO_x
  - *Lift Off*
  - *VCSEL dry etch*
    The SiO_x is used as a hard mask for the dry etch of the VCSEL mesa. During the ICP recipe, SiO_x is etched at a rate of 22 nm /min leading to a remaining 100 nm. Dry etch is stopped to reach a global thickness of 6µm
  - *VCSEL oxidation*
    After mesa etching, the VCSEL is oxidized in the dedicated furnace.
    Due to the thick stack above the $Al_{0.98}Ga_{0.02}As$ layer, it is very difficult to measure the oxide aperture. The oxidation rate is thus measured at the beginning and interpolated to be stopped at the precise expected oxide aperture value, between 3 and 9 µm to avoid qny shadowing of the beam with the top EAM and metal aperture.

- **Step 5: VCSEL passivation**
  - 5^{th} *Photolithography*
    Spin-coating of LOR and SPR resists
    Insulation with MJB3 Karl Suss mask aligner to protect the EAM and VCSEL device, only a few µm ring is opened to deposit the ground access
    Development

  - *SiO_x deposition*
    Deposition of 400 nm of SiO_x to ensure a perfect covering of the mesa, in particular on the vertical (due to the hard mask) sidewalls.
  - *Lift Off*

- **Step 6: Ground contact and planarization**
  - *6^{th} Photolithography*
    Spin-coatting of LOR and SPR resists
    Insulation with MJB3 to define the ground plane
    Development
  - *Metal deposition*
    Deposition of 50 nm Ti / 600 nm Au
  - *Lift Off*
  - *BCB spin coatting*
    By using ramp up to optimize the covering on the sample
  - *BCB planarization*
    As described in the Section 4.1.2.2

- **Step 7: Via opening and GSG contacts**
  - *7^{th} Photolithography*
    Insulation with MJB3
    Development in DS300 between 30 and 35 °C
  - *BCB etch*
    With recipe developed in 4.1.2.4
  - *Photolithography*
  - *BCB etch*
  - *Photolithography*
  - *Metal deposition*
  - *Lift-Off*

In Fig. 4.24 we show a microscope top view of the final device (a) and a 3D image taken with confocal microscope (b).

4.5 CONCLUSION

In conclusion, we have demonstrated in this chapter the fabrication and the design optimization, thanks to the BCB characterization up to 67 GHz, to decrease as much as

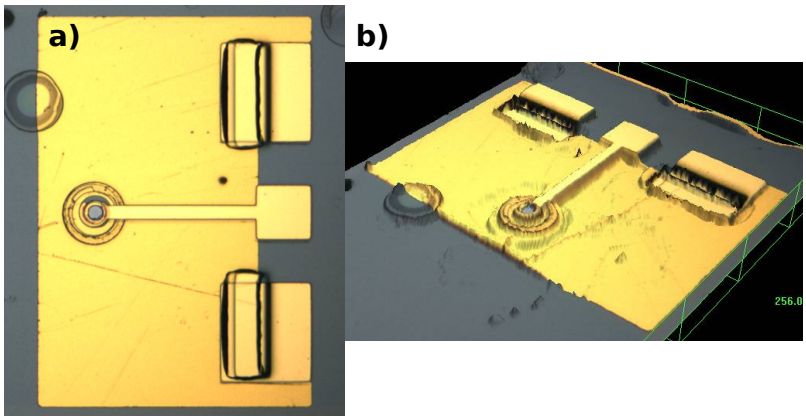

Figure 4.24: Global view of the EAM-VCSEL device. a) Microscop top view b) 3D confocal image

possible the losses and to maximize the coupling for the high-frequency injection in the EAM for high-speed operation.

First we described the BCB planarization process. Indeed, an innovative self-aligned technique was presented with the use of a mechanical press combined with high pressure and temperature to reach a flat surface. The dry etching recipes following the planarization step were studied to control the final top level of the BCB layer while maintaining the surface smooth enough for high speed electrical injection.

In the second section we described, the high-frequency electrical contact optimization to minimize the injection losses. Indeed, we first worked with a standard coplanar waveguide pattern which demonstrated significant losses due to the substrate doping. To avoid the Foucault and leakage current, we move to a microstrip line design where the ground plane allows to overcome the coupling between the access and the substrate. We characterized the BCB permittivity up to 67 GHz, thanks to a new de-embedding method, and thus designed an optimum access close to 50 Ω impedance.

In the third section we described, with the combination of the previous technological unlocks, the EAM and EAM-VCSEL fabrication samples with double mesa geometry. The differents steps were described. More details and tips about the technological process flow can be found in Annexs A and B.

The next chapter will be focused on the High Frequency characterization of the EAM and EAM-VCSEL structures previously fabricated.

5 HIGH-FREQUENCY OPERATION

We described in the previous chapters the static characterization of the EAM and EAM-VCSEL devices. Based on high-frequency simulations and the BCB characterization, we optimized the design of the pad and the line access to get the lowest possible losses and coupling with the substrate thanks to the microstrip design. Then, we described the global process flow based on several technological developments. This chapter will focus on the high-frequency modulation characterization up to 40 GHz of the EAM and EAM-VCSEL devices.

The first section will be dedicated to the EAM high-frequency characterization. First, we describe the fiber optical alignment for injecting and detecting light into and reflected from the modulator. Then, the implementation of the VNA to measure very small electrical signal coming from the photodiode is presented. We also propose to do the measurements with a synthesiser to understand each loss contribution in the "tee - cable - probe - pad" system. Finally, to extract the exact response of the stand-alone EAM, we characterized the photodiode response at the device operating wavelength (850 nm) and thus measure accurately the electro-optical response of the EAM.

In the second section, thanks to a loan by TU Berlin of a higher bandwidth photodiode and electrical amplifier, we were able to measure the high-frequency characteristics at frequencies up to 40 GHz. We thus could measure and compare the response of the EAM both with the synthesiser set up and with the VNA. We also studied the influence of the temperature, the mesa diameter and the applied voltage on the electro-optical response of the EAM. Cut-off frequency of the stand-alone EAM higher than 28 GHz was measured for larger (25 µm) diameter devices, whatever the used measurement conditions. Then, thanks to the previous deembedding method, we extracted the impedance of the modulator as a function of its diameter and were able to propose an electrical model of this structure.

Finally, we measured the electro-optical response of the EAM-VCSEL for different applied voltages on the EAM and different drive currents of the VCSEL and demonstrated

again a cut-off frequency of 29 GHz, limited by the EAM EO response. The EAM and the EAM-VCSEL high-frequency responses are the topic of **paper F and G**.

5.1 EAM HIGH-FREQUENCY CHARACTERIZATION

We will carry out in this section the electro-optical high speed characterization of EAM and EAM-VCSEL.

In such a setup at high frequency, the electrical losses due to the different elements have to be carefully considered for the efficient injection of a constant voltage at the terminal of the modulator to extract its cutoff frequency. Another problem in such a characterization, compared to VCSEL modulation, is the high impedance of the modulator, acting like a capacitance, which implies to inject a voltage of several volts on the modulator pads to be above the noise measurement level.

About the EAM device, the characterization principle developed here is to measure the modification of the light amplitude when it is reflected by the modulator when subjected to a high frequency signal. For the EAM-VCSEL the light directly comes from the VCSEL itself so in such configuration the optical transmission of the EAM will be modulated.

5.1.1 *Optical alignement*

To check the good quality of the top and bottom electrical contacts of the EAM device, it is possible to have an electroluminescence (EL) emission of the QWs with a direct current of the device. Indeed, at 2V for the sample B, an emission is observed on the CCD camera of the microscope which certifies the good operation of the device. Once the device to be characterized has been identified it is necessary to ensure a perfect alignment of the fiber on the optical window of the EAM.

We decided to work for this measurement with single mode fiber to avoid all the parasitics effects due to a multimode one. However this complicates the alignment since the core diameter of such a fiber is 6 µm while the outside diameter, with the polyimide protection, is 125 µm. It is thus very complicated to adjust with the vertical microscope the X and Y position to perfectly inject light vertically. The alignment is even more difficult for the stand alone EAM device since there is not emission, or at least the EL does not provide sufficient power.

To overcome this problem and facilitate the maximum coupling between the fiber and the EAM we used a lock-in system as described in Fig. 5.1. The tunable laser source wavelength is set at the precise value of the modulation, i.e. 838 nm for the sample B. A sinusoïdal signal is injected in the EAM with a low frequency generator at 2 kHz with a reverse offset biais of 2 V and an amplitude of 1 V. This signal is synchronised

with the Thorlabs FDS02 Si-photodiode response (responsivity of 0.5 A/W) in a lock-in system which compares the two signal. The amplitude of the measured signal gives an indication of how good is the alignment.

It is also necessary to note that, to avoid any vibration in the extremity of the fiber, we have to protect the set up from any airflow. Then, to avoid the mechanical vibration, the fiber is set in contact on top of the device which also increases the re-injected signal.

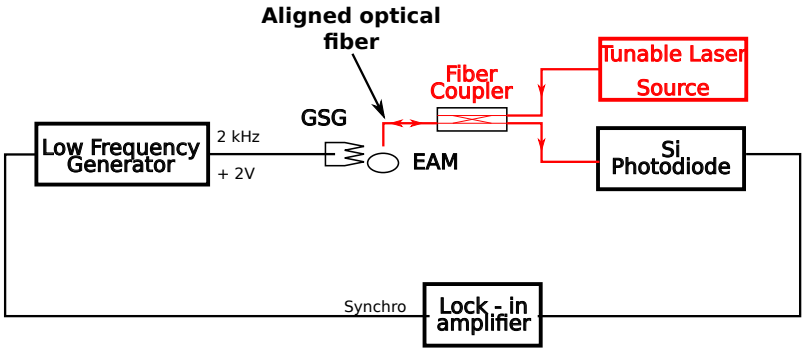

Figure 5.1: Schematic of the set up used for the optical alignment of a single mode fiber on top of the EAM for an optimum light injection. In red the optical paths, in black the electrical paths.

We will depict in the next subsection the way to realize this complex measurement and the several steps and improvements before reaching an acceptable characterization of the EAM device.

A dedicated electro-optical characterization setup has been developed to vertically inject and detect light through a single-mode Y fiber coupler on the modulator top surface. The incident monochromatic light is supplied by a tunable laser source (TLS) and the reflected EAM-modulated signal is measured using a high-speed photodiode as seen in red in Fig. 5.2. The TLS is a Superlum BS-840-1 (820 - 870 nm, linedwidth = 0.06 nm) and the employed InGaAs Discovery DSC20H-39 photodiode displays a cut-off frequency of 32 GHz at 1550 nm. The RF injection is either carried out by a VNA source or by a RF synthesizer as described in the next subsections. Finally, the -3 dB cut-off frequency of the device is obtained by normalizing the photodetected EAM response under RF voltage excitation with the response obtained at the lowest frequency voltage.

5.1.2 *Vector Network Analyzer (VNA) implementation*

The first implementation is displayed in Fig. 5.2a. A VNA Agilent PNA-X 67 GHz is used to extract the EAM response. Since the signal retrieved by the photodiode is too low due to several cumulative factors (EAM reflectivity, fiber misalignment and photodiode responsivity in the near-infrared range), a power amplifier (PA) featuring a maximum

output power of +24 dBm has been inserted between VNA and EAM RF input. The port 2 is connected to the EAM through this PA, a bias Tee, a coaxial K-band cable and a Cascade Infinity 40 GHz coplanar on-wafer RF probe. Any change in EAM reflectivity is measured by the photodiode and sent to VNA port 1. The EAM bandwidth is extracted from the measured transmission parameter S_{12} and the PA-limited 10 MHz - 18 GHz frequency range is covered in one sweep by the VNA.

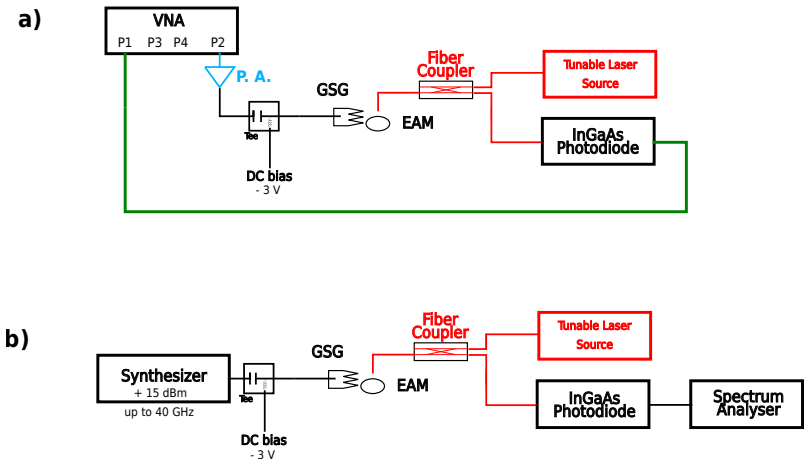

Figure 5.2: Schematic of the electro-optic characterization setup of the EAM with a VNA (a) and with a synthesiser (b)

Preliminary results

The first set of measurements is plotted in Fig. 5.3. As we can see in red, green and black, any modification in the EAM DC voltage bias and TLS wavelength changes the S_{12} magnitude observed on the VNA. This clearly indicates that a modulation effect takes place within the EAM section, thus demonstrating the effective electro-absorption modulation at such frequencies. It is interesting to note that the slope observed between 1 GHz and 18 GHz remains unchanged whatever the voltage and wavelength values.

Jointly, we have measured the electrical losses in the "PA + bias tee + Cable" response, in black at the top in Fig. 5.3. This result confirms that the slope seen in all S_{12} curves is strongly related to the RF signal injection losses. If these losses are subtracted from the raw transmission measurements, a very flat response from the EAM is obtained over all the 1-18 GHz frequency range (blue curve).

Limitations

This result shows that we are especially limited by the bandwidth of the PA and by the losses within the test bench between VNA and EAM device. Indeed note that even with the PA we are measuring electrical levels of -90 dB. One solution to overcome these limitations, and so be able to measure at higher power level than the noise, should be to change the available power set at the input of the EAM for each frequency point to

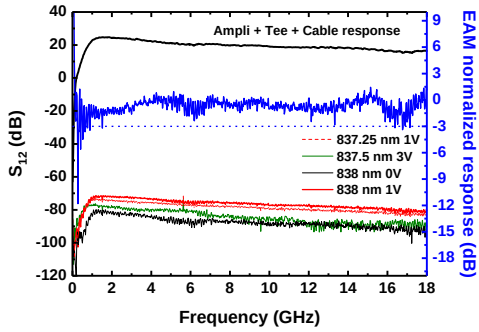

Figure 5.3: EAM response (S_{12}) measured by the VNA-based test setup.

not be limited by the electrical losses of the probe, cable and tee. Unfortunately such an option is usually not available in VNAs.

5.1.3 *RF synthesizer and spectrum analyzer*

In this subsection we present the second measurement setup we have developed, which mainly consists in replacing the VNA by an RF synthesizer (Anritsu MG 3694B) coupled with a spectrum analyzer (Fieldfox N9951 A from Keysight) at the photodiode output. This second version of the measurement bench is shown in Fig. 5.2b. The most important improvements brought by this new configuration are the nearly constant power delivered by this RF synthesizer all over the 40 GHz bandwidth as well as the pre-amplifier integrated within the spectrum analyzer which increases the electrical signal level issued by the photodiode.

Calibration

We have gained a valuable experience with previous measurements and we now know that the losses calibration is the key point of the setup. Firstly, the output power of the synthesizer, set to a value of +15 dBm, is verified by using a powermeter (Anritsu ML 2437A). This measurement value, plotted in Fig. 5.4 (black curve), presents a variation of 0.9 dB in the 1 - 40 GHz frequency range. The insertion of the bias tee and cable system lowers the available power by a maximum value of 3.5 dB in the same frequency range (blue curve). These losses have to be compensated to extract the realistic EAM response.

Preliminary results

Previous results are used to adjust the power delivered by the RF synthesizer so as to provide a constant value of +15 dBm at the input of the RF probe connected to EAM pads.

Several measurements carried on various EAM (diameters from 18 to 27 µm) devices or integrated onto VCSELs have revealed that the VCSEL cavity has no influence on

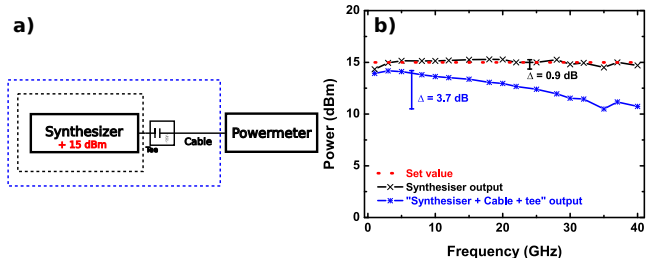

Figure 5.4: Power calibration of the RF synthetiser set to +15 dBm alone (black curve) and with the system "bias tee + cable" (blue curve).

EAM response. But whatever the tested configuration, a constant −5 dB/dec slope is still observed all over the measured frequency range.

However, since the cut-off frequency is linked to the capacitance of the device and thus to its mesa diameter, we should have observed different slopes for each tested diameter. The absence of difference clearly indicates that this observed slope cannot be attributed to the low-pass nature of EAM devices.

Microstrip line access characterization

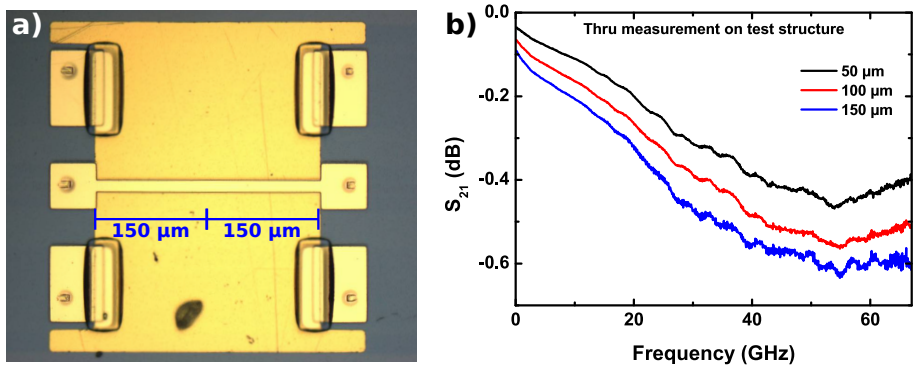

Figure 5.5: a) Top view of a thru line design to extract the losses in such access lines. b) S21 measurement of lines lengths of 50 (black) 100 (red) and 150 µm (blue)

To clarify the losses in the EAM pad and microstrip access line, we anticipated and designed a test structure on the sample and measured thru (lines) structures with different lengths, as shown in Fig. 5.5a. Results, shown in Fig. 5.5b indicate losses of -0.5 dB at 40 GHz for 100 µm access line which are very satisfaying and fit very well with the results described in the previous section. The losses due to the access line itself can not be responsible for a such drop. Furthermore, the RF probe exhibits losses of 1 dB at 40 GHz. We thus estimate the injected power in the system as described in the next part.

After this last measurement we can detail the losses in all the different parts of the system as described in Fig. 5.6.

Losses compensation

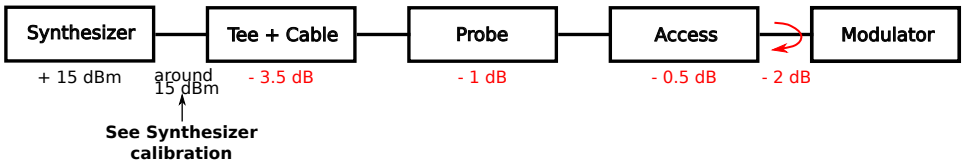

Figure 5.6: Representation of all the losses in each part of the injection system and reflection at the extremity of the modulator taken at 40 GHz and measured with a 50 Ω load

As already stated before, the EAM RF input presents a very high impedance. All the measurement chain starting from RF source up to the RF probe tips is loaded by an impedance approaching an open circuit at the lowest frequencies. This impedance decreases with increasing frequencies but still remains much larger than 50 Ω at 40 GHz. The determination of the EAM response based on the measurement of the available power cannot be satisfactory explained to be due to the frequency varying mismatch. Since the EAM is fundamentally a voltage driven device, a more natural approach is to use the applied voltage magnitude to recover its frequency response. This voltage can be assessed from the knowledge of the available power from RF source, the scattering parameters of the test setup, and the EAM impedance. This problem is illustrated in Fig.5.7. The RF source is modeled by its Thevenin generator V_g followed by a serie resistance $R_g = 50\ \Omega = R_0$. The test setup comprising the bias tee, the cable and the RF probe is depicted by the two-port network and its scattering matrix. Finally, V_L is the voltage across the input impedance of the EAM.

Figure 5.7: Schematic of the RF signal injection from RF source to EAM input.

Let Γ_L, Γ_g and Γ_{in} be the reflection coefficients displayed by the EAM, the RF source and the two-port network input, respectively.

$$\Gamma_L = \frac{Z_L - R_0}{Z_L + R_0} \tag{5.1}$$

$$\Gamma_g = \frac{R_g - R_0}{R_g + R_0} \tag{5.2}$$

$$\Gamma_{in} = S_{11} + \frac{S_{12}S_{21}\Gamma_L}{1 - S_{22}\Gamma_L} \tag{5.3}$$

The signal flow graph technique [129] is used to find the relationship between voltage V_L and V_g, using the two-port scattering parameters, Γ_L, Γ_g and Γ_{in} :

$$\mathbf{V_L} = \frac{S_{21}}{2} \cdot \frac{1+\Gamma_L}{1-\Gamma_L S_{22}} \cdot \frac{1-\Gamma_g}{1-\Gamma_g \Gamma_{in}} \cdot \mathbf{V_g} \tag{5.4}$$

V_g is deduced from the available power measured across R_0 which is also the input impedance of the powermeter:

$$P_{disp} = \frac{1}{2} \cdot \frac{|V_g|^2}{4R_0} \implies |V_g| = \sqrt{8R_0 P_{disp}} \tag{5.5}$$

In practice, the complete two-port scattering matrix cannot be measured easily because of the different nature of input (SMA cable) and output (RF probe tips) terminals of this box. So, S_{ij} parameters are extracted from SHORT or OPEN test fixtures while $S_{11} = S_{22}$ are assumed to be zero, which is not too far from reality. Using this assumption, $|V_L|$ becomes

$$|V_L| = |S_{21}| \cdot |1+\Gamma_L| \cdot \sqrt{2R_0 P_{disp}} \tag{5.6}$$

With this last equation, we are now able to link the EAM voltage to the available power measured at the RF source output. The idea is now to calculate the power we need to set so as to maintain a constant voltage at EAM pads all over the studied frequency range.

The determination of the V_g is done by measuring the voltage over R_0 which is the input load of the powermeter as described in Fig. 5.4. If we assume that the load of the synhtesizer is precisely equal to 50 Ω and constant with the frequency, likewise the R_0, then the output power of the synthesizer (P_{disp}) is expressed:

$$P_{disp} = \frac{1}{2} \cdot \frac{|V_g|^2}{4R_0} \implies |V_g| = \sqrt{2R_0 P_{disp}} \tag{5.7}$$

In practice we do not have the full parameters (module + phase) of the probe which involves an approximation that the reflection on the probe it self, and so $S_{11} = S_{22} = 0$, $|V_L|$ becomes

$$|V_L| = |S_{21}| \cdot |1+\Gamma_L| \cdot \sqrt{2R_0 P_{disp}} \tag{5.8}$$

With this last equation we are now able to predict the required power to reach a precise voltage on the pads. Four measurements are necessary to this aim:

- Calibrate the output and input of the VNA
- Measure Open and Short of the "cable + tee + probe" system with the probe on a calibration sample. In the case of a perfect impedance matching of the probe the module of open should be the opposite of the short one;
- Measure the synthesizer output in frequency for a set value (as done in Fig. 5.4 b);
- Measure the S_{22} of the "access + modulator" which will be the characterized.

To validate the formulas we compare the result from equation 5.4 (in red in Fig. 5.8) and the simulation done with Advanced Design System (ADS) while extracting the volt-

age taken at the output of the S quadripole representing our setup in Fig. 5.7 (in black-symbol in Fig. 5.8). We can notice a perfect agreement between the two approaches when we consider the probe in the system.

With the approximation done in eq. 5.8, the probe is considered perfect (without any reflection) and we obtain the result in green in Fig. 5.8 which still fit very well with the extraction results.

Finally, with the calibration of the setup with open and short measurement (shown in Fig. 5.9, we can extract the global contribution of the whole system + the EAM access line and pad. Results are shown in blue (from the open measurement) and in violet (from the short measurement) in Fig. 5.8. The average done with this calibration, in thin black, is in very good agreement with the simplified approach of Eq. 5.8 (in green). The small discrepancy comes from the losses in the probe itself.

About the open and short results, two modules are not superimposed meaning that the characteristic of the probe is not so perfect and reflections occur. To decrease the uncertainty about that we considered the average of both open and short and so do a mean of both as

$$|S_{11}| = \frac{|\text{Open}| + |\text{Short}|}{2} \tag{5.9}$$

The mean is then divided by two because losses occur both to and from the extremity of the modulator.

We can notice in Fig. 5.8 that if we set the voltage at 0.6 V at low frequency, it drops very fast when the frequency increases to 40 GHz to reach 0.25V. This is the perfect illustration of the losses in our system that have to be considered.

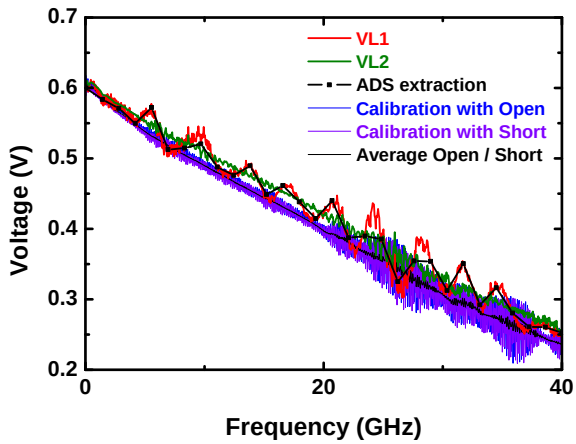

Figure 5.8: Simulation of the voltage in the plane of the probes on the pads for a constant output power of the synthesizer.

Now, we can predict the required output power of the synthesiser to be injected to maintain a constant voltage in the plane of the modulator pads. To maintain an ampli-

tude signal of 1 V at the extremity of the EAM access we calculated from eq. 5.8 the required P_{disp}. Result is shown in red Fig. 5.9 b). We can see that if at 1 GHz 11.2 dBm are necessary, this value increases to 14.1 dBm at 10 GHz, then 16.8 and 19.9 at respectively 20 and 30 GHz. To validate the average done previously, we plotted in black and blue respectively the extraction results from the Open and Short measurements.

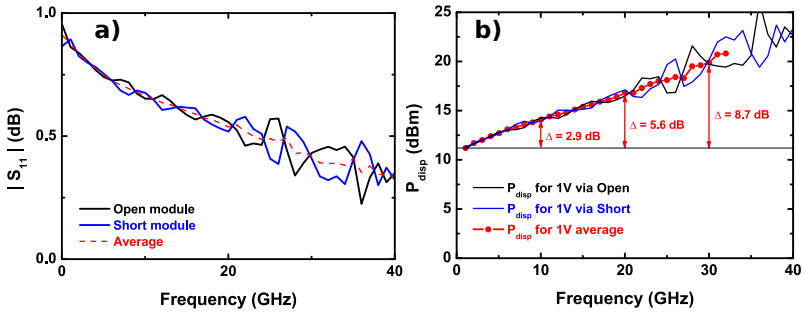

Figure 5.9: Measurement of the open and short modules of our system after calibration of the VNA output and input a). Injected power to achieve a constant voltage on the modulator pads b)

We have seen in this section the measurement of the EAM while considering a constant voltage on the modulator pads and how the P_{disp} has to be implemented at each frequency. This will be done for next measurements. It is now important to remove another unknown contribution, the pads themself and the reflection at the extremity of the modulator.

5.1.4 *De-embedding*

This de-embedding is crucial to remove all the uncertainties and extract the precise value of the electro-optic response of the EAM. Here the de-embedding is realized manually by measuring the S_{11} of the EAM and the thru test devices. In commercial devices, these values are well known and the electronics driver controls the applied power to do the same job than us when we modify manually the P_{disp} for each frequency.

We have already seen in Fig. 5.5b the measurement of thru lines for the three lengths after the calibration in the probe plane. We also measured open and short structure. Now, it is necessary to measure the S_{11} of the "access + modulator" system to extract the pad and line parasitics, shown respectively in green and orange in Fig. 5.17.

The EAM is embedded in a 50 to 150 µm microstrip line terminated by the three coplanar pads. To de-embedd pads and line contribution, two lines displaying the same geometrical characteristics but of different length are processed on the same wafer. Pads

and lines are recovered using the method described in part 4.2.1.2. Defining $\mathbf{T}$ the chain matrix of pads $\mathbf{T_A}$ followed by access transmission line $\mathbf{T_l}$,

$$\mathbf{T} = \mathbf{T_A}\mathbf{T_l} = \begin{pmatrix} t_{11} & t_{12} \\ t_{21} & t_{22} \end{pmatrix} \tag{5.10}$$

modulator impedance Z_{mod} is deduced from measured impedance Z_{meas} by using the following equation:

$$Z_{mod} = \frac{t_{22}Z_{meas} - t_{12}}{t_{11} - t_{21}Z_{meas}} \tag{5.11}$$

5.1.5 *Photodiode calibration*

We have seen previously how to consider all the losses in the system "Tee - cable - probe" and then "access + modulator". The last thing to take into account in the electro-optic setup is the photodiode frequency response at 850 nm. In the previous measurement we considered the supplier data sheet at 1550 nm however an essential question remains, is the response the same at 1550 nm than at 850 nm ? To clarify it, we measured it by an heterodyne beat technique [130], and built a setup with two lasers, one at a fixed wavelegnth, regulated in temperature and the other one a tunable laser source. The wavelength splitting between both lines can be easily linked to frequency with

$$\nu \cdot \lambda = c \text{ and by carring out the differentiation as } \Delta\nu = \frac{c}{\lambda^2} \cdot \Delta\lambda \tag{5.12}$$

with ν the frequency, c the speed of light and λ the wavelength.

We thus have for example 125 MHz and 10.0 GHz at 1550 nm corresponding to a splitting wavelength of 1 pm and 80 pm.

5.1.5.1 *At 1550 nm*

At 1550 nm we used an InGaAs DFB at 1537.2 nm driven by an IXL Ligthwave LDC-3722 B at 22.9 °C biased at 70.1 mA to deliver -3 dBm in the photodiode under test. The used tunable laser is a Santec TSL-510 and is connected to the photodiode through a polarization maintaining coupler.

The wavelength range of the TLS is 1537.25 nm to 1537.55 nm with 31 steps. The photodiode response is sent in a Rohde & Schwarz spectrum analyzer with bandwidth of 20 Hz to 40 GHz. The resolution bandwidth is set at 1.10^8 and the video bandwidth, which is inversely proportional to the integration time, 5.10^5. For each wavelength we acquired 10 spectra and do an average to decrease the uncertainty due to the vibration or air flow in the room. The global acquisition measurement is presented in Fig. 5.10 a),

we then extract all the maximum values (blue circles in Fig. 5.10 b)) and do an average (red).

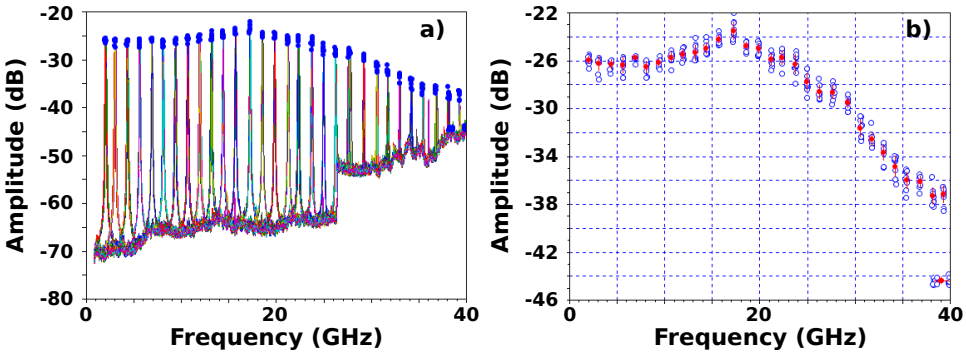

Figure 5.10: Extraction of the photodiode frequency response at 1550 nm. a) All spectrum are ploted and maximum noted in blue, b) average of these maximum and plot in red.

We now have the electro-optic response of the photodiode at 1550 nm + the cable and the tee. Indeed, we decided to keep our tee to be in the same configuration as for the EAM measurement and so to be able to substract the whole contribution "cable + tee" that we already measured in Fig. 5.4. After substracting this contribution we obtain the result plotted with a broad blue line in Fig. 5.11. We positively found the same response as the supplier one (thin blue line), demonstrating the relevance of our setup to measure the photodiode frequency response.

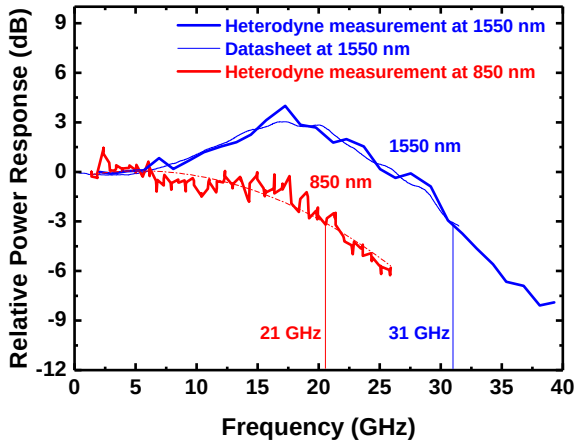

Figure 5.11: Chracterization of the InGaAs photodiode used for the electro-optical characterization of the EAM. Thin and broad blue lines are respectively the supplier data and our characterization at 1550 nm. The red curve is obtained at 850 nm.

5.1.5.2 *At 850 nm*

For the characterization of the PD around 850 nm, the fixed wavelength laser is a homemade laser formed with a LED and a Cavity Resonator Integrated Grating Filter (CRIGF) [131] which filters a precise wavelength, here 854 nm. The Laser Diode is biased at 52 mA, 1.7 V and is maintained at 20 °C to maintain single mode operation. The other tunable laser is a Vantage TLB7100 from Newfocus.

Here, to sweep the frequency we modified the voltage on the piezo membrane in the Labview program. The same characterization as the previously done at 1550 nm results in the red curve in Fig. 5.11. The photodiode is a RC circuit and so behaves like a low-pass filter. Its response can thus be fitted with a second order polynomial:

$$R_{photodiode} = -0.3271 + 0.1453 \cdot f - 0.0136 \cdot f^2 \tag{5.13}$$

As we can see, the photodiode response at 850 nm is really different from the one at 1550nm. The cutoff frequency is reduced from 31 GHz to 21 GHz and there is no gain at 18 GHz as for 1550 nm. This new photodiode characteristics is then used to have a more precise measurement of the modulator cut-off frequency.

5.1.6 *Results*

We show in Fig. 5.12 the EAM device response with a constant P_{disp}, as seen in Fig. 5.9, in the pad plane with the photodiode response at 1550 nm (blue) and 850 nm (red).

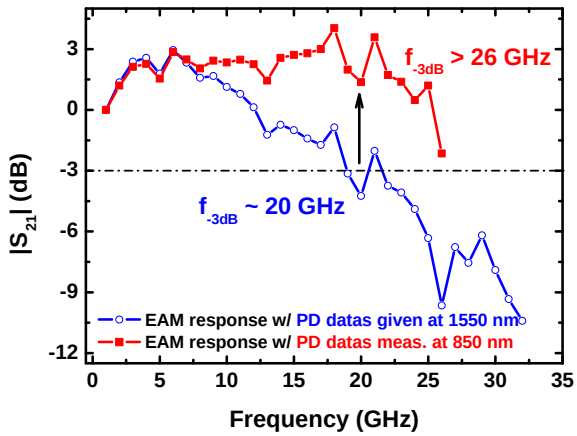

Figure 5.12: High frequency characterization of the 27 µm-EAM, cut access of 50µm, with the photodiode response given by the supplier at 1550 nm (in blue) and with the extraction of our measurements at 850 nm (red)

We have, in this measurement, only considered a constant voltage on the pads plane. However, due to the divided current bridge, we have over-estimated the applied voltage

at high frequency as shown in subsection 5.1.4. Furthermore, we only measured here the larger mesa (27 μm), the measurement of the smaller one (18 μm) will increase this cut-off frequency.

To conclude this section, we have seen how difficult is the measurement and the extraction of the S_{21} parameter for the electro-optic characterization of the EAM. Indeed, the high impedance of the modulator requires substantial voltage to be delivred. Furthermore, the injection system losses upstream of the modulator have to be estimated and compensated to apply a constant voltage at the extremity of the modulator and thus extract the cut-off frequency of the device itself. We first optimized the optical alignement of the fiber on the EAM. Secondly we tried to measure the EAM response with a VNA but preferred, with the material at our disposal at this moment, the solution of the synthesizer and a spectrum analyser for the high electrical bandwidth and the possibility to increase the output power to compensate the losses. Then we set a constant voltage in the pads plane and measured a f-3dB higher than 25 GHz for the larger diameter EAM. However the applied voltage was over-estimated but measured on a 27 μm mesa diameter. We will see in the next section the measurement improvements thanks to higher bandwidth of the equipments.

5.2 HIGH-FREQUENCY CHARACTERIZATION OF EAM AND EAM-VCSEL — NEW PHOTODIODE

In this section we present the very last results obtained with high bandwidth GaAs photodiode loan by TU Berlin (a NewFocus 1434) and an appropriate electrical amplifier (+12 dBm from 30 kHz to 45 GHz). With this new equipment we are able to measure the EAM response to higher frequency since the measured cut-off frequency at 980 nm for the Newfocus PD is 25 GHz and the responsivity is improved compared to the previous one. We first present the results obtained with the synthesiser as described previously for the EAM characterization. Then, we carry out, thanks to the +12 dBm amplifier connected at the output of the photodiode, the same measurement with the VNA. Furthermore, based on the S_{11} measurement and with the extraction method developed for the BCB permittivity it is also possible to extract the pad impedance, the matrix parameters corresponding to the line and the modulator impedance. From the modulator impedance we developped a new equivalent circuit for which we are able to extract the resistance and capacitance of each section of the device. Then, we are able to simulate the electrical response of the EAM as a function of its diameter. Finally, encouraged by the success of the VNA measurement, we measured the response of a EAM integrated onto the VCSEL and demonstrated the high-frequency operation of the device.

5.2.1 *Newfocus photodiode response*

As described above, we also characterized the Newfocus photodiode by a heterodyne beat measurement at 850 nm to compare with the data obtained by TUB at 980 nm by using a time-domain measurement technique [132]. We used the same optical and electrical material than previously. We acquired two set of values with the Rodhe & Schwarz analyzer that we compared with the FielFox analyzer to improve the accuracy of the measurement. Results are presented in Fig. 5.13.

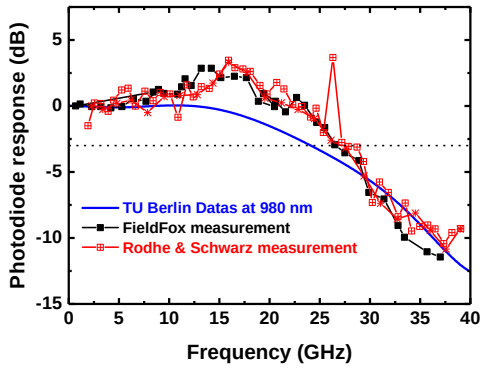

Figure 5.13: Characterization of the InGaAs Newport 1434 photodiode with data given by TUB at 980 nm (blue) and our heterodyne measurement at 850 nm (red and black)

We obtained more or less the same response shape with the same -3 dB cut-off frequency (27 GHz). Differences come from the +3dB gain observed between 15 and 18 GHz and the slope which seems to be more abrupt at 850 nm than at 980 nm.

For the next sections we used the data given by TUB to improve the measurement precision of the modulator response.

5.2.2 *Characterization with the synthesiser set up*

We describe in this section the EAM response with a constant applied voltage on the pads. Compared to previous measurements we calibrated the synthesiser output in all the frequency range and at all the output power levels to have a better control of the injected power.

All the measurements described here were realized with a 838 nm illumination wavelength, 3 V bias and a modulation voltage of 0.7 V on the pads. Since the measurement is integrated during few minutes, we check after the last step that the optical fiber did not move by measuring again the level of the first point that we positively found to be the same.

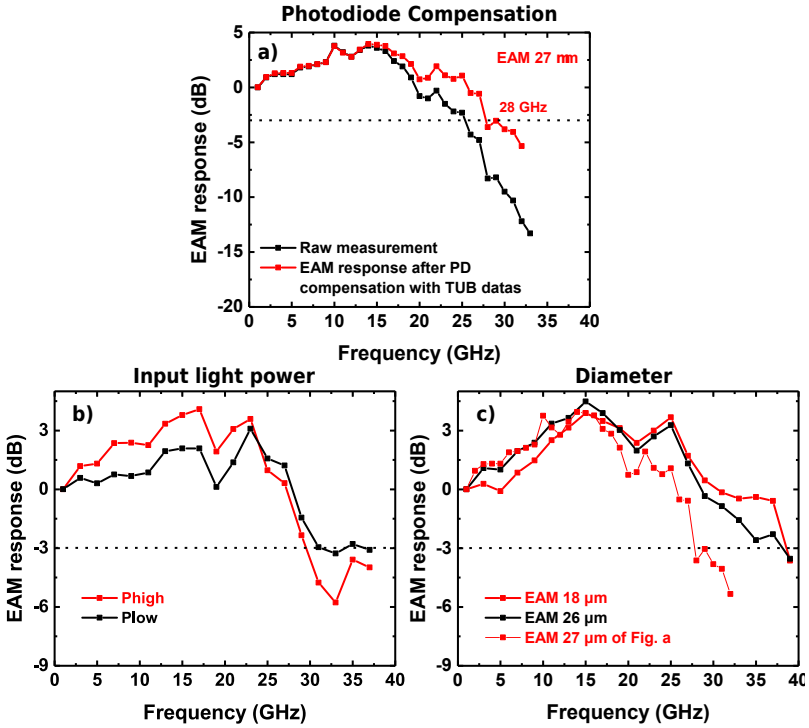

Figure 5.14: EAM responses measured with the synthesiser and the high speed photodiode. a) before and after the PD compensation. b) for two injected light power. c) different diameters

The substraction of the photodiode response influence can be seen in Fig. 5.14 a). An optical bandwidth of 28 GHz is measured for EAM mesa of 27 µm. This characteristic is also measured regardless of the injected light power (Fig. 5.14 b)). Indeed, the shape of the graph is the same considering the possible error measurements. Indubitably, with lower injected power the reflected power is lower and so is the output signal of the photodiode (around 4 - 5 dB) but here we normalized the response for clarity reasons.

About the diameter influence (Fig. 5.14 c)) we also positively found the same shape of the EAM responses. However, here the bandwidth seems to be higher than the previous measurements which can be explained by a better electrical injection in the devices.

We have undeniably measured, thanks to the synthesiser associated to the spectrum analyser and the fast photodiode, an optical modulation bandwidth of the EAM higher than 28 GHz.

5.2.3 *Characterization with the VNA set up*

Thanks to the high gain amplifier working up to 45 GHz we are able to go beyond the limitations described in 5.1.2 and so use the VNA as source. In this section we will strive to focus on the VNA measurement by comparing both methods and measuring parameters as previously: the mesa diameters influence and the injected light power but also the temperature and the applied voltage consequences.

5.2.4 *Comparaison VNA - synthesiser*

To validate the established method with the synthesiser and the VNA we compare the EAM response using both equipments. About the VNA measurement it is necessary to do a calibration of the injection circuit. Indeed, we first calibrated the input with the amplifier with a thru connector and then the VNA output with the tee, cable and probe on a Cascade calibration kit. We thus have a calibrated system up to the probe.

We then measured three EAMs of 18 µm, 23 µm and 26 µm diameters. Results are plotted in Fig. 5.15. Thick lines correspond to the synthesiser and spectrum analyser measurements, noisy lines to the VNA. We fitted this last measurement with a polynomial fit (thin lines).

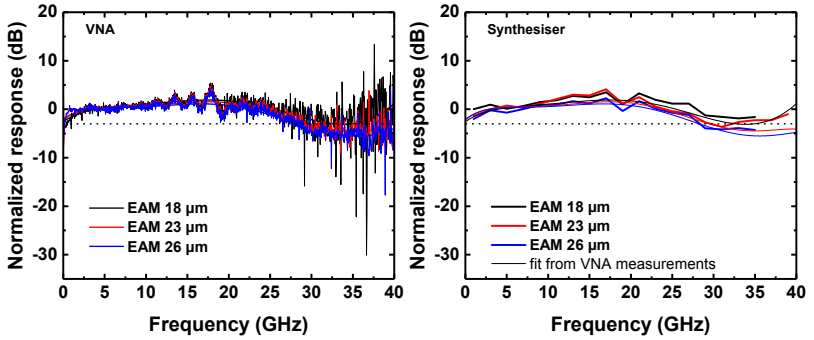

Figure 5.15: Comparaison of electro-optic characterization with a VNA (left) and with a synthesiser (right). For a better comparison, fits of the VNA measurements are also plotted with the synthesiser results.

We observe the same response for both measurement methods except increased noise in the case of VNA. Peak and valley, due to the impedance mismatch, are located at the same frequency, at the measurement accuracy since with the synthesiser we measured the EAM response every 1 GHz. Indeed, we find a peak after 13 GHz and 17.5 GHz and a valley at 19 GHz. About, the cut-off frequency, we normalized the response to have a plateau around 2 - 5 GHz. The cut-off frequency is found at lower frequency with the VNA than the synthesiser which can be explained by the over estimated losses with this

system. Indeed, as described in 5.1.4, the impedance of the modulator is lower than the "pad - line - modulator" so when we apply a constant voltage on the pad plane we over estimate the losses in this system.

Anyway, the bandwidth measured here is 28.3 GHz, 29.7 GHz and 32.4 GHz respectively for 26, 23 and 18 μm.

5.2.5 *Study with several parameters*

Buoyed by the confidence of the VNA measurement with the amplifier we move forward in the electro-optic characterization of the modulator and we studied the influence of the mesa diameter, the temperature, the applied voltage and the injected light power on the EAM response.

Before studying all these parameters we also checked the linear behavior of the component. Indeed, if we apply + 4 dBm at the output of the VNA, we have exactly the same response than for -5 or 0 dBm.

In the next two subsections we worked on the sample B (doped DBR), then with the modulator integrated onto the VCSEL (sample E).

5.2.5.1 *EAM mesa diameter*

We already answered this question in the previous subsection and demonstrated a higher frequency by 4 GHz namely 28.3 GHz to 32.4 GHz when the diameter is decreased from 26 to 18 μm. Unfortunatelly, the very low output signal of the photodiode complicates the precise extraction of the cut-off frequency as a function of the different diameters.

5.2.5.2 *Chuck temperature influence on integrated EAM*

The temperature is an important parameter in this device since, once integrated on the VCSEL, the EAM will be subject to high temperature around 60 - 70 °C. It is thus very important to check its good operation at such temperatures.

To this objective we measured the response of a 27 μm-mesa EAM integrated onto a VCSEL. Results are shown in Fig. 5.16 a).

Of course the temperature increase will affect the modulation properties (position of the excitonic peak, modulation depth, contrast ratio) of the device as described earlier in Chapter 3 but on an electro-optical point of view at high-frequency, its response remains the same.

5.2.5.3 *Illumination wavelength for integrated EAM*

Still integrated on the VCSEL we also measured the high frequency response of a 18 µm - EAM for different illumination wavelengths. We can see in Fig. 5.16 b) that the response is once again identical even if the output level is modified since it depends on the reflectivity spectrum of the modulator which absorbs more or less at certain wavelengths as seen in the inset. The amplitude minimum is found around 865 nm which corresponds to the FP resonance wavelength of the EAM.

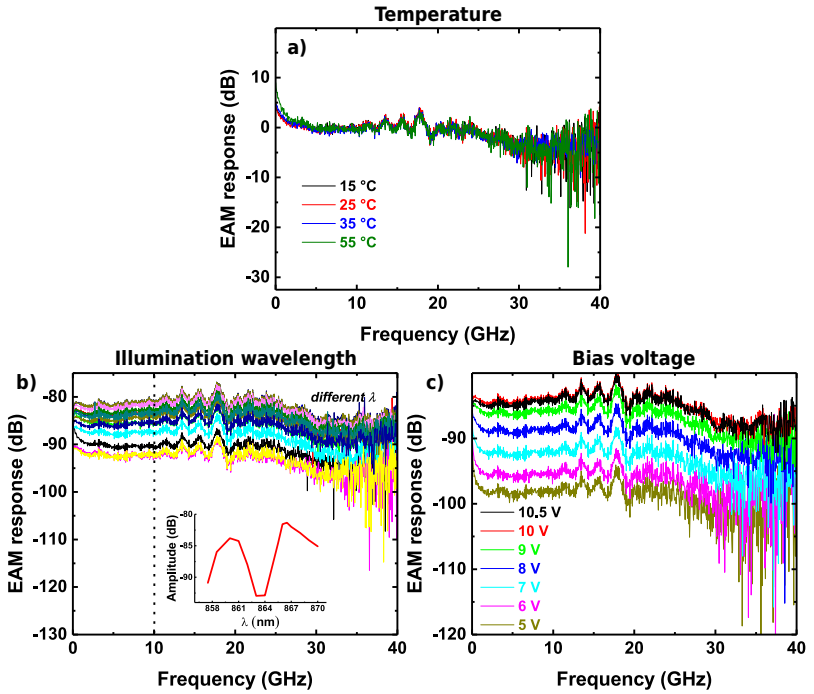

Figure 5.16: EAM (sample E) response under different temperatures (a), illumination wavelengths from 858 nm to 870 nm (b) as seen inset where the extraction of the output power of the photodiode at 10 GHz is plotted ; and for different applied votlages (c).

We can imagine, in a case of a less noisy measurement, to reproduce the reflectivity spectrum of the modulator from this kind of measurement.

5.2.5.4 *DC bias of the integrated EAM*

On the same EAM diameter, always integrated on the VCSEL, we also compared the electro-optic response at 865.5 nm under different DC bias voltages. As we can see in Fig. 5.16 c) that the shape is one more time identical. In this measurement we also see the modulation phenomena which increases when the bias increases up to 10V and then, as in static, the output signal decreases.

5.2.6 *Impedance extraction*

We have seen previously that the temperature, the applied voltage and the amplitude of the modulated signal does not affect the frequency response of the modulator. However, despite the noise measurement, it seems that the mesa diameter plays an important role at high frequency, as it can be expected. It is now important, based on earlier studies on the pad and line de-embedding, to extract the impedance of the modulator and have an electrical equivalent circuit to predict the behavior of smaller devices.

5.2.6.1 *Equivalent circuit*

The de-embedding method has been described in Section 5.1.4, which allows now to extract the equivalent circuit of the global device "pad - line -EAM" and more precisely the Real and Imaginary part of the EAM impedance magnitude.

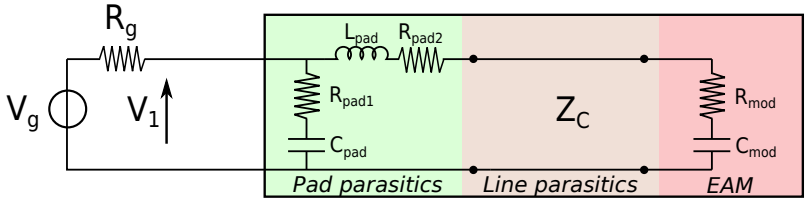

Figure 5.17: Microstrip line access for EAM-VCSEL device.

The EAM, due to the active region of 485 nm acts like a capacitance at low frequency. Its impedance is thus more significant for smaller diameter as seen in Fig. 5.18. At high frequency, the impedance of both diameter tends to getting closer which corresponds to a modification of the electrical behavior of the EAM. It can now be considered as a resistance in serie with a capacitance more than a single capacitance.

We can notice after the de-embedding, that the impedance of the EAM alone is higher than the global circuit. Indeed, the presence of the pad and the line between the probe extremity and the modulator itself considerably decreases the efficiency of the electrical injection in the device. The difference between with and without de-embedding is furthermore significant when the diameter is smaller (hierh impedance) since the pad and line contribution is more important. This clearly demonstrates the de-embedding requirement to know precisely the electrical behavior of the EAM.

By extracting the real and imaginary part of the impedance we plot in Fig. 5.19 the resistance (R_{mod}) and capacitance (C_{mod}) of the EAM according to the equivalent circuit in Fig. 5.17. As expected the capacitance of the smaller mesa is lower than the larger one. Respectively 51.6 fF and 33.4 fF at 10 Ghz, meaning a ratio of 1.55 between both. Surprisingly, it is more or less constant in the 0-40 GHz range contrary to the 25 µm-device. Resistances are also getting closer when frequency increases.

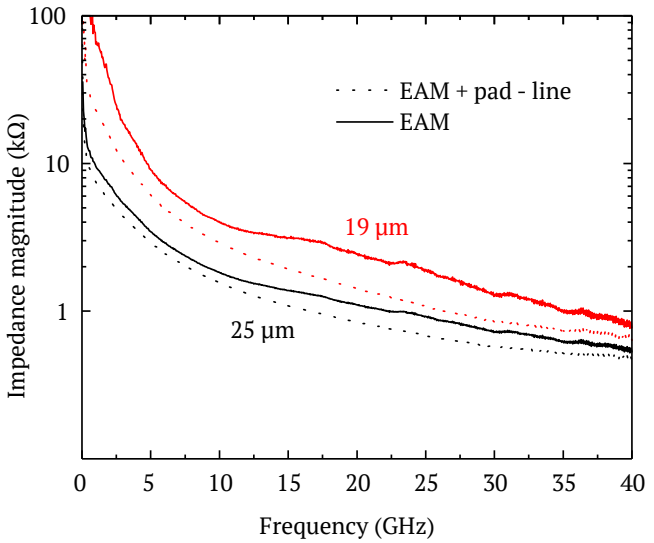

Figure 5.18: Impedance of 19 µm (red) and 25 µm (black) EAM (thin lines) and "EAM + pad + line" (dashed lines) extracted from the S_{11} parameter.

5.2.6.2 *EAM modelling*

We have seen in Fig. 5.17 the schematic of the injection circuit from the probe to the modulator. Now, we focus on the right section, about the EAM alone device. After the de-embedding, the losses assigned to the pad and the line are substracted and we extract the Magnitude and Phase of the EAM from the S_{11} measurement.

From the real and imaginary part of the EAM impedance we notice that at low frequency the component behaves like a capacitance of low value while at high frequency it behaves like a low resistance which corresponds to the serie resistance R_S.

We modelled the EAM with three distinct element regions as described in Fig. 5.20. Up to the dashed line, on the left, we already de-embedded the line losses with the scattering matrix.

Between the mesa sidewalls and this dashed line, a small volume of BCB is not yet considered. We thus have a first capacitance, called C_{BCB1}, between the metal mid-contact and the metal top contact, corresponding to a BCB thickness of 2.4 µm. This area remains constant and the capacitance is estimated to be 1.9 fF.

In parallel we have another capacitance between the highly P-doped contact layer and the top metal contact leadding to a 3 µm-thick BCB layer. As the top metal contact dimension remains identical whatever the EAM diameters, the area between the mid-contact metal and the mesa edge is reduced when the mesa diameter increases. We called this second capacitance C_{BCB2} which varies from 4.7 fF (⌀ of 18 µm) to 2.85 fF (⌀ of 25 µm).

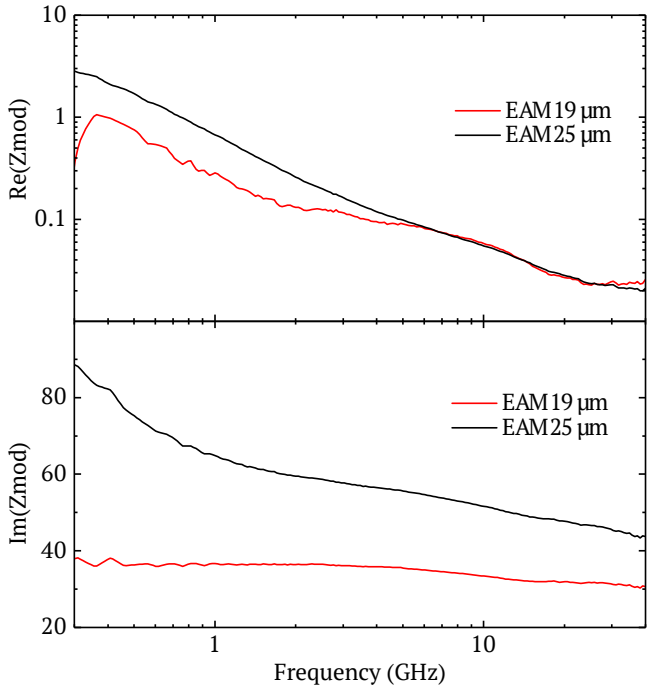

Figure 5.19: Resistance and capacitance of 19 µm (red) and 25 µm (black) EAM.

Then, we have a series resistance which corresponds to the electrical contact in series with two parallel RC blocks. One for the DBR regions and the other one for the cavity. The influence of both N and P-mirrors are gathered in this R/C branch.

We present in Fig. 5.21 the modulator resistance and capacitance extracted from this equivalent circuit. Thick lines are the extracted values after de-embedding and thin lines the extraction from our model.

The different values for the resistances and capacitances elements are summarized in Table 5.1:

EAM	C_{BCB2} (fF)	R_s (Ω)	R_{DBR} (Ω)	C_{DBR} (fF)	R_{cav} (Ω)	C_{cav} (fF)
18	4.7	47.8	114	140	131,000	28.5
19	4.5	36.1	114.4	150	125,070	30.3
20	4.2	33.3	126.4	150.5	26,500	34.2
21	4.0	31	102.4	159.3	65,0000	37
22	3.7	32	132.4	150.3	10,100	40.4
23	3.4	27.5	114.4	185.3	12,400	46.4
24	3.1	25.5	107	185	11,300	49.4
25	2.8	23.5	90.4	200	10,040	53.9

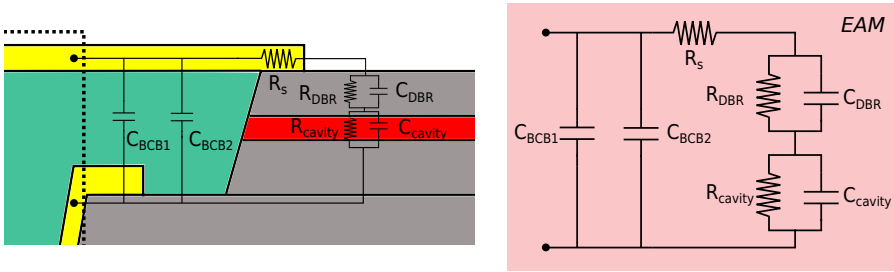

Figure 5.20: Equivalent circuit of the EAM from the end of the line de-embedding to cavity.

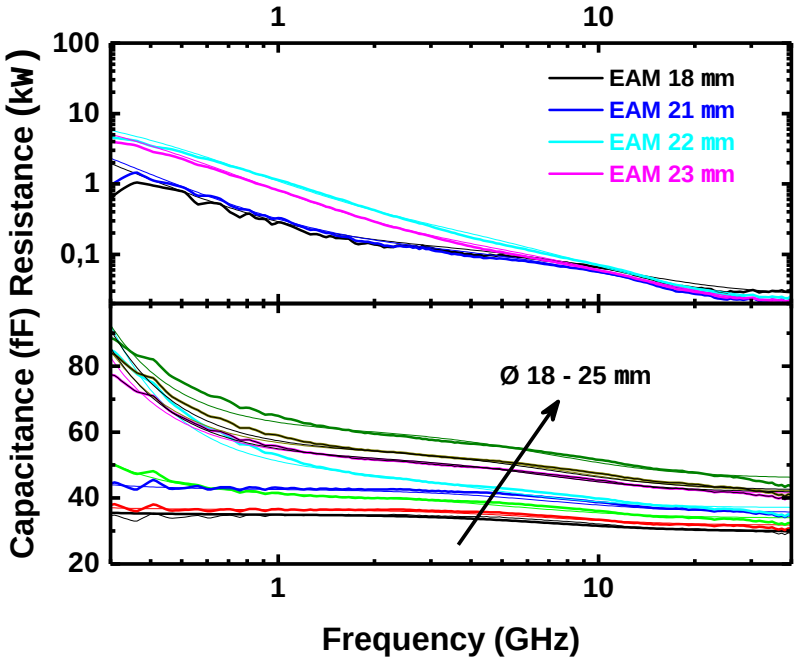

Figure 5.21: Real and Imaginary part of the EAM impedance fitted with our double R//C model.

Table 5.1: Extracted R and C parameters from the equivalent model for the EAM structure.

It is also possible to have a fit of the S_{11} measurement with amplitude and phase simulations as presented in Fig. 5.22.

We can observe a good agreement of our model for the S11 up to 10 GHz and up to 25 GHz for the phase due to the distributed phenomena of the capacitance that have not been considered here.

We summarized all the parameters in Fig. 5.24 where we can see the evolution function of the diameter

The serie resistance decreases from 47.8 Ω (⌀ of 18 µm) to 23.5 Ω (⌀ of 25 µm) which can be linked to the increase of surface and thus a decrease of $\rho l/S$.

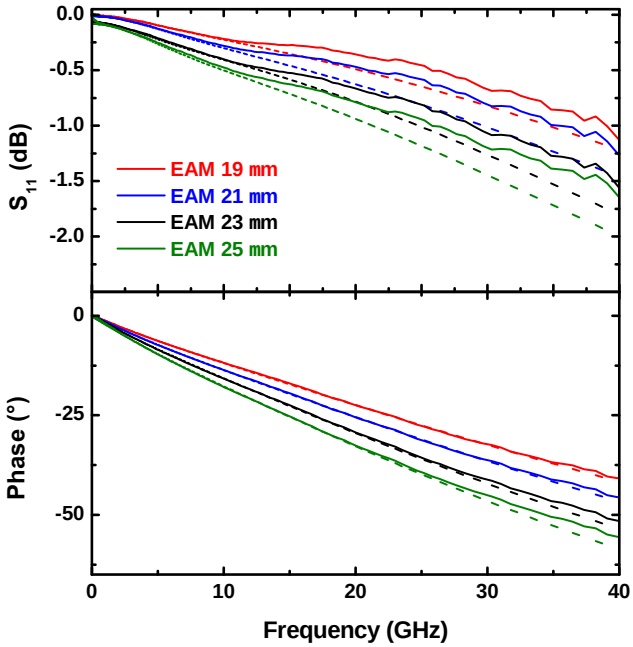

Figure 5.22: S11 and Phase of the EAM impedance fitted with our double R//C model.

About the DBR, resistance is more or less constant around 120 Ω. Its capacitance is, as expected, increased when the diameter increases and a polynomial fit can be done (thin red line).

About the cavity, the capacitance is closely linked to the mesa diameter and can be also fitted by a second order polynom (thin blue line). Its resistance decreases very fast by a factor of 13 between small diameters and larger one.

At this stage it is not yet possible to determine precisely the impact of each DBR and extract their resistance and capacitance. However, we can estimate the resistance of each DBR around R_{DBR} / 2 = 60 Ω and their capacitance around C_{DBR} * 2.

Our model is in very good agreement in the frequency range 1 - 10 GHz for the real part and up to 25 GHz for the imaginary part. For higher frequencies it seems that the distributed capacitance phenomenon is increased and affects the extraction of the real part. Indeed, we do not considered the capacitance between the mid-contact and the top DBR, throw the BCB, neither the capacitance between the top metal contact and bottom DBR. Furthermore, due to the process uncertainty, it is possible that the RF injection is not homogenous on all the top contact ring. This electrod model could have been improved with separated measurement.

The de-embedding realized previously has been done from lines of 300 µm and 1000µm length. Using both lines of 300 µm and 700 µm for the extraction method gives an excellent agreement for the actual Amplitude and Phase extraction.

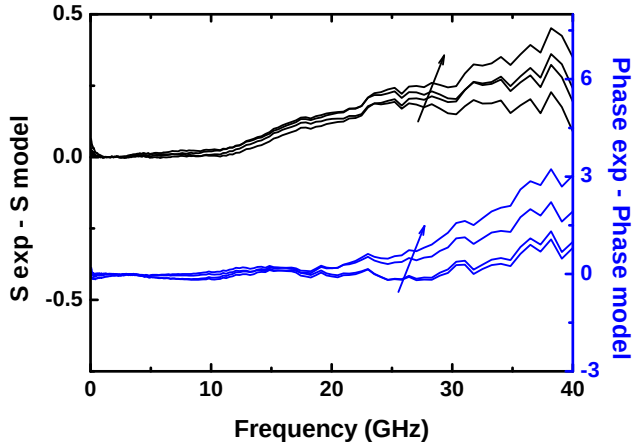

Figure 5.23: Discrepancy between our experimental datas and simulations of the S11 (black) and Phase (blue) for diameters of 19, 21, 23 and 23 µm. The arrows indicate the diameter increase.

If we stricly consider this equivalent model it is possible to simulate the transfert function of the equivalent circuit. With ADS we thus added a voltage source and measured at the terminal of the cavity the output voltage. Results are shown in Fig. 5.25 for diameters of 18 µm (black) and 25 µm (green) where we can see a cut-off frequency at respectively 75 GHz and 85 GHz. By extrapolating the parameters as C_{BCB2} = 6.1 fF, R_s = 44.5 Ω , C_{DBR} = 120 fF and C_{cav} = 18 fF, while maintaning R_{cav} at 10 kΩ and R_{DBR} at 114 Ω we can estimate the electrical response of a 10 µm-EAM (orange) as shown in orange which demonstrates a cut-off frequency higher than 160 GHz.

A better reproducibility on the fabrication process and more precisely the electrical contact fabrication would have give us a better understanding of the electrical model of the EAM. However we demonstrated a suitable model to understand the electrical losses and parasitics capacitance of the device.

We demonstrated previously a cut-off frequency variation of only 4 GHz between 18 µm (32 GHz) and 26 µm (28 GHz). Even if the simulation is clearly optimistic without the consideration of the other capacitance effects, we can gain a factor two on the cut-off frequency by decreasing the diameter up to 10 µm, meaning a 60 GHz bandwidth without any improvements on the fabrication process or the device design. However this scaling would of course make the process more complicated for the top contact alignement but feasible with the actual equipments.

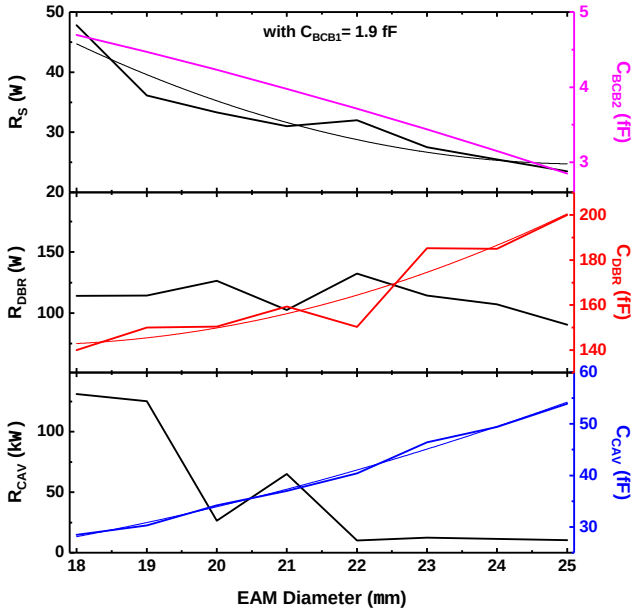

Figure 5.24: R and C values function of the EAM diameter

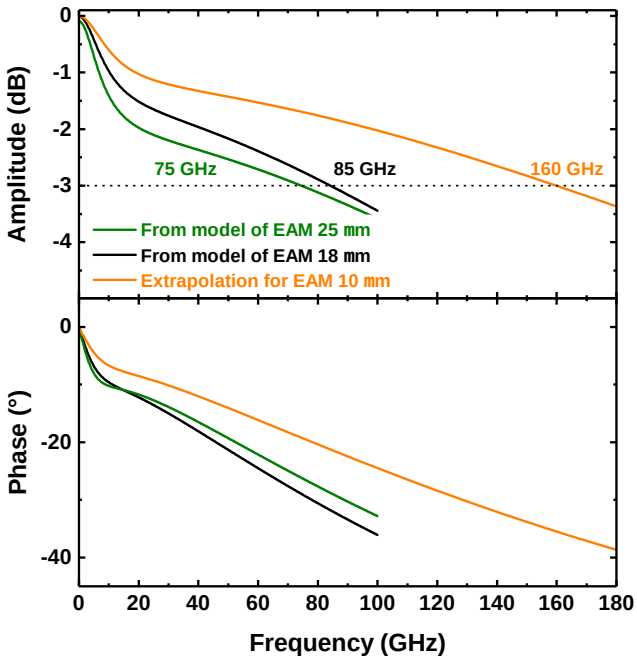

Figure 5.25: Transfert functions calculated from our electrical model for 18 µm (black) and 25 µm (green). In orange is represented the extrapolation for a 10 µm-EAM.

5.2.7 *EAM-VCSEL*

Once the experimental setup for the high frequency characterization of the EAM stand-alone is validated and well known it is possible to move forward to the EAM-VCSEL

characterization. We present in this subsection the results on a 71 µm VCSEL and 24 µm EAM by varying the VCSEL drive current (Fig. 5.26) or the EAM applied voltage (Fig. 5.27).

First, based on the static characterizations of the sample E, we applied 8 V on the EAM pad and we measured the electro-optic response of the device above threshold at 2.5 mA, 2.7 mA and 2.9 mA. The increase for 2.5 mA is an artefact and cannot be linked to physical phenomenon.

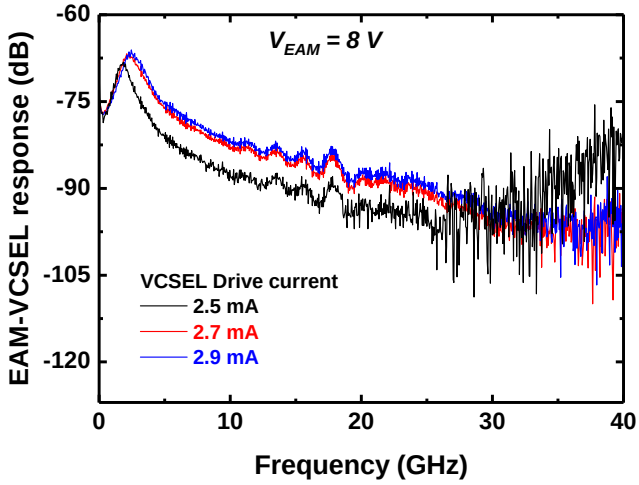

Figure 5.26: Electro-optic characterization of the EAM-VCSEL. EAM bias of 8 V and VCSEL powered at 2.5, 2.7 and 2.9 mA.

Then, for a 2.9 mA VCSEL drive current, we measured the response for different EAM applied voltages. As already shown in Fig. 5.16 b), the output modulated signal increases when the bias voltage is increased.

We observe for all the couples (current, voltage) a peak a low frequency and then a slope up to 20 GHz and then a more abrupt slope. This behavior was not observed on EAM alone. When increasing the bias, this peak goes to a minimum frequency at 2.5 GHz while decreasing in intensity, until it vanishes for a bias of 8.5 V, for which the frequency response is flat up to 20 GHz. For higher values of the bias, the resonance peak arises again, and its frequency increase again towards the same frequency than at low bias. This evolution has been explained by Yakimov et al. [87] as an additional modulation of the mirror reflectivity thus impacting on the photon density in the laser cavity, giving rise to a relaxation frequency resonance.

At 8.5 V and 2.9 mA (red curve) we have exactly the same electro-optic response than for the EAM stand-alone. If we extract and plot this precise response we can see in Fig. 5.28 a plateau then the typical slope of the EAM response. Here, the cut-off frequency of the device is 29 GHz as shown previously.

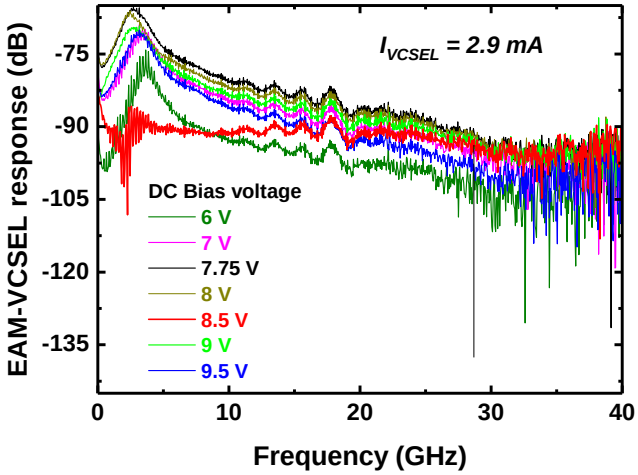

Figure 5.27: Electro-optic characterization of the EAM-VCSEL. VCSEL powered at 2.9 mA and EAM at 8.5 V.

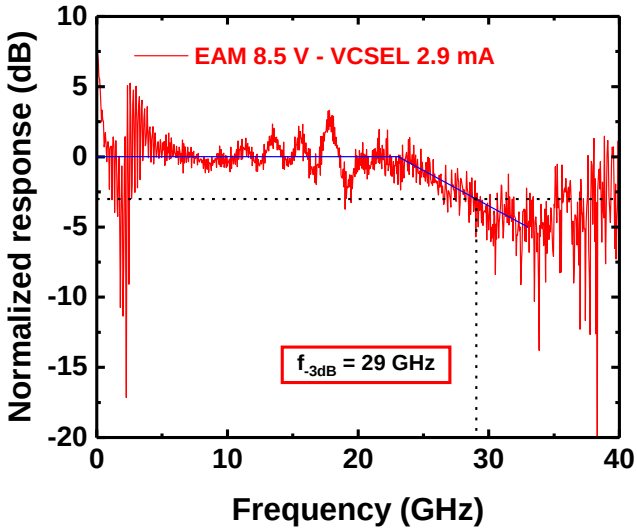

Figure 5.28: Electro-optic characterization of the EAM-VCSEL. VCSEL powered at 2.9 mA and different EAM bias voltages.

This result is the best ever achieved modulation bandwidth for a EAM-VCSEL compared to the last record by Van Eisden at 20 GHz. It can be faced to the actual reccord of Chalmers of 30 GHz for a single VCSEL modulation. We of course still have to understand the behavior for other (current, voltage) operation and improvement about the design are obviously still possible to enhance the bandwidth and output power.

5.3 CONCLUSION AND POSSIBLE IMPROVEMENTS

In conclusion, we have demonstrated in this chapter the feasability of the vertical integration of an electro-absorption modulator onto a VCSEL for high-speed operation.

First, we built an electro-optical setup for the high-frequency characterization of the stand-alone EAM and of the EAM-VCSEL. At an initial stage, we worked with a synthesiser and a spectrum analyser to apply a constant voltage in the pad plane. Indeed, due to the significant losses in the bias tee, cable and probe, no measurements were possible at high frequency with the VNA. Especially as the EAM, measured with a power amplifier, seemed to have a cut-off frequency higher than the PA bandwidth (18 GHz in our case). In the second phase, thanks to the high speed photodiode and amplifier loan by TUB, we were able to measure the electro-optic response of the EAM. We positively found the same EAM response with the VNA and the synthesiser which demonstrate the efficiency of both setups. We demonstrated a bandwidth of 28 GHz and 32 GHz for respectively 26 μm and 18 μm diameter of EAM mesa. This bandwidth and the frequency response shape in the studied ranges are not influenced by the bias voltage, neither by the temperature nor by the illumination wavelength which makes the EAM device really competitive for data communications.

The reflection coefficient measurement, combined with the method developed for the de-embedding, makes possible the extraction of the EAM impedance itself. Based on this de-embedding procedure we schematized the component with three blocks corresponding to the BCB area close to the mesa sidewalls, the DBRs, and the cavity. We fitted the experimental datas with our model and obtained a very good agreement for the real part up to 10 GHz and for the imaginary part up to 25 GHz. We are then able to extract the different parameters values as a function of the diameter of the device. The model, even if it is clearly optimistic, gives an excellent idea of the scaling required to improve significantly the bandwidth. Actually, a shrinkage of the diameter from 18 μm to 10 μm would increase the bandwidth by a factor 2. We might expect to reach, with the same electrical and optical design, a bandwidth of 60 GHz. Of course, optical design improvements and process fabrication modifications, such as top metal contact, will increase once again the bandwidth of the device. All these improvements will be discussed in the Section 6.3.

Finally, we measured the electro-optic response of an EAM-VCSEL. Despite measurement issues, we have clearly identified the influence of the VCSEL drive current and the EAM bias voltage. For a given couple of parameters, 2.9 mA and 8.5 V, we demonstrated the same frequency response than for the stand-alone EAM with a cut-off frequency of 29 GHz. This last result, considering the previous ones on EAM, in addition with the low chirp (< 0.1 nm) and the obtained modulation depth confirms the potential of the

EAM-VCSEL to substitute VCSEL direct modulation for high-speed communications.

To go further in this high-speed operation, optimization can be realized both on the device design and on the process fabrication. First, we have to work with graded-interface DBR to decrease the resistance. Over-doping can be used in the P-region as commonly done for the VCSEL. It could be interesting also, to grow low temperature active region to increase defects and thus increase the recombination rate. This has been studied by Van Eisden [133] but at only one setpoint temperature. Of course, the defect integration will degrade the optical properties of the device and a trade-off will have to be found.
Second, about the fabrication process improvements, it should be better to have the mid-contact layer closer to the EAM active region in order to decrease the influence of the middle DBR. We also have to use circular top-contact to improve the electrical injection at high-frequency. Then, we have seen that smaller diameters have to be processed to increase the cut-off frequency of the device.
Finally, the heterodyne beat measurement technique, used for the photodiode characterization, can be applied to the EAM. Indeed, if we really improve its properties it will not be possible to measure the cut-off at very high frequencies (> 50 GHz) with the current equipment.

6 CONCLUSION

6.1 WORK DONE AND COLLABORATIONS

We have presented this manuscript all the aspects of the desgin, the fabrication and the characterization of vertical-cavity electro-absorption modulator and its integration with a Vertical-Cavity Surface-Emitting Laser. The splitting of the emitting and modulating sections allows in principle to avoid the inherent limitations of the carrier dynamics. With the VCSEL powered in CW and the modulation of the top cavity we should be only limited by the photon lifetime in the absorber region. Indeed, the electro-absorption phenomena has been preferred to the electro-refraction due to the lower required electric field and the lower requirement for the epitaxy growth.

The project we conducted, has been a collaboration between the photonics team of the LAAS-CNRS (Toulouse, France) and the B-Phot group of the Vrije Universiteit Brussel (Belgium). A previous work has been realized by Mateusz Zujewski at the VUB about Coupled-Cavity VCSEL but it is the first time vertical-cavity EAMs and EAM-VCSELs are realized from the epitaxy to the high-frequency characterization. Indeed, the VUB has a strong experience in the VCSEL modelling and the LAAS-CNRS in the technological fabrication of photonic devices. Simple VCSEL structures have already been grown in the epitaxy reactor of the LAAS but never such a complex structure as the integrated EAM-VCSEL. The process fabrication of a such double mesa structure was also innovative for the group even if previous work has been done on BiVCSEL structures [134]. This work also benefited by the strong collaboration between the High-Frequency (MOST) and the Photonics groups in LAAS leading to a better understanding of the different phenomena and to the implementation of new experimental setup for the high-frequency characterization of EAM and EAM-VCSEL.

It seems important to me to remind that this project has been successfully completed thanks to several collaborations. Indeed, the simulation has been done in strong col-

laboration with Prof. Krassimir Panajotov. The fabrication part has been done with the support of team members of the LAAS-CNRS clean-room and more specifically with the help of Dr. Alexandre Arnoult for the MBE growth. This part was closely monitored by Dr. Guilhem Almuneau. The static characterization was supported by Dr. Stephane Calvez, Dr Olivier Gauthier-Lafaye and Dr Antoine Monmayrant and the high-frequency measurements by Alexandre Rumeau. Finally, the high-frequency simulation and discussions has been supported by Dr. Christophe Viallon.

This PhD project was composed of three complementary parts. The first one comprises the simulation and optimization of the EAM cavity design, the Asymetric Fabry-Perot multilayer structure and its integration on the VCSEL. The second one comprises the fabrication of stand-alone EAM and integrated EAM-VCSEL leadding to remove the technological obstacles inherent to the double mesa structure and high-frequency operation requirements. Finally, the third part comprises the static and high-frequency characterization of the EAM and EAM-VCSEL.

This last section of the manuscript will be first dedicated to the summary of the important steps of the project and the achieved results, and then, to the different perspectives to improve the knowledge of the EAM and EAM-VCSEL operation and to further enhance their modulation bandwidths.

6.2 PRINCIPAL RESULTS

We summarize in this section the realized significant advances in each part of the project

6.2.1 *Simulation of EAM and EAM-VCSEL*

We implemented a simple electro-absorption model and have optimized the physical parameters of a single QW as its thickness, the Al-content and the applied electric field to maximize the modulation depth while maintaining a low drive voltage. We then combined the electro-absorption model with the Transfer Matrix Method, which allowed us to design the whole EAM structure. We thus obtained a MQW cavity composed of 25 QW to reach a 2-λ thick cavity of 8.5 nm thick QW separated by 30 % Al-content barriers. This cavity is sandwhiched between 6 and 10 periods DBRs.
Then, we extended our simulation work toward the designing of integrated EAM-VCSEL. The top VCSEL DBR of 22 periods was used to decrease the coupling between the EAM and the VCSEL cavities and on top VCSEL structure we placed a MQW electro-absorber surrounded by the top EAM DBR.

This work has lead to a journal publication: Journal of Applied Physics: Physics D and was presented at several conferences: ICTON 2017 (invited talk), SPIE photonics Europe 2018 (oral), Photonics West 2018 (oral), VCSEL Day 2017 (oral).

6.2.2 *Fabrication of EAM and EAM-VCSEL*

The fabrication was focused on three essential points.
First, the epitaxy of the complicated structure for which we developed new calibration method and quick feedback characterization.
Then, we developed an innovative self-aligned processs for the mesa etch, the sidewalls passivation and the metallization. This process is usefull for air-post VCSEL and has been used for the EAM fabrication for static operation. Later, we implemented this process with an additional lateral oxidation step for oxide-confined VCSEL.
Finally, we work extensively on the process steps necessary to enable high-frequency operation of the device. To this aim we simplified the planarization step by using a mechanical press to flatten the BCB surface and we worked on the dry etch recipe. Thanks to these developments we were able to fabricate the global EAM-VCSEL device with a double mesa structure and microstrip access lines for the high-frequency signal injection.

These technological developments have led to the following publications:

- 2 Journal papers:
  - **paper A** Materials Science in Semiconductor Processing about the air-post self-aligned VCSEL, and
  - **paper B** Semiconductor Science and technology about the oxide confinement;
- 4 Conferences: VCSEL Day 2016 (oral) and MNE 2016 (poster) for the self-aligned process, and SPIE Photonics Europe 2016 (poster) for the BCB planarization and presented in a national workshop about etching techniques (Journees RTB Gravure, 2015 oral invited)

6.2.3 *Characterization of EAM and EAM-VCSEL*

6.2.3.1 *Static characterization*

After the fabrication of stand-alone EAM we characterized samples A (undoped DBR) and B (doped DBR) on a dedicated optical bench. We measured for all the samples modulation depth of 40 % for respectively 50 V and 4 V.
We demonstrated for the integrated EAM-VCSEL a modulation depth of 40 % and close to that we assembled a 70 % at threshold. We also measured the optical spectrum of the

emitted light with applied voltage on the EAM. We demonstrated a wavelength variation (chirp) lower than 0.1 nm, which is beneficial for data communications.
We studied the variation of the excitonic peak and Fabry-Perot resonance position as a function of the applied voltage and the temperature and used the experimental results as a feedback to our electro-absorption model. We improved our electro-absorption model to take it into account and electro-refractive and electro-absorption effects and obtained very good agreement with the experiment. This simulation, characterization and feedback work has been published in Journal of Physics D: Applied Physics (**paper C**) and presented in the conferences: VCSEL Day 2017 (oral), SPIE Photonics West 2018 (oral), SPIE Photonics Europe 2018 (oral).

6.2.3.2 *High-frequency characterization*

We preferred the microstrip access line compared to coplanar lines due to the induced coupling with the highly doped substrate in the last case. We characterized the BCB permittivity up to 67 GHz to design an optimum signal access line. Thanks to this method we were able to extract the pad and access line contributions.
These developments, in parallel of the BCB technological improvements, has been submitted for publication to IEEE Journal of Lightwave Technology (**paper E**).

We performed high-frequency characterization of the stand-alone EAM with a Vector Network Analyzer (VNA). Due to the significant losses in the setup we added a Power Amplifier (PA) but were then limited by its electrical bandwidth. We developed an alternative setup by using a synthesizer and a spectrum analyser and were able to modify manually the output power to compensate for the losses in bias tee, cable and probe. We measured bandwidth higher than 25 GHz limited by the photodiode responsivity.

Thanks to the material loan by TU Berlin (photodiode and PA), we measured with the synthesiser a cut-off frequency of 28 GHz and 32 GHz for 26 μm and 18 μm. The PA is used at the output of the photodiode and thus we were able to use the VNA as an efficient RF source. We positively found the same results. We also studied the frequency response of the EAM as a function of the applied bias voltage, temperature and wavelength illumination and concluded that they do not impact the EAM modulation characteristics in the parameter range investigated.

Additionally, we measured the S_{11} parameter and extracted, thanks to the de-embedding method we previosuly developed, the EAM impedance as a function of the EAM diameter. We modelled the EAM with an equivalent circuit and extracted the different resistances and capacitances. Our model is somewhat optimistic but allows to have an information when we decrease the EAM diameter. Indeed, decreasing it up to 10 μm result in an increased modulation bandwidth by a factor two.

Finally, we measured the EAM-VCSEL response and clearly see the impact of the EAM voltage and VCSEL drive current on the output photodiode level. We obtained exactly the same response as for the EAM alone. We thus reached cut-off frequency of 29 GHz for the integrated EAM-VCSEL which is comparable to the actual record at 850 nm directly modulated VCSEL of Chalmers of 30 GHz [39]. Our result is also a considerable improvement of the modulation bandwidth of 20 GHz obtained by Van Eisden [135].

The high-frequency characterization and equivalent circuit will be the topic of a upcoming publication, first with the EAM-VCSEL (**paper F**) and another one about the EAM parameter influence and electrical equivalent circuit (**paper G**).

All these results will published in two journal papers.

6.3 PERSPECTIVES

We described previously the different progress achieved, it is now crucial to step back and analyze the possible improvements to be done and the remaining work.

6.3.1 *Design of EAM and EAM-VCSEL*

Based on the characterization feedback of the EAM at different temperatures and voltage, it is now possible to design an optimum structure which considers the best wevelength detuning between the excitonic peak, gain peak and cavity resonance walvengths for high temperature operation once integrated onto the VCSEL.
It will be important to estimate the optical losses due to the addition of the top DBR which increases the top reflectivity seen by the VCSEL cavity and thus decreases the gain. It would be interesting to estimate the required number of QWs in order to completely remove the top DBR while keeping the same modulation depth.

6.3.2 *Improved epitaxial structures*

About the EAM:

- use DBR grading to facilitate the current spreading at high frequency and thus decrease its resistance and increase the cut-off frequency;
- add a thin barrier in QWs to shift the envelop function on each sides of the QW with a lower applied voltage;
- grow a EAM wafer with low temperature active region to increase the carrier recombination and thus the cut-off frequency. (note that it will affect the optical properties).

About the VCSEL:

- improve the confinement with a second oxide layer and a Al-content shape in the bottom DBR;
- use only 3 steps in the DBR gradding about 15-20 nm instead of 10;
- use two $\lambda/2$ highly doped layers in DBR to increase the current uniformity and thus decrease the resistance;

6.3.3 *Fabrication*

6.3.3.1 *Epitaxy*

For the next epitaxy run, the calibration will be realized with the superlattice method which seems to increase the pertinence of the cells flow calibration. Thanks to the new equipment developed by Alexandre Arnoult, it will be possible to simulate the structure reflectivity spectrum as a function of the growth time and compare it in real time with the measurement. We will thus be able to adjust the cell flow during the epitaxy growth if we observe a divergence.
After several epitaxial growth of VCSEL we will be able to anticipate the variation in the top DBR after the cavity growth.

6.3.3.2 *Process*

The fabrication of EAM-VCSEL has really been complicated but can be facilitated by increasing the alignment tolerances. Improvements are also necessary to optimize the current injection in both EAM and VCSEL.

About the EAM:

- use a circular top contact to have a better uniformity of the signal injection;
- process smaller mesa diameters and thus decrease the width of the ring contact;
- Take the electrical contacts closer to the active region to decrease the impact of the DBRs.

About the VCSEL:

- use a test sample before the lateral oxidation of the VCSEL to have a precise calibration;
- improve the current spreading by putting the mid-contact ring closer to the EAM mesa foot. The larger will be this ring, the lower precision is required for the alignment for passivation deposition. Furthermore the contact will be more homogenous and thus improve the high-frequency injection.

Global:

- use thicker metal contact layer and try to grow copper for the mid- and bottom-contact to diffuse heat;
- use the new alignment machine for more precise photolithography steps.

6.3.4 *Characterization*

It will be interesting to compare the high-frequency results obtained with standard RF characterization with a heterodyne beat technique. In that case, the characterization setup is the same than for the photodiode. It is necessary to have two lasers at the precise wavelength of the modulation of the EAM and move away one of them. The electrical signal collected on the EAM pads will give an information about its frequency response as done in [136]. This method could be, if it demonstrates the same results than the VNA, usefull for very high-speed EAM. Indeed, if we want to compare EAM alone the heterodyne beat measurement can be a good alternative to measure higher frequency responses than the photodiode response.

Finally, a new process run has to be done to reach the adequate oxidation aperture of the VCSEL and then, to measure again the LIV response of the device. It will be also possible, with the remaining samples, to measure more precisely the high-frequency response of the EAM-VCSEL as a function of the EAM and VCSEL diameters. Finally, data transmission experiments has to be carried out with this structure to measure the data bandwidth in Gbit/sec and check the operational feasability of this device.

7 APPENDIX A: PROCESSING LIST OF EAM-VCSEL DEVICE

1. **Epitaxy** Growth of the whole stack considering the DBR gradding, digital alloy barrier etc.
2. **EAM top contact**
   a) Sample cleaning : Aceton - IPA - DIW - heat 105°C 2 min.
   b) LOR30B coating : 3000 rpm, 3000 rpm/sec, 30 sec
   c) LOR30B soft bake: 170°C 5 min.
   d) SPR 2.3µm coating : 1000 rpm, 3000 rpm/sec, 30 sec
   e) SPR 2.3µm soft bake: 95°C 60 sec.
   f) MJB3 insulation, mask E176 L1.1 VCSELEAM PHOTO20.03.17, 7.5 sec., soft contact
   g) Development: MFCD26 room temperature 40 sec. and rinse with DIW
   h) Desoxidation: HCl 1 : 5 DIW 30 sec.
   i) Metallization: EVA600 Ti 50 nm at 0.5 nm/sec, then Au 600 nm at 0.2 nm/sec.
   j) Lift-Off: DMSO 80°C 5 min. then aceton with pipette
   k) Sample cleaning: Aceton - IPA - DIW - heat 90°C 2 min.
3. **EAM mesa etch**
   a) Sample cleaning: Aceton - IPA - DIW - heat 105°C 2 min.
   b) SPR 2.3µm coating : 1000 rpm, 3000 rpm/sec, 30 sec
   c) SPR 2.3µm soft bake: 95°C 60 sec.
   d) MJB3 insulation, mask E176 L2 VCSELEAM PHOTO21.12.16, 7.5 sec., soft contact
   e) Development: MFCD26 room temperature 60 sec. and rinse with DIW
   f) Mesa etch
      - Stuck the sample on the 3 or 4" susceptor with fomblin oil, stucked itself on a 6" Si wafer

- Chamber conditioning for 1' with the T1E2050 recipe
- III-V material etch with Cl2 = 20 sccm, N2 = 50 sccm, P = XX, T =
- remove fomblin oil with chemical baths of: PFS 1min., HFE 1 min., Aceton 5 min., IPA 30 sec., DIW

g) Optional oxidation of Al0.9Ga0.1As layers in dedicated furnace

- Desoxidation HCl 1 : 5 DIW
- Recipe of the oxidation .....

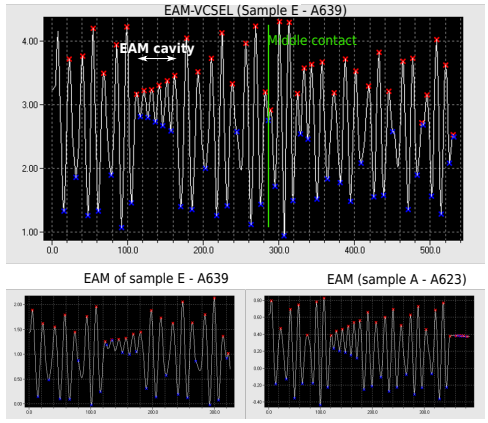

Figure 7.1: Laser reflectitivity measurement during dry etchs on samples E, EAM-VCSEL, and EAM alone on sample E, and EAM on sample A. EAM cavity and middle contact are represented.

Other End-point detection pictures can be found in the computer of ICP2 in C - EtchDirectorWork - RunData - Ludo

4. **VCSEL top contact**

a) Sample cleaning : Aceton - IPA - DIW - heat 105°C 2 min.

b) LOR30B coating : 3000 rpm, 3000 rpm/sec, 30 sec

c) LOR30B soft bake: 170°C 5 min.

d) SPR 2.3µm coating : 1000 rpm, 3000 rpm/sec, 30 sec

e) SPR 2.3µm soft bake: 95°C 60 sec.

f) MJB3 insulation, mask E176 L3.1 VCSELEAM PHOTO20.03.17, 7.5 sec., soft contact

g) Development: MFCD26 room temperature 40 sec. and rinse with DIW

h) Desoxidation: HCl 1 : 5 DIW 30 sec.

i) Metallization: EVA600 Ti 50 nm at 0.5 nm/sec, then Au 600 nm at 0.2 nm/sec.

j) Lift-Off: DMSO 80°C 5 min. then aceton with pipette

k) Sample cleaning: Aceton - IPA - DIW - heat 90°C 2 min.

5. **EAM passivation, VCSEL etch and oxidation**

a) Sample cleaning : Aceton - IPA - DIW - heat 105°C 2 min.
b) LOR30B coating : 3000 rpm, 3000 rpm/sec, 30 sec
c) LOR30B soft bake: 170°C 5 min.
d) SPR 2.3µm coating : 1000 rpm, 3000 rpm/sec, 30 sec
e) SPR 2.3µm soft bake: 95°C 60 sec.
f) MJB3 insulation, mask E176 L4.1 VCSELEAM PHOTO19.04.17, 7.5 sec., soft contact
g) Development: MFCD26 room temperature 40 sec. and rinse with DIW
h) Desoxidation: HCl 1 : 5 DIW 30 sec. NOT IF EAM Oxidized
i) ICPECVD : recipe "adr-SiOxGuilhem100C-cor", deposition rate around 100 nm / 12 minutes. Here need to deposit 400 nm to provide next step
j) Lift-Off: DMSO 80°C 5 min. then aceton with pipette
k) Sample cleaning: Aceton - IPA - DIW - heat 90°C 2 min.
l) VCSEL etch with T1E2050 recipe assisted by the end-point detection system to stop the etching in the bottom DBR.
m) Desoxidation: HCl 1 : 5 DIW 30 sec.
n) Recipe of the oxidation ..... to reach 5 µm on the 69 µm VCSEL diameter.

6. **VCSEL passivation**

a) Sample cleaning : Aceton - IPA - DIW - heat 105°C 2 min.
b) LOR30B coating : 3000 rpm, 3000 rpm/sec, 30 sec
c) LOR30B soft bake: 170°C 5 min.
d) SPR 2.3µm coating : 1000 rpm, 3000 rpm/sec, 30 sec
e) SPR 2.3µm soft bake: 95°C 60 sec.
f) MJB3 insulation, mask E176 L5.2 VCSELEAM PHOTO20.03.17, 7.5 sec., soft contact
g) Development: MFCD26 room temperature 40 sec. and rinse with DIW
h) ICPECVD : recipe "adr-SiOxGuilhem100C-cor", deposition rate around 100 nm / 12 minutes. Here 300 nm are enough.
i) Lift-Off: DMSO 80°C 5 min. then aceton with pipette
j) Sample cleaning: Aceton - IPA - DIW - heat 90°C 2 min.

7. **Ground contact**

a) Sample cleaning : Aceton - IPA - DIW - heat 105°C 2 min.
b) LOR30B coating : 3000 rpm, 3000 rpm/sec, 30 sec
c) LOR30B soft bake: 170°C 5 min.
d) SPR 2.3µm coating : 1000 rpm, 3000 rpm/sec, 30 sec
e) SPR 2.3µm soft bake: 95°C 60 sec.

f) MJB3 insulation, mask E176 L6.1 VCSELEAM PHOTO20.03.17, 7.5 sec., soft contact

g) Development: MFCD26 room temperature 40 sec. and rinse with DIW

h) Metallization: EVA600 Ti 50 nm at 0.5 nm/sec, then Au 600 nm at 0.2 nm/sec.

i) Lift-Off: DMSO 80°C 5 min. then aceton with pipette

j) Sample cleaning: Aceton - IPA - DIW - heat 90°C 2 min.

8. **BCB planarization**

a) Sample cleaning : Aceton - IPA - DIW - heat 105°C 2 min.

b) AP3000 (in the solvent cabinet):

c) BCB spin-coating with ramp up v / a : 500 / 500 for 5", 1500 / 2000 for 5" then 6000 / 4000 for 30"

d) BCB soft bake 80°C 1 min

e) Nano-imprint

- Pump 2'
- Pre-imprint 100 °C
- Pre-pressure 120 PSI
- Process: Temperature = 120 °C (thermocouple offset of + 20°C) - Pressure = 250 PSI - Time = 5'59 (max. allowed)
- Vent when 50°C

f) carefull separation

9. **BCB photolithography - via opening**

a) MJB3 insulation, mask E176 L7.3 VCSELEAM PHOTO25.07.17, 45 sec., soft contact

b) Development: DS3000 between 30 and 35 °C during 2 - 3minutes. Need to use a test sample before.

c) Rince: 1' in DWI then DS3000 / 1' in DWI then DS3000 - 3 times

10. **BCB and SiO_x etching**

a) Glue the sample, on the dedicated susceptor stored in the shelf, with Fomblin

b) Recipe called BCB in ICP2: O_2 / SF_6 : 99 / 2 sccm - ICP / RF : 500 / 40 at 70 mTorr and 17°C - with End-point detection system

c) Dry etch of the SiO_x once you reached the topmost layer of the mesa. Two recipes are available on ICP3

- JULSEL: CHF_3 50 sccm, ICP/RF : 50/50 W, 5mT, 17°C for 22 nm/min, or
- CF_4 40W: CF_4 40 sccm, ICP/RF : 500/40 W, 5 mT, 17°C around 120 nm/min but maybe better selectivity with GaAs

d) Remove Fomblin with PFS / HFE / Aceton / IPA / DWI

In case of problem during the BCB development it is possible that the via depth, even after the global etching, is not deep enough to reach the ground plane. In that case, provide another lithography to open it again.

BCB via etching

a) Sample cleaning : Aceton - IPA - DIW - heat 105°C 2 min.
b) SPR 2.3µm coating : 1000 rpm, 3000 rpm/sec, 30 sec
c) SPR 2.3µm soft bake: 95°C 60 sec.
d) MJB3 insulation, mask E176 L7.3 VCSELEAM PHOTO25.07.17, 7.5 sec., soft contact
e) Development: MFCD26 room temperature 60 sec. and rinse with DIW
f) Dry etch. Recipe BCB

If the open window still has BCB or SiO_x and you need to etch it again, without etching the whole sample due to planarization and the 6 µm thick BCB for the HF pads design, you can add another photolithography with the mask number 2 with NLOF. It will just open the required size for the electrical contact.

11. **Top HF contact**

a) Sample cleaning : Aceton - IPA - DIW - heat 105°C 2 min.
b) LOR30B coating : 3000 rpm, 3000 rpm/sec, 30 sec
c) LOR30B soft bake: 170°C 5 min.
d) SPR 2.3µm coating : 1000 rpm, 3000 rpm/sec, 30 sec
e) SPR 2.3µm soft bake: 95°C 60 sec.
f) MJB3 insulation, mask E176 L8.3 VCSELEAM PHOTO14.12.17, 7.5 sec., soft contact
g) Development: MFCD26 room temperature 40 sec. and rinse with DIW
h) Metallization: EVA600 Ti 50 nm at 0.5 nm/sec, then Au 600 nm at 0.2 nm/sec.
i) Lift-Off: DMSO 80°C 5 min. then aceton with pipette
j) Sample cleaning: Aceton - IPA - DIW - heat 90°C 2 min.

Or can be done with 5 µm-thick NLOF resist with the mask
E176 L8.4 VCSELEAM PHOTO14.12.17

List of the masks used during the PhD

- Self-aligned process - Air-post configuration
  1. Mask1 : D117 L1 BiVCSEL06 PHOTO 22.06.06 (red box written Almuneau, Ref: BiVCSEL 06, Date: Juin06 Mesa1)
  2. Mask2 : E209 L1 BiVCSEL PHOTO 19.04.17
- Self-aligned process - Oxidation
  1. Mask1 : E137 L2 AlOx PHOTO 19.07.2016
  2. Mask2 : E137 L4 AlOx PHOTO 19.07.2016
- Global process
  1. Mask1 : E176 L1 VCSEL PHOTO 21.12.16 and E176 L1.1 VCSEL PHOTO 20.03.17 exist. L1 has maybe been realized when the Heidelberg equipment was not calibrated and thus the circles are not so well defined. E176
  2. Mask2 : E176 L2 VCSEL PHOTO 21.12.16 OK
  3. Mask3 : E176 L3 VCSEL PHOTO 21.12.16 and L3.1 VCSEL PHOTO 20.03.17 (problem of mirror effect during writting ?)
  4. Mask4 : E176 L4 VCSEL PHOTO 21.12.16 and L4.1 VCSEL PHOTO 19.04.17 (problem of mirror effect during writting ?)
  5. Mask5 : E176 L5.1 VCSEL PHOTO 20.03.17 OK (use it to open the SiO_x in case of problem with the previous step) and L5.2 VCSEL PHOTO 15.11.17, two copies
  6. Mask6 : E176 L6.1 VCSEL PHOTO 20.03.17 OK
  7. Mask7 : E176 L7.2 VCSEL PHOTO 25.07.17 problem of mirror effect and E176 L7.3 VCSEL PHOTO 25.07.17 to realize the lift off to transfer the ground plane on top in case of problem with the BCB opening. Three copies. 2 transparents are the same, 1 with more than 50 % of copper to have both polarities: NLOF or LOR/SPR.
  8. Mask8 : E176 L8.2 VCSEL PHOTO 25.07.17 : narrow width (20 µm) and E176 L8.3 VCSEL PHOTO 14.12.17 : large width (40 µm) idem for E176 L8.4 VCSEL PHOTO 14.12.17
- Other
  - All masks E198 L1, L2, L3 and L4 02.03.17 have been insulated at the center and not repeated

8 APPENDIX B

8.1 TIPS

We present here all the tips for the fabrication of the EAM-VCSEL in the LAAS-CNRS clean-room. Pay attention that process may differs from one clean-room to another one.

About the **LOR-SPR**, which is actually the key of the simplicity of these multi-step process, a development calibration is required since the MJB3 lamp has been changed which modifies the insolation dose. Still about the MJB3, there is on the bottom right of the equipment a latch that can be on 'Integer' or 'Timer'. Always put it on Timer otherwise it takes into account the lamp ageing (which does not work) so the illumination time is altered.

In the process you have maybe seen that the developement for lift-off lasts only 40" instead of 60" or evenmore when the SPR resists is used for etching. Indeed, if we develop too much, the LOR recess will be too important and the SPR will collapsed during SiO_x deposition.

About the LOR soft bake, supplier give information about the temperature and we can see that moving from 170° to 200° divide by two the etching rate which could be interesting to have a better control and reproducibility. However, in that case more solvent are evaporated during the soft bake and the later on lift-off is more complicated. We suggest to work at 170°.

If you work with an hydrophobic surface, it is required to do an heating at 120° and then a O_2 plasma. If necessary you can check the hydrophobic surface state by the water drop test. In all cases, on SiO_x it is preferable to apply a heating ramp up for the LOR soft bake. Get the sample closer and closer to the hot plate, set at 110°, and then increase manually the temperature to 140° and then 170°. Set the chrono once you are at 170°.

This problem has been encountered for the ground metal lift-off (step 7).

About the LOR and BCB deposition, these resists are very difficult to remove from the bwoll spinner. We have a dedicated bowl in the cupboard above the spinner no 1.

About the **spin-coating**, for all the deposition, since we are working with small samples (around 1.5 cm x 1.5 cm), edge effects can be really significant with viscous resist and a beading occurs. To remove it, or at least, minimize it, it is necessary to apply another rotation step of 1" with a speed of at least 2000 rpm higher than the standard process.

About the **lift-off**, SiO_x can be difficult to lift if processed after the mesa etching. To facilitate it, it is possible to put the sample in Ultrasons for few minutes. A maximum of 50 % at 135 kHz should be used since higher power or even lower frequency (we have 30 kHz) are too violent and can lead to a peel off of the dielectric or metal.

The lift-off has been realized with metal thicknesses of 650 nm without any problem by using the 5 µm-thick LOR. Lift-off of 700 or 800 nm can be achieved.

About the **chemical product** itself, for lift-off DMSO is most often used at 80 ° (hot plate at 90 °) but Remover PG can also be used and is very more efficient. However, due to its cancerigen aspect it should be avoid as much as possible.

For the resist developer, MF-CD-26 is always used, other products are available like AZ400K or AZ100 developer which are very efficient to remove the LOR resist. However these two last products etch very quickly the Al-content layers, even at 90 %. It is also the case of MFCD26 but etching rate is very low.

About the **metal deposition**, to provide a very continuous deposit it is necessary to select 0.2nm/sec for the Au otherwise discontinuity may occur at the edge of mesa, especially when we use a hard mask (Au or SiO_x) then the sidewalls are more or less of 90 °

About the **dry etching**, samples are stuck on a GaAs 4 inches wafer with fomblin oil $\Rightarrow$ constant temperature during the whole process. Better uniformity and reproducibility between samples and between different runs. Possible to put three samples on the same 4" GaAs wafer, uniformity is good enough

About the **separation after nanoimprint**, use a razzor blade very carefully on a sample edge and wait for the sample to be at room temperature otherwise scratch may appears. it is also necessary to provide a FDTS treatment on the Si wafer, this chemical treatment is no more efficient after several months so repeat it.

We also tried, to increase the metal thickness to 2 µm, electrochemical deposition. When the substrate is doped and without undoped vertical region it is possible to realize it just by sticking the sample on a 4" wafer with Au on top. Take care that this wafer presents Au until the edge (no Evap in EVA600) for the electrical contact.

However, with EAM or VCSEL this operation is not possible and it is necessary to take the electrical contact on the edges of the samples with conductive tape. A calibration sample has to be done to validate the growth rate as a function of the Au surface.

Unfortunatelly, in that case it is absolutely necessary to have straight sides to not increase the width of the final metal ring. This process can not be realize directly on GaAs since the next steps consists in etching the metal, which has be deposited on all the sample,and the Gold etchant chemical solution etchs very fast the GaAs even in presence of Ti above.

8.2 MASK IMPROVEMENTS

We present in Fig. 8.1 the top view of the Clewin masks.

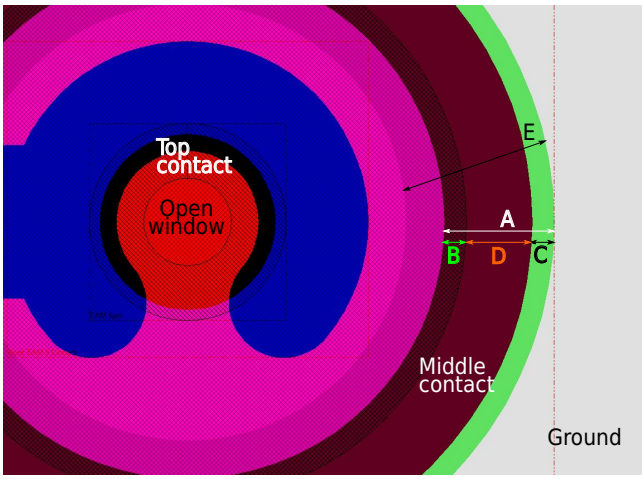

Figure 8.1: Global top view of the different masks

The EAM top ring contact is represented in hatched lines arround the open window.
The red circle corresponds to the SPR resist for the EAM mesa etching.
The middle contact is represented in green but hiden by other layers. Its width is represented by the letter A, A = 10µm
The SiO_x layer is represented in hatched lines from the center to the right side of B, B = 2µm.
The dielectric layer covers the metal with a width of B + D = 8 µm.
Then the VCSEL is etched, oxidized and finally passivated. The bottom SiO_x covers the middle metal with a width of C, C = 2 µm.
Finally, the ground contacts comes on the middle level with a total width of around 14 µ depending on the VCSEL diameter. The coverage between both metal layers is done on a width of D.

These dimensions have been considered to have enough space between the middle metal and the EAM mesa to follow, thanks to the optical system, the VCSEL oxidation.

However some problems occured due to the alignements.

First, but not due to the mask, the alignement between the EAM mesa and the middle contact is of high importance since it will define the VCSEL aperture position. Take care on this step.

B and C have been designed too small. 5 µm would have been great, so A has to be increased too. Maybe 20 µm. In taht case D will be 10 µm which is good for the coverage and thus the electrical injection.

Modify the shape of the blue top contact to have a uniform electrical injection.

in Fig. 8.2, we show the first mask used for the ground contact transfer on top of the sample.

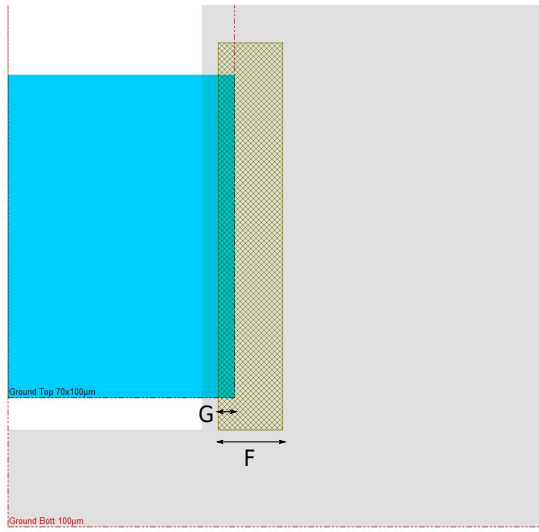

Figure 8.2: BCB aperture for ground transfer on top

Dimension F corresponds to the first design for the via opening. It turns out that this dimension has been increased in the 2nd mask generation from 20 to 40 µm. However, without etching, even this value is not sufficient to open the BCB layer. It might be increased again. A study can be done about this photolithography to ensure a good opening without etching.

Dimension G has been first set at 5 µm which is really too low. Finally the top metal ground was patterned to recover all the via access to ensure a perfect contact.

About test structures, it is necessary to implement other test structure for:

- testing the electrical contacts, between the top and middle contact, and middle and bottom contact
- improve the oxidation design test to have a better control on the lateral oxidation

9 APPENDIX C: EPITAXY RECIPES

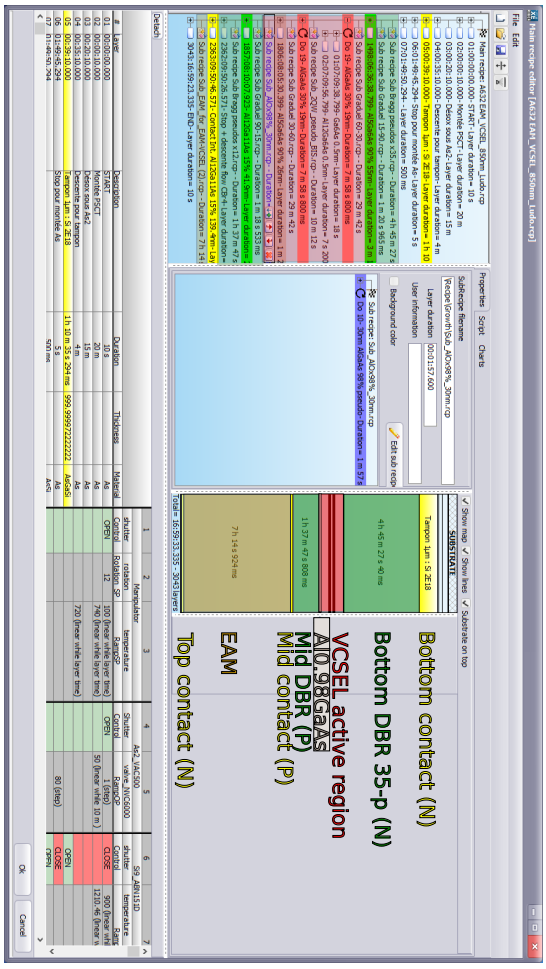

Figure 9.1: Crystal recipe for the EAM-VCSEL structure.

Figure 9.2: Crystal recipe for the VCSEL QWs.

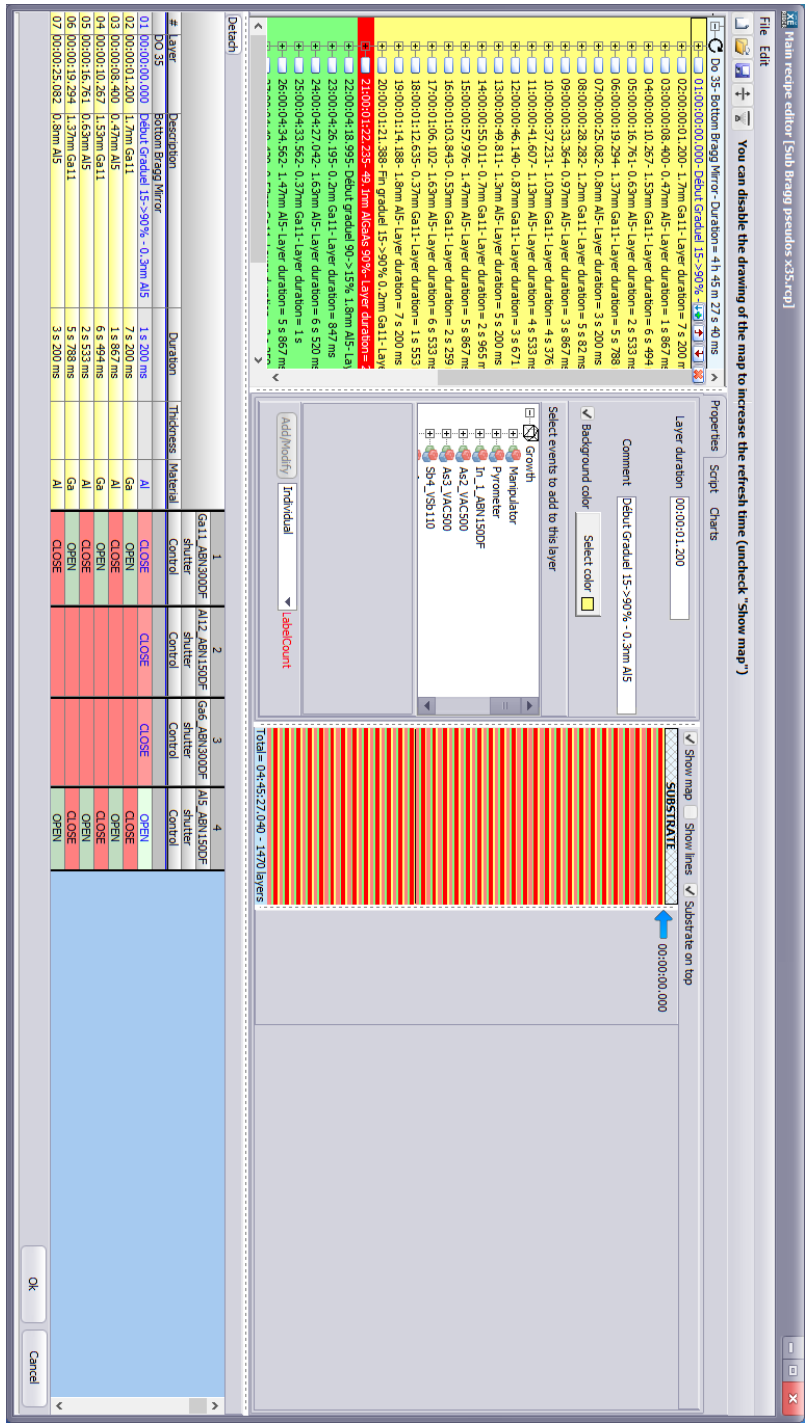

Figure 9.3: Crystal recipe for the bottom VCSEL DBR.

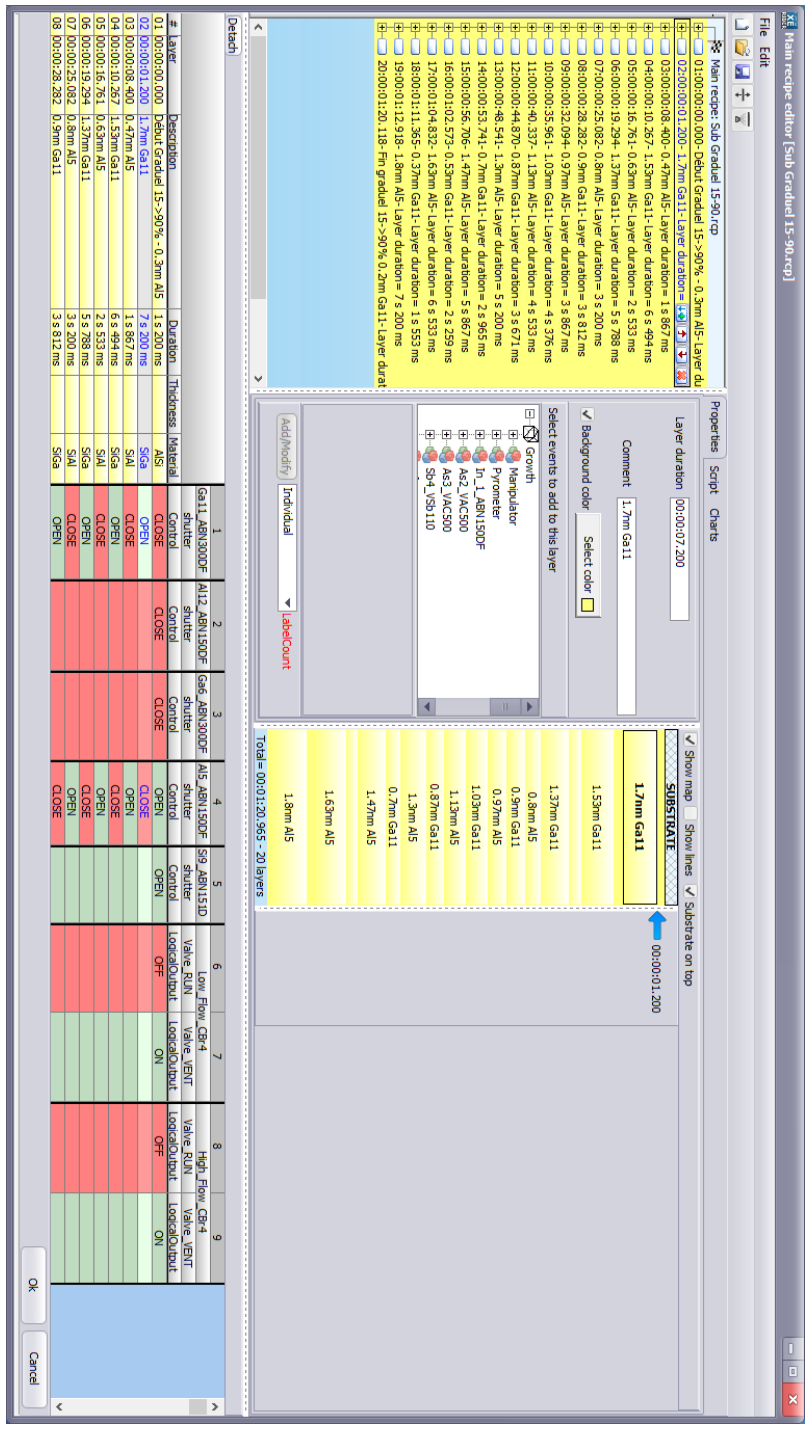

Figure 9.4: Crystal recipe for the DBR grading from 15 to 90%.

Figure 9.5: Crystal recipe for the EAM without grading interface.

10 APPENDIX D: METAL THICKNESS

Thickness required for high-frequency injection

The skin depth corresponds to the metal thickness where the HF current is confined. It is calculated by:

$$\delta_m = (\sigma_m \mu_0 \mu_r \pi f)^{-1/2} \quad \text{with} \begin{cases} \mu_0 = 4\pi 10^7 \text{ H/m}, \\ \sigma_{Cu} = 5.96 \cdot 10^7 \text{ S/m}, \\ \sigma_{Au} = 4.52 \cdot 10^7 \text{ S/m} \end{cases} \tag{10.1}$$

We plotted in Fig. 10.1 the skin depth for copper, gold and titanium. To deacrease as possible the losses in the access it is necessary to consider a metal thickness of $2 \cdot \delta_m$

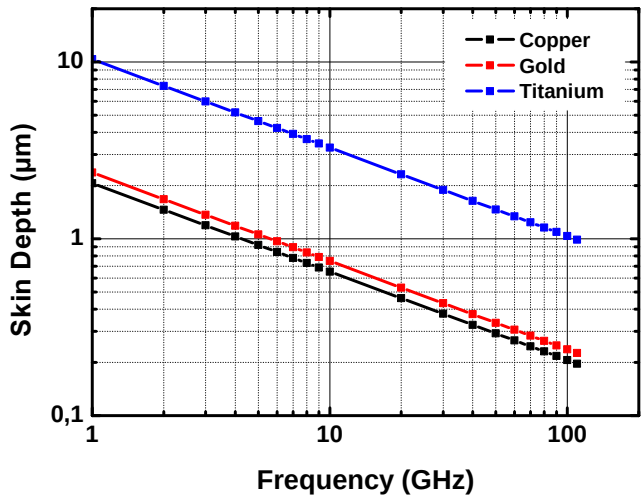

Figure 10.1: Skin depth over frequency calculated for copper (black), gold (red) and titanium (blue) metal

BIBLIOGRAPHY

[1] http://www.photonics.philips.com/application-areas/sensing.

[2] https://www.finisar.com/sites/default/files/resources/finisar-vcsel-product-guide.pdf.

[3] https://www.photonics.com/Article.aspx?AID=57110.

[4] https://www.intel.com/content/dam/support/us/en/documents/emerging-technologies/intel-realsense-technology/intel-realsense-d400-series-datasheet.pdf.

[5] https://appleinsider.com/articles/18/03/08/apple-vcsel-supplier-suggests-truedepth-coming-to-multiple-iphones-this fall.

[6] http://www.semiconductor-today.com/news-items/2018/jul/ams 100718.shtml.

[7] https://www.neowin.net/news/huaweis-facial-recognition-tech-could-be-10-times-better-than-face id.

[8] http://www.mwee.com/news/3d-solid-state-lidar-using-3d-sensing-vcsel-illumination-ces 2018.

[9] Jim A. Tatum, Deepa Gazula, Luke A. Graham, James K. Guenter, Ralph H. Johnson, Jonathan King, Chris Kocot, Gary D. Landry, Ilya Lyubomirsky, Andrew N. MacInnes, Edward M. Shaw, Kasyapa Balemarthy, Roman Shubochkin, Durgesh Vaidya, Man Yan, and Frederick Tang. VCSEL-based interconnects for current and future data centers. *Journal of Lightwave Technology*, 33(4):727–732, 2015.

[10] Jim A Tatum. Evolution of vcsels. In *Vertical-Cavity Surface-Emitting Lasers XVIII*, volume 9001, page 90010C. International Society for Optics and Photonics, 2014.

[11] MarketsandMarkets. Vcsel market - global forecast to 2020.

[12] https://globenewswire.com/.

[13] http://www.photonics.com/Article.aspx?AID=56571.

[14] Petter Westbergh. High speed vcsels and optical interconnects, 2014.

[15] Alan Benner. Optical interconnect opportunities in supercomputers and high end computing. In *Optical Fiber Communication Conference and Exposition (OFC/NFOEC), 2012 and the National Fiber Optic Engineers Conference*, pages 1–60. IEEE, 2012.

[16] Daniel Mahgerefteh, Craig Thompson, Chris Cole, Gilles Denoyer, Thelinh Nguyen, Ilya Lyubomirsky, Chris Kocot, and Jim Tatum. Techno-economic comparison of silicon photonics and multimode VCSELs. *Journal of Lightwave Technology*, 2015.

[17] http://www.datacenterknowledge.com/storage/supercomputers-have-been-slow-adopt-flash-storage-cray-wants change.

[18] https://www.actu-environnement.com/ae/dossiers/efficacite-energetique/data-centers-reduire-facture-energetique-rester competitifs.php.

[19] https://www.sciencesetavenir.fr/high-tech/informatique/numerique-et-ecologie-les-data-centers-des-gouffres-energetiques 121838.

[20] Christoforos Kachris and Ioannis Tomkos. The rise of optical interconnects in data centre networks. In *Transparent Optical Networks (ICTON), 2012 14th International Conference on*, pages 1–4. IEEE, 2012.

[21] https://news.microsoft.com/features/under-the-sea-microsoft-tests-a-datacenter-thats-quick-to-deploy-could-provide-internet-connectivity-for years/.

[22] https://www.facebook.com/notes/fort-worth-data-center/hello-fort worth/857508384342899.

[23] https://www.google.com/about/datacenters/renewable/index.html.

[24] L. A. Coldren, S. W. Corzine, and M. L. Mashanovitch. *Diode lasers and photonic integrated circuits*, volume 218. John Wiley & Sons, 2012.

[25] Henry Mathieu and Hervé Fanet. *Physique des semiconducteurs et des composants électriques: cours et exercices corrigés*. Dunod, 2009.

[26] H. A. Macleod. Thin-film Optical Filters, 1986.

[27] Emanuel P. Haglund, Sulakshna Kumari, Petter Westbergh, Johan S. Gustavsson, Gunther Roelkens, Roel Baets, and Anders Larsson. Silicon-integrated short-wavelength hybrid-cavity VCSEL. *Optics Express*, 23(26):33634–33640, 2015.

[28] Connie J. Chang-Hasnain and Weijian Yang. High-contrast gratings for integrated optoelectronics. *Advances in Optics and Photonics*, 4(3):379–440, 2012.

[29] Ye Zhou, M. C. Y. Huang, C. Chase, V. Karagodsky, M. Moewe, B. Pesala, F. G. Sedgwick, and C. J. Chang-Hasnain. High Index Contrast Grating (HCG) and Its Applications in Optoelectronic Devices. *IEEE Journal of Selected Topics in Quantum Electronics*, 15(5):1485–1499, 2009.

[30] Zhou Y. Huang M. C. and Chang-Hasnain C. J. A surface-emitting laser incorporating a high-index-contrast subwavelength grating. *Nature photonics*, 1(2):119, 2007.

[31] J. Ferrara, W. Yang, L. Zhu, P. Qiao, and C. J. Chang-Hasnain. Heterogeneously integrated long-wavelength VCSEL using silicon high contrast grating on an SOI substratesubstrate. *Optics express*, 23(3):2512–2523, 2015.

[32] D. B. Young, J. W. Scott, F. H. Peters, M. G. Peters, M. L. Majewski, B. J. Thibeault, S. W. Corzine, and L. A. Coldren. Enhanced performance of offset-gain high-barrier vertical-cavity surface-emitting lasers. *IEEE Journal of Quantum Electronics*, 29(6):2013–2022, jun 1993.

[33] Rainer Michalzik. *VCSELs: fundamentals, technology and applications of vertical-cavity surface-emitting lasers:*, volume 166. Springer, 2012.

[34] Y.-C. Chang, C. S. Wang, and L. A. Coldren. High-efficiency, high-speed VCSELs with 35 Gbit/s error-free operation. *Electronics Letters*, 43(19):1022, 2007.

[35] P. Westbergh, J. S. Gustavsson, A. Haglund, M. Skold, A. Joel, and A. Larsson. High-Speed, Low-Current-Density 850 nm VCSELs. *IEEE Journal of Selected Topics in Quantum Electronics*, 15(3):694–703, 2009.

[36] A. J. Danner, T. S. Kim, and K. D. Choquette. Single fundamental mode photonic crystal vertical cavity laser with improved output power. *Electronics Letters*, 41(6):325, 2005.

[37] Tomasz Czyszanowski, Robert P. Sarzała, Maciej Dems, Hugo Thienpont, Włodzimierz Nakwaski, and Krassimir Panajotov. Strong modes discrimination and low threshold in cw regime of 1300 nm AlInGaAs/InP VCSEL induced by photonic crystal. *physica status solidi (a)*, 206(7):1396–1403, jul 2009.

[38] Petter Westbergh, Rashid Safaisini, Erik Haglund, Johan S Gustavsson, Anders Larsson, Matthew Geen, Russell Lawrence, and Andrew Joel. High-speed oxide confined 850-nm vcsels operating error-free at 40 gb/s up to 85 c. *IEEE Photonics Technology Letters*, 25(8):768–771, 2013.

[39] E. Haglund, A. Larsson, M. Geen, J. S. Gustavsson, E. P. Haglund, A. Joel, and P. Westbergh. 30 ghz bandwidth 850 nm vcsel with sub-100 fj/bit energy dissipation at 25–50 gbit/s. *Electronics Letters*, 51(14):1096–1098, 2015.

[40] Daniel M Kuchta, Alexander V Rylyakov, Clint L Schow, Jonathan E Proesel, Christian W Baks, Petter Westbergh, Johan S Gustavsson, and Anders Larsson. A 50

gb/s nrz modulated 850 nm vcsel transmitter operating error free to 90 c. *Journal of Lightwave technology*, 33(4):802–810, 2015.

[41] Daniel Kuchta, Alexander V Rylyakov, Clint L Schow, Jonathan Proesel, Christian Baks, Petter Westbergh, Johan S Gustavsson, and Anders Larsson. 64gb/s transmission over 57m mmf using an nrz modulated 850nm vcsel. In *Optical Fiber Communication Conference*, pages Th3C–2. Optical Society of America, 2014.

[42] Daniel Kuchta, Alexander Rylyakov, Clint Schow, Jonathan Proesel, Fuad Doany, Christian W. Baks, Brendan Hamel-Bissell, Chris Kocot, Luke Graham, Ralph Johnson, Gary Landry, Ed Shaw, Andy MacInnes, and Jim Tatum. A 56.1gb/s NRZ Modulated 850nm VCSEL-Based Optical Link. In *Optical Fiber Communication Conference and Exposition and the National Fiber Optic Engineers Conference (OFC/NFOEC), 2013*, pages 1–3. IEEE, 2013.

[43] Ricardo Rosales, Martin Zorn, and James A Lott. 30-ghz bandwidth with directly current-modulated 980-nm oxide-aperture vcsels. *IEEE Photonics Technology Letters*, 29(23):2107–2110, 2017.

[44] James A. Lott, Nasibeh Haghighi, Gunter Larisch, Ricardo Rosales, Tomasz Czyszanowski, Leszek Frasunkiewicz, and Marcin Gębski. Simplicity VCSELs. In *Vertical-Cavity Surface-Emitting Lasers XXII*, volume 10552, page 105520N. International Society for Optics and Photonics, 2018.

[45] M. Nadeem Akram, Y. Xiang, X. Yu, Thomas Zabel, and Mattias Hammar. Influence of base-region thickness on the performance of pnp transistor-VCSEL. *Optics Express*, 22(22):27398–27414, 2014.

[46] Sui F Lim, Janice A Hudgings, Leonard P Chen, Gabriel S Li, Wupen Yuen, Kam Y Lau, and Constance J Chang-Hasnain. Modulation of a vertical-cavity surface-emitting laser using an intracavity quantum-well absorber. *IEEE Photonics Technology Letters*, 10(3):319–321, 1998.

[47] Xiaodong Gu, Masanori Nakahama, Akihiro Matsutani, Moustafa Ahmed, Ahmed Bakry, and Fumio Koyama. 850 nm transverse-coupled-cavity vertical-cavity surface-emitting laser with direct modulation bandwidth of over 30 ghz. *Applied Physics Express*, 8(8):082702, 2015.

[48] Hamed Dalir and Fumio Koyama. 29 ghz directly modulated 980 nm vertical-cavity surface emitting lasers with bow-tie shape transverse coupled cavity. *Applied Physics Letters*, 103(9):091109, 2013.

[49] J. van Eisden, M. Yakimov, V. Tokranov, M. Varanasi, E. M. Mohammed, I. A. Young, and S. R. Oktyabrsky. Optically decoupled loss modulation in a duo-cavity VCSEL. *IEEE Photonics Technology Letters*, 20(1):42–44, 2008.

[50] Tim David Germann, Werner Hofmann, Alexey M. Nadtochiy, Jan-Hindrik Schulze, Alex Mutig, André Strittmatter, and Dieter Bimberg. Electro-optical resonance modulation of vertical-cavity surface-emitting lasers. *Optics express*, 20(5):5099–5107, 2012.

[51] Petter Westbergh, Johan S. Gustavsson, and Anders Larsson. VCSEL arrays for multicore fiber interconnects with an aggregate capacity of 240 gb/s. *IEEE Photonics Technology Letters*, 27(3):296–299, feb 2015.

[52] C. Chen, P. O. Leisher, C. Long, D. M. Grasso, and K. D. Choquette. High-speed electroabsorption modulation of composite-resonator vertical-cavity lasers. *IET optoelectronics*, 3(2):93–99, 2009.

[53] Krassimir Panajotov, Mateusz Zujewski, and Hugo Thienpont. Coupled-cavity surface-emitting lasers: spectral and polarization threshold characteristics and electrooptic switching. *Optics express*, 18(26):27525–27533, 2010.

[54] H. C. Casey, D. D. Sell, and K. W. Wecht. Concentration dependence of the absorption coefficient forn- andp-type GaAs between 1.3 and 1.6 eV. *Journal of Applied Physics*, 46(1):250–257, 1975.

[55] Yatendra Pal Varshni. Temperature dependence of the energy gap in semiconductors. *physica*, 34(1):149–154, 1967.

[56] MoDo Sturge. Optical absorption of gallium arsenide between 0.6 and 2.75 ev. *Physical Review*, 127(3):768, 1962.

[57] Fabio Novelli, Daniele Fausti, Francesca Giusti, Fulvio Parmigiani, and Matthias Hoffmann. Mixed regime of light-matter interaction revealed by phase sensitive measurements of the dynamical franz-keldysh effect. *Scientific reports*, 3:1227, 2013.

[58] D. A. B. Miller, D. S. Chemla, D. J. Eilenberger, P. W. Smith, A. C. Gossard, and W. T. Tsang. Large room-temperature optical nonlinearity in GaAs/Ga1- x Al x As multiple quantum well structures. *Applied Physics Letters*, 41(8):679–681, 1982.

[59] D. A. B. Miller, D. S. Chemla, T. C. Damen, A. C. Gossard, W. Wiegmann, T. H. Wood, and C. A. Burrus. Electric field dependence of optical absorption near the band gap of quantum-well structures. *Physical Review B*, 32(2):1043, 1985.

[60] Claude Weisbuch and Borge Vinter. *Quantum Semiconductor Structures Fundamentals and Applications*. 1991.

[61] Joseph S Weiner, David AB Miller, and Daniel S Chemla. Quadratic electro-optic effect due to the quantum-confined stark effect in quantum wells. *Applied physics letters*, 50(13):842–844, 1987.

[62] T. E. Van Eck, L. M. Walpita, W. S. C. Chang, and H. H. Wieder. Franz–keldysh electrorefraction and electroabsorption in bulk inp and gaas. *Applied physics letters*, 48(7):451–453, 1986.

[63] R-H Yan, RJ Simes, and LA Coldren. Surface-normal electroabsorption reflection modulators using asymmetric fabry-perot structures. *IEEE journal of quantum electronics*, 27(7):1922–1931, 1991.

[64] G Lengyel, KW Jelley, Reinhart WH Engelmann, et al. A semi-empirical model for electroabsorption in gaas/algaas multiple quantum well modulator structures. *IEEE journal of quantum electronics*, 26(2):296–304, 1990.

[65] D. A. B. Miller, D. S. Chemla, T. C. Damen, A. C. Gossard, W. Wiegmann, T. H. Wood, and C. A. Burrus. Band-edge electroabsorption in quantum well structures: The quantum-confined Stark effect. *Physical Review Letters*, 53(22):2173, 1984.

[66] G Bastard and J Brum. Electronic states in semiconductor heterostructures. *IEEE Journal of Quantum Electronics*, 22(9):1625–1644, 1986.

[67] H. Yamamoto, M. Asada, and Y. Suematsu. Theory of refractive index variation in quantum well structure and related intersectional optical switch. *Journal of Lightwave Technology*, 6(12):1831–1840, Dec 1988.

[68] K. Nishi and T. Hiroshima. Enhancement of quantum confined Stark effect in a graded gap quantum well. *Applied physics letters*, 51(5):320–322, 1987.

[69] P. J. Stevens, M. Whitehead, G. Parry, and K. Woodbridge. Computer modeling of the electric field dependent absorption spectrum of multiple quantum well material. *IEEE journal of quantum electronics*, 24(10):2007–2016, 1988.

[70] Nobuhiko Susa and Tatsushi Nakahara. Design of AlGaAs/GaAs quantum wells for electroabsorption modulators. *Solid-state electronics*, 36(9):1277–1287, 1993.

[71] M. E. Chin and W. S. C. Chang. Theoretical design optimization of multiple-quantum-well electroabsorption waveguide modulators. *IEEE journal of quantum electronics*, 29(9):2476–2488, 1993.

[72] M. K. Chin, P. K. L. Yu, and W. S. C. Chang. Optimization of multiple quantum well structures for waveguide electroabsorption modulators. *IEEE Journal of Quantum Electronics*, 27(3):696–701, 1991.

[73] D. T. Neilson. Optimization and tolerance analysis of QCSE modulators and detectors. *IEEE journal of quantum electronics*, 33(7):1094–1103, 1997.

[74] Thomas H Wood. Multiple quantum well (mqw) waveguide modulators. *Journal of Lightwave Technology*, 6(6):743–757, 1988.

[75] H. Cho, P. Kapur, and K. C. Saraswat. A modulator design methodology minimizing power dissipation in a quantum well modulator-based optical interconnect. *Journal of lightwave technology*, 25(6):1621–1628, 2007.

[76] K-K Law, JL Merz, and LA Coldren. Very low-voltage mbe-grown asymmetric fabry-perot reflection modulator based on superlattice wannier-stark localization. In *AIP Conference Proceedings*, volume 227, pages 210–213. AIP, 1991.

[77] RJ Simes, RH Yan, CC Barron, D Derrickson, DG Lishan, J Karin, LA Coldren, M Rodwell, S Elliot, and B Hughes. High-frequency electrooptic fabry-perot modulators. *IEEE Photonics technology letters*, 3(6):513–515, 1991.

[78] RH Yan, RJ Simes, and LA Coldren. Extremely low-voltage fabry-perot reflection modulators. *IEEE Photonics Technology Letters*, 2(2):118–119, 1990.

[79] Tohya Hiroshima and Kenichi Nishi. Quantum-confined stark effect in graded-gap quantum wells. *Journal of applied physics*, 62(8):3360–3365, 1987.

[80] Takuya Ishikawa and Kunio Tada. Observation of quantum-confined stark effect in a graded-gap quantum well. *Japanese Journal of Applied Physics*, 28(11A):L1982, 1989.

[81] LD Zhu, FK Xiong, CM Wang, CM Chen, YL Hsie, GAB Feak, and JM Ballantyne. Gaas/gaalas graded index separate confinement single quantum well single-mode waveguide electroabsorption light modulator. *IEE Proceedings J-Optoelectronics*, 138(5):313–318, 1991.

[82] Nacer Debbar, Songcheol Hong, Jasprit Singh, Pallab Bhattacharya, and Rajeshwar Sahai. Coupled gaas/algaas quantum-well electroabsorption modulators for low-electric-field optical modulation. *Journal of applied physics*, 65(1):383–385, 1989.

[83] P Zouganeli, PJ Stevens, D Atkinson, and G Parry. Design trade-offs and evaluation of the performance: attainable by gaas-al/sub 0.3/ga/sub 0.7/as asymmetric fabry-perot modulators. *IEEE journal of quantum electronics*, 31(5):927–943, 1995.

[84] Byung Hoon Na, Gun Wu Ju, Chang Young Park, Soo Kyung Lee, Hee Ju Choi, Yong Chul Cho, Yong Hwa Park, and Yong Tak Lee. Electro-absorption modulator with an asymmetric coupled triple quantum well for low-voltage operation. *Optics letters*, 40(14):3376–3379, 2015.

[85] M. A. Afromowitz. Refractive index of ga1- xalxas. *Solid State Communications*, 15(1):59–63, 1974.

[86] Max Born and Emil Wolf. *Principles of optics: electromagnetic theory of propagation, interference and diffraction of light*. Elsevier, 2013.

[87] M. Yakimov, J. van Eisden, V. Tokranov, M. Varanasi, S. R. Oktyabrsky, E. M. Mohammed, and I. A. Young. Concept of feedback-free high-frequency loss modulation in detuned duo-cavity vertical cavity surface-emitting laser. *Journal of Vacuum Science & Technology B, Nanotechnology and Microelectronics: Materials, Processing, Measurement, and Phenomena*, 28(3):C3G32–C3G37, may 2010.

[88] K. Tai, L. Yang, Y. H. Wang, J. D. Wynn, and A. Y. Cho. Drastic reduction of series resistance in doped semiconductor distributed Bragg reflectors for surface-emitting lasers. *Applied Physics Letters*, 56(25):2496–2498, jun 1990.

[89] M. G. Peters, B. J. Thibeault, D. B. Young, J. W. Scott, F. H. Peters, A. C. Gossard, and L. A. Coldren. Band-gap engineered digital alloy interfaces for lower resistance vertical-cavity surface-emitting lasers. *Applied Physics Letters*, 63(25):3411–3413, dec 1993.

[90] R. Kaspi and G. P. Donati. Digital alloy growth in mixed As/Sb heterostructures. *Journal of Crystal Growth*, 251(1-4):515–520, apr 2003.

[91] Paul R Pinsukanjana, Jeremy M Marquis, Jared Hubbard, Mehul A Trivedi, Roger F Dickey, Jerry M-S Tsai, Sam P Kuo, Philip S Kao, and Yung-Chung Kao. Ingaas composition monitoring for production mbe by in situ optical-based flux monitor (ofm). *Journal of crystal growth*, 251(1-4):124–129, 2003.

[92] Ahmad N Al-Omari and Kevin L Lear. Vcsels with a self-aligned contact and copper-plated heatsink. *IEEE Photonics Technology Letters*, 17(9):1767–1769, 2005.

[93] T. F. Krauss, R. M. DeLaRue, P. J. R. Laybourn, B. Vogele, and C. R. Stanley. Efficient semiconductor ring lasers made by a simple self-aligned fabrication process. *IEEE Journal of Selected Topics in Quantum Electronics*, 1(2):757–761, 1995.

[94] Sangwook Kim, Jaechul Park, Changjung Kim, Sunil Kim, Inhun Song, Huaxiang Yin, Jaecheol Lee, Eunha Lee, and Yongsoo Park. High-performance oxide thin film transistors passivated by various gas plasmas. In *The Electrochemical Society, 214th ECS Meeting*, number 2317, page 1. Citeseer, 2008.

[95] M.-C. F. Chang, P. M. Asbeck, K. C. Wang, G. J. Sullivan, Neng-Haung Sheng, J. A. Higgins, and D. L. Miller. AlGaAs/GaAs heterojunction bipolar transistors

fabricated using a self-aligned dual-lift-off processprocess. *IEEE Electron Device Letters*, 8(7):303–305, 1987.

[96] C. L. Chua, R. L. Thornton, and D. W. Treat. Planar laterally oxidized vertical-cavity lasers for low-threshold high-density top-surface-emitting arrays. *IEEE Photonics Technology Letters*, 9(8):1060–1062, 1997.

[97] Eva M. Strzelecka, Robert A. Morgan, Yue Liu, B. Walterson, J. Skogen, Edith Kalweit, S. Bounak, H. Chanhvongsak, Terry Marta, D. Skogman, Jim Nohava, J. Gieske, John A. Lehman, and Mary K. Hibbs-Brenner. VCSEL-based modules for optical interconnects. In *Vertical-Cavity Surface-Emitting Lasers III*, volume 3627, pages 2–14. International Society for Optics and Photonics, 1999.

[98] Ludovic Marigo-Lombart, Alexandre Arnoult, Laurent Mazenq, Pascal Dubreuil, Benjamin Reig, Nicolas Mauran, Hugo Thienpont, Krassimir Panajotov, and Guilhem Almuneau. Single lithography-step self-aligned fabrication process for Vertical-Cavity Surface-Emitting Lasers. *Materials Science in Semiconductor Processing*, 61:35–38, 2017.

[99] Emilie Vanhove, Aliki Tsopela, Laurent Bouscayrol, Adrien Desmoulin, Jérôme Launay, and Pierre Temple-Boyer. Final capping passivation layers for long-life microsensors in real fluids. *Sensors and Actuators B: Chemical*, 178:350–358, 2013.

[100] F. Chouchane, G. Almuneau, O. Gauthier-Lafaye, A. Monmayrant, A. Arnoult, G. Lacoste, and C. Fontaine. Observation of overstrain in the coalescence zone of alas/alox oxidation fronts. *Applied Physic Letters*, 98(26):261921, july 2011.

[101] S. R. Kisting, P. W. Bohn, E. Andideh, I. Adesida, B. T. Cunningham, G. E. Stillman, and T. D. Harris. High precision temperature- and energy-dependent refractive index of GaAs determined from excitation of optical waveguide eigenmodes. *Applied Physics Letters*, 57(13):1328–1330, 1990.

[102] T. Skauli, P. S. Kuo, K. L. Vodopyanov, T. J. Pinguet, O. Levi, L. A. Eyres, J. S. Harris, M. M. Fejer, B. Gerard, L. Becouarn, and E. Lallier. Improved dispersion relations for GaAs and applications to nonlinear optics. *Journal of Applied Physics*, 94(10):6447–6455, 2003.

[103] Vivek Srinivas, John Hryniewicz, Yung Jui Chen, and Colin E. C. Wood. Intrinsic linewidths and radiative lifetimes of free excitons in GaAs quantum wells. *Physical Review B*, 46(16):10193, 1992.

[104] Hidetoshi Iwamura, Hideki Kobayashi, and Hiroshi Okamoto. Excitonic absorption spectra of gaas–alas superlattice at high temperature. *Japanese Journal of Applied Physics*, 23(10A):L795, 1984.

[105] G. Almuneau, R. Bossuyt, P. Colliere, L. Bouscayrol, M. Conde, I. Suarez, V. Bardinal, and C. Fontaine. Real-timein situmonitoring of wet thermal oxidation for precise confinement in VCSELs. *Semiconductor Science and Technology*, 23(10):105021, 2008.

[106] P. E. Ganrou, W. B. Rogers, D. M. Scheck, A. J. G. Strandjord, Y. Ida, and K. Ohba. Stress-buffer and passivation processes for Si and GaAs IC's and passive components using photosensitive BCB: Process technology and reliability data. *IEEE transactions on advanced packaging*, 22(3):487–498, 1999.

[107] David Burdeaux, Paul Townsend, Joseph Carr, and Philip Garrou. Benzocyclobutene (bcb) dielectrics for the fabrication of high density, thin film multichip modules. *Journal of Electronic Materials*, 19(12):1357–1366, 1990.

[108] Alireza Modafe, Nima Ghalichechian, Michael Powers, Michael Khbeis, and Reza Ghodssi. Embedded benzocyclobutene in silicon: An integrated fabrication process for electrical and thermal isolation in MEMS. *Microelectronic Engineering*, 82:154–167, 2005.

[109] Wu-Sheng Shih, J. Yota, and Ketan Itchhaporia. CON-TACT® planarization process of spin-on dielectrics for device fabrication. *Journal of the Electrochemical Society*, 6(3):501–522, 2007.

[110] S. Abada, B. Reig, E. Daran, J. B. Doucet, T. Camps, S. Charlot, and V. Bardinal. Uniform fabrication of thick SU-8 patterns on small-sized wafers for micro-optics applications. In *Micro-Optics 2014*, volume 9130, page 91300R. International Society for Optics and Photonics, 2014.

[111] Yang Yang, Zhen Song, Yuxin Du, and Zheyao Wang. Reactive ion etching characteristics of partially-cured benzocyclobutene. In *Electronic Packaging Technology (ICEPT), 2014 15th International Conference on*, pages 862–866. IEEE, 2014.

[112] H. V. Demir, J. F. Zheng, V. A. Sabnis, O. Fidaner, J. Hanberg, J. S. Harris, and D. A. B. Miller. Self-Aligning Planarization and Passivation for Integration Applications in III–V Semiconductor Devices. *IEEE transactions on semiconductor manufacturing*, 18(1):182–189, 2005.

[113] http://www.dow.com/cyclotene/prod/402646.htm.

[114] Ludovic Marigo-Lombart, Jean-Baptiste Doucet, Aurélie Lecestre, Benjamin Reig, Bernard Rousset, Hugo Thienpont, Krassimir Panajotov, and Guilhem Almuneau. Self-aligned BCB planarization method for high-frequency signal injection in a VCSEL with an integrated modulator. In SPIE, editor, *Semiconductor Lasers and Laser Dynamics VII*. SPIE, apr 2016.

[115] W. B. Weir. Automatic measurement of complex dielectric constant and permeability at microwave frequencies. *Proceedings of the IEEE*, 62(1):33–36, January 1974.

[116] A. Ghannam, C. Viallon, D. Bourrier, and T. Parra. Dielectric microwave characterization of the SU-8 thick resin used in an above IC process. In *Microwave Conference, 2009. EuMC 2009. European*, pages 1041–1044, 2009.

[117] Jiming Song, Feng Ling, G. Flynn, W. Blood, and E. Demircan. A de-embedding technique for interconnects. In *IEEE 10th Topical Meeting on Electrical Performance of Electronic Packaging (Cat. No. 01TH8565)*, pages 129–132, 2001.

[118] Hiroyuki Ito and Kazuya Masuy. A simple through-only de-embedding method for on-wafer S-parameter measurements up to 110 GHz. In *2008 IEEE MTT-S International Microwave Symposium Digest*, pages 383–386, June 2008.

[119] Y. Tretiakov, K. Vaed, W. Woods, S. Venkatadri, and T. Zwick. A new on-wafer de-embedding technique for on-chip rf transmission line interconnect characterization. In *ARFTG 63rd Conference, Spring 2004*, pages 69–72, June 2004.

[120] I. J. Bahl and R. Garg. Simple and accurate formulas for a microstrip with finite strip thickness. *Proceedings of the IEEE*, 65(11):1611–1612, 1977.

[121] E. Hammerstad and O. Jensen. Accurate Models for Microstrip Computer-Aided Design. In *MTT-S International Microwave Symposium Digest*. MTT006, 1980.

[122] https://www.cascademicrotech.com/files/probe-selection guide.pdf.

[123] Anders Larsson, Petter Westbergh, Johan Gustavsson, Åsa Haglund, and Benjamin Kogel. High-speed VCSELs for short reach communication. *Semiconductor Science and Technology*, 26(1):014017, nov 2010.

[124] Philip Moser, James A. Lott, and Dieter Bimberg. Energy Efficiency of Directly Modulated Oxide-Confined High Bit Rate 850-nm VCSELs for Optical Interconnects. *IEEE Journal of Selected Topics in Quantum Electronics*, 19(4):1702212–1702212, jul 2013.

[125] M. Zujewski, H. Thienpont, and K. Panajotov. Electrical design of high-speed electro-optically modulated coupled-cavity vcsels. *Journal of Lightwave Technology*, 29(19):2992–2998, Oct 2011.

[126] J. van Eisden, M. Yakimov, V. Tokranov, M. Varanasi, E. M. Mohammed, I. A. Young, and S. R. Oktyabrsky. Optically Decoupled Loss Modulation in a Duo-Cavity VCSEL. *IEEE Photonics Technology Letters*, 20(1):42–44, 2008.

[127] Anagnostis Paraskevopoulos, Hans-Jürgen Hensel, Wolf-Dietrich Molzow, Holger Klein, Norbert Grote, Nikolai Ledentsov, Vitali Shchukin, Carsten Möller, Alexey Kovsh, Daniil Livshits, et al. Ultra-high-bandwidth (> 35 ghz) electrooptically-modulated vcsel. In *Optical Fiber Communication Conference*, page PDP22. Optical Society of America, 2006.

[128] C. Chen and K. D. Choquette. Multilevel amplitude modulation using a composite-resonator vertical-cavity laser. *IEEE Photonics Technology Letters*, 21(15):1030–1032, aug 2009.

[129] D. M. Pozar. *Microwave Engineering*, 2011.

[130] J. E. Bowers R. Schimpe and T. L. Koch. Characterisation of frequency response of 1.5 um ingaasp dfb laser diode and ingaas pin photodiode by heterodyne measurement technique. *Electronics Letters*, 22(9), 04 1986.

[131] X. Buet, O. Gauthier-Lafaye, A. Monmayrant, F. Lozes-Dupuy, A. Guelmami, S. Calvez, and C. Tourte. Wavelength-stabilised external-cavity laser diode using cavity resonator integrated guided mode filter. *Electronics Letters*, 48(25):1619–1621, 2012.

[132] T. S. Clement, P. D. Hale, K. C. Coakley, and C. M. Wang. Time-domain measurement of the frequency response of high-speed photoreceivers to 50GHz. In *Tech. Dig. Symp. Optical Fiber Measurement*, pages 121–124, 2000.

[133] J. van Eisden, M. Yakimov, V. Tokranov, M. Varanasi, E. M. Mohammed, I. A. Young, and S. Oktyabrsky. Modulation properties of VCSEL with intracavity modulator. In *Proc. SPIE*, volume 6484, page 64840A, 2007.

[134] C. Bringer. *Technologie et caracterisation des VCSELs a diaphragme d'oxyde. Application a la detection en cavite verticale*. PhD thesis, 2005.

[135] J. van Eisden, M. Yakimov, V. Tokranov, M. Varanasi, O. Rumyantsev, E. M. Mohammed, I. A. Young, and S. R. Oktyabrsky. High frequency resonance-free loss modulation in a duo-cavity VCSEL. In *Vertical-Cavity Surface-Emitting Lasers XII*, volume 6908, page 69080M. International Society for Optics and Photonics, 2008.

[136] P. D. Grant, R. Dudek, L. Wolfson, M. Buchanan, and H. C. Liu. Ultra-high frequency monolithically integrated quantum well infrared photodetector up to 75 GHz. *Electronics Letters*, 41(4):214, 2005.